UNIVERSITY OF BIRMINGHAM

LOW FLAMMABILITY HYDROFLUOROCARBON WORKING FLUIDS FOR CRYOGENIC-ENHANCED ORGANIC RANKINE CYCLES

by

SALMAN FARRUKH

A thesis submitted to the University of Birmingham for the degree of

DOCTOR OF PHILOSOPHY

Department of Mechanical Engineering

School of Engineering

College of Engineering and Physical Sciences

University of Birmingham

November 2024

[THIS PAGE IS LEFT INTENTIONALLY BLANK]

Abstract

The global shift away from emission-intensive fossil fuels has spurred the rise of low-carbon cryogenic liquid alternative fuels, such as hydrogen and ammonia. The regasification of cryogenic liquid fuels releases high-quality waste cryogenic exergy, with cryogenic-enhanced Organic Rankine Cycles (ORCs) emerging as the preferred reutilisation technology. This PhD project aims to investigate the feasibility of low flammability hydrofluorocarbons as working fluids for cryogenic-enhanced ORCs, which have traditionally utilised flammable hydrocarbons as working fluids.

An experimental testing rig of the cryogenic-enhanced ORC was constructed, using R410A, hot water, and liquid nitrogen as the working fluid, heat source, and cryogenic heat sink, respectively. The parametric study included varying working fluid flow rates and evaporation temperatures. The operational flexibility, namely preheating of the low-carbon fuel, provided by the cryogenic-enhanced ORC to the downstream applications of cryogenic low-carbon fuels was highlighted. Higher heat exchanger effectiveness was observed at higher temperatures and flow rates. The condenser exhibited the largest exergy destruction, pinpointing optimisation routes. Comparison with hydrocarbon-based cryogenic-enhanced ORCs in literature (Tian et al., 2022) revealed the viability of low flammability hydrofluorocarbon working fluids. The R410A cryogenic-enhanced ORC system achieved a maximum net-work output, thermal efficiency, cryogenic energy efficiency, and cryogenic exergy efficiency of 501.44 W, 7.29 %, 7.67 %, and 8.38 %, respectively.

An advanced dynamic numerical model, based on the physical components employed in the experimental setup, was developed to address the research gap in literature, which only utilise steady-state modelling techniques. Six different low flammability hydrofluorocarbon working fluids were investigated, and system charge was introduced, for the first time, as an objective parameter. The analysis demonstrated that thermophysical properties, particularly density and molar mass, significantly influenced system performance, with lower values providing enhanced system performance. Overcharging led to reduced performance due to condenser flooding and increased

pump suction pressure, while undercharging caused pump cavitation and failure. System charge optimisation depended on the working fluid's density and fixed system volume. Environmental emissions were dependent on leak prevention protocols and marine classification societies-based scenarios were employed. R452B emerged as the optimal working fluid, delivering a maximum net-work output, thermal efficiency, cryogenic energy efficiency, exergy efficiency, and GHG emission reduction of 714.73 W, 10.44%, 11.81%, 7.79%, and 90%, respectively.

"Knowledge is a paradox.

The more one understands,

the more one realises the

vastness of his ignorance"

- *Aristotle*

Acknowledgements

I would firstly like to express my gratitude towards my parents. None of this would have been possible without their continued support over the course of my academic career, especially the patience they have exhibited over the years towards my unruly and unpredictable behaviour. They have allowed me the freedom to always express the truth, regardless of associated consequences. I would also like to thank my siblings for gracefully enduring the relentless torture I have inflicted over the course of our shared existence and pretending to laugh at my rather dry humour.

I would like to thank my supervisor, Dr Dawei Wu, for his continued support and guidance since the start of my academic career. He remains the focal point of my development as a scientist and independent thinker. I am deeply grateful for his sustained understanding of my varying needs, which others would perceive as neurodivergent. His persistent belief in my abilities continues to astonish me. Our mentor-mentee relationship has evolved over the years into something very few people experience; a healthy work-place friendship. I hope our entwined academic futures stay aligned and shine bright.

I would also like to express my sincerest thanks to Mr Anil Taskin, who spent a better part of 3 years developing the experimental testing rig with me. His technical expertise is unparalleled, and I have learnt a lot from him, and he from me (I hope), over the course of our PhD journeys. The countless hours spent discussing and arguing with him in the lab are some of the best and worst memories of my time at UoB, something he would certainly concur and be amused with. Our entire time together can be condensed into one phrase, concocted through a compilation of both our idiosyncrasies, “We are stupid idiots”.

Finally, I would like to express my thanks to everyone who has provided guidance and support, especially when I wasn’t open to suggestions. Suggestions, even when unwelcome, offer a chance at self-reflection, which ultimately leads to sustained persistence.

Mr Salman Farrukh

إِنَّا لِلَّهِ وَإِنَّا إِلَيْهِ رَاجِعُونَ

[THIS PAGE IS LEFT INTENTIONALLY BLANK]

Contents

Nomenclature

Abbreviations

ASHREA	American Society of Heating, Refrigerating and Air-Conditioning Engineers
DNV	Det Norske Veritas
EU	European Union
F-gas	Fluorinated greenhouse gas
GWP	Global Warming Potential
GHG	Green House Gas
HFC	Hydrofluorocarbon
LNG	Liquid Natural Gas
MVR	Mass to Volume Ratio
ORC	Organic Rankine Cycle
UK	United Kingdom

Symbols

ε	Absolute surface roughness
$\left(\frac{dP}{dz}\right)_a$	Acceleration pressure drop
φ_{ALR}	Annual leakage rate
H_{ch}	Chamber height
$cdim$	Characteristic length of exchange
p_c	Critical pressure
ρ_{suc}	Density
$disp$	Displacement
μ	Dynamic viscosity
η	Efficiency
φ_{EOL}	End-of-life leakage rate
h	Enthalpy
s	Enthalpy
E_x	Exergy

I	Exergy destruction rate
dmh_{exp}	Expander enthalpy flowrate decrease
φ_{cv}	Forced convection contribution
F	Fouling factor
ξ	Friction factor
$\left(\frac{dP}{dz}\right)_F$	Friction pressure drop
$\left(\frac{dP}{dz}\right)_z$	Gravitational pressure drop
Q	Heat transfer
φ	Heat transfer coefficient
D_h	Hydraulic diameter
tau	Initial liquid volume
υ	Kinematic viscosity
LT	Lifetime
$\dot{m}_{LN_2}$	Liquid nitrogen mass flow rate
H_{vl}	Liquid-vapor interface height
X_{tt}	Martinelli Parameter
G	Mass velocity
W	Mechanical Work
φ_{NcB}	Nucleate boiling contribution
p	Pressure
dmh_{pump}	Pump enthalpy flowrate increase
x	Quality
rr	Relative roughness
N	Rotational speed
Δp_{sat}	Saturated pressure difference
Cp	Specific heat
$\bar{\mu}$	Specific viscosity
$\bar{v}$	Specific volume
S	Suppression factor
T	Temperature

λ	Thermal conductivity
$\frac{dP}{dz}$	Total pressure drop
u	Velocity
e	Volumetric vapor content
$\dot{m}_{WF}$	Working fluid mass flow rate
M_{wf}	Working fluid specific mass

List of publications

Journal papers:

1. ***"A review of integrated cryogenic energy assisted power generation systems and desalination technologies" – Applied Thermal Engineering* (2022)**

   Salman Farrukh, Dawei Wu, Raya Al-Dadah, Wenzhong Gao, and Zhongcheng Wang

   https://doi.org/10.1016/j.applthermaleng.2022.119836

2. ***"Pathways to Decarbonization of Deep-Sea Shipping: An Aframax Case Study" – Energies* (2023)**

   Salman Farrukh, Mingqiang Li, Georgios D. Kouris, Dawei Wu, Karl Dearn, Zacharias Yerasimou, Pavlos Diamantis, and Kostas Andrianos

   https://doi.org/10.3390/en16227640

3. ***"Cryogenic energy assisted power generation utilizing low flammability refrigerants" – Energy* (2024)**

   Salman Farrukh, Dawei Wu, Anil Taskin, Karl Dearn

   https://doi.org/10.1016/j.energy.2024.132770

4. ***"Experimental investigation of non-flammable hydrofluorocarbons for cryogenic-enhanced Organic Rankine Cycles" – Applied Energy* (2024)**

   Salman Farrukh, Anil Taskin, Dawei Wu, Karl Dearn

   (Submitted for peer-review)

Conference papers:

1. ***"Dual utilization of waste thermal and cryogenic energy onboard an LNG fuelled marine vessel using ORC technology" - Proceedings of International Conference Royal Institution of Naval Architects***

   Salman Farrukh, Dawei Wu, Raya Al-Dadah

List of Figures

List of Tables

Chapter 1. Introduction

1.1 UK climate ambitions

In 2019, the UK became the first country in the world to provide a legislative basis for a net-zero economy by amending the Climate Change Act 2008 [1] [2]. The commitment by the UK government conforms to the Paris Agreement, where global economies pledged to limit global warming to 1.5 degrees above pre-industrial levels [3]. Transitioning toward a low carbon economy will not only spur investment into the development and implementation of clean technologies and infrastructure, ensuring long-term economic prosperity, but also provide an environmental imperative, cementing the UK's position at the forefront of a global green economy.

The heart of the UK net zero strategy lies in the decarbonisation of key sectors such as energy, transport, industry, agriculture, and the built environment. In 2020, the UK announced a multifaceted approach towards decarbonisation, The Ten Point Plan for a Green Industrial Revolution, outlining specific goals and investments required within key sectors [4]. By 2022, the UK had already reduced its greenhouse gas emissions by 46.9 % since 1990, leading among all G7 countries [5]. Most of this reduction comes from a switch towards renewable electricity. The UK has over 10 GW of offshore wind energy, 14 GW of onshore wind energy, and 13 GW of solar energy capacity, contributing to almost 43 % of the UK's electricity demand [6]. To complement the clean electricity, the UK government has also significantly invested in electric vehicles and related infrastructure and introduced a ban on the production and sale of new petrol and diesel cars by 2035 [7]. It is worth noting that this transition towards a green economy has not come at the cost of stunted economic growth, but rather the UK economy has grown by over 75 % compared to 1990 [5].

The UK's sixth carbon budget, due in 2035, provides a set goal during the transitionary period towards a fully carbon neutral economy by 2050 [8]. The budget sets a legally binding target of reducing greenhouse gas emissions by 78 % compared to 1990 and provides recommendations on how different sectors may achieve the targets. It includes

energy (increasing renewable energy deployments across the UK), transport (development of carbon neutral fuels and accelerating the shift towards electric vehicles), buildings (increased emphasis on energy efficiency and utilisation of low-carbon heating alternatives), industry (implementation of carbon capture technologies and a shift away from fossil fuels), and land (carbon sequestration through afforestation and sustainable agricultural practices). The budget has set near terms targets to assess the investment, technological, and policy support required to enable the UK to be a green global economy leader.

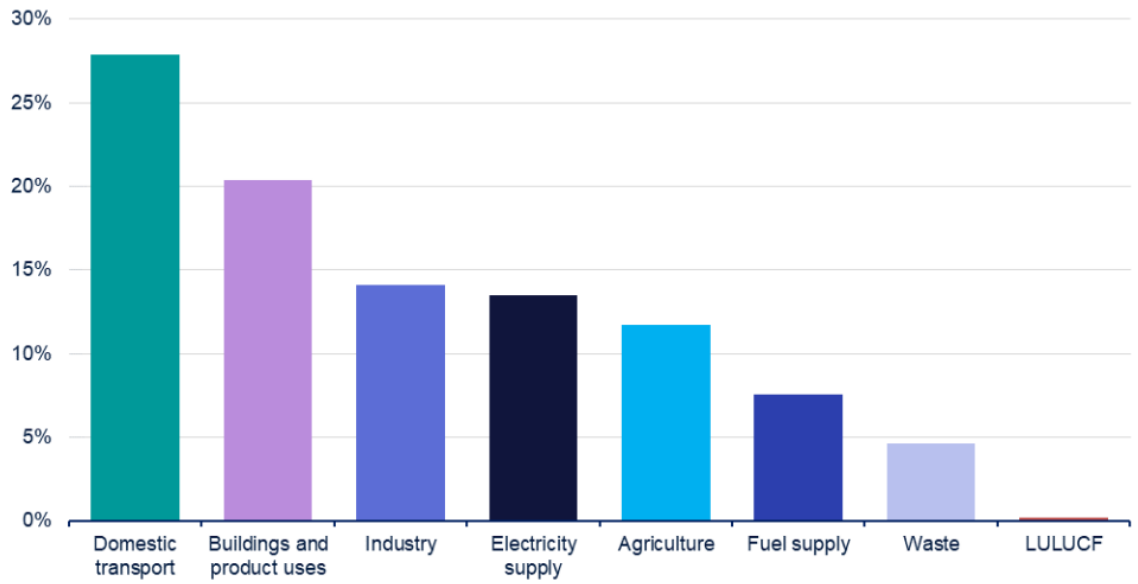

Figure 1.1: The UK greenhouse gas emissions by sector [5].

While commendable, the efforts of the UK government towards achieving the 2050 net zero targets still pose significant challenges. One of the primary obstacles is the deep decarbonisation of hard-to-decarbonise sectors, such as the transportation sector. Recent government reports have shown that the transport sector is the most emissions intensive within the UK, as illustrated in Figure 1.1. In recent years, scientists have concluded that a shift away from emission intensive fossil fuels is the only way to achieve a sustainable transition towards a carbon-neutral green economy [9] [10]. International regulatory bodies have concurred and introduced regulations to limit greenhouse gas emissions. Specifically in the maritime sector, which was responsible for 2.89 % of global emissions in 2018 [11], the International Maritime Organisation (IMO) has introduced a resolution to reduce emissions by at least 50 % by 2050, compared to 2008 levels [12].

The European Union (EU) has introduced even more stringent regulations regarding marine shipping emissions than the IMO, releasing the EU “Fit for 55” directive in 2021 [13]. The directive provides a legal basis to ensure 55 % emissions reduction from the maritime sector by 2030, and a carbon-neutral maritime sector by 2050, compared to 2008 levels. Currently, most of the global shipping fleet relies on Heavy Fuel Oil (HFO) as the combustion medium, releasing significant amounts of carbon dioxide, sulphur oxides, nitrogen oxides, and particulate matter emissions. In fact, HFO releases 5.51 kg equivalent CO_2 emissions on a mass-per-mass basis and is directly responsible for 400,000 premature human fatalities in the EU through anthropogenic emissions [14].

The push from global government policymakers and international regulatory bodies has accelerated the emergence of several low-carbon fuels within the maritime industry. Decarbonisation within the heavy transportation industry cannot be a single unilateral solution but rather requires a multi-faceted approach that evolves constantly and encompasses a variety of different decarbonisation technologies [15]. At the forefront of these lie alternative fuels and electrification. Electrification of the maritime industry has been discussed by many researchers and includes full- or partial-electrification techniques. Indeed, with the UK’s renewable electricity share rising to 50.9 % in 2024, complete electrification could prove to be a viable solution. However, the volumetric energy densities of batteries pose serious space- and weight-constraint issues in deep-sea shipping. Kersey et al. [16] performed a comparative study on fully electric deep-sea vessels and discovered that batteries cannot be cost-effective over distances of 2000 km. Minnehan et al. [17] had previously arrived at the same conclusion, solidifying their stance that batteries are only viable for short duration trips. Thus, liquid alternative fuels are being researched since they have higher volumetric energy density than batteries.

To combat the limitations of electrification, scientists have proposed alternative fuels for combustion engines and fuel cells. The most commercialised of these is Liquified Natural Gas (LNG), and the emerging carbon-neutral fuels are hydrogen and ammonia. Biofuels have also been proposed, which are fuels produced from biomass. Although sustainable fuels, research into the supply chain availability of biofuels has shown that their availability will always be subject to unreliability. In fact, most researchers believe that biofuels simply cannot be produced on a large enough scale to replace fossils fuels

[18] [19] [20] [21] [22] [23]. Hence, current efforts for deep-sea marine decarbonisation are focused on LNG, hydrogen, and ammonia, which are all cryogenic liquid low-carbon fuels (LNG is classed as a transitional fuel and only provides marginal CO_2 reduction compared to hydrogen and ammonia, which are truly carbon neutral).

1.2 Liquid cryogenic alternative fuels

Since the start of the new millennium, Liquified Natural Gas (LNG) has been extensively researched as an alternative to traditional fossil fuels as a combustion medium for deep-sea vessels. The combustion of LNG presents several advantages over HFO combustion, almost eliminating sulphur oxide emissions and greatly reducing nitrogen oxide emissions. Statistically, when compared to the exhaust of HFO, LNG exhaust presents with 11 % less CO_2, 98 % less sulphur oxides, 86 % less nitrogen oxides, and 96 % less particulate matter emissions [24] [25]. The number of LNG-fuelled marine vessels reached 772 in 2023, and the number is projected to increase till 2030 [26]. This comes as a direct result of IMO emission control strategies, which limits fuels with more than 0.5 % sulphur content [27]. The cost-effectiveness of LNG remains a debate among researchers. Yoo [28] states that LNG is very economical for vessels where low capital investment is required, such as CO_2 carriers, while Balcombe et al. [29] argue that the economic viability of LNG is dependent on its price being consistently lower than fossils fuels. Indeed, the global energy crisis of 2021 because of the Russia-Ukrainian conflict showcased the importance of price fluctuation on LNG economic viability. Economics aside, research has shown that while LNG produces lower carbon dioxide, nitrogen oxide, sulphur oxide, and particulate matter emissions, it emits direct methane emissions. The phenomenon, known as methane slip ranges from 2-5.5 g/kWh of methane emissions, which are significantly more potent than CO_2 emissions. In fact, methane has a 100 year GWP of 87, compared to the GWP of 1 for carbon dioxide [14]. Hence, Hwang et al. [30] have recommended the utilisation of LNG as a transitionary fuel up to 2030, with LNG consumption paving the way for truly clean carbon-neutral energy carriers, such as hydrogen and ammonia, to become technologically competitive.

Hydrogen has been hailed as a versatile energy vector, with the potential of long-term deep decarbonisation of hard-to-decarbonise sectors. Indeed, a defining moment in the UK Net Zero goals was the UK government's ambition in utilising hydrogen and alternative hydrogen carrying fuels as the fuels of the future, subsequently releasing the UK Hydrogen Strategy in 2021. The Department of Business, Energy, and Industrial Strategy estimates that 30 % of the UK's total energy consumption would be met by hydrogen by 2050, amounting to 460 TWh of hydrogen [31]. If electrolytic green hydrogen production process using renewable electricity, such as wind or solar, is considered, hydrogen presents as a virtually carbon-free fuel. Hydrogen as an enabler in the transportation industry takes the form of combustion engines and fuel cells. Extensive feasibility studies have revealed that hydrogen may be the key for long-term sustainable transportation [32] [33]. In terms of combustion, hydrogen presents with several advantages over traditional fossil fuels, such as diesel. The heating value of hydrogen is three times higher than diesel, and it presents with a fast combustion speed and high diffusivity with varying concentrations. In fact, only nuclear energy has a higher heating value than hydrogen [34]. One versatility hydrogen offers over traditional fossil fuels is its ability to undergo electrochemical changes to produce electricity without the need for combustion. Fuel cells are devices that realise these electrochemical reactions, where hydrogen undergoes oxidation to produce an electric current. The most notable achievement of fuel cells is the production of water and heat as byproducts, with virtually no emissions released. Hence, if green hydrogen is utilised, clean electricity is produced. This has led to the development of hybrid- and fully-electric powertrains, powered by hydrogen fuel cells, for land- and marine-based transportation applications [33]. Figure 1.2 illustrates a roadmap for hydrogen as a green economy enabler.

Ammonia, often referred to as a hydrogen carrier, has also emerged as carbon-neutral fuel capable of being utilised as a combustion medium, and in fuel cells for electricity production. In fact, specifically within the maritime sector, the DNV classification society projects that ammonia will take 25 % of the market share of maritime fuels by 2050 and will be the preferred fuel for new build ships by 2042 [35]. The utilisation of ammonia in fuel cells and combustion engines has been widely researched, partly because ammonia has been used extensively as an important industrial chemical and agricultural fertiliser

and is readily available and has an established supply chain [36]. Additionally, the green ammonia production process can be achieved using electrolytic green hydrogen and nitrogen captured from the air, which results in a much lower price than green hydrogen, due to lower investment costs related to ammonia infrastructure and storage as compared to hydrogen, specifically in the marine industry requiring long-distance transmission [10]. Ammonia fuel cells either utilise the hydrogen content of ammonia by utilising a cracker or directly utilise ammonia in solid oxide fuel cells. Zhang et al. [37] reported that ammonia fuelled fuel cells could present as an alternative to hydrogen fuel cells, where the storage of hydrogen, due to its low volumetric energy density, poses a limitation. Nevertheless, ammonia combustion produces NO_x emissions, which presents significant challenges, but according to Ref. [36], research is underway for ammonia exhaust gas treatment to minimise this effect through catalytic treatment.

The volumetric energy densities and the gravimetric energy densities of different fuels are illustrated in Figure 1.3. It can be clearly seen that while hydrogen has the highest energy content on a mass-basis, the volumetric energy density of hydrogen is the worst out of all fuels, owing to its low density and small particle size. LNG presents with a much higher volumetric energy density than hydrogen and ammonia. However, due to its emission intensive combustion, LNG will soon be phased-out, as pointed out by Ref. [15], in favour of hydrogen and ammonia.

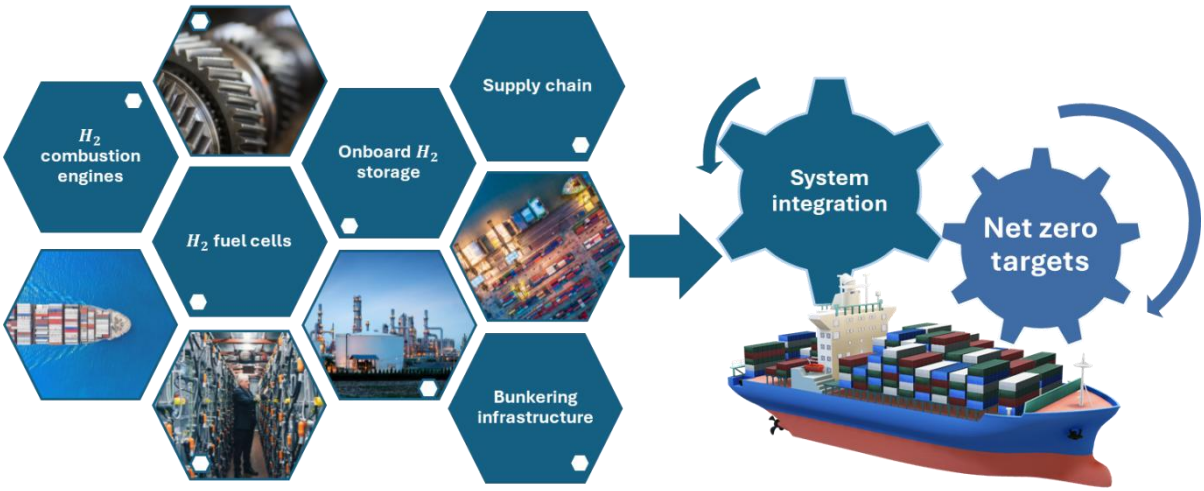

Figure 1.2: Hydrogen roadmap for the marine industry

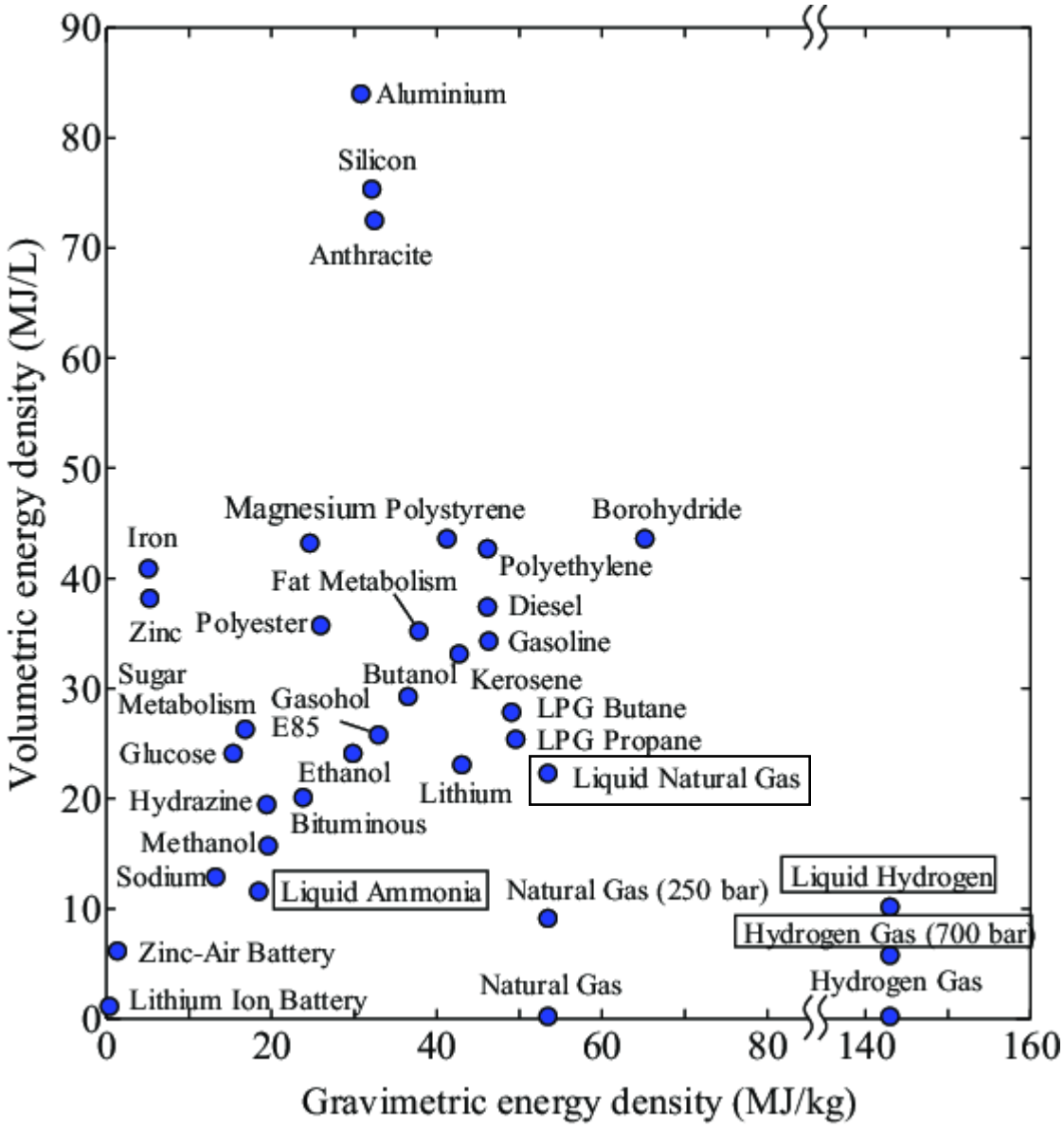

Figure 1.3: Energy densities of different fuels [5]

Comparing the volumetric energy densities of natural gas with LNG and gaseous hydrogen and ammonia with liquid hydrogen and ammonia from Figure 1.3 clearly indicates the benefits of fuel liquification. However, it must be noted that while these fuels may be stored as a cryogenic liquid, their utilisation in combustion engines and fuel cells requires regasification, and hence the liquification energy is wasted.

1.3 Cryogenic energy quantisation

The storage conditions for alternative liquid cryogenic low-carbon fuels are presented in Table 1.1, along with the average liquification energy exhausted in the process.

Table 1.1: Storage requirements for alternative cryogenic fuels [38] [39] [40] [41].

Cryogenic fuel	Storage conditions		Liquification energy (MJ/kg)
	Temperature (°C)	Pressure (bar)	
LNG (Methane)	-162	1.1	6.7
Liquid hydrogen	-253	1.1	36
Liquid ammonia	-34	1.1	0.4

To fully gauge the cryogenic potential of each fuel, an exergy analysis must be conducted to determine the maximum theoretical cryogenic exergy available, released as a sum of the heat of vaporisation and the sensible heat required to reach the reference state temperature [42]. The reference state is usually set to 15 °C at atmospheric pressure, represented as state 0 in Table 1.2. Once the thermophysical properties of the cryogenic fuels have been determined at their storage conditions, represented as state 1 in Table 1.2, the following equation can be used to calculate the maximum cryogenic exergy available to reach the reference state:

$$e_{x1} = h_1 - h_0 - T_0(s_1 - s_0) \quad (1.1)$$

The thermophysical properties of the alternative cryogenic fuels are presented in Table 1.2, along with the maximum available cryogenic exergy.

Table 1.2: Thermophysical properties of liquid cryogenic low-carbon fuels [43]

State points	Temperature (°C)	Pressure (bar)	Enthalpy (kJ/kg)	Entropy (kJ/kg K)	Available waste cryogenic exergy (MJ/kg)
Liquified Natural Gas (Methane)					
0	15	1.01	887.75	6.600	1.015
1	-162	1.01	-1.8	-0.016	
Liquid Hydrogen					
0	15	1.01	3786.7	52.908	11.467
1	-253	1.01	-1.2291	-0.060	
Liquid Ammonia					
0	15	1.01	1668.1	7.001	0.286
1	-33.4	1.01	191.59	0.882	
Liquid Nitrogen					
0	15	1.01	298.85	6.8007	0.725
1	-196	1.01	-122.44	2.8288	

Many applications have been proposed for the reutilisation of this high-quality waste cryogenic exergy. The most promising application that has emerged is the utilisation of cold energy as the heat sink in power generation cycles, significantly increasing their efficiency and system performance [44]. One of the main limitations of these low carbon fuels are their low volumetric energy densities, requiring considerable storage capacity. Deep-sea marine vessels, one of the hardest to decarbonise, present as the ideal application for these cryogenic fuels. The waste heat availability, and utilisation, from alternative fuel combustion or fuel cell technologies has been extensively studied. The generalised quantisation of waste heat in terms of exact energy and exergy content is inherently difficult, due to the dependency on engine or fuel cell size and exhaust gas/fluid flow rates. However, these can generally be characterised in terms of temperatures. Low-grade waste heat, comprising of 66 % of total global waste heat, has a temperature below 200 °C. Most marine engines, due to exhaust gas recirculation, and

hydrogen proton exchange membrane fuel cells emit waste heat within this range [45] [46] [47] [48]. With energy efficiency measures already in place on marine vessels, the exhaust gas temperatures have decreased considerably, paving the way for low-temperature power generation cycles that can utilise the cryogenic energy as the heat sink [49] [50]. Low temperature waste heat cannot be easily utilised for steam generation onboard marine vessels, hence presenting an opportunity for power generation cycles, that can utilise this low temperature heat efficiently. Furthermore, these low temperature power generation cycles also have the ability to reutilise the cryogenic regasification energy from low-carbon fuels.

Organic Rankine Cycles (ORCs) have emerged as the ideal dual waste energy reutilisation technology. While considerable theoretical research has been done on low-temperature cryogenic enhanced Organic Rankine Cycle technologies [44], many gaps exist in literature regarding experimental analysis of these technologies. Another factor that is consistently overlooked in literature is the working fluid flammability of cryogenic enhanced ORC technologies. The research gap has been identified through an extensive literature review and presented in *Chapter 2,* and is displayed in Figure 1.4. Figure 1.4 firstly presents the production of the low-carbon fuels (except in the case of LNG), and their subsequent liquefication to maximise the storage capacity. The liquefied cryogenic fuels must then be regasified for utilisation in either combustion engines or fuel cells, where waste thermal heat is released. The regasification process releases high quality cryogenic energy. Thus, the waste thermal energy acts as the heat source for the power generation cycles, whereas the cryogenic energy acts as the heat sink. In terms of the cryogenic-enhanced ORCs, the research gap is presented in detail in Section 2.6.

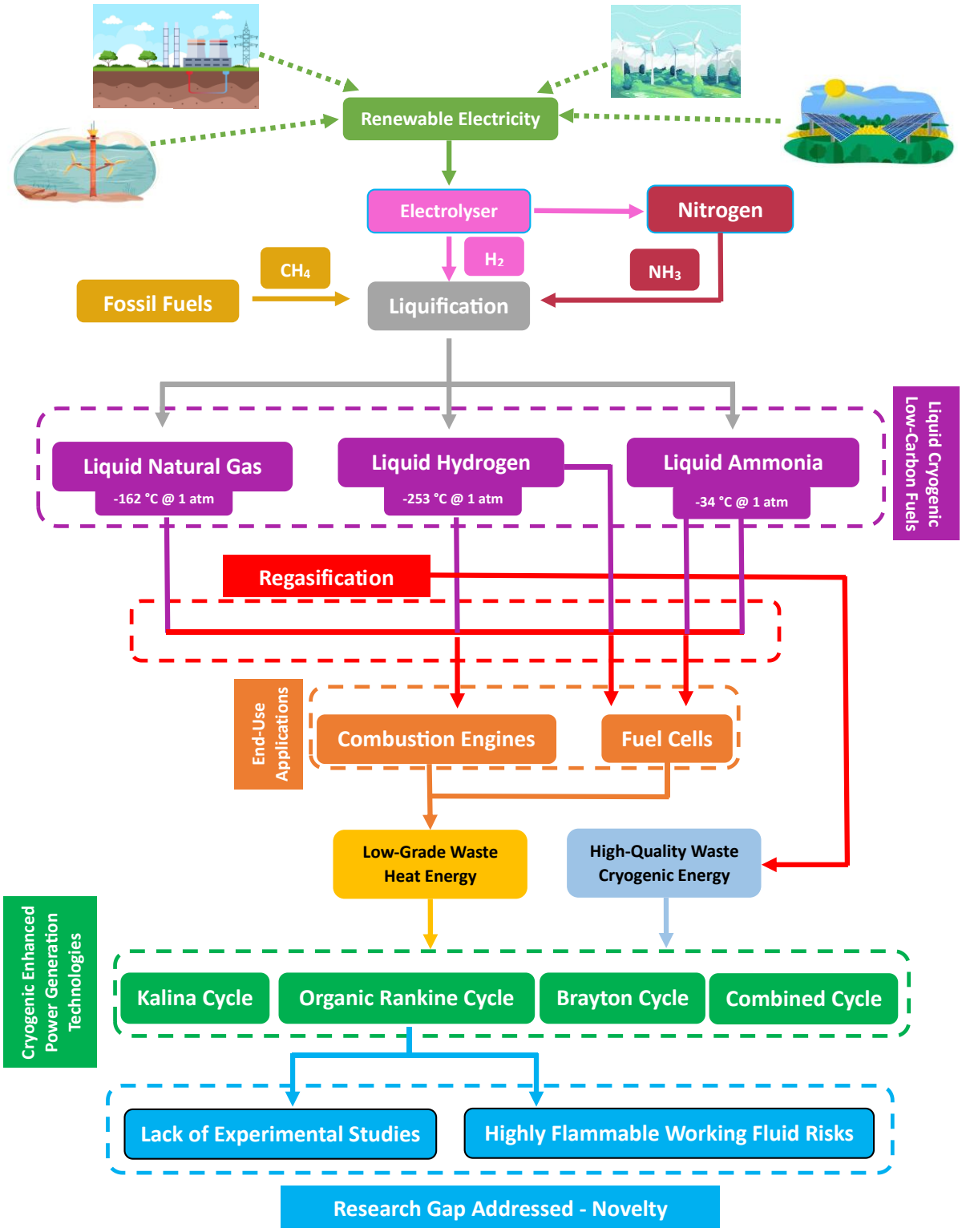

Figure 1.4: Novelty of the research study within the low-carbon green economy

1.4 Aims and objectives

The aim of this PhD research is to numerically and experimentally investigate cryogenic-enhanced Organic Rankine Cycles for dual utilisation of waste thermal energy and waste cryogenic energy by utilising low-flammability hydrofluorocarbons. The research consists of extensive dynamic numerical modelling of a micro-scale Organic Rankine Cycle and experimental whole system analysis for feasibility and parametric optimisation. The feasibility of different low flammability hydrofluorocarbons was assessed using the numerical model, and one refrigerant was used to prototype the experimental setup. The research objectives are summed up as follows:

1. To identify the main components of the Organic Rankine Cycle experimental rig, suitable for cryogenic temperature applications, considering a whole-systems approach towards the establishment of cryogenic testing rig.
2. To select the low flammability working fluids from an environmental and regulatory perspective, stressing the importance and novelty of low flammability refrigerants while simultaneously not compromising on system key performance indicators.
3. To develop the dynamic numerical model of the micro-scale cryogenic Organic Rankine Cycle in Siemens Amesim to determine optimal system working conditions. These involve identification of system variables that would lead to steady-state operation, such as flow rates, evaporation and condensation pressures and temperatures, and cryogenic cooling source inlet conditions.
4. To establish the experimental testing rig and testing one of the chosen working fluids. This involves understanding system charging and discharging procedures and testing system behaviour leading to steady-state based on the system variables obtained from the numerical model
5. To validate the dynamic numerical model through the experimental testing rig by comparing key performance indicators at specific system operational parameters, such as evaporation temperatures.

1.5 Thesis layout

This PhD thesis has been divided into seven chapters. The layout of the chapters is described below:

- *Chapter 1. Introduction*: introduces the background and motivation of the thesis and defines the aims and objectives.
- *Chapter 2. Literature review*: reviews the cryogenic energy reutilisation potential of the direct expansion cycle, organic Rankine cycle, Brayton cycle, and Kalina cycle for power generation applications present in literature and identifies the research gap and the novelty of the study.
- *Chapter 3. Methodology*: provides the detailed experimental system configuration, component and sensor selection, and rig setup of the dual waste thermal and cryogenic energy reutilisation Organic Rankine Cycle system for the investigation of non-flammable working fluids.
- *Chapter 4. Dynamic Numerical Model*: supplies the dynamic numerical model of the cryogenic enhanced Organic Rankine Cycle in the industrial thermodynamic modelling software Siemens Amesim. An environmental, regulatory, and performance framework is employed for the selection of suitable low flammability. Also expresses the thermodynamic energy and exergy model to define system key performance indicators.
- *Chapter 5. Experimental Analysis*: presents the results of the experimental parametric analysis of the chosen low flammability working fluid and describes the system charging procedure.
- *Chapter 6. Dynamic Numerical Model Analysis*: presents the parameter search conducted using the dynamic numerical model developed in Siemens Amesim, and provides a comparative analysis, based on the key performance indicators, of the selected low flammability working fluids.

- *Chapter 7. Conclusions and future work:* presents the validation of the dynamic numerical model through the experimental analysis, summarises the key discoveries of the research, and provides avenues for future research endeavours.

Chapter 2. Literature Review[1]

2.1 Advent of cryogenic energy utilisation for power generation applications

This chapter delves into the relevant literature utilising cryogenic waste energy for power generation applications. Firstly, the Direct Expansion cycle for the mechanical exergy utilisation of LNG is discussed. Then, the Organic Rankine Cycle is presented, with its many different configurations and integrations with the Direct Expansion cycle. For high-temperature waste heat utiilisation, the Brayton Cycle is reviewed, utilising cryogenic fluid regasification as the heat sink. Finally, the Kalina Cycle, which utilises ammonia-water mixture as the working fluid, is evaluated for cryogenic energy reutilisation. Hence, the research gap is identified and presented to conclude the chapter.

Rising global greenhouse gas emissions during the twentieth century forced global governments to move away from emission intensive fossil fuels, such as coal, towards natural gas. The first Liquified Natural Gas (LNG) process was developed by Godfrey Cadot, to address the concerns surrounding volumetric energy density of natural gas [51]. Since natural gas liquification is an energy intensive process, scientists started researching ways to utilise the high-quality waste cold energy present in LNG, since LNG can only be utilised as a gas for combustion processes. In terms of power generation applications of this high-quality cryogenic energy, the breakthrough came from Grienpentrog and Sacharendt [52], who proposed a cryogenic assisted closed Brayton cycle. The novelty of their work lied in the utilisation of the LNG cold energy to cool the working fluid at the compressor inlet, thereby increasing the cycle efficiency and initiating LNG regasification. Building on the work of Grienpentrog and Sacharendt [52], Krey [53] conducted an optimisation study on the Brayton cycle and discovered that nitrogen was the optimal working fluid for cryogenic assisted Brayton cycle. Together with Angelino [54], who proposed the first cryogenic energy assisted Organic Rankine Cycle

[1] The literature review conducted in this chapter was published in the journal "Applied Thermal Engineering" under the title "A review of integrated cryogenic energy assisted power generation systems and desalination technologies". https://doi.org/10.1016/j.applthermaleng.2022.119836

(ORC), Ref. [52] [53] are considered to be the pioneers for the power generation applications of cryogenic energy reutilisation.

The commercialisation of LNG in Japan in the 1970s led to the development and implementation of power generation technologies reutilising LNG cold energy, with the world's first commercial cryogenic assisted power generation plant starting operation in 1979 [55] [56]. To fully utilise the potential of LNG cryogenic energy, a combined cycle was used, providing an output of over 400 kW. The LNG cryogenic energy was utilised by the Organic Rankine Cycle (detailed in Section 2.3), whereas the mechanical exergy of the LNG was utilised by the Direct Expansion (DE). Building upon the success of the first commercial cryogenic assisted power generation plant, the Japanese natural gas company "Osaka Gas" commissioned a 1450 kW plant, which became operational in early 1980 [56]. By the end of the 1980s, Japan was considered world-leading in cryogenic energy assisted power generation technologies [57] [58]. Table 2.1 illustrates the commercial cryogenic assisted power generation plants developed in Japan in the twentieth century.

Table 2.1: Chronological advent of commercial LNG cryogenic assisted power generation technologies in Japan in the twentieth century [59].

Date of commission	Location	Cycle configuration	Power output (MW)
December, 1979	Osaka	Steam Rankine Cycle	1.45
December, 1981	Chita City	Steam Rankine Cycle	1
February, 1982	Osaka	Steam Rankine Cycle + Direct Expansion	6
November, 1982	Fukuoka	Steam Rankine Cycle + Direct Expansion	9.4
June, 1983	Chubu	Steam Rankine Cycle + Direct Expansion	7.2
March, 1984	Chubu	Steam Rankine Cycle + Direct Expansion	7.2
September, 1984	Niigata	Direct Expansion	5.6

April, 1985	Tokyo	Organic Rankine Cycle	4
May, 1986	Kawasaki	Direct Expansion	3.3
March, 1987	Kansai	Steam Rankine Cycle	2.8
September, 1987	Kawasaki	Direct Expansion	8.8
February, 1989	Kansai	Direct Expansion	2.4
December, 1989	Kansai	Steam Rankine Cycle + Direct Expansion	7
September, 1991	Kawasaki	Direct Expansion	1.5
March, 2000	Kansai	Direct Expansion	8.8

The commercialisation of cryogenic energy assisted power generation technologies in Japan spurred development in other countries. Different optimisation techniques were applied by researchers to maximise the cryogenic energy reutilisation. Najjar and Zaamout [60] [61] performed a working fluid optimisation study on the closed Brayton cycle. In two different studies, they investigated hydrogen and propane, achieving 5 MW power output with hydrogen and 2 MW with propane, concluding that system performance is greatly improved by introducing a cryogenic heat sink. To circumvent the immediate utilisation of the waste cryogenic energy, Uchiyama et al. [62] developed an air liquification system for storing energy. Hence, the waste cryogenic energy could be stored as liquid air, and the author's concluded that liquid air storage was more cost-effective than compressed air, presenting higher power conversion efficiencies. Ref. [62] arrived at this conclusion by stating that the compressor power can be reduced by two thirds using LNG regasification energy, compared to compressing from room temperature, and reheating the liquid air removes the need for an additional compressor before the turbine. By the mid-1990s, complex cycle configurations were being developed. A complex integration of the traditional steam Rankine cycle with two organic Rankine cycles, utilising propane and methane as working fluids, was proposed by Wong [63]. He concluded that combined cycles could achieve better system performance, evidenced

in his study with the combined cycle providing a 3 MW increase in power output from the standalone cryogenic assisted closed Brayton cycle. Cheisa [64] performed a comparative study on different combined cryogenic assisted power generation cycles and arrived at the same conclusion, although questioned the economic viability of combined cycles. Bisio et al. [65] developed a combined power generation cycle using solar energy as the heat source and LNG cold energy as the heat sink. They used nitrogen as the working fluid for the Brayton cycle, achieving a thermal efficiency of 18.5 % and an exergy efficiency of 17.3 %. Further cycle integration was proposed by Hisazumi et al. [66], who combined the open Brayton cycle with the traditional Rankine cycle, using steam as the working fluid, for waste cryogenic energy reutilisation, and then added the direct expansion cycle for mechanical exergy utilisation of the LNG. By the end of the twentieth century, many different cycle configuration were proposed, with different objective parameter optimisation and analysis techniques [67].

The optimisation techniques of power generation technologies, utilising cryogenic energy as the heat sink, have evolved over the years and four key performance indicators have emerged. A combination of these four key performance indicators, namely the thermal efficiency, exergy efficiency, net-work output, and GHG emissions/ environmental impact, are often used to gauge system performance [15]. The performance of cryogenic assisted power generation cycles on multiple system variables, including the working fluid and cycle configurations. While the optimisation of such systems requires a simultaneous multi-faceted approach, performance indicators often require trade-off to achieve optimal system performance. The first aspect of designing any power generation system is to select the specific power generation cycle, requiring consideration of many different factors, the foremost of which is feasibility, safety, and performance. While many different cryogenic assisted power generation cycles exist, each is suited to different working conditions and a particular application to maximise system performance.

2.2 Direct expansion

The direct expansion cycle, illustrated in Figure 2.1, utilises the mechanical exergy of the cryogenic energy source and has only been tested with LNG. Based on the physical expansion of LNG, due to pressure differentials, through a turbine to generate mechanical power [57] [68], the direct expansion cycle starts with a supply of LNG, stored at -161 °C at atmospheric pressure. The LNG is then pressurised using a cryogenic pump and flows to evaporator, where it vaporises to produce high-pressure vapor. The pressurised vapour then passes through a turbine and rotates the turbine shaft, producing mechanical power. The expanded vapour is then heated to reach the required natural gas supply temperature.

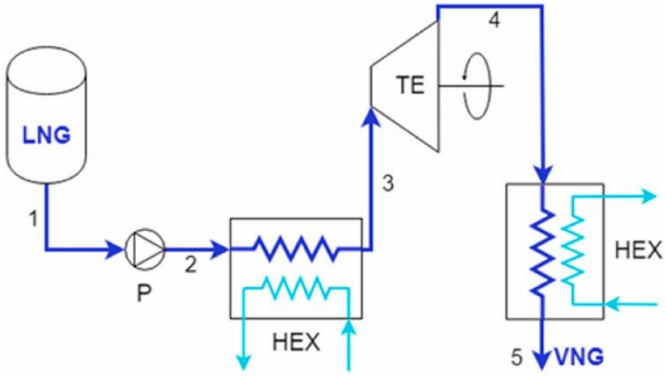

Figure 2.1: Direct expansion cycle mechanism [69]

Due to the simplicity of the structure, research on standalone direct expansion cycles in literature is scarce. The integration of an additional turbine in the direct expansion cycle was proposed by Franco et al. [70], leading to a two-stage direct expansion cycle. The exhaust of the first turbine served as the inlet of the second turbine, achieving a maximum power output of 160 kJ/kg of LNG. Other researchers have also proposed similar high-pressure direct expansion cycles, but these only utilise the mechanical exergy of the cryogenic fuel and waste the high-quality cryogenic exergy [71] [72]. Hence, the feasibility of standalone direct expansion cycles is always under question since they don't utilise any cryogenic regasification energy and rely on the mechanical exergy, and it is recommended to combine direct expansion cycles with other cycles so as to utilise the cryogenic exergy of the liquified low-carbon fuels.

2.3 Organic Rankine Cycle

Having been considered an efficient and simple waste heat utilisation technology for decades, Organic Rankine Cycles (ORCs) have simple cycle configurations and can work over a wide range of waste energy input temperatures, effectively reutilising low temperature waste energy. They work on the principle of the traditional Rankine cycle, with the distinction that the ORC utilises organic working fluids rather than water [73]. Figure 2.2 illustrates the configuration of a simple ORC system, utilising the waste cold energy of LNG in the condenser. The cycle starts at the pump inlet, which pressurises the liquid working fluid and induces flow. The pressurised liquid working fluid then flows to the evaporator. In the evaporator, the liquid working fluid changes phase to vapour by absorbing the heat from the heat source. The pressurised vapour working fluid then flows to the expander. The expansion device, normally a turbine, is responsible for producing the mechanical work output. When the pressurised high temperature vapour rotates the blades if the expander, it rotates the connected expander shaft to deliver mechanical power. The expansion process reduces the pressure of the vapor, and it then condenses in the condenser, by rejecting heat to the cryogenic fuel heat sink, back into liquid phase. During the heat rejection in the condenser, regasification of the cryogenic liquid fuel occurs [57].

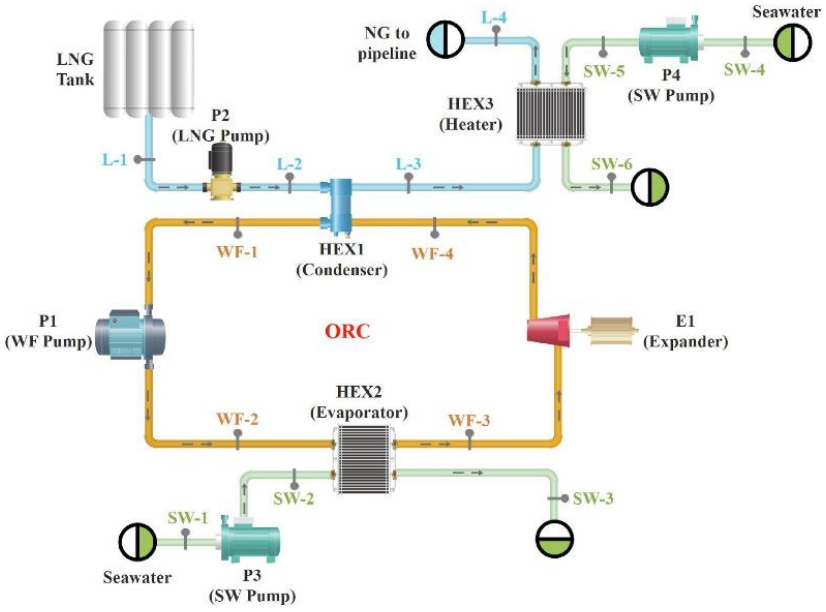

Figure 2.2: Organic Rankine Cycle with LNG as the cold energy heat sink [74]

Many different techniques for optimisation of cryogenic assisted ORCs for waste energy recovery have been adopted over the last two decades, but the foremost of these include the cycle configuration and working fluid selection.

2.3.1 Cycle configuration

The first step in designing an Organic Rankine Cycle system involves the cycle configuration selection process. ORCs are a mature waste energy recovery technology, with researchers proposing many different cycle configurations. Often, these cycle configurations can be grouped into two categories: multi-stage ORC configurations and cascade ORC configurations. Figure 2.3 illustrates the different types, non-exhaustive, of ORC configurations available in literature.

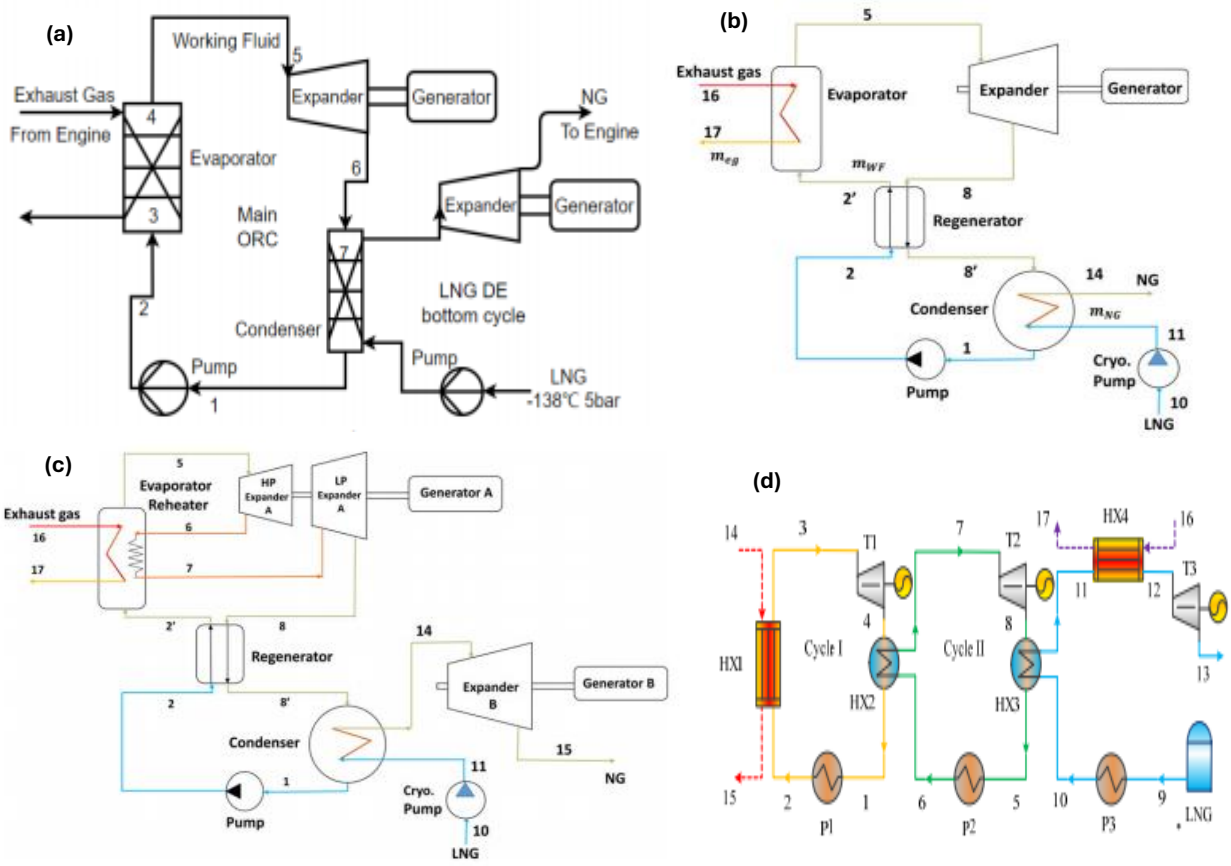

Figure 2.3: Organic Rankine Cycle configurations integrated with direct expansion cycle: (a) simple; (b) recuperative; (c) recuperative two-stage; (d) cascade two-stage [75] [76].

Multi-stage ORC configurations include the utilisation of one ORC cycle, but with multiple expanders or recuperative heat exchangers. Many different multi-stage ORC configurations have been proposed in literature, but often include simple, recuperative, and two- or three-stage (multiple expanders) ORC configurations, usually combined with the direct expansion cycle to maximise cycle efficiency [77]. Multiple comparative studies have been conducted on these different ORC configurations to determine the most efficient cycle configuration.

The interest of many researchers has been the integration of the direct expansion cycle with the ORC. The idea behind this integration comes from the mechanical exergy of the LNG, which must be pressurised for pipeline distribution. Researchers proposed pressuring the LNG to a higher pressure than the distribution pressure, then vaporising it in the condenser of the ORC system and expanding it with an additional expander to provide additional power. To prove that the direct expansion cycle integration with the ORC does indeed increase system performance, many researchers performed comparative studies. Rao et al. [78] integrated the direct expansion cycle with a recuperative ORC, with the novelty that the heat source for the ORC would be provided by solar energy. The recuperator ensured that the working fluid would be pre-heated from the expander exhaust heat before it was heated by the solar energy, thereby increasing system efficiency. They reported that the area of the solar collector could be decreased by 82 %, with a decrease of nearly 32 % in the overall heat transfer area, when compared to the standalone recuperative ORC without direct expansion cycle integration. They also reported a combined system exergy efficiency of 10.62 %, whereas the standalone recuperative ORC exergy efficiency was 3.96 % and the standalone direct expansion exergy efficiency was 7.39 %, clearly evidencing the increased system performance of the combined cycle. Liu and Gao [79] also achieved similar results for their combined cycle, integrating the simple ORC with the direction expansion cycle, reporting an increase of more than 60 % in thermal efficiency compared to the standalone simple ORC configuration.

Multiple expansion processes within a single ORC, utilising multiple expanders, was first proposed by Liu et al. [80]. In their proposed novel multi-stage configuration, the ORC working fluid is expanded twice, first by the high-pressure turbine, and then the exhaust

of the high-pressure turbine is reheated and expanded again by the low-pressure turbine, utilising LNG cryogenic waste energy in the condenser. Utilising a binary mixture of CF_4 and propane, they achieved a 66 % increase in system performance metrics compared to the standalone ORC configuration, with the system efficiency and power generation increasing from 14.1 % and 124.1 kJ/kg to 23.5 % and 206.42 kJ/kg, respectively. They concluded that for high temperature heat sources, multi-stage ORCs will always outperform standalone simple ORC configurations. Tsougranis and Wu [75] investigated the hydrocarbons C_3H_8, C_4H_{10}, and C_2H_4 as working fluids for single- and two-stage recuperative ORCs for LNG-fuelled marine vessels. They reported that at the optimum working conditions, using ethylene as the working fluid, the two-stage ORC outperformed the single-stage ORC by 33 %, providing a thermal efficiency and work output of 34.7 % and 587 kW, compared to the single-stage ORC thermal efficiency and work output of 23.58 % and 428 kW. The results of these two studies were reiterated by Ref. [81] [82] [83], conclusively exhibiting the efficacy of utilising multi-stage ORCs over simple ORC configurations.

Cascade ORC configurations differ from multi-stage ORC configurations in that the cascade ORC systems utilise two or more different ORCs, integrated through the utilisation of a common heat exchanger. The first cycle, referred to as the top cycle, utilises the waste thermal energy in its evaporator. After expansion, the top cycle condenses by rejecting the heat to the working fluid of the second cycle. Hence, the evaporator of the second cycle doubles-up as the condenser of the first cycle. The cryogenic waste energy is utilised in the last cycle, referred to as the bottom cycle [81] [83] [84] [85] [86]. The illustration of a two-stage cascade ORC configuration can be seen in Figure 2.3 (d). Cascade ORCs have been investigated by several researchers to determine their feasibility. Choi et al. [85] investigated the two-stage and the three-stage cascade ORC configurations using ethane and propane as the working fluids, Sun et al. [81] proposed a two-stage cascade ORC configuration integrated with the direct expansion cycle, and Li et al [87] investigated the influence of solar energy heat source on the performance of a two-stage cascade ORC. Although using different fluids and objective parameters, all studies agreed that the cascade ORC configurations are only feasible at medium to high waste heat temperatures (> 200 °C), since the top cycle

requires a higher temperature (> 200 °C which is higher than low grade waste heat) to be able to reject low temperature waste heat (after expansion) as the energy input to the bottom cycle.

Organic Rankine Cycle configurations have clearly evolved from their simple configuration to encompass increasingly complex configurations involving the utilisation of multiple expansion processes, recuperative heat exchangers, and cascade cycles with co-dependent heat exchangers. While the inclusion of these process has undoubtedly optimised the performance metrics of the cryogenic ORC for maximum waste energy recovery, the question regarding economic feasibility and cycle complexity makes the desirability of such configurations uncertain [44]. Furthermore, the cycle configuration is heavily reliant on the specific application, as complex multi-stage ORC configurations generally require high temperature waste heat source. The overly complex system configurations with high capital costs and extensive components are unlikely to be commercialised. Hence, in most cases, especially in the low- to mid-range temperature heat sources (<200 °C), it might be better to adopt the simple ORC configuration, so as to trade-off the performance against the inevitable high-cost and extensive maintenance requirements of complex multi-stage and cascade ORC system configurations.

2.3.2 Working Fluids

Once the ORC system configuration has been decided, a suitable working fluid needs to be selected. The selection criteria of working fluids for cryogenic ORCs across multiple thermophysical properties, such as density, cryogenic saturation temperatures, low critical temperatures, and low specific heat capacity. It also includes the availability and cost of the working fluid, while considering the toxicity and flammability of the working fluid. Due to the rising global emissions, the environmental impact of working fluids cannot be neglected, and the selected working fluid needs to have zero Ozone Depletion Potential (ODP) and a low Global Warming Potential (GWP) [57] [88] [89].

Discounting the flammability selection criterion, hydrocarbons have traditionally been utilised as the working fluids in cryogenic ORCs, due to their low environmental impact and high system performance capabilities. Several researchers have performed

comparative studies to prove that hydrocarbons indeed perform better than traditional fluorine-based ORC working fluids. Emadi et al. [90] performed a working fluid optimisation study for their two-stage cascade cryogenic enhanced ORC system using 20 different working fluids and concluded that the combination of ethane and pentane exhibited the highest system performance. They achieved a maximum system exergy efficiency 51.6 % with a net-work output of 1.04 MW. Rao et al. [78], investigating 16 different working fluids and achieving the best performance with propane and propene, Sun et al. [81], comparing 64 working fluids for their two-stage cascade ORC configuration reporting ethane as the best performing working fluid, and Sun et al. [91], proposing a novel multi-fluid condenser for their cryogenic ORC achieving a maximum exergy efficiency of 49.68 % using ethylene as the working fluid, all concluded that hydrocarbon working fluids are the preferred choice for cryogenic energy reutilisation for power generation applications utilising Organic Rankine Cycles.

Zeotropic fluids are a mixture of two or more pure working fluids and are believed to provide a better performance for low-temperature waste heat reutilisation applications. This is because the saturations curves for zeotropic fluids are suited better for low-grade waste heat, decreasing the gliding temperature difference between the thermal heat source and the working fluid in the evaporator [92], hence absorbing more thermal energy from the heat source, as compared to pure fluids. Yu et al. [92], using binary mixtures of hydrocarbons propane and propylene, Kim et al. [93], using binary mixtures of methane, ethane, butane, propane, and pentane in a three-stage cascade cryogenic ORC system, Bao et al. [94], investigating different fluid compositions of binary mixtures of hydrocarbons for a two-stage cryogenic ORC, and Tian et al. [95], using a two-stage cryogenic ORC for comparative studies on binary mixtures of ethane, ethylene, and propylene, all arrived at the same conclusion that the system performance is marginally improved by utilising zeotropic working fluid mixtures. However, the studies were of the consensus that only low-grade temperature waste heat provided a slightly improved performance for zeotropic fluids, and pure fluids outperform zeotropic fluids at higher waste thermal heat source temperatures. Yet, these zeotropic working fluids still consist of hydrocarbons, which present a significant safety risk.

Many researchers have hailed hydrocarbons as the best performing working fluid for cryogenic ORCs yet have always discounted the flammability risks associated with hydrocarbon working fluids. Hydrocarbons are extremely flammable and explosive, and hence present with extreme safety risks regarding their use in space-confined applications, such as onboard a marine vessel. While limited studies exist regarding fire-retardant working fluid mixtures for non-cryogenic ORCs [96] [97] [98], only one study exists that considers fluid flammability as an objective fluid selection parameter for cryogenic enhanced ORCs. Farrukh et al. [99] proposed the utilisation of non-flammable and low flammability refrigerants for dual waste energy reutilisation, the waste thermal energy in the evaporator, and the waste cryogenic energy in the condenser. Choosing three non-flammable working fluids, based on the ASHRAE safety index (discussed in detail in Chapters 3 and 4), namely R407C, R410A, and R450A, and three low flammability working fluids, namely R452B, R454C, and R455A, they performed a parametric analysis using their dynamic model of a simple cryogenic enhanced ORC system. They reported a maximum work-output of 45.64 kJ/kg and a first and second law efficiency of 10.43 % and 12.75 %, respectively, using R452B as the working fluid. This study was the first of its kind, introducing the desperately required aspect of safety to the traditionally flammable hydrocarbon working fluid dominated field of cryogenic enhanced ORCs.

2.3.3 Parametric studies

The development of a cryogenic enhanced ORC system requires careful consideration of cycle configurations and working fluid selection, which is immediately followed by an extensive parameter search to determine the optimal working conditions. These parameters generally evaporation and condensation temperatures and pressures, mass flow rate variations, and heat source temperatures [76] [82] [83] [93] [100] [101] [102] [103]. A summary of different cryogenic enhanced ORC systems found in literature is presented in Table 2.2.

Table 2.2: Chronological tabulation of cryogenic enhanced ORCs since 2010.

Reference study	Optimisation parameters	Cycle configurations	Best performing fluid	Cycle temperature difference (K)	Study type	Flammable	Key performance indicators			
							Energy	Exergy	Net-work	Cost
[80] 2011	Pressure	Two-stage ORC with absorber	CH_4 + C_3H_8	455	Steady-state numerical	Yes	23 %	N/A	0.2 MW	N/A
[78] 2013	Cycle structure, temperature and pressure, working fluid selection, recuperator	Direct expansion integrated with solar ORC	R143A	408	Steady-state numerical	Yes	24.92 %	13.72 %	1.5 MW	N/A
[85] 2013	Cycle structure, evaporation and condensation pressure	Two- and three-stage cascade ORCs	CH_4 + C_2H_6 + C_3H_8	447	Steady-state numerical	Yes	12.5 %	65.2 %	0.1 MW	$ 9.43/W
[91] 2014	Working fluid, evaporation and condensation pressures	Simple ORC with three-fluid condenser	CH_4 + C_2H_6 + C_3H_8	462	Steady-state numerical	Yes	N/A	49.7 %	36 MW	N/A
[83] 2015	Flow rate, evaporation temperature	Two-stage ORC	R227ea + R116	564	Steady-state numerical	Yes	25.64 %	31.02 %	1.77 MW	$ 6.3/W
[93] 2015	Evaporation temperature, working fluid	Three-stage cascade ORC	R14 + C_3H_8	458	Steady-state numerical	Yes	23.8 %	36.5 %	0.25 MJ/kg LNG	N/A
[76] 2017	Working fluid, evaporation and condensation pressures	Two-stage ORC with direct expansion	R22 + NH_3	585	Steady-state numerical	Yes	N/A	30.3 %	N/A	N/A
[103] 2017	Flow rate, expander inlet and outlet temperatures	Two-stage solar recuperative ORC with direct expansion	C_5H_{12}	630	Steady-state numerical	Yes	N/A	19.59 %	1.6 MW	$ 2.42/W
[75] 2018	Cycle structure, condensation pressure, working fluid selection	Two-stage ORC	C_2H_4	675	Steady-state numerical	Yes	31.34 %	35.43 %	0.59 MW	$ 4.31/W

[94] 2018	Evaporation and condensation temperatures	Two-stage ORC	C_5H_{12}	414	Steady-state numerical	Yes	12.17 %	30.5 %	0.1 MJ/kg LNG	N/A
[101] 2019	Cycle structure, condensation temperature	Two- and three-stage ORCs	C_2H_4	396	Steady-state numerical	Yes	N/A	N/A	0.2 MW	$ 7.52/ W
[102] 2019	Cycle structure	Novel three-stage cascade ORC	C_3H_8	512	Steady-state numerical	Yes	N/A	28.43 %	0.32 MW	$ 9.87/ W
[82] 2020	Cycle structure, condensation pressure, working fluid selection	Two-stage ORC with direct expansion	NH_3	635	Steady-state numerical	Yes	N/A	30.54 %	0.09 MW	M/A
[104] 2020	Working fluid selection	Simple ORC with direct expansion	C_2H_6 +R23	561	Steady-state numerical	Yes	16 %	23 %	N/A	N/A
[95] 2021	Temperature difference	Two-stage parallel ORC	C_2H_4 + C_4H_{10}	532	Steady-state numerical	Yes	22%	23 %	0.15 MW	N/A
[105] 2022	Evaporation temperature	Recuperative ORC	C_3H_8	523	Experimental	Yes	6.49 %	28.99 %	894 W	N/A
[99] 2024	Evaporation temperature, system charge	Simple ORC	R452B	575	Dynamic numerical	No	10.43 %	12.75 %	45.64 kJ/kg	N/A

2.4 Brayton Cycle

Cryogenic energy assisted power generation applications were first realised using the Brayton cycle, proposed by Grienpentrog and Sacharendt [52], who utilised the cryogenic energy of LNG to cool the working fluid at the compressor inlet. Two distinct configurations of the Brayton cycle exist, the open Brayton cycle and the closed Brayton cycle. The distinction between the ORC and the Brayton cycle is that in the Brayton cycle, the working fluid does not change phase and remains in gaseous form throughout the heat exchange and expansion processes. The cycle starts at the compressor, which pressurises the vapour-phase working fluid, which then goes to the evaporator. In the

evaporator, the pressurised working fluid absorbs the waste heat energy from the thermal energy source, increasing its enthalpy. The high temperature pressurised vapor working fluid then rotates the turbine blades, producing mechanical power. The distinction between the open and the closed Brayton cycle configurations is that in the open Brayton cycle configuration, the turbine exhaust is released into the environment, whereas in the closed Brayton cycle configurations, there exists another heat exchanger before the compressor, where the waste cryogenic energy is utilised. The compression and expansion processes in the Brayton cycles are considered to be adiabatic [57] [106]. Extensive literature review has revealed that the usual cryogenic assisted Brayton cycle working fluids are noble gases, namely nitrogen, argon, and helium, while some studies have also utilised air, methane, and ethane [57] [65] [107] [108]. The open and closed Brayton cycle configurations are shown in Figure 2.4.

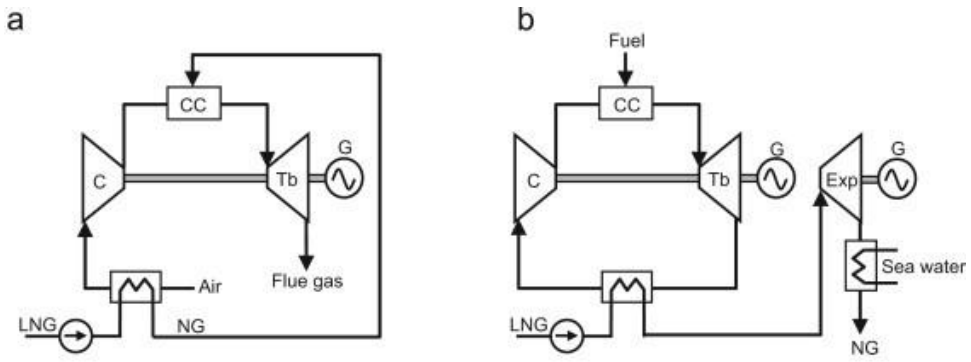

Figure 2.4: Configuration diagrams of the (a) open Brayton cycle, (b) closed Brayton cycle integrated with the direct expansion cycle. [72]

2.4.1 Brayton-Brayton cycle integrations

Similar to the ORC, different Brayton cycle configurations have been developed to optimise system performance. These include combining the open Brayton cycle configuration with the closed Brayton cycle configuration, and the implementation of multiple expansion devices within one Brayton cycle configuration, known as multi-stage Brayton cycles, and Brayton cycle configurations with co-dependant heat exchangers, known as cascade Brayton cycles.

The integration of the open and closed Brayton cycle configurations with the direct expansion cycle is illustrated in Figure 2.5. First proposed by Dispenza et al. [109] [110], the cycle is split into the top cycle and the bottom cycle. The top cycle is a high-temperature cycle, which utilises high-temperature thermal energy as the heat input. The exhaust from the top cycle turbine serves as the heat source for the bottom cycle. The bottom cycle is a closed Brayton cycle configuration. The waste cryogenic energy is utilised by the condenser of the bottom cycle, where the LNG absorbs heat from the working fluid, and is then expanded through an additional turbine. They performed a comparative working fluid study using nitrogen and helium as the working fluid, and discovered that nitrogen exhibits higher system performance, compared to helium. They achieved a maximum thermal efficiency of 72 % and maximum exergy efficiency of 53 % using nitrogen as the working fluid, compared to a thermal efficiency of 69 % and exergy efficiency of 51 % using helium. This study paved the way for further optimisation studies on the open and closed integrated Brayton cycle configurations, such as those performed by Tsatsaronis and Morosuk [71] [111]. The first study [71] revealed that the direct expansion cycle provided little value to the overall system performance, achieving a thermal efficiency of 75.5 % and exergy efficiency of 52.6 %. Hence, they removed the direct expansion cycle for the second study, achieving a thermal efficiency of 78.1 % and exergy efficiency of 52.1 %. Hence, they concluded that the direct expansion cycle adds unnecessary complexity to the cycle configuration and recommended an advanced exergy analysis of individuals components to minimise system complexity and maximise performance. Adding to the studies performed by Tsatsaronis and Morosuk [71] [111] on the open and closed Brayton cycle integration, Salimpour et al. [112] used the waste cryogenic energy to cool the working fluid at the inlet of the top cycle compressor, as well as the outlet of the bottom cycle turbine, achieving an increase of 23 % in thermal efficiency and 27 % in exergy efficiency. Brayton cycles are high-temperature cycles, evidenced by their fuel combustion energy input requirement, and hence would be unsuitable for low-grade waste thermal energy applications. This limits their applications to land-based power stations, and industrial applications producing high-temperature waste thermal energy.

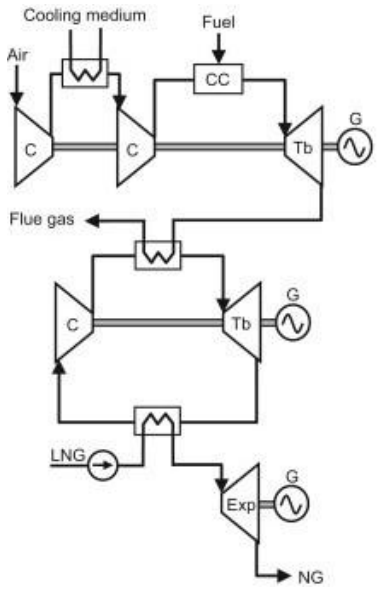

Figure 2.5: Integration of the open and closed Brayton cycle configurations with the direct expansion cycle [72]

Ma et al. [113] conducted a comparative study by integrating the closed Brayton cycle configurations, illustrated in Figure 2.6. The first integration involves two individual closed Brayton cycles in series, hence utilising the cryogenic energy in two separate heat exchangers. The second integration proposed the cascade two-stage Brayton cycle, where the condenser of the top cycle served as the evaporator of the bottom cycle. The two-stage series Brayton cycle integration provided an energy efficiency of 20.49 % and an exergy efficiency of 13.26 %. Comparatively, the cascade two-stage integration achieved a thermal efficiency of 12.12 % and an exergy efficiency of 7.53 %. Their analysis revealed that the integration of closed Brayton cycles does not provide adequate system optimisation and does not warrant the increased system complexity accompanied by such integrations. Hence, they suggested integrating low-temperature power generation cycles, such as the ORC, with the high-temperature Brayton cycles.

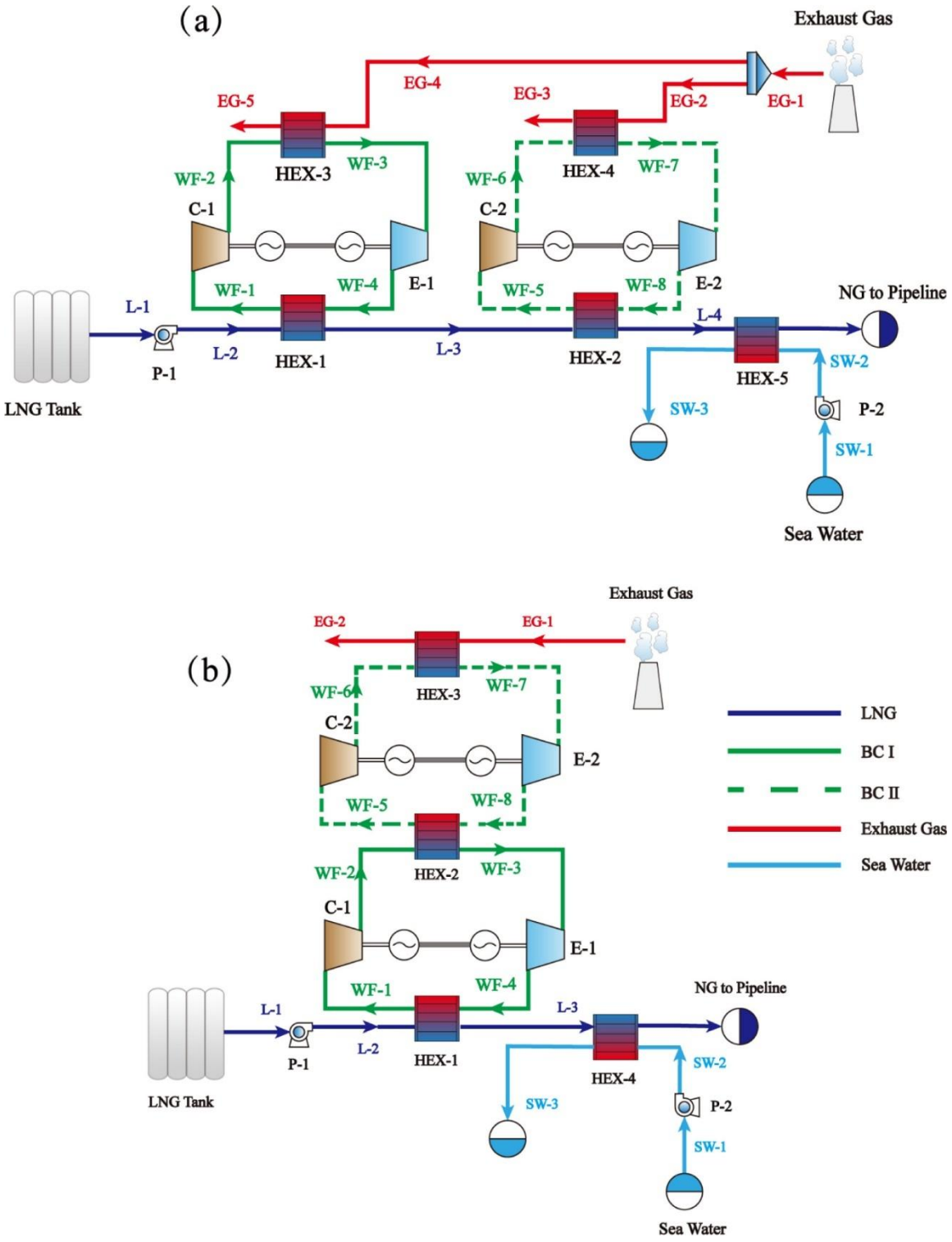

Figure 2.6: a) two-stage series closed Brayton cycle configuration; b) cascade two-stage Brayton cycle configuration

2.4.2 Hybrid Brayton cycle integrations

Hybrid Brayton cycle integrations have recently emerged by integrating low-temperature cold energy assisted power generation cycles with the high-temperature Brayton cycles. In these integrations, the top cycle is always a Brayton cycle configuration, due to its high temperature operation. The high-temperature turbine exhaust then serves as the heat source for the bottom cycles, which also utilises the waste cryogenic energy. The most common integration of the Brayton cycle for waste cryogenic energy reutilisation is with different variations of the Rankine cycle, such as the traditional Rankine cycle, using steam as the working fluid, the organic Rankine cycle, and the trans-critical CO_2 cycle, which is a variation of the ORC using CO_2 as the working fluid.

Figure 2.7 illustrates the integration of the closed Brayton cycle with the traditional steam Rankine cycle, proposed by Gomez et al. [108]. Using helium and steam as the working fluids for the Brayton and Rankine cycle, respectively, they achieved a maximum thermal efficiency of 56.74 % and a maximum power output of 3.058 MW. In the second study conducted by the same authors [114], they replaced the steam Rankine cycle with the trans-critical CO_2 cycle and reported an energy efficiency of 67.6 %. From the results of both these studies, the authors' concluded that multi-objective optimisation requires a trade-off, meaning that both objective parameters cannot be optimised simultaneously. Following the lead of Ref. [108] [114], Cao et al. [115] proposed a novel integration of the closed Brayton cycle, which served as the high-temperature top cycle, and a two-stage cascade trans-critical CO_2 cycle, which served as the bottom cycle. They reported that their proposed integrated cycle outperforms the single Brayton cycle by 17.03 % in terms of overall system efficiency. Cha et al. [116] also proposed the integration of the closed Brayton cycle with the trans-critical CO_2 cycle, with the novelty that the compressor inlet of the Brayton cycle would be cooled by the CO_2 from the pump outlet of the trans-critical CO_2 cycle, on its way to the evaporator. Using this configuration, they reported a maximum system efficiency of 65.8 % and a maximum power output of 102.5 MW. Other complex integrations with the Brayton cycle have been proposed, such as that by Moghimi et al. [117], who proposed the integration of the Brayton cycle with the ORC, steam Rankine cycle, and the Stirling cycle, achieving a thermal and exergy efficiency of

53.51 % and 47.43 %, respectively. Other complex configurations have been proposed for cryogenic assisted Brayton cycles, but the system configuration complexity raises questions about their practicality and real-world implementation. Table 2.3 presents a summary of the literature available on cryogenic assisted Brayton cycles. However, it must be kept in mind that the high-temperature thermal energy input requirement of the Brayton cycle severely limits their waste-heat reutilisation potential, and constraints their applications to large-scale land-based applications, which may or may not use fuel combustion as the heat source to the Brayton cycle. The combustion of fuel as heat input defeats the purpose of dual utilisation of waste thermal and cryogenic energy. Hence, the characterisation of heat comes into play, where modern energy efficiency methods look to reutilise the available waste heat. An example of this is seen in marine vessels, where exhaust gas output temperature is considerably lower than it used to be, due to the implementation of exhaust gas recirculation as a method to increase the balance of plant efficiency [49] [50]. Hence, the high-temperature energy input requirement of the Brayton cycles makes them unfeasible as a dual waste energy reutilisation solution in applications favouring energy efficiency, resulting in lower waste-heat temperatures.

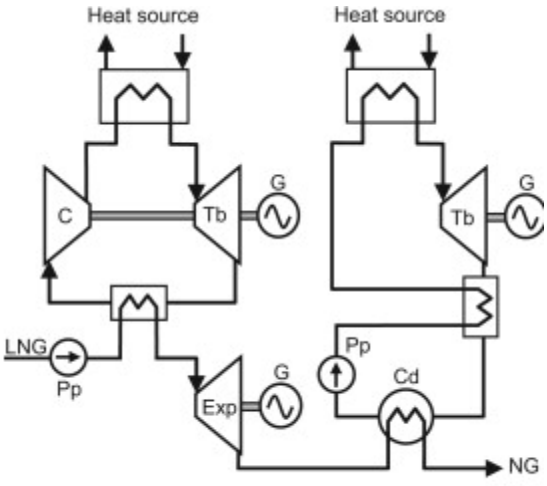

Figure 2.7: Integration of the closed Brayton cycle with the steam Rankine cycle [72]

Table 2.3: Chronological tabulation of cryogenic enhanced Brayton cycles and hybrid CHP systems.

Reference study	Optimisation parameters	Cycle configurations	Best performing fluid	Study type	Cycle temperature difference (K)	Key performance indicators			
						Energy	Exergy	Net-work	Cost
[118] 2007	Evaporation temperature and pressure	Closed Brayton cycle with Rankine cycle	Air and steam	Steady-state numerical	1733	N/A	59 %	0.25 GW	N/A
[109] [110] 2009	Evaporation and condensation pressure	Open and closed Brayton cycle	Nitrogen and helium	Steady-state numerical	1012	N/A	72 %	14.6 GW	N/A
[71] [111] 2010	Individual component exergy analysis	Open and closed Brayton cycle with direct expansion	Nitrogen and natural gas	Steady-state numerical	842	78 %	52 %	0.14 GW	N/A
[107] 2011	Evaporation and condensation pressure, working fluid selection	Closed Brayton cycle	Nitrogen and argon	Steady-state numerical	1235	N/A	69 %	0.75 MW	N/A
[112] 2012	Evaporation and condensation temperatures and pressures	Open and closed Brayton cycle with direct expansion	Nitrogen and air	Steady-state numerical	1912	68.5 %	73.3 %	0.1 MW	N/A
[108] [114] 2014	Evaporation and condensation pressure, compressor temperature	Closed Brayton cycle with Rankine cycle	Helium and steam	Steady-state numerical	1417	56.7 %	55.1 %	2.8 MJ/kg LNG	N/A
[115] 2017	Condensation temperatures and pressures, flow rate, turbine efficiency	Closed Brayton cycle with cascade CO_2	Air and CO_2	Steady-state numerical	944	52.5 %	N/A	3.5 MW	N/A
[117] 2019	Evaporation and condensation pressure, flow rate	Closed Brayton cycle with ORC, Rankine cycle, and Stirling cycle	Steam, argon, nitrogen and R13	Steady-state numerical	1614	53.5 %	47.4 %	24.7 MW	N/A

[119] 2019	Working fluid selection, heat source temperature	Closed Brayton cycle with liquid air energy storage and direct expansion	Nitrogen	Steady-state numerical	625	N/A	57 %	0.300 MJ/kg LNG	N/A
[116] 2021	Cycle configuration, condensation temperatures	Closed Brayton cycle with cascade CO_2	Air and CO_2	Steady-state numerical	889	65.8 %	N/A	0.11 GW	N/A

2.5 Kalina Cycle

The Kalina cycle, developed by Kalina [120], is based on the working principle of the Rankine cycle, but employs ammonia-water mixture as the working fluid. Figure 2.8 illustrates the cryogenic assisted Kalina cycle. The separator, absorber, reheater, and condenser form the distiller sub-system, which controls the composition of the ammonia-water working fluid. By controlling the composition of the working fluid, the temperature glide can be controlled and set up to match with the thermal energy source temperature. This leads to lower exergy destruction in the evaporator, hence increasing system performance [121]. Studies conducted on the Kalina cycle performance have shown that the performance of the Kalina cycle is superior to that of the traditional Rankine cycle [122] [123] [124]. Since the working fluid of the Kalina cycle is always an ammonia-water mixture, optimisation techniques usually focus on cycle configurations. Cryogenic enhanced Kalina cycles are usually configured into multi-stage Kalina cycles or combined with other power generation cycles, such as the ORC and the Brayton cycle. Unlike the Brayton cycle, which requires a high-temperature thermal energy input, the Kalina cycle can utilise low-temperature waste energy, like the ORC. Hence, Kalina cycles can be integrated with geothermal waste energy sources and solar energy [125] [126] [127] [128] [129].

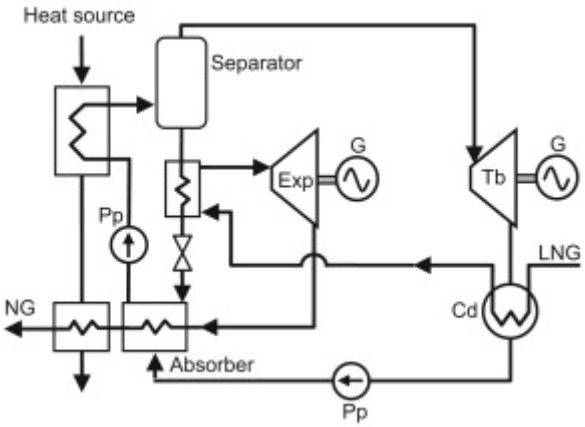

Figure 2.8: Kalina cycle for cryogenic energy reutilisation [72]

2.5.1 Kalina cycle configurations

The most basic integration of the Kalina cycle is firstly with the direct expansion cycle, as is the case with the ORC and the Brayton cycle. Shi et al. [130] were the first to integrate the Kaline cycle with the direct expansion of LNG for cryogenic thermal and mechanical exergy reutilisation, reporting an exergy efficiency of 48.87 %. Wang et al. [121] proposed a novel heat exchanger for the basic cryogenic enhanced Kalina cycle, which acted as the evaporator and the ammonia-water distiller sub-system. They conducted an extensive parametric optimisation, including the pinch point temperature difference in the evaporator, ammonia/water composition, and evaporation and condensation temperatures and pressures, and concluded that performance trade-offs were required to achieve optimal system performance, and individual performance indicators could not be simultaneously maximised. After an extensive parametric optimisation, they achieved an exergy efficiency of 27.45 %. Kim et al. [131] conducted a similar optimisation study on the simple Kalina cycle and the recuperative Kalina cycle. They concluded that the cryogenic enhanced recuperative Kalina cycle was superior to the basic Kalina cycle, reporting a maximum energy and exergy efficiency of 37.7 % and 36.1 %, respectively.

Zhang et al. [132] conducted a comparative study between the cryogenic enhanced Kalina cycle and the cryogenic enhanced ORC. They reported that while the Kalina cycle exhibits a marginally superior performance than the ORC for cryogenic enhanced power

generation applications, the Kalina cycle is inferior to the ORC when considering cost-effectiveness. In terms of the multi-stage Kalina cycle configurations, Ghaebi et al. [84] proposed a two-stage cascade Kalina cycle configuration, integrated with the direct expansion cycle. The configuration is illustrated in Figure 2.9. They reported a net-work output of 9.04 MW, thermal efficiency of 29.87 %, and an exergy efficiency of 43.19 %. One of the most important realisations from this study was the investment costs related to Kalina cycles, due to the high pressure-ratio requirements of the turbines, and the ammonia-water distillation sub-systems.

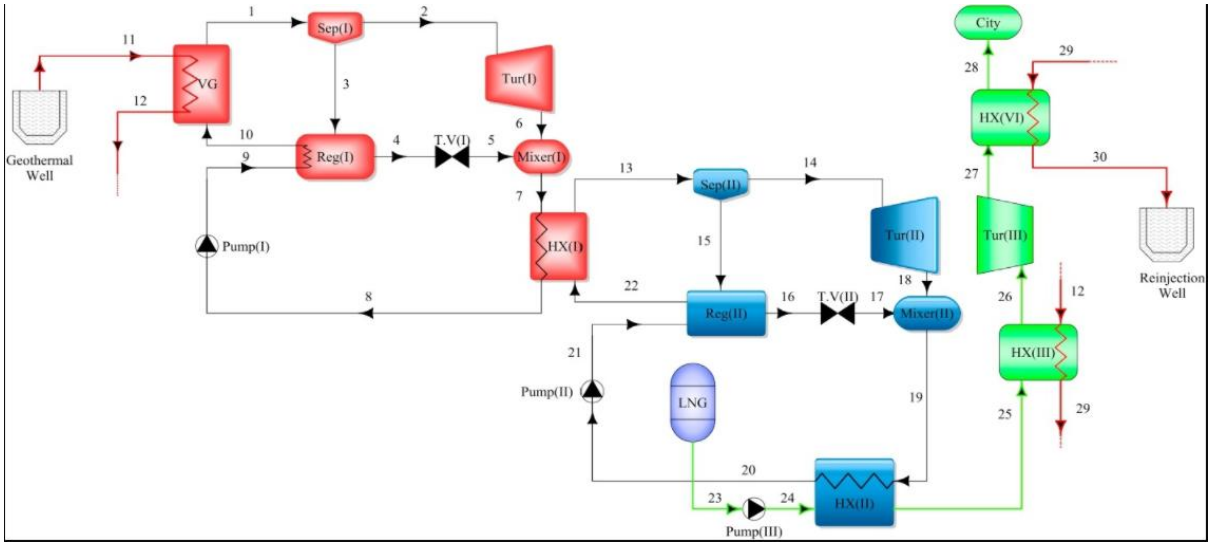

Figure 2.9: Cascade two-stage Kalina cycle integrated with direct expansion [84]

2.5.2 Hybrid Kalina cycle integrations

There is a prevailing a trend towards the integration of the Kalina cycle with other processes, such as heating and cooling, for multi-generation integrated configurations. These configurations usually involve multiple power generations cycles integrated into one system for cold energy reutilisation.

Abdolalipouradl et al. [133] proposed many different integrations of the Kalina cycle with the trans-critical CO_2 cycle and direct expansion cycle for cryogenic assisted power generation. The trans-critical CO_2 is an ORC configuration, albeit with CO_2 as the exclusive working fluid. They reported a maximum thermal and exergy efficiency of 16.63 % and 63.78 %, respectively, and achieved a net-work output of 19.45 MW. In terms of the

ORC integration with the Kalina cycle, Fang et al. [134] integrated a three-stage cascade ORC with the Kalina cycle and direct expansion cycle for multi-generation of power, cooling, and heating. They reported an energy and exergy efficiency of 43.43 % and 70.4 %, respectively, and proved that the system performance and cost can be significantly improved by employing extensive optimisation techniques. Kalina cycle integration with the Brayton cycle has also been proposed by Mosaffa et al. [135], who also integrated a modular reactor with the cycle. In fact, in the past few years, many complex multi-generation system configurations have emerged involving the Kalina cycle.

Li et al. [136] recommended the integration of the Kalina cycle with the Rankine cycle and the Brayton cycle for combined cooling and power. Ghorbani et al. [137] integrated the Kalina cycle with the Brayton cycle and ORC for combined cooling, heating, and power. Ghorbani et al. [138] further added to the system proposed by Ref. [137] to produce methanol as a fuel by-product. Parikhani et al. [139] proposed the integration of the Kalina cycle with the direct expansion cycle and a PEM electrolyser for multi-generation of power, cooling, and hydrogen. Ayou et al. [140] integrated the Kalina cycle with a refrigeration unit for multi0generation of power, cooling, and heating. Ansarinasab et al. [141] proposed the integration of the Kalina cycle with the Striling cycle, refrigeration unit, and a water desalination plant. Ebrahimi et al. [142] developed a combined cycle for air liquification by integrating the recuperative Kalina cycle with the closed Brayton cycle for energy storage. While the development of these complicated cycle configurations for cryogenic energy reutilisation is commendable, it is equally important to question the applicability and implementation of these combined cycles in real-world scenarios. The complexity would significantly add to the system investment cost, and require extensive maintenance, thus increasing operational costs [132]. A summary of the research conducted on cryogenic enhanced Kalina cycles is presented in Table 2.4.

While the Kalina cycle offers marginally higher performance than the ORC, as evidenced by Table 2.2 and Table 2.4, it must be kept in mind that the simplicity of the simple ORC configuration, compared to the simple Kalina cycle configuration, provides a significant advantage. Simple cycle configurations lead to less operating and maintenance costs, and lower overall initial investments costs, as evidenced by comparing the cost data and plant size in Table 2.2 and Table 2.4. Additionally, the Kalina cycle operates exclusively on

the ammonia-water mixture as a working fluid. It must be kept in mind that ammonia is a toxic and flammable substance, and any application requires extreme caution and extensive risk assessment routines. Hence, the slight performance enhancement over cryogenic enhanced ORCs does not circumvent the limitations revolving around cryogenic enhanced Kalina cycles.

Table 2.4: Chronological tabulation of cryogenic enhanced Kalina cycles and hybrid Kalina cycles (CHP systems).

Reference study	Optimisation parameters	Cycle configuration	Cycle temperature difference (K)	Study type	Key performance indicators			
					Energy	Exergy	Net-work	Cost
[130] 2009	Evaporation and condensation temperatures and pressures, ammonia-water composition	Kalina cycle with direct expansion	583	Steady-state numerical	39.3 %	55.6 %	8.7 MW	N/A
[121] 2013	Evaporation and condensation temperatures and pressures, ammonia-water composition, pinch point temperature difference	Simple Kalina cycle with novel evaporator	509	Steady-state numerical	N/A	25.9 %	0.39 MW	N/A
[135] 2017	Condensation temperatures and pressures, ammonia-water composition, pinch point temperature difference	Kalina cycle integrated with Brayton cycle	1283	Steady-state numerical	63.7 %	45 %	382 MW	$ 0.97 / W
[84] 2018	Evaporation and condensation temperatures and pressures, ammonia-water composition, pinch point temperature difference, heat source temperature	Two-stage cascade Kalina cycle	539	Steady-state numerical	29.9 %	43.2 %	9.04 MW	$ 16.6 / W
[139] 2019	Evaporation and condensation temperatures and pressures, ammonia-water composition, heat source temperature	Kalina cycle with direct expansion	596	Steady-state numerical	68.9 %	23.5 %	1.15 MW	$ 16.28 / W
[143] 2019	Evaporation and condensation temperatures and pressures, ammonia-water composition, pinch point temperature difference, turbine pressure-ratios	Kalina cycle integrated with trans-critical CO_2 cycle	617	Steady-state numerical	29.2 %	56.9 %	30.6 MW	N/A

[140] 2020	Heat source temperature, ammonia-water composition, pinch point temperature difference, turbine pressure-ratios	Kalina cycle with direct expansion and chiller	565	Steady-state numerical	33 %	35.7 %	N/A	N/A
[136] 2020	Ammonia-water composition, turbine pressure-ratio	Kalina cycle integrated with Brayton cycle and direct expansion	555	Steady-state numerical	N/A	35.1 %	3.48 MW	N/A
[137] 2020	Pinch point temperature difference, flow rates	Kalina cycle integrated with ORC, Brayton cycle, and Rankine cycle	1063	Steady-state numerical	55.2 %	67.7 %	158.5 MW	N/A
[141] 2021	Turbine pressure-ratio and efficiency, pump pressure-ratio and efficiency	Kalina cycle integrated with Stirling cycle, water desalination, and refrigeration unit	605	Steady-state numerical	N/A	42.9 %	7.78 MW	N/A
[142] 2021	Pinch point temperature difference, flow rates, pressure	Kalina cycle integrated with Brayton cycle and liquid air energy storage	759	Steady-state numerical	79.8 %	40.2 %	11.6 MW	N/A
[134] 2021	Evaporation and condensation temperatures and pressures, ammonia-water composition, pinch point temperature difference, heat source temperature, turbine efficiencies	Kalina cycle integrated with three-stage cascade ORC and direct expansion	903	Steady-state numerical	43.4 %	70.4 %	1.26 MW	$ 6.23 / W

Some other cryogenic reutilisation power generation technologies exist, such as the thermoelectric generator. However, these do not utilise working fluids and have low efficiency and thus have been excluded.

2.6 Research gap

An extensive literature review regarding the reutilisation of waste cryogenic energy for power generation applications was presented in this chapter. For the thermal exergy reutilisation of cryogenic low-carbon liquid fuels, the organic Rankine cycle, Brayton cycle, and the Kalina cycle emerged for power generation applications. Extensive optimisation techniques have been employed by researchers to improve system performance for each cycle. Each cycle presents with different advantages and disadvantages depending on various factors, such as the heat source temperature and the specific application.

Close inspection of Table 2.2, Table 2.3, and Table 2.4 revealed that the Brayton cycle in unfeasible for low-temperature waste heat reutilisation, and the ORC and the Kalina cycle are preferred for such applications. This limits the utilisation of Brayton cycles to high-temperature land-based applications, such power stations and industrial plants. In terms of the ORC and the Kalina cycle, the Kalina cycle presented with a slightly higher system performance compared to the ORC, at similar waste heat temperatures. However, the simple ORC configuration is less complex compared to the simple Kalina cycle configuration, which requires a distiller sub-system to control the ammonia-water mixture concentration. The second advantage of the ORC over the Kalina cycle is the utilisation of ammonia-water as the working fluid in the Kalina cycle. Ammonia is a highly toxic and flammable fluid and requires strict control and health and safety protocols. While it is true that hydrocarbons, which are highly flammable, are the preferred choice of working fluids for cryogenic enhanced ORCs, Farrukh et al. [99] (Author) proved the feasibility of low flammability working fluids for cryogenic ORCs. One of the most interesting observations that were made from the literature review was that the studies conducted on cryogenic energy reutilisation for power generation applications are

theoretical in nature. None of the studies in literature conducted any experimental analysis[2].

Hence, the novelty of this PhD thesis is three-fold:

1. Utilisation of low flammability working fluids for cryogenic enhanced ORCs.
2. Dynamic numerical modelling of cryogenic-enhanced ORCs. The literature review exhibited an over-reliance on steady-state modelling, which cannot accurately predict system charge and its effects on system performance.
3. Experimental analysis of low flammability working fluids for cryogenic enhanced ORCs. Current research focuses solely on flammable hydrocarbon working fluids, with almost all studies focusing on numerical models and discounting experimental analysis and validation.

Subsequent chapters develop the methodology to address the research gaps identified in this chapter, through numerical and experimental methods and analysis. A paradigm for low flammability working fluid selection was also presented, based on current regulations regarding flammability limits (based on ASHRAE safety index) and F-gas utilisation limitations in marine shipping environments.

[2] One study, conducted by Ref. [105] on experimental cryogenic ORC using highly flammable propane as working fluid exists in literature.

Chapter 3. Methodology

3.1 Introduction

The discussion in Chapter 2, Literature Review, revealed the potential of cryogenic energy recovery from low-carbon fuels for integrated power generation applications within the green economy. Cryogenic Organic Rankine Cycles not only reutilise the cryogenic energy from the fuel regassification but also enhance energy efficiency by reutilising waste thermal energy from fuel combustion or fuel cell operation. Traditionally, cryogenic ORCs utilise hydrocarbons as the working fluid, owing to their high performance and low boiling temperatures. However, hydrocarbons are extremely flammable and pose a huge safety risk. Despite considerable research on cryogenic ORCs, no work has been focused on low flammability working fluids. Additionally, the extensive literature research revealed that all studies conducted on cryogenic ORCs are theoretical and simulation based. Experimental studies surrounding cryogenic ORCs are extremely limited[3].

This chapter describes the methodology of the establishment of an experimental cryogenic ORC test rig for non-flammable and low-flammability hydrofluorocarbon working fluids. It contains the system configuration description, main system components' selection, sensing instrumentation setup, pressure and leak testing procedures, safety device implementation, and how the experimental methodology feeds into the numerical modelling.

3.2 System configuration

[3] The one experimental study found in literature used propane as the working fluid, which is a highly flammable and explosive substance, by Ref. [105].

With liquid cryogenic low-carbon fuels being hailed as the future of the green global economy, it is imperative that certain energy efficient technologies be developed that fully utilise the entire range of low and high temperature waste energy available [44]. Liquifying low-carbon fuels, such as hydrogen and ammonia, is an energy intensive process, and regassification of these fuels usually wastes all the high-quality cryogenic energy. While waste thermal heat reutilisation technologies have been employed within all major industries, waste cryogenic energy reutilisation is yet to be commercialised. Therefore, cryogenic enhanced Organic Rankine Cycles have been proposed, providing a compact dual waste thermal and cryogenic energy reutilisation solution. Extensive literature review (*Chapter 2: Literature Review*) revealed the lack of experimental studies on cryogenic ORCs, and none of the theoretical studies considered fluid flammability.

Based on the literature review conducted in Section 2.3, it was concluded that the simple ORC configuration be chosen for this research, owing to its simplicity and cost-effectiveness. The schematic of the experimental dual waste thermal and cryogenic energy reutilisation Organic Rankine Cycle is demonstrated in Figure 3.1. The arrows indicate the direction of flow of the different fluid mediums. The experimental cryogenic ORC rig consists of three distinct loops, each differentiated by working fluid medium. The heating loop is represented by the red line and utilises hot water as the heating medium to provide heat to the working fluid, inducing evaporation and superheating. The heating loop mimics the waste thermal heat component of the ORC. The cooling loop is represented by the blue line and employs liquid nitrogen as the cooling medium to condense the working fluid after expansion. The vaporisation of liquid nitrogen provides the cryogenic energy reutilisation component of the ORC. The ORC loop is represented by the green line, and R410A is used as the non-flammable hydrofluorocarbon working fluid. The photograph of the cryogenic-enhanced experimental test rig constructed at the School of Engineering, University of Birmingham is illustrated in Figure 3.2. Table 3.1 tabulates a summary of the main components, while Table 3.2 provides an overview of the sensing instrumentation.

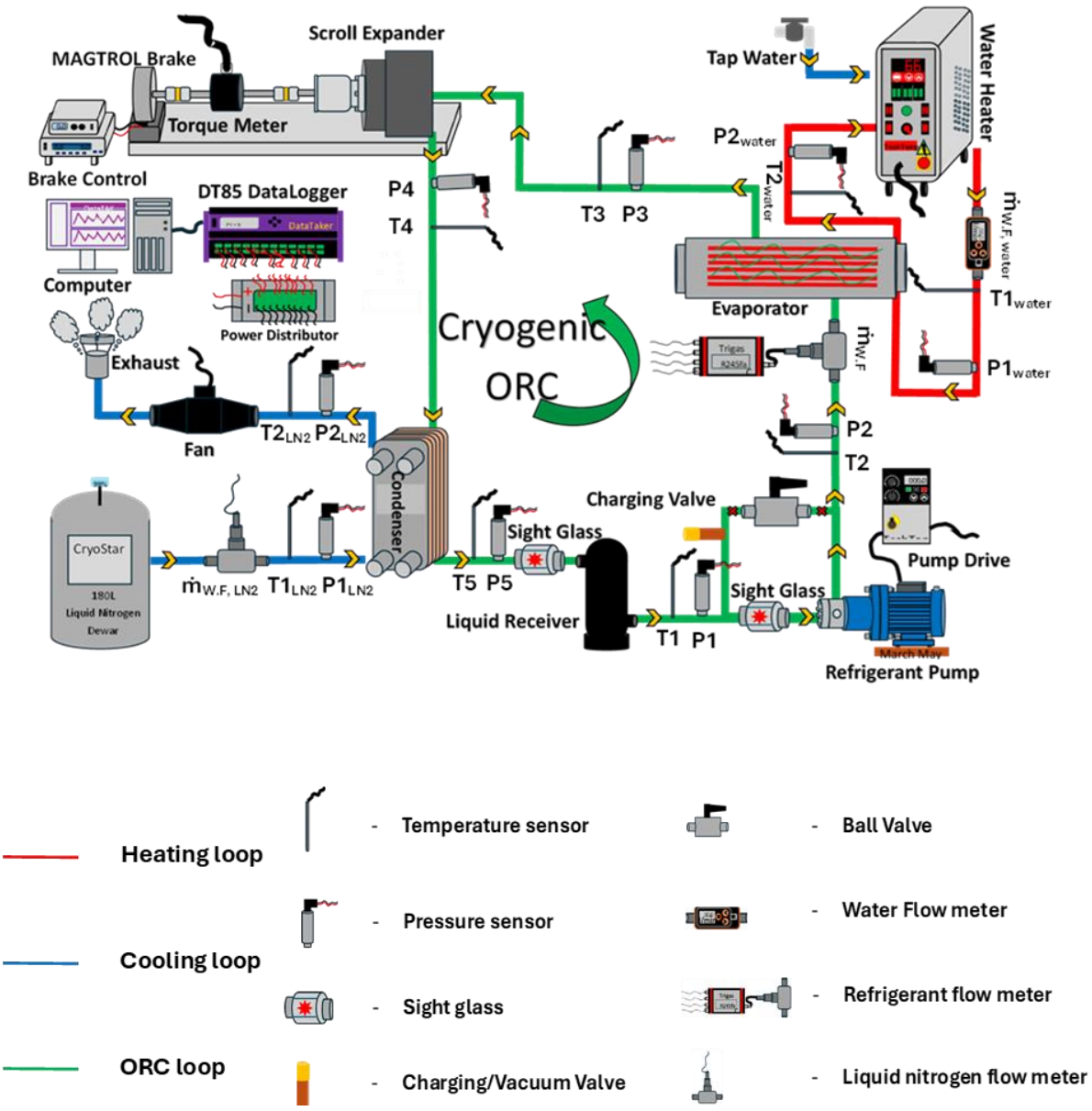

Figure 3.1: Schematic diagram of the experimental cryogenic ORC rig

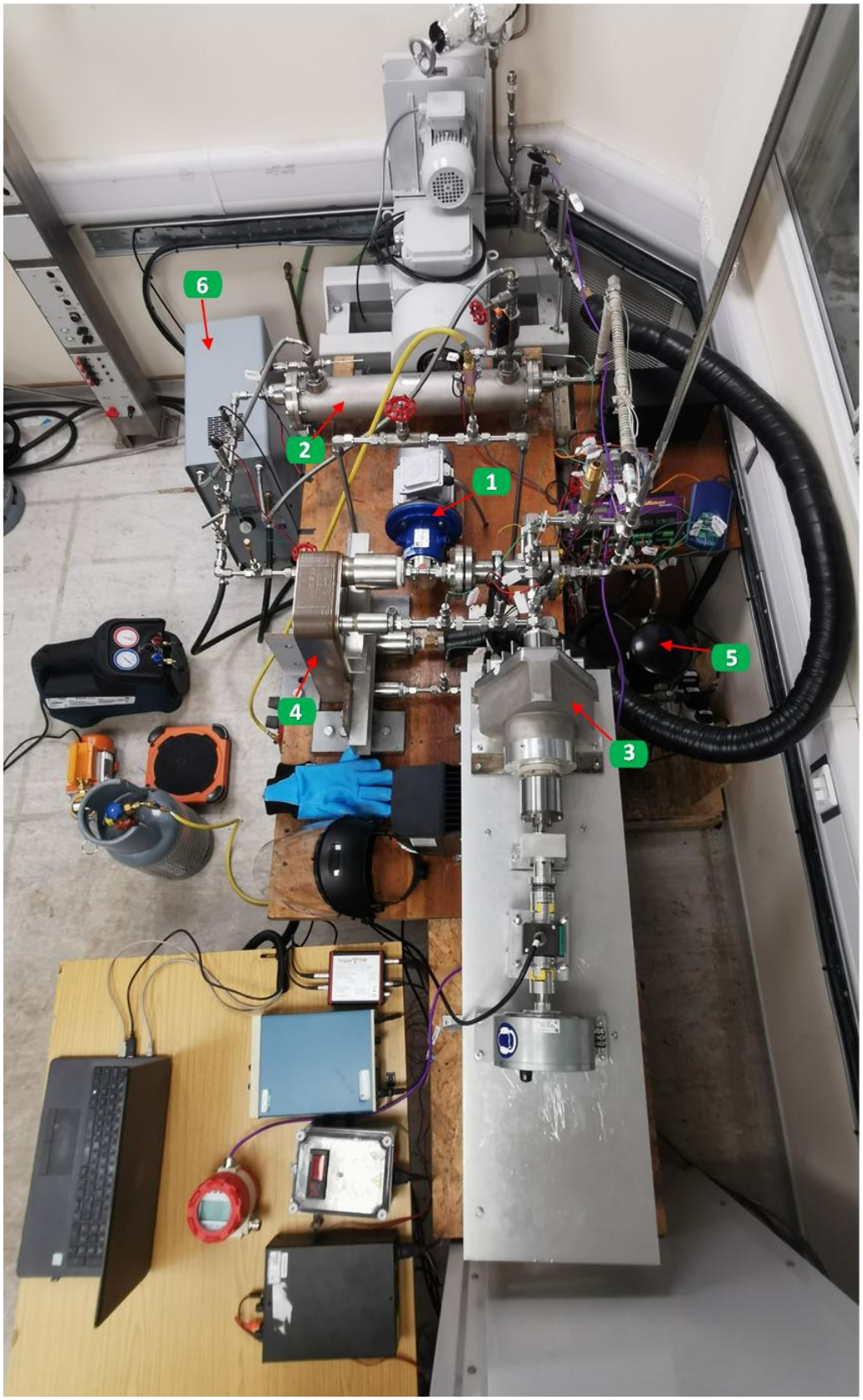

Figure 3.2: Picture of the cryogenic ORC lab setup

Table 3.1: Summary of the main components of the experimental cryogenic-enhanced ORC.

Component	Manufacturer	Description	Identifier in Figure 3.2
Main components			
Pump	March May SVM 1 x 100 [144]	Rotary vane, 0.37 kW rated power, 14 bar maximum outlet pressure, up to 75 L/hr flow	1
Evaporator	EJ Bowman SC4508-4 [145]	Shell and tube-type, heat exchange area = 1.964 m^2, Volume = 2.9 L	2
Expander	Air-squared E15H022A-SH [146]	Scroll expander, 1 kW rated power	3
Condenser	SWEP B185x36 [147]	Plate-type, heat exchange area: 3.11 m^2, volume = 4.095 L	4
Liquid receiver	Danfoss VLR 160x345 [148]	5.7 L, 34 bar maximum pressure	5
Water heater	TOOLTEMP TT181 [149]	9 kW rated power, 95 °C maximum temperature	6
Liquid nitrogen dewar	Statebourne Cryogenics Cryostor 180 [150]	180 L, self-pressurising	Not pictured

Table 3.2: Summary of the sensing instrumentation of the experimental cryogenic-enhanced ORC.

Parameter	Manufacturer	Category	Range	Accuracy	Quantity

Temperature	Farnell	K-type thermocouple	-200 – 1200 °C	± 0.5 °C	10
Pressure	RS Pro	Pressure transducer	0-40 barg	± 0.25 %	10
R410A flow	Trigas	Turbine flow meter	0.1 – 13 L/min	± 0.03 %	1
Water flow	IFM	Vortex flow meter	1 – 20 L/min	± 2 %	1
LN_2 flow	Sino-Inst	Gear flow meter	0.16 – 8.5 L/min	± 0.5 %	1
Torque and rotational speed	Applied measurements	Strain gauge transducer	0 – 20 N.m 0 – 15000 rpm	± 0.3 %	1

3.2.1 Heating loop

Cryogenic enhanced ORCs require a much lower heat input than traditional ORCs, owing to the lower heat sink temperatures [44]. Hence, for the experimental study, tap water was utilised to fill the 9-kW water heater, which circulated the hot water through the evaporator. Equipped with a temperature control system, the heater provided up to 90 °C of hot water. To adjust the flow of the hot water, globe valves were employed, and the digital display flow meter ensured the precise control of hot water flowing through the evaporator. The hot water flowed through the shell side of the shell and tube type evaporator, heating the working fluid and returning to the electrical water heater, where it was heated again to complete the closed loop system. Pressure and temperature sensors were fitted at the inlet and outlet of the evaporator to gauge the heat energy rejected by the hot water to the working fluid.

3.2.2 Cooling loop

Liquid nitrogen was utilised as the cryogenic cold energy source and was stored outside the lab in a dedicated cryogenic enclosure, inside a vacuum insulated dewar. The liquid nitrogen was piped to the lab using a vacuum insulated piping system to minimise heat losses. Cryogenic valves were used to control the flow of liquid nitrogen through the condenser, with the digital liquid nitrogen flowmeter constantly displaying the flow rate. Since the liquid nitrogen dewar had a pressure regulator, the pressure of the liquid nitrogen could be varied between 1.5-3 bars. The nitrogen exhaust was piped outside the lab using an inline exhaust fan.

3.2.3 ORC loop

The Organic Rankine Cycle loop consisted of a liquid receiver, refrigerant pump, shell and tube-type evaporator, scroll expander, and a plate-type condenser. The low-pressure non-flammable cryogenic hydrofluorocarbon liquid working fluid was pressurised by the pump, flowing to the evaporator and passing through the working fluid flow meter. Upon entering the evaporator, the high-pressure liquid working fluid was vaporised into a high-pressure superheated vapor. This high-pressure superheated vapor then flowed to the scroll expander. Due to the pressure differential at the inlet and outlet of the expander, the high-pressure superheated vapor rotated the scroll expander, causing the shaft to rotate and produce power. After expansion, the low-pressure superheated vapor flowed to the condenser, where it rejected heat to the liquid nitrogen, and changed back into liquid phase. The low-pressure sub-cooled working fluid liquid then flowed back to the liquid receiver, hence forming a closed loop system. The behaviour of a closed-loop system is heavily dependent on the fluid properties at different state points, and these were gauged by employing pressure and temperature sensors at the inlet and outlet of all system components. Sometimes, especially at the pump inlet and the condenser outlet, it is paramount that the working fluid be in liquid-phase. Hence, sight glasses were fitted to gauge the quality of working fluid entering and exiting the liquid receiver. This allowed to adjust the liquid nitrogen flow rate. The flow rate of the refrigerant was controlled using the variable frequency drive attached to pump, and the rotational speed of the expander was controlled by adjusting the torque of the magnetic brake.

3.2.4 Working fluid selection

Cryogenic enhanced Organic Rankine Cycles for power generation applications have always utilised hydrocarbons as the working fluids, owing to their excellent system performance at cryogenic temperatures [15]. However, hydrocarbons are extremely flammable and explosive, presenting a need for alternative working fluids with comparable performance. A detailed working fluid selection criterion was defined for different low flammability hydrofluorocarbons in *Section 4.4* of *Chapter 4: Dynamic Numerical Model*. For this study, R410A was chosen due to its availability, low cost, and non-flammability. In the ASHRAE refrigerant safety classification [151], R410A is classed as A1, which is the safest class of refrigerants. A1 denotes that the fluid is non-toxic and non-flammable. The thermophysical properties of R410A are tabulated in Table 3.3, and the T-s curve of R410A is illustrated in Figure 3.3.

Table 3.3: R410A fluid properties at atmospheric pressure [43]

Property	Value
ASHRAE Safety Index	A1
Global Warming Potential	2088
Ozone Depletion Potential	0
Boiling point	-51.44 °C
Freezing point	-155 °C
Liquid density	1062 kg/m^3
Critical temperature	72.13 °C

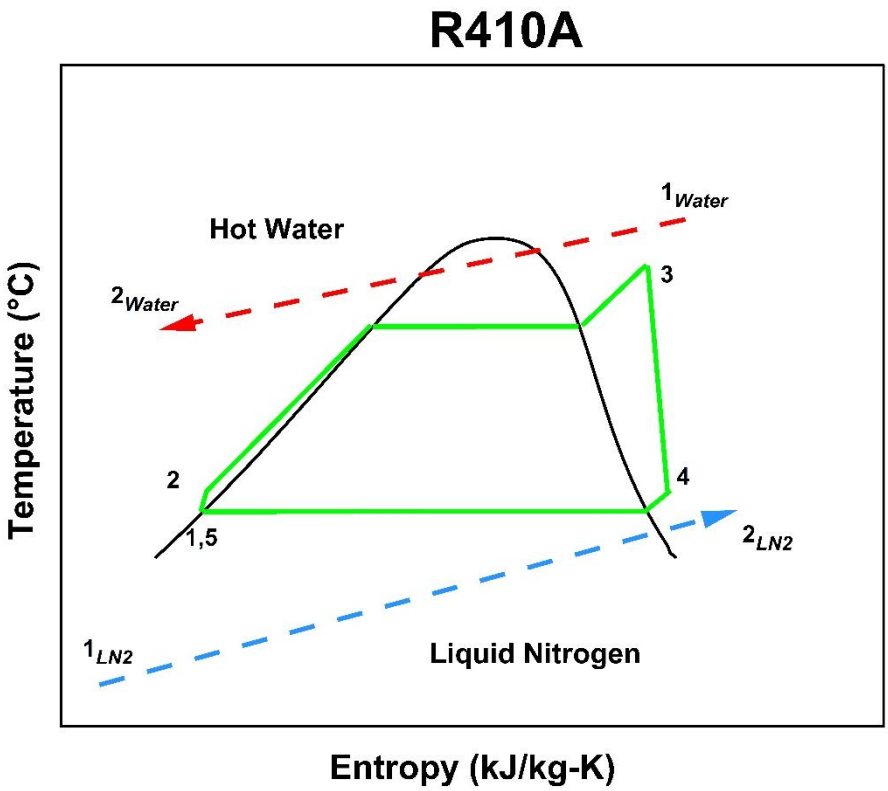

Figure 3.3: T-s diagram of the cryogenic enhanced ORC system using R410A

In the temperature – entropy diagram above, the process labels are the same as in Figure 3.1. The pressurisation of the working fluid (R410A) was represented by process 1-2, during which the pump increased its pressure. Process 2-3 described the isobaric heat transfer within the evaporator, where thermal energy from hot water was transferred to R410A. Initially, the working fluid absorbed heat to reach its saturation temperature, continued to absorb latent heat of vaporisation during phase change, and eventually underwent superheating. The corresponding heat loss from the hot water was indicated by process 1_{Water} -2_{Water}. The expansion of R410A vapor through the scroll expander, marked as process 3-4, facilitated shaft rotation which led to the power output, resulting in significant pressure and temperature drops. The subsequent condensation phase, described by process 4-5, involved the expanded R410A vapor releasing heat to the cryogenic liquid nitrogen, transitioning back to a sub-cooled liquid state. The heat absorbed by the liquid nitrogen during this process was denoted as process 1_{LN2} – 2_{LN2}, highlighting the cryogenic-enhanced ORC's critical role in effectively utilising cryogenic energy.

3.3 Main components

3.3.1 Pump

In the case of the ORC flow-inducing device, a rotary vane pump was selected, which is a positive displacement pump. The pump performance curves are shown in Figure 3.4. As illustrated in Figure 3.5 (a), the SVM 1x100 was selected as the working fluid pump, supplied by March May Ltd. and tailored for low-temperature applications. Equipped with a TECUK 0.37 kW electric motor, the pump could provide up to 14 bar pressure and 75 l/hr of flow. The purpose of the pump was to induce high-pressure liquid flow, which ultimately rotates the expander to produce power. The pump inlet was connected to the liquid receiver, which served as a buffer tank to guarantee a continuous liquid supply to the pump, thus eliminating the phenomenon of cavitation, which has a considerable impact on bearing lifespan and may ultimately lead to pump failure.

Modifications were made to the pump to enable its use with liquid R410A, which has a viscosity of 0.31 centipoise, a specific gravity of 1.06, and an operational temperature range between -50°C and +60°C. In consideration of the low-temperature application, the standard O-rings were substituted with PTFE O-rings, and the cartridges were replaced with graphite. Standard Viton O-rings and the carbon graphite cartridges would undergo shrinking at low temperatures, resulting in the formation of cracks, which could potentially lead to a critical failure. To regulate the pump's rotational speed, a variable frequency drive (VFD) was provided by the pump manufacturer (TECDrive E3 0.75kW 3PH 400V), as illustrated in Figure 3.5 (b). The frequency drive was used to control the pump's rotational speed. A detailed pump model is presented in Section 4.3.3.

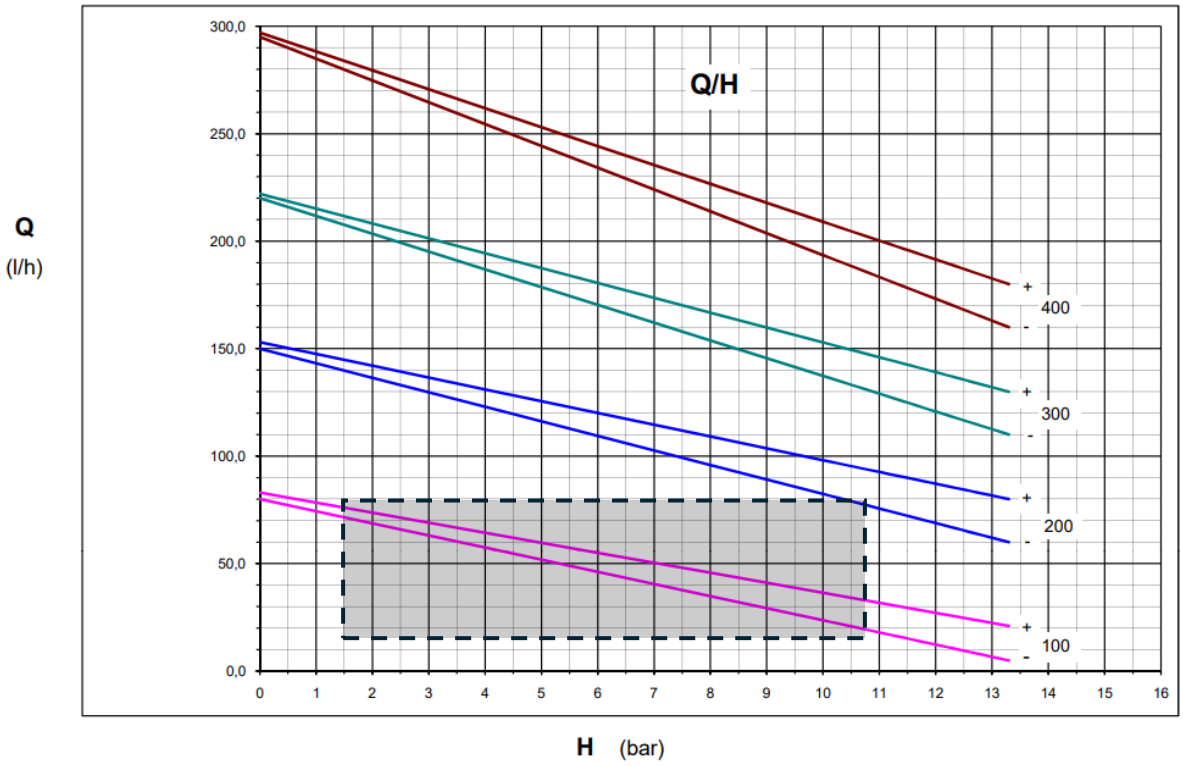

Figure 3.4: SVM 1x100 refrigerant pump performance map

a)

b)

Figure 3.5: (a) March May SVM 1x100 refrigerant pump; (b) Variable frequency drive

3.3.2 Expander

Expansion devices are integral to an ORC system and rely on pressure differentials to rotate and produce power. The air squared E15H022A-SH 1 kW scroll expander [152] was chosen for this system. The semi-hermetic scroll expander provides lubrication-free expansion and is compatible with refrigerants. The expander has a volume ratio of 3.5,

displacement of 14.5 cm^3, and a weight of 9 kg, providing a compact expansion solution. The performance curves provided by the manufacturer are shown in Figure 3.6. The high-pressure superheated working fluid vapor expands to produce power through the rotating scrolls inside the expander, which rotates the expander shaft, consequently rotating the internal magnetic rotor. The internal rotor, covered by a containment shroud, is then connected to a magnetic coupling, which has an external shaft, which is then connected to a torque sensor and a magnetic brake. A detailed expander model is presented in Section 4.3.4.

The outer diameter of the containment shroud of the internal rotor of the expander and the internal diameter of the magnetic coupling had a 1 mm clearance. Hence, the alignment of the expander external shaft assembly with the magnetic coupling, torque sensor, and the magnetic brake was critical to reduce friction. Figure 3.7 illustrates the assembly of the scroll expander. An aluminium block, with a thickness of 30 mm, was fitted to the aluminium strut assembly to align the height of expander outlet connection with the condenser inlet connection.

The inlet pressure of the expander was dependent on the pump outlet pressure (less pressure losses), while the expander torque was controlled by the magnetic brake described in Section 3.4.5.

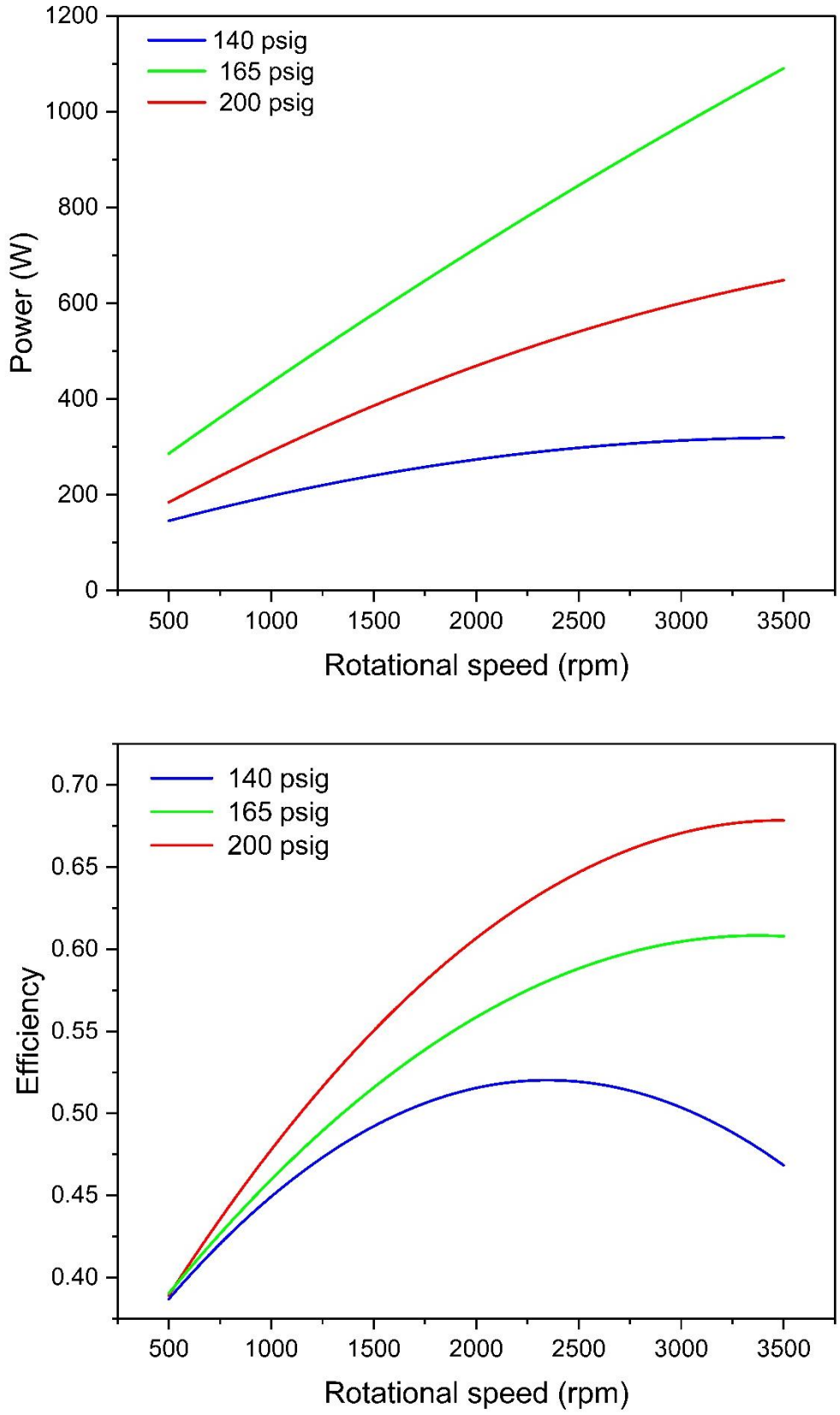

Figure 3.6: Scroll expander performance curves with R-134A refrigerant

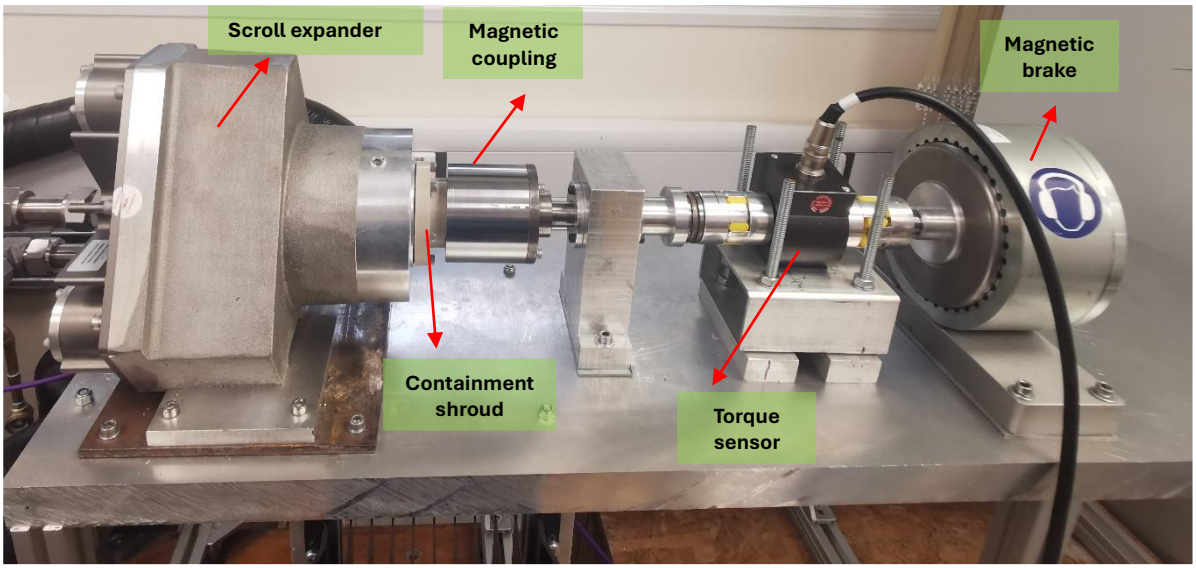

Figure 3.7: New expander assembly with 30 mm base and reassembled magnetic coupling

3.3.3 Liquid receiver

The liquid receiver is a critical component of the ORC and allows for the storage of the condensed refrigerant so that the pump may have a continuous liquid supply. The liquid receiver was sized at 40 % capacity of the total system charge, which was determined through the dynamic numerical model described in *Chapter 4,* based on the recommendations of Dickes et al. [153]. The liquid receiver chosen for this system was supplied by Dean and Wood, the VLR 160x345 [148], with a height of 345 mm, diameter of 160 mm, volume of 5.7 L, and a maximum working pressure of 34 bars, with the inlet at the top and the outlet at the bottom. The inlet of the liquid receiver was connected to the condenser, situated at the top to ensure free flow of the liquid refrigerant to the liquid receiver. The outlet of the liquid receiver was connected to the pump, situated at the bottom to ensure a fully liquid supply to the pump, as the vapor would accumulate at the top of the liquid receiver. The liquid receiver and sight glass assembly is illustrated in Figure 3.8. The sight glasses selected were the Danfoss SGP12 and are vital to visually inspect the quality of the working fluid at the inlet and outlet of the liquid receiver. It is imperative that the working fluid must be liquid at both stages to ensure that the pump

runs smoothly. If, upon inspection, the working fluid was not liquid, the flow rate of the liquid nitrogen was adjusted so a fully liquid working fluid enters the liquid receiver.

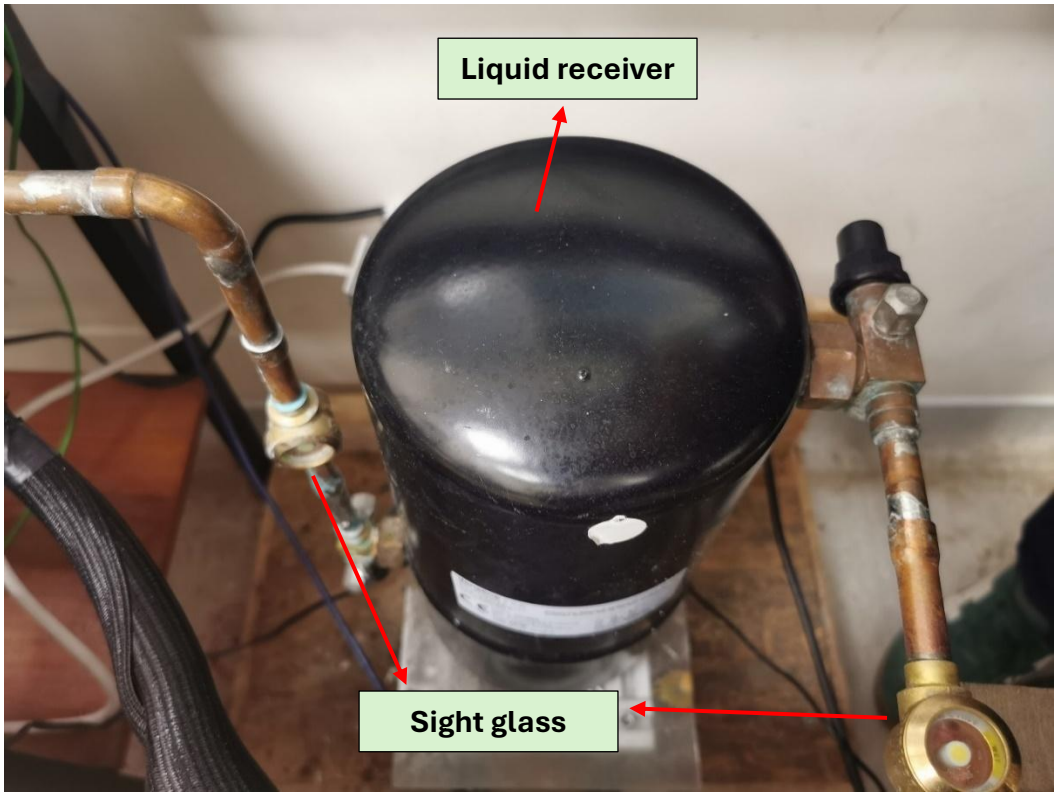

Figure 3.8: Liquid receiver and sight glass assembly

3.3.4 Evaporator

The evaporator is responsible for the heat exchange at the high temperature side of the ORC, resulting in evaporation and superheating of the working fluid through heat exchange with the hot water. A counterflow stainless-steel shell and tube type heat exchanger was chosen as the evaporator, manufactured by EJ-Bowman [152]. The SC4508-4 provides a heat dissipation capability of 35 kW, with 57 tubes, each with a thickness of 0.7 mm, 650mm length, and 9.52mm outer diameter. The heat exchanger has 9 baffles which comprise the shell, with a total shell volume of 2.9 Liters. The evaporator had a length of 764 mm, diameter of 114 mm, and a weight of 21 kg. The total heat exchange area for the shell side was 1.021 m^2 and the tube side was 0.943 m^2. The heating medium (water) passed through the shell, effectively transferring heat to the

working fluid, and returned to the water heater to be heated again to the set temperature. The working fluid flowed through the tubes of the evaporator, absorbing the heat from the water to change phase into superheated vapor on its way to the expander. Figure 3.9 illustrates the internal and external geometry of the SC4508-4 shell and tube type heat exchanger. A detailed evaporator model is presented in Section 4.3.5.

Figure 3.9: SC4508-4 Shell and tube-type evaporator

3.3.5 Condenser

The condenser is responsible for heat exchange at the low temperature side of the ORC, facilitating condensation of working fluid through heat exchange with the liquid nitrogen. The B185x36 from SWEP [152] was chosen as the condenser, which is a stainless-steel brazed plate counterflow heat exchanger. The specific heat exchanger type was chosen

based on research into cryogenic heat exchanger safety and availability. The B185x36 has 36 plates, each with 2 mm thickness. The heat exchanger has a length of 425.2 mm, width of 203.2 mm, and a thickness of 88 mm. The refrigerant side channel volume is 0.1169 dm^3, and the liquid nitrogen channel volume is 0.1106 dm^3. The condenser has a maximum working pressure of 140 bar, and can sustain a maximum flow of 38.8 m^3/h. The refrigerant flowed through one channel, rejecting heat to the liquid nitrogen and condensed back into liquid form. The liquid nitrogen passed through the second channel opposite to the direction of the working fluid, absorbing the heat from the working fluid and vaporising. The condenser is illustrated in Figure 3.10. A detailed condenser model is presented in Section 4.3.5.

Figure 3.10: SWEP B185x36 condenser

3.3.6 Liquid nitrogen dewar

The liquid nitrogen dewar was placed outside to minimise asphyxiation risks, and the liquid nitrogen was piped into the lab using vacuum insulated pipes and hoses. The liquid

nitrogen dewar was manufactured and supplied by Statebourne Cryogenics; the Cryostor 180, with a capacity of 180 L of liquid nitrogen. The stainless-steel liquid nitrogen dewar is vacuum insulated and can provide liquid nitrogen at a pressure of up to 4.5 bar. The outlet pressure can be manually controlled through a pressure regulator, and the presence of a dip tube ensures a fully liquid supply. The liquid nitrogen dewar is shown in Figure 3.11.

Figure 3.11: Cryostor 180 Liters liquid nitrogen dewar

3.3.7 Water heater

Hot water was circulated through the evaporator utilising the Tool-Temp TT181 [152] water heater, which is equipped with a 0.75 kW motor pump, capable of delivering up to 4.5 bar of pressure and 75 l/min of flow. The TT181 has a heating capacity of up to 9kW and is equipped with a digital temperature control system, providing up to 95 °C of hot water. The TT181 has length of 670mm, width of 270 mm, height of 650mm, and a

volumetric capacity of 7 Liters of water and provides a constant flow of hot water with a 0.1 °C accuracy of the set temperature. Since the TT181 is not equipped with a flow control system, a globe valve was installed downstream of the heater, which was manually used to set the water flow rate. The TT181 water heater and its pump performance curves are shown in Figure 3.12.

a)

b)

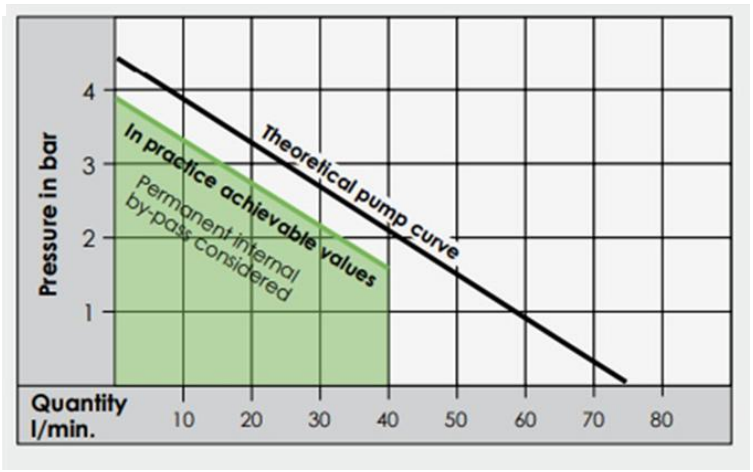

Figure 3.12: (a) Electrical water heater; (b) Water heater pump performance curve [149]

3.4 Sensing instrumentation

3.4.1 Data acquisition device

Data acquisition devices allow for the storage of analogue data from the sensors and provide an interface between the sensors and the computer. The DataTaker DT85 Series 4 is a comprehensive data acquisition device, capable of receiving various analogue and digital inputs. The DT85 is supplied with its own software, which allows for setting the scaling of each individual sensor based on the port it is connected to. It also provides the ability for real-time monitoring of collected data. The DT85 data acquisition device is illustrated in Figure 3.13. The DT85 had an inbuilt zero drift recalibration option.

Figure 3.13: DataTaker DT85 data acquisition device

3.4.2 Temperature sensors

K-type thermocouples were utilised to measure the process temperatures, illustrated in Figure 3.14. All thermocouples in the test rig were Farnell JUMO UK LTD 90/00056813 stainless-steel with a probe diameter of 3mm, a length of 100 mm, a temperature range of -200 °C to 1200 °C, and a measurement error of ± 0.5 °C.

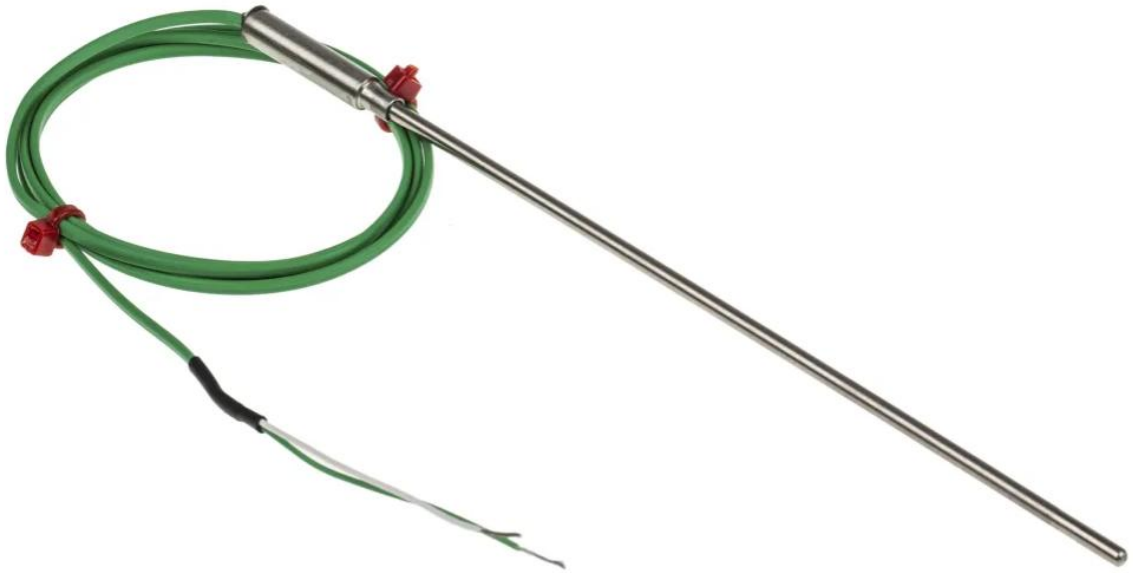

Figure 3.14: Thermocouple and associated gland assembly

3.4.3 Pressure sensors

The RS-PRO PS-G4002-5A4 pressure transducers were employed to measure the process pressure, illustrated in Figure 3.15. The pressure transducers have a range of 0 bar_g to 40 bar_g, an analogue output of 4-20 mA, measurement error of <± 0.25 %, and operate at an input voltage of 9-32 V DC. Since the DT85 data acquisition device measures analogue input, scaling was necessary to obtain the correct pressure reading. The atmospheric pressure was measured to be 1.013 bars, and hence the 4 mA output was set at this pressure. The maximum absolute pressure the transducer can detect is 41.013 bars, hence the 20 mA output was set at this pressure. The software then applies a linear relationship and calculates the real-world value at the specific analogue input.

Figure 3.15: Pressure transducer and associate fitting assembly

3.4.4 Flow sensors

3.4.4.1 Heating loop

The IFM SV4200 vortex water flow meter was used to measure the volumetric flow rate of water flowing through the evaporator and is shown in Figure 3.16. The flow meter has a range of 1 L/min to 20 L/min, operating voltage of 18-30 V DC, a measurement accuracy of <± 2 %, and is equipped with a digital display. The analogue output of the flow meter is frequency, and a scaling of 200 Hz at 0 L/min and 2000 Hz at 20 L/min was set in the data acquisition device. The SV4200 is a volumetric flow meter and converting to mass flow readings required the calculation of water density at the inlet of the evaporator, where the flow meter was attached. Using the temperature and pressure readings of water at the evaporator inlet, the density of the water was calculated. Equation 3.1 was then used to calculate the mass flow rate ($\dot{m}$) using the density (ρ) and volumetric flow rate ($\dot{v}$), obtained from the SV4200, of the water flowing through the evaporator.

$$\dot{m} = \rho * \dot{v} \quad (3.1)$$

Figure 3.16: IFM SV4200 vortex water flow meter

3.4.4.2 Cooling loop

The Sino-Inst GF06 gear flow meter was used to measure the volumetric flow rate of liquid nitrogen through the condenser. The GF06 flow meter has a flow range of 0.16 L/min – 8.5 L/min, temperature range of -196 °C – 80 °C, an analogue output of 4-20 mA, operates at a voltage of 24 V DC, a measurement error of ± 0.25 %, and has a digital display, as illustrated in Figure 3.17. A scaling of 4 mA at 0.16 L/min and 20 mA at 8.5 L/min was set in the DEX software. Since the GF06 measures the volumetric flow rate, the temperature and pressure of the liquid nitrogen inlet were used to compute the density, and Equation 3.1 is then employed to calculate the mass flow rate of the liquid nitrogen.

Figure 3.17: Sino-Inst GF06 liquid nitrogen gear flow meter and digital display

3.4.4.3 ORC loop

The Trigas DM4-8AN-BA-1-S turbine mass flow meter was utilised as the mass flow measurement instrument for the refrigerant. The refrigerant flow meter is a very high precision device with a mass flow range of 0 – 0.1248 kg/s, a temperature range of -270 °C – 400 °C, and a measurement error of <± 0.03 %. The flow meter was supplied with a TriLIN-T3-01-R4-O-I1-V1 lineariser control box, which is connected to the pick-off of the flow meter and provides an analogue frequency output. A scaling of 200 Hz at 0 kg/s and 2000 Hz at 0.1248 L/min was set in the data acquisition device. The LIN control box can be connected to the computer, and using the Flowhow+ software, real-time flow data can be observed. Using the LIN control box and the calibration data provided by the manufacturer, the refrigerant flow meter was configured to liquid R410A. The flow meter and control box are illustrated in Figure 3.18.

Figure 3.18: Trigas DM4-8 refrigerant flow meter and the TriLIN flow meter control box

3.4.5 Torque sensor

The DRBK torque sensor was used to measure the torque and rotational speed of the expander, illustrated in Figure 3.19. The sensor has a range of 0 – 20 N.m and can measure rotational speeds of up to 15000 rpm, with a measurement error of <± 0.3 %. The torque analogue output is 0-5 V, and the rotational speed has a pulse output. In the data acquisition device, the pulse input for the rotational speed measurement does not require any scaling, and the torque scaling was set to 0 at 0 V and 20 N.m at 5 V. The torque sensor shaft was connected to the expander magnetic coupling shaft and the MAGTROL magnetic hysteresis brake shaft using adjustable shaft couplings.

Figure 3.19: Applied measurements DRBK torque and rotational speed sensor

3.4.6 Magnetic Brake

The expander in the ORC requires a load, otherwise the shaft's rotational speed would keep increasing until failure. To induce a load, a brake was employed so that the rotational speed and the torque of the expander shaft could be controlled. The magnetic brake chosen was the MAGTROL AHB-5 which allows for precise control of the torque by adjusting the current through the MAGTROL 5210 0-35 V DC power supply. By adjusting the torque, the rotational speed of the expander can be controlled to the manufacturer specified maximum rotational speed of below 3600 rpm. The MAGTROL AHB-5 is an air-cooled brake and works on the principle of hysteresis utilising magnetic braking, hence rendering them frictionless. The magnetic brake and power supply are illustrated in Figure 3.20.

a)

b)

Figure 3.20: (a) MAGTROL AHB-5 magnetic hysteresis brake; (b) MAGTROL 5210 power supply and current control box

3.4.7 Power supply

Except for the temperature sensors, all other measurement instruments require a DC power supply. The PS-3010DS DC power supply was chosen, through which the voltage can be controlled between 0 – 30 V DC and was within the range of all sensors. A waterproof power distribution board was designed by the author to enable the

distribution of power to all the sensors without any voltage drops. The is illustrated in Figure 3.21.

Figure 3.21: PS-3010DS DC power supply

3.5 Piping and sealing mechanism

Robust piping and sealing mechanisms are necessary to prevent leakage, which would lead to significant environmental damage [99]. Stainless-steel tubes were utilised, since they are compatible with refrigerants and can withstand high pressures and cryogenic temperatures associated with refrigerant and liquid nitrogen use. Stainless-steel twin ferrule compression fittings were used to connect the system components and sensing instrumentation with the piping network. Several pressure relief valves were employed to ensure personnel safety. In the ORC loop, a pressure relief valve was fitted before the expander. The pressure relief valve chosen for this system was the Henry 5232A PRV 350 PSI / 20.7 BAR and automatically opens when the set pressure is reached, hence preventing failure in case of pressure buildup. Additionally, two pressure relief valves and a safety valve were installed on the cryogenic liquid medium line, ensuring the liquid nitrogen pressure remained within safe operating limits. All components were fixed to the

table, and appropriate insulation was used, not only to prevent heat losses, but also to prevent cryogenic burns in case of accidental contact with the piping. The insulation utilised was the cryogenic K-Flex Insulation Class O with 1” thickness. The lab was also fitted with a mechanical ventilation system and oxygen monitoring system to minimise the risks of asphyxiation.

Each segment of pipe assembly was individually tested for leaks using compressed nitrogen and held underwater to detect the presence of bubbles. While the common practice is using leak detection spray, it was found that the leak detection spray could not detect extremely minor leaks, and the water test yielded better results. Hence, the water test and the leak detection spray were used in tandem to ensure the system was leak-free. An example of the water test and leak detection spray testing during the experimental test rig building process is depicted in Figure 3.22 and Figure 3.23.

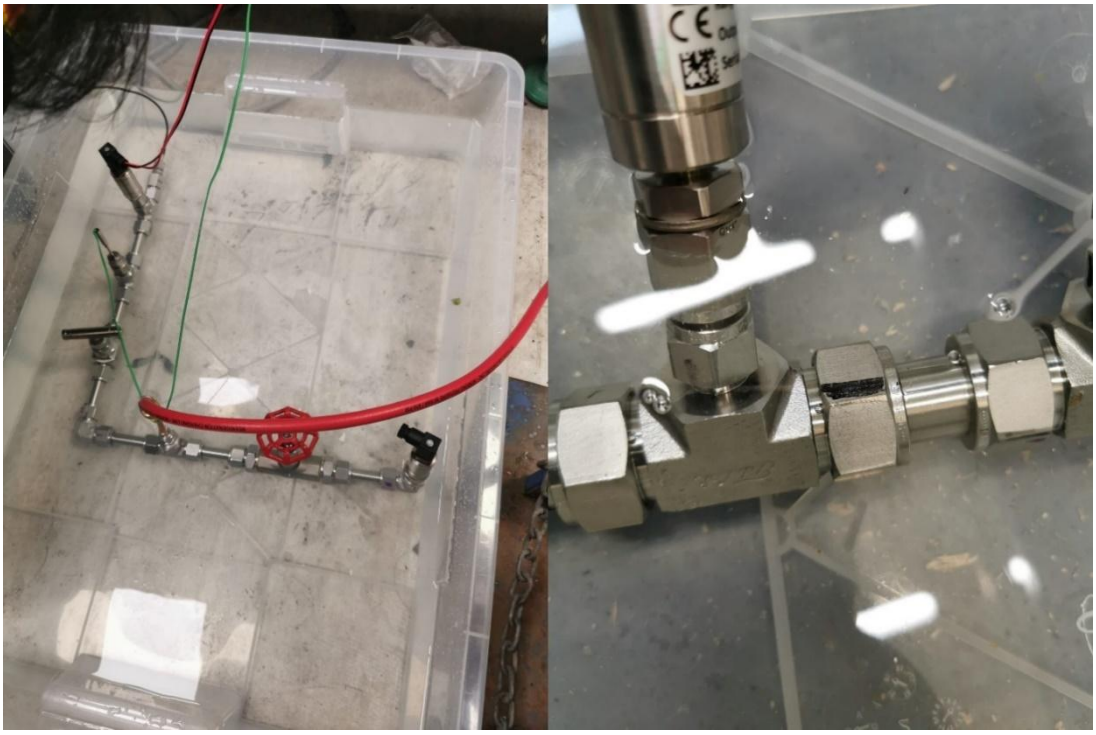

Figure 3.22: Water tank and compressed nitrogen leak testing

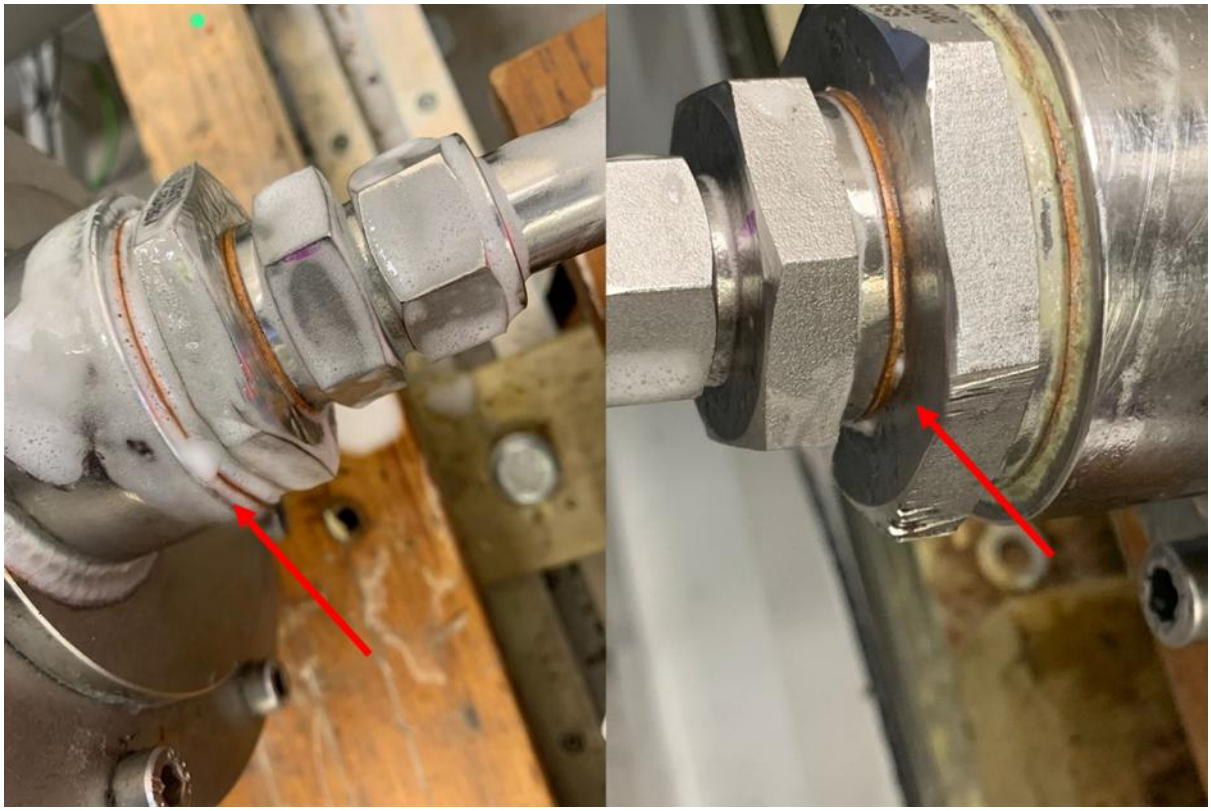

Figure 3.23: Leak detection spray and compressed nitrogen leak testing

Refrigeration pressure regulations require that any system containing hydrofluorocarbons be pressure and leak tested. The requirements are two-pronged, and each system must pass both tests, namely the strength and tightness tests, before operation [154]. To pass the strength test, the system must be kept at twice the operating pressure for 1 hour. In the tightness test, the system must be pressurised to 1.1 times its operating pressure and held for 24 hours. If the pressure drop is <1% (temperature change may affect pressure), then the system is leak-free [154]. The maximum operating pressure using R410A was 15 bars. The results of the strength test and tightness test conducted for this experiment rig are illustrated in Figure 3.24 and Figure 3.25.

Figure 3.24: Strength test reading on pressure gauge at 30 bars; one hour apart

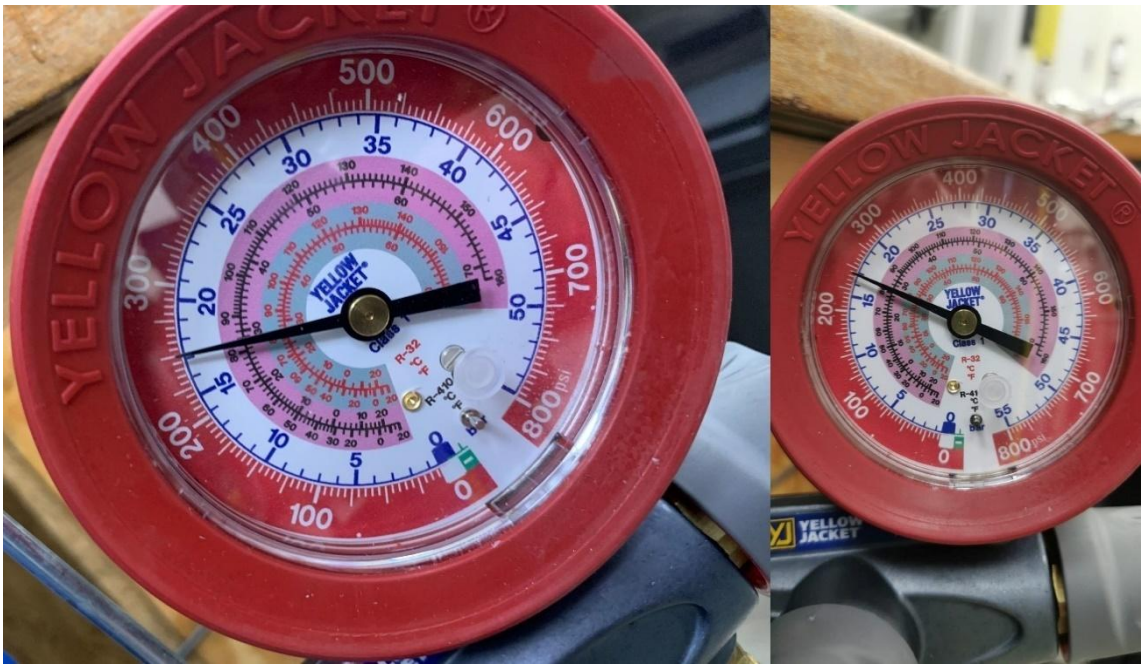

Figure 3.25: Tightness test reading on pressure gauge at 17 bars; 24 hours apart

3.6 Standard operating procedure

The standard operating procedure of the cryogenic-enhanced ORC experimental test rig is summarised as follows:

1. Switch on the DT85 data acquisition device, connect to the laptop, and mirror the time on the laptop.
2. Induce a deep vacuum (BACOENG vacuum pump) to remove air and moisture from the system. The vacuum should be held below 300 microns [154].
3. Place the refrigerant bottle on the weighing scales.
4. Connect the liquid line of the refrigerant bottle to the charging Schraeder valve.
5. Zero the scales before beginning charging.
6. Control the flow through the control valves attached to the charging hose and charge 9 kg of R410A into the system.
7. Once charging is complete, close the valve on the charging hose and remove the charging hose from the Schraeder valve.
8. Open the liquid nitrogen valve to allow it to flow through the condenser and maintain the flow at 1.5 lpm as shown on the digital liquid nitrogen flow meter.
9. After 10 minutes, R410A should be in liquid form below 1.5 bar pressure and -45 °C. Visually inspect the sight glass at the pump inlet and check the pressures and temperatures on the laptop.
10. Switch on the electrical water heater and set the temperature to 25 °C. Control the flow of water, through the globe valve, at 12 lpm as shown on the digital water flow meter.
11. Switch on the magnetic brake connected to the expander shaft and set the torque at 2 N.m.
12. Turn on the working fluid pump through the variable frequency drive and set the rotational speed at 900 rpm. The mass flow rate of R410A corresponds to the

rotational speed such that at 900, 1000, 1100, and 1200 rpm, the mass flow is 10 g/s, 12 g/s, 14 g/s, and 16 g/s.

13. Monitor the expander inlet temperature. Once it reaches the desired testing temperature, record the time. Three readings at 5 s interval will be averaged to obtain the final test reading.
14. Repeat step 11 and 12 for each expander inlet testing temperature, allowing for 2 minutes at each test condition for the system to stabilise.
15. Once the test is completed, turn of the refrigerant pump, water heater, magnetic brake, and close the liquid nitrogen valve.
16. Save the data files from the data acquisition device before switching it off.
17. Wait 2 hours to allow the cryogenic working fluid to vaporise.
18. Recover the working fluid back into the refrigerant bottle using the Bosch RG 4.0 refrigerant recovery machine

3.7 Numerical model basis

Many numerical and simulation-based models of cryogenic ORCs have been proposed in literature, yet none have tackled non-flammable and low flammability refrigerants. Additionally, most studies utilise steady-state numerical models which, due to the low-temperature operation and constant phase change occurring within the cryogenic ORC, cannot accurately predict the system performance. Hence, the experimental setup feeds into the dynamic modelling of the cryogenic ORC, developed in Siemens Amesim. Siemens Amesim is a professional dynamic modelling software, and allows for detailed system component and pipe modelling, complete with two-phase correlations. Additionally, the software contains an extensive library of refrigerant properties, thus eliminating the need for connecting to a separate fluid properties database (e.g. REFPROP). The geometries and efficiencies of the main components and pipes were essential to develop a numerical model to compliment the experimental study.

The performance metrics for the experimental analysis have been defined in *Chapter 4*. REFPROP 9.1 [43] was utilised to compute the specific enthalpies and entropies at specific state points, using the temperature and pressure values obtained from the experimental rig.

3.8 Summary

In this chapter, the experimental setup of the cryogenic Organic Rankine Cycle was described in detail. The schematic and the lab setup were illustrated, and all components and sensing instrumentation were discussed. The cryogenic Organic Rankine Cycle consisted of three loops, namely the heating loop, cooling loop, and the ORC loop. The heating loop utilised an electric heater to heat and circulate tap water through the evaporator, acting as the heating medium to superheat the working fluid. The cooling loop applied liquid nitrogen as the cryogenic cooling medium to condense the working fluid in the condenser. In the ORC loop, the pump acted as the flow-inducing pressurisation device, evaporator as the hot side heat exchange device, scroll expander as the power production device, the condenser as the cold side heat exchange device, and the liquid receiver as a buffer tank between the condenser and the pump. All components were fitted with temperature and pressure sensors at their inlet and outlet ports, and each loop was fitted with a flow measurement device. The piping and sealing mechanisms were described in detail, and extensive leak testing was employed to ensure a leak-proof system. The system component parameters, pipe geometries, and components efficiencies were used for the development of the dynamic numerical model in Chapter 4. The findings are discussed and illustrated in *Chapter 5: Experimental analysis*.

Chapter 4. Dynamic Numerical Model

4.1 Introduction

Cryogenic enhanced ORCs found in literature are often modelled as static or steady-state numerical models. Due to the two-phase flow and multiple phase-change cycles occurring in the cryogenic ORC, a dynamic model is required for a better understanding of system behaviour at ultra-low cryogenic temperature conditions. This chapter describes the development of the dynamic numerical model for the cryogenic enhanced ORC for simultaneous reutilisation of waste thermal and cryogenic energy, developed in Siemens Amesim. As mentioned in Chapter 3, Methodology, the main component geometries and performances and pipe dimensions were directly fed into the dynamic numerical model to ascertain real-world applicability. The dynamic model also provides a better understanding of the effect of system initial charging conditions on the system performance and correct system charge prediction.

This chapter firstly provides an overview of the dynamic numerical model and provides the conceptualisation of a modularised cryogenic ORC system. Secondly, this chapter delves into the system and individual component level modelling, complete with two-phase flow considerations. Thirdly, a complete low-flammability cryogenic working fluid selection criterion is described in this chapter, considering thermophysical and environmental attributes, based on current hydrofluorocarbon regulations. Lastly, the energy and exergy models are presented, and the performance metrics are defined. The dynamic numerical model methodology depicted in this chapter has been published in the Elsevier journal “Energy”, under the title “Cryogenic Energy Assisted Power Generation Utilizing Low Flammability Refrigerants” [99]. The digital identifier is https://doi.org/10.1016/j.energy.2024.132770.

4.2 Overview

Through extensive literature review, Chapter 2, a research gap was identified in that the cryogenic ORC numerical models were either static or steady-state models. Hence, an extensive dynamic model for a micro-scale cryogenic enhanced ORC was developed, utilising low flammability hydrofluorocarbon working fluids. The Siemens Simcenter Amesim [155] thermodynamic modelling tool was utilised, which is a professional industrial software and contains in-built two-phase flow correlations and fluid thermophysical properties database. Figure 4.1 illustrates the flowchart of the methodology.

Figure 4.2 illustrates the modularised unit of the cryogenic enhanced ORC for thermal and cold waste energy reutilisation. The cycle starts at the working fluid pump, which enables suction of the low-pressure liquid cryogenic working fluid and pressurises it to initiate flow. The high-pressure liquid working fluid is then pumped to the evaporator, where it changes phase from liquid to superheated vapor by absorbing the waste heat energy. The pressurised superheated vapor working fluid then flows to the expander, producing mechanical work by rotating the expander shaft, effectively reducing the pressure and temperature of the working fluid. The expanded superheated vapor working fluid then flows to the condenser, rejecting heat to the cryogenic liquid fuel. The working fluid condenses back into liquid phase, subsequently initiating regasification of the cryogenic fuel. After condensation, the liquid working fluid collects in the liquid receiver, ensuring a constant liquid supply to the working fluid pump. Hence, the evaporator acts as the waste thermal energy reutilisation device and the condenser acts as the waste cryogenic energy reutilisation device. The automatic leak detector and associated electrical controls are all containerised into a compact plug-and-play modularised solution for waste energy reutilisation. With the advent of hydrogen as the green fuel of the future global economy, a modularised liquid cryogenic fuel-regassification and waste energy reutilisation technology would provide a smooth energy-efficient transition away from fossil fuels and enable holistic decarbonisation.

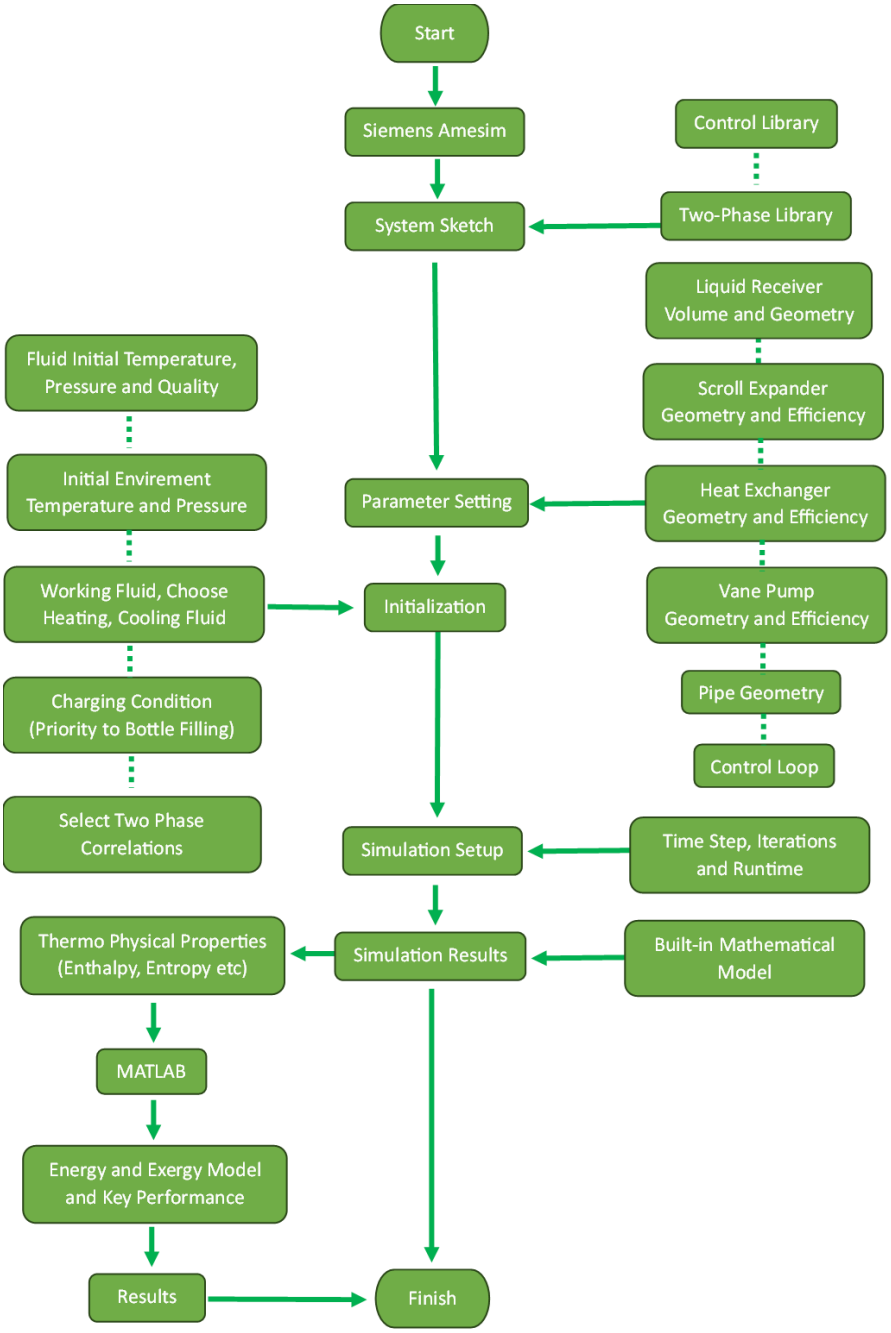

Figure 4.1: Flowchart of the dynamic numerical model methodology

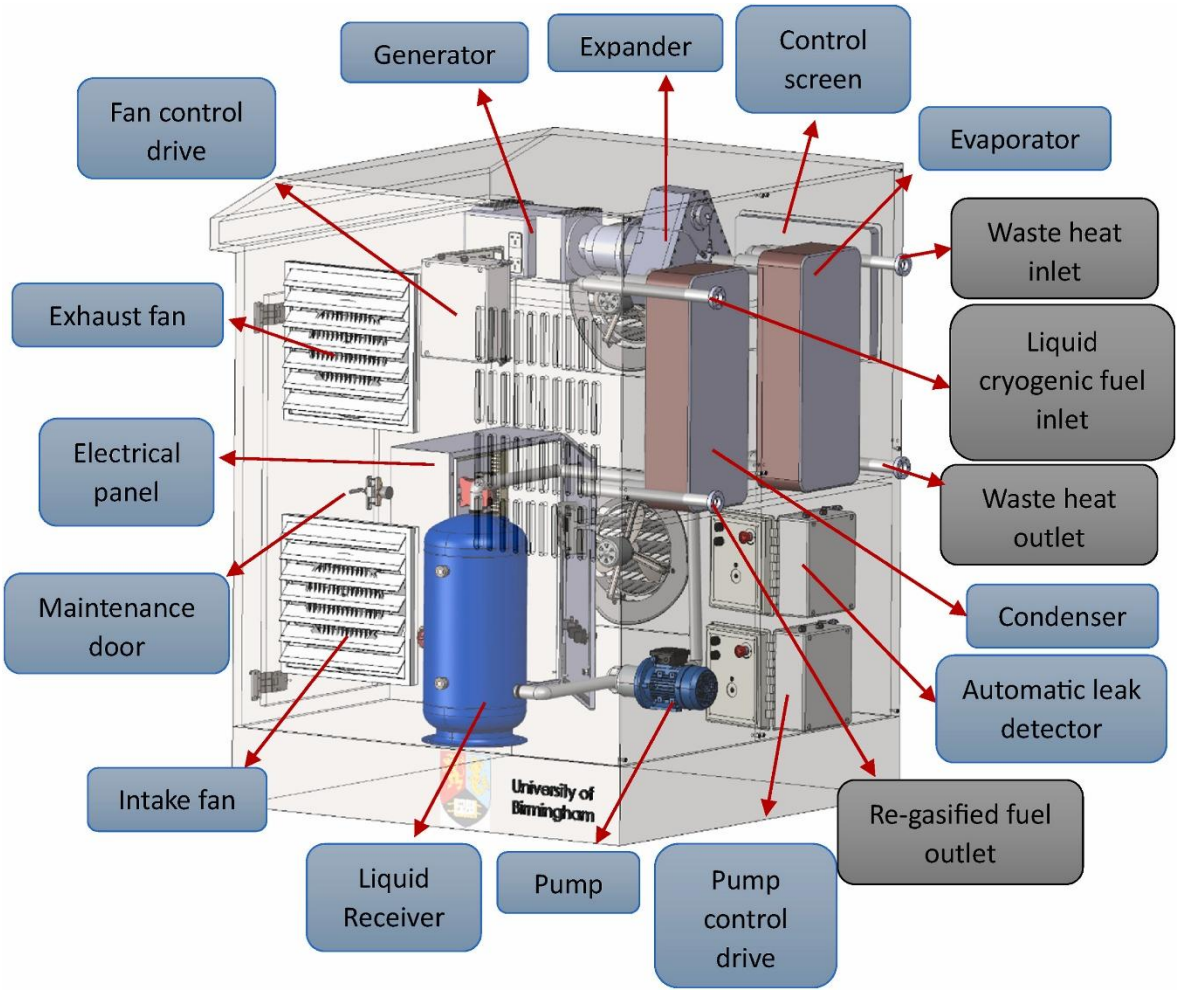

Figure 4.2: Modularised unit of the cryogenic enhanced ORC.

4.3 Individual component modelling

Siemens Amesim [155] was used to develop the numerical model of the cryogenic ORC. Siemens Amesim contains an in-built fluid thermophysical properties database, comparable to NIST standards, and eliminates the need to connect to additional fluid properties databases. In the Siemens Amesim environment, comprehensive two-phase flow individual component and system-level modelling can be performed, and control mechanisms can be established to understand and control system behaviour under transient conditions. The utilisation of a dynamic numerical model over a steady-state model can be justified by considering the charging conditions. Cryogenic hydrofluorocarbon working fluids have low saturation temperatures, leading to the

fluctuation of working fluid quality. The working fluid system charge determines the liquid to vapor ratio in the liquid receiver, which in turn significantly affects the performance of the system. Hence, a steady-state numerical model is an inaccurate depiction of ultra-low temperature cryogenic enhanced ORCs, as it cannot accurately represent the constantly fluctuating density and quality of the working fluid. Additionally, cryogenic enhanced ORCs require extensive control measures to prevent system failure during start-up and shut-down procedures, which are dependent on working fluid charging conditions and cannot be implemented through traditional steady-state modelling techniques.

The Siemens Amesim environment system sketch is illustrated in Figure 4.3, using the two-phase component library. The heating, cooling, and ORC loops were indicated using red, blue, and green colours. The heating and cooling loops, corresponding to waste thermal energy and waste cryogenic energy, respectively, were modelled as open-loop configurations while the ORC loop was developed as a closed-loop system. As discussed in Chapter 3, Methodology, the incorporation of real-world individual component design parameters, utilised in the experimental setup, ensured that the dynamic numerical model would be applicable in the real-world. The geometries of each system component were validated by the manufacturers.

In terms of the simulation run setup, the timestep of the simulation was set at 10 ms, and the model was run for 4000 s. Siemens Amesim does not provide considerations for insulation, hence it was assumed that the system was perfectly insulated, i.e. there was no heat transfer to or from the environment. The atmospheric temperature and pressure were set to 20 °C and 1.015 bars, respectively, and it was assumed that these remained constant throughout the run time. The limitations of this study are based on these assumptions, as perfectly insulated systems are almost impossible to achieve and the only known alternative would be super-vacuum insulated piping, which is very costly. Additionally, the environmental conditions vary throughout the day, and running a real-world system in a controlled environment would significantly increase the complexity and cost of the system. Also, the entrance and exit pressure losses were discounted.

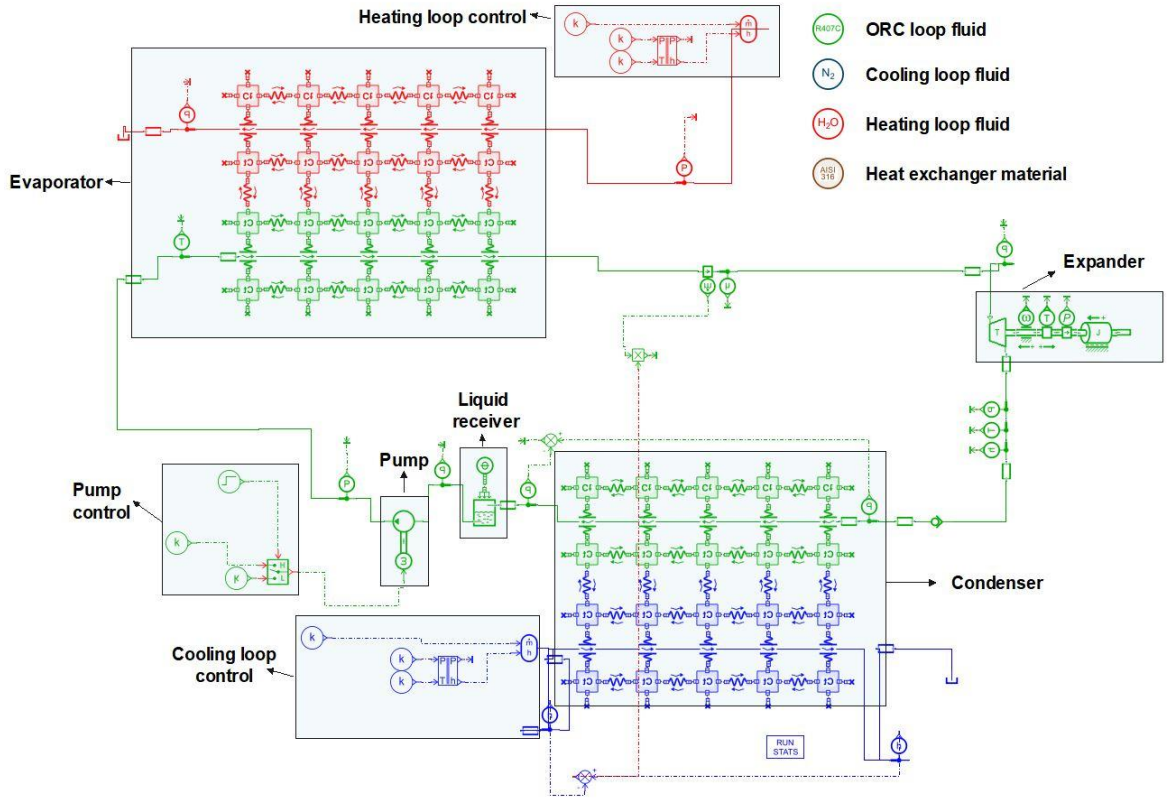

Figure 4.3: Sketch of the proposed dynamic numerical model of the cryogenic enhanced ORC in Siemens Amesim.

4.3.1 Heating loop

Figure 4.3 illustrates the heating loop in red. Within the open-loop configuration control mechanisms were implemented, which guaranteed constant inlet conditions for the heating medium, namely the flow rate, temperature, and pressure. Water was utilised as the heating medium. The control loop was set up such that the heating medium would not exceed its normal boiling temperature, so as to remain in liquid phase. The control loop ensured this by increasing the pressure of the heating medium as it reached its boiling temperature. The flow rate of the hot water was controlled at 0.2 kg/s, while the temperature was varied between 70 °C and 110 °C.

4.3.2 Cooling loop

Liquid nitrogen was employed as the cryogenic energy source in the open-loop configuration, illustrated in blue in Figure 4.3. A control loop was implemented, enabling the adjustment of the inlet conditions of the liquid nitrogen. While the inlet temperature and pressure of the cooling medium were set at -196 °C and 1.5 bars, respectively, the mass flow rate was determined by the control loop to ensure that the working fluid condensation pressure was maintained close to the atmospheric pressure. Through constant monitoring of the working fluid quality at the condenser outlet, the control loop ensured that the working fluid remained in liquid phase by adjusting the liquid nitrogen flow rate. Currently, cryogenic liquid hydrogen thermo-fluid properties and behaviours are relatively unknown and untested, and hence, liquid nitrogen was employed as the cryogenic energy source.

4.3.3 Pump model

The working fluid pump was modelled based on the selected rotary vane pump during the experimental setup, as described in Chapter 3, Section 3.3.1. The input parameters of the SVM 1x100 [144] are presented in Table 4.1. The pump control loop, depicted in Figure 4.3, was designed to emulate a variable frequency drive and was employed to regulate the rotational speed of the pump. It guaranteed that the pump operated under optimal conditions as indicated by the manufacturer. Once the input parameters and initialisation conditions were set, the simulation tool utilised the following equations to model the working fluid pump:

The mass flow rate ($\dot{m}_{WF}$) of the working fluid flowing through the pump was calculated as:

$$\dot{m}_{WF} = \eta_v \cdot \rho_{suc} \cdot N \cdot disp \tag{4.1}$$

Where η_v, ρ_{suc}, N, and $disp$ were the volumetric efficiency, suction density, pump rotational speed, and the pump displacement, respectively.

The isentropic efficiency (η_{is}) was computed as:

$$\eta_{is} = \frac{h_{2,is} - h_1}{h_2 - h_1} \tag{4.2}$$

Where $h_{2,is}$, h_1, and h_2 were the isentropic discharge specific enthalpy, suction specific enthalpy, and the discharge specific enthalpy.

The pump enthalpy increase (Δh_p) was evaluated using:

$$\Delta h_p = h_2 - h_1 = \frac{h_{2,is} - h_1}{\eta_{is}} \tag{4.3}$$

The enthalpy flow rate increase (dmh_{pump}) was given as:

$$dmh_{pump} = \dot{m}_{WF} \cdot \Delta h_p \tag{4.4}$$

The suction enthalpy flow rate (dmh_1) was calculated as:

$$dmh_1 = -\dot{m}_{WF} \cdot h_1(p_1, T_1) \tag{4.5}$$

Where, p_1 and T_1 were the pressure and temperature at the pump inlet.

The discharge enthalpy flow rate (dmh_2) was calculated using:

$$dmh_2 = -dmh_1 + \dot{m}_{WF} \cdot \Delta h_p \tag{4.6}$$

Table 4.1: Input parameters for the working fluid pump model [144].

Parameter	Value
Displacement	1.58 cm^3
Volumetric efficiency	0.9
Isentropic efficiency	0.6
Mechanical efficiency	0.9

4.3.4 Expander model

The input parameters, shown in Table 4.2, were based on the E15H022A-SH scroll expander [146] selected during the experimental setup, and formed the basis of the expander numerical model. After the input parameters were defined and initialised, the dynamic simulation tool then modelled the expander by employing the following equations:

The mass flow rate ($\dot{m}_{WF}$) through the expander was calculated as:

$$\dot{m}_{WF} = \eta_v \cdot \rho_{up} \cdot N \cdot disp \tag{4.7}$$

Where, η_v = volumetric efficiency; ρ_{up} = upstream density; N = expander rotational speed; $disp$ = expander displacement.

The isentropic efficiency (η_{is}) was given as:

$$\eta_{is} = \frac{h_3 - h_4}{h_3 - h_{4,\text{is}}} \tag{4.8}$$

Where, h_3 = upstream specific enthalpy; h_4 = downstream specific enthalpy; $h_{4,is}$ = isentropic downstream specific enthalpy.

The enthalpy decrease (Δh_{exp}) was calculated using:

$$\Delta h_{exp} = h_4 - h_3 = \left(h_{4,is} - h_3\right) \cdot \eta_{\text{is}} \tag{4.9}$$

The enthalpy flow rate decrease (dmh_{exp}) was computed using:

$$dmh_{exp} = \dot{m}_{WF} \cdot \Delta h_{exp} \tag{4.10}$$

The upstream enthalpy flow rate (dmh_3) was calculated using:

$$dmh_3 = -\dot{m}_{WF} \cdot h_3(p_3, T_3) \tag{4.11}$$

Where, p_3 = pressure and T_3 = temperature, calculated before the expander.

The downstream enthalpy flow rate (dmh_4) was calculated using:

$$dmh_4 = -dmh_3 + \dot{m}_{WF} \cdot \Delta h_{exp} \tag{4.12}$$

Table 4.2: Input parameters for the expander model [146].

Parameter	Value
Displacement	14.5 cm^3
Volumetric efficiency	0.9
Isentropic efficiency	0.65
Mechanical efficiency	0.9

4.3.5 Heat exchanger model

The evaporator in the ORC loop was modelled based on the shell and tube-type heat exchanger SC4508-4 [152] selected during the experimental setup describe in Chapter 3. The condenser was modelled based on the SWEP plate-type heat exchanger B185x36 [147]. Table 4.3 illustrates the input parameters of the heat exchangers.

Table 4.3: Input parameters for the heat exchanger models [147].

Parameter	Value	Unit
Evaporator		
Shell side area	1.021	m^2
Tube side area	0.943	m^2
Shell Volume	2.9	Liters
Tube thickness	0.7	mm
Tube diameter	9.52	mm
Tube length	650	mm
Number of tubes	57	N/A
Condenser		
Refrigerant channel length	3.701	m
Liquid nitrogen channel length	3.365	m
Cross sectional area	450	mm^2
Hydraulic diameter	4.2	mm
Convective heat exchange area	2.57	m^2

For dynamic numerical modelling of cryogenic ORCs, where the working fluid changes phase in both the evaporator and condenser, it was necessary to consider two-phase flow correlations. During the system design and sketch phase, Siemens Amesim provides heat exchange elements specifically for two-phase flow considerations, with embedded correlations, and these were used for both heat exchanger models. Since fluid boiling and condensation are separate phase-change processes, different correlations were used to

consider these processes. A simplified two-phase flow modelling correlation flowchart for the heat exchangers is presented in Figure 4.4.

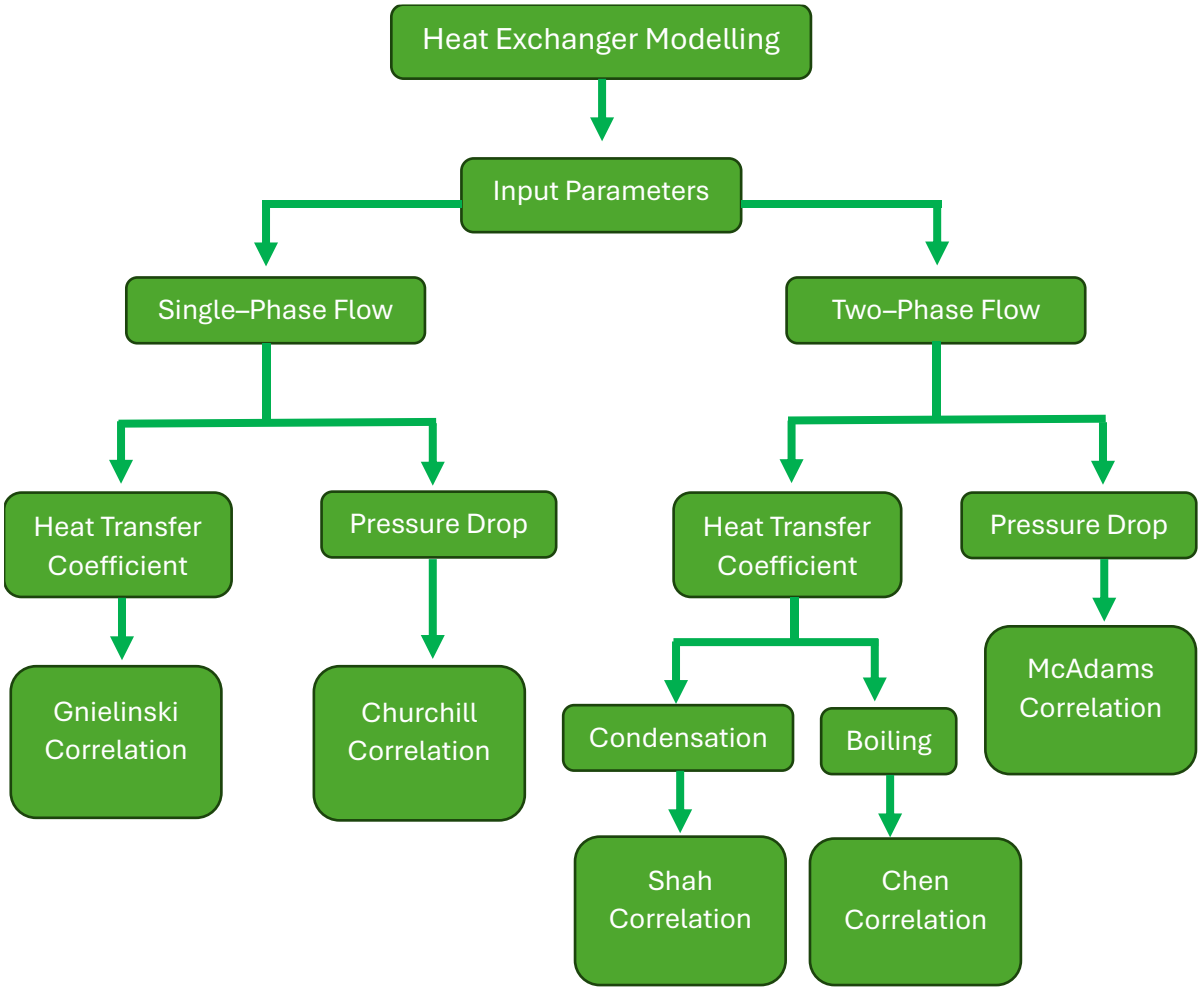

Figure 4.4: Heat exchanger modelling methodology.

4.3.5.1 Single-phase flow

The Gnielinski [156] correlation was used for single-phase flow computation of the convective heat transfer coefficient (φ):

$$\varphi = \frac{(\frac{\xi}{8}) \cdot [Re - 1000] \cdot Pr}{1 + 12.7\sqrt{\frac{\xi}{8}} \cdot [Pr^{2/3} - 1]} \cdot \frac{\lambda}{D_h} \tag{4.13}$$

The friction factor (ξ) was calculated using the Churchill correlation [157]:

$$\xi = 8 \cdot \left[\left(\frac{8}{\mathrm{Re}} \right)^{12} + \left[2.457 \cdot \ln \left[\frac{1}{\left[\frac{7}{\mathrm{Re}} \right]^{0.9} + 0.27 \cdot \mathrm{rr}} \right] \right]^{16} + \left[\frac{37530}{\mathrm{Re}} \right]^{16} \right]^{-\frac{3}{2}} \Bigg]^{\frac{1}{12}} \tag{4.14}$$

The Reynolds number (Re) and Prandtl number (Pr) were calculated as:

$$Re = \frac{u \cdot cdim}{\upsilon} \tag{4.15}$$

$$Pr = \frac{\mu \cdot Cp}{\lambda} \tag{4.16}$$

Where, rr = relative roughness; u = velocity; $cdim$ = characteristic length of exchange; υ = kinematic viscosity; μ = dynamic viscosity; Cp = specific heat; λ = thermal conductivity; D_h = hydraulic diameter. The fluid remained in the turbulent range, with a Reynolds number greater than 6000.

4.3.5.2 Two-phase condensation

The heat transfer coefficient (φ) for condensation was calculated using the Shah correlation [158]:

$$\varphi = \varphi_L \cdot \left[(1-x)^{0.8} + 3.8 \frac{x^{0.76} \cdot (1-x)^{0.04}}{(p_{red})^{0.38}} \right] \tag{4.17}$$

Where, the reducing pressure (p_{red}) was expressed as:

$$p_{\mathrm{red}} = \frac{p}{p_c} \tag{4.18}$$

The liquid heat transfer coefficient (φ_L) was calculated as:

$$\varphi_L = \mathrm{Nu_L} \frac{\lambda_L}{D_h} = 0.023 \cdot \mathrm{Re_L^{0.8}} \cdot Pr_L^{0.4} \cdot \frac{\lambda_L}{D_h} \tag{4.19}$$

Where, x = quality; p = pressure; p_c= critical pressure. The subscript L represented the liquid phase.

4.3.5.3 Two-phase boiling

The coefficient of the two-phase boiling heat transfer (φ) was calculated using the Chen correlation [159]:

$$\varphi = S \cdot \varphi_{NcB} + F \cdot \varphi_{cv} \tag{4.20}$$

The nucleate boiling contribution (φ_{NcB}) was calculated using:

$$\varphi_{\mathrm{NcB}} = 0.00122 \cdot \frac{\lambda_L^{0.79} \cdot \mathrm{Cp}_L^{0.45} \cdot \rho_L^{0.49}}{\sigma^{0.5} \cdot \mu_L^{0.29} \cdot h_{\mathrm{fg}}^{0.24} \rho_v^{0.24}} \cdot (T_w - T_{\mathrm{sat}})^{0.24} \cdot \Delta P_{\mathrm{sat}}^{0.75} \cdot S \tag{4.21}$$

The saturated pressure difference (Δp_{sat}) was computed using as:

$$\Delta p_{sat} = \frac{h_{fg}(T_w - T_{sat})}{T_{sat}[\frac{1}{\rho_v} - \frac{1}{\rho_L}]} \tag{4.22}$$

The suppression factor (S) was expressed using:

$$S = (1 + 2.53 \cdot 10^{-6}(\mathrm{Re}_L \cdot F^{1.25})^{1.17})^{-1} \tag{4.23}$$

The forced convection contribution (φ_{cv}) was calculated using:

$$\varphi_{\mathrm{cv}} = \mathrm{Nu}_{\mathrm{cv}} \cdot \frac{\lambda_L}{D_h} = 0.023 \cdot Re_L^{0.8} \cdot Pr_L^{0.4} \cdot \frac{\lambda_L}{D_h} \tag{4.24}$$

The fouling factor (F) was calculated using:

$$F = MAX(1.0, 2.35(\frac{1}{X_{\mathrm{tt}}} + 0.213)^{0.736}) \tag{4.25}$$

The Martinelli Parameter (X_{tt}) was calculated using:

$$X_{\mathrm{tt}} = \left(\frac{1-x}{x}\right)^{0.9} \cdot \left(\frac{\rho_g}{\rho_l}\right)^{0.5} \cdot \left(\frac{\mu_L}{\mu_g}\right)^{0.1} \quad (4.26)$$

Where, T_w = wall temperature; T_{sat} = saturation temperature; h_{fg} = latent heat of vaporisation. Convective, gas, liquid, and vapor corresponded to the subscripts $cv, g, L, and\ v$, respectively.

4.3.6 Liquid receiver

The liquid receiver was modelled as the VLR 160x345 [152] selected during the experimental setup, as discussed in Chapter 3. The purpose of the liquid receiver was to provide the pump inlet with a constant supply of liquid working fluid, thereby eliminating pump failure due to inadequate working fluid supply and consequent pump cavitation and dry running. The user-defined liquid receiver volume ($H_{vl} = 5.7\ L$) was used to determine the liquid-vapor interface height in the liquid receiver using the following equation:

$$H_{vl} = tau \times H_{ch} \quad (4.27)$$

where, tau = initial liquid volume; H_{ch} = chamber height (0.345 m). The software also required the user to input height of the outlet port, and it was defined such that the liquid-vapor interface was always higher than the outlet port. This ensured that the pump received a liquid working fluid supply rather than a liquid-vapor mixture, thus eliminating the cavitation phenomenon.

In the previous sections, the geometries of the individual components were defined. The pipe geometries were modelled based on the pipe dimensions of the real experimental setup. After the dynamic numerical model setup and initialisation is complete, Siemens Amesim uses the in-build extensive thermophysical fluid property routines to calculate the system charge. The system charging conditions were set as liquid. During the

computation of system charge, the simulation tool also calculated the quality, density, and viscosity of the working fluid. Hence, the working fluid charge directly affected all working fluid thermophysical attributes. These in turn affected the enthalpy and entropy, which directly influenced the system Key Performance Indicators (KPIs). Hence, the dynamic numerical model helped predict the system behaviour during the charging procedure, and the system charge quantity directly affected the system performance by determining the quality of working fluid entering the pump.

4.3.7. Pressure drop

The total pressure drop ($\frac{dP}{dz}$) in the system was computed using:

$$\frac{dP}{dz} = \left(\frac{dP}{dz}\right)_F + \left(\frac{dP}{dz}\right)_a + \left(\frac{dP}{dz}\right)_z \tag{4.28}$$

where, friction pressure drop = $\left(\frac{dP}{dz}\right)_F$; acceleration pressure drop = $\left(\frac{dP}{dz}\right)_a$; gravitational pressure drop = $\left(\frac{dP}{dz}\right)_z$.

The friction pressure drop in the system was calculated separately for single-phase flow and two-phase flow.

The friction pressure drop ($-\left(\frac{dP}{dz}\right)_F$) for single-phase flow was calculated using:

$$-\left(\frac{dP}{dz}\right)_F = \frac{\xi \cdot G^2 \cdot \bar{v}}{2D_h} \tag{4.29}$$

where, G = mass velocity; ε = absolute surface roughness. The friction factor (ξ) was calculated using the Churchill correlation [157]:

$$\xi = 8 \cdot \left[\left(\frac{8}{Re}\right)^{12} + \frac{1}{\left(\left[2.457 \cdot ln\left(\left(\frac{7}{Re}\right)^{0.9} + 0.27 \cdot \left(\frac{\varepsilon}{D_h}\right) \right) \right]^{16} + \left[\frac{37530}{Re}\right]^{16} \right)^{\frac{3}{2}}} \right]^{\frac{1}{12}} \tag{4.30}$$

The same equations were used to calculate the two-phase flow friction pressure drop, albeit the McAdams correlations [160] for the specific volume ($\bar{v}$) and specific viscosity ($\bar{\mu}$) (to calculate the Reynolds number) were substituted to account for the two-phase flow:

$$\bar{v} = x \cdot v_v + (1 - x) \cdot v_l \tag{4.31}$$

$$\frac{1}{\bar{\mu}} = \frac{x}{\mu_v} + \frac{1 - x}{\mu_l} \tag{4.32}$$

The liquid and vapor phases were represented by the subscripts l and v, respectively.

The acceleration pressure drop ($-\left(\frac{dP}{dz}\right)_a$) was calculated as:

$$-\left(\frac{dP}{dz}\right)_a = G^2 \cdot \frac{d\bar{v}}{dz} \tag{4.33}$$

The gravitational pressure drop ($-\left(\frac{dP}{dz}\right)_z$) was calculated as:

$$-\left(\frac{dP}{dz}\right)_z = g \cdot sin\theta[e \cdot \rho_v + (1 - e) \cdot \rho_l] \tag{4.34}$$

where, e = volumetric vapor content; ρ = density. Since the experimental test rig was designed such that the pipes were either horizontal or vertical, the value of θ was either 0° for horizontal pipes or 90° for vertical pipes.

4.4 Hydrofluorocarbon working fluid limitations

The Montreal Protocol [161] and the Kyoto Protocol [162] are widely regarded as the defining driving forces behind the complete phase-out of ozone depleting chlorinated refrigerants, and are the basis of the phase-out of emission intensive hydrofluorocarbons. Environmental impact of hydrofluorocarbons is an important factor during the selection of cryogenic enhanced ORC working fluids, and regulatory body recommendations are normally a good indicator of whether a cryogenic refrigerant would meet increasingly stringent global environmental policies.

4.4.1 EU regulations on F-gases

The European Union (EU) government introduced regulations in 2006 to reduce the dependence on emission intensive fluorinated greenhouse gases (F-gases). These included different certification requirements for refrigeration engineers and equipment, highlighting the need for proper documentation of refrigerant charging and discharging procedures, and presented leak prevention and detection mechanisms [163]. To strengthen the 2006 regulations, they introduced REGULATION (EU) No 517/2014, which limited the hydrofluorocarbon supply chain network and strongly emphasised the importance of leak prevention and timely detection [164]. New refrigeration systems were prohibited from using hydrofluorocarbons with a global warming potential (GWP) greater than 2500 (from 2020), and any system with a charge of more than 500 tonnes of eCO2 was required to be installed with an automatic leak detection system. Although these regulations apply to all EU-based applications, marine classification society recommendations hold more sway within the marine industry, as they provide certification to maintain safety, technical, and emission standards upheld by the International Maritime Organisation (IMO).

EU regulations regarding the utilisation of F-gases were updated in 2024, providing timelines for the phase-out of high GWP HFCs. For commercial refrigeration equipment, it was mandated that only HFCs with a GWP of less than 150 would be permitted for new build refrigeration equipment after 2032. However, an exception was provided such that in the case of meeting stringent safety requirements, HFCs with a GWP of up to 750 would be permitted [164]. Hence, the regulations clearly permit the utilisation of low-flammability hydrofluorocarbon working fluids in marine applications up to 750 GWP from 2032 onwards, since stringent safety regulations are implemented onboard marine shipping vessels.

4.4.2 Marine classification societies

Det Norske Veritas (DNV) is a Norwegian-based marine classification society and provides detailed regulations regarding hydrofluorocarbon utilisation onboard marine vessels [165] [166]. DNV provides recommendations on most aspects of marine hydrofluorocarbon usage and have classified the notation of 'clean' to refrigerants with a GWP of less than 2000. They also provide guidance regarding oxygen depletion sensors, ventilation, and automatic leak detection devices. The most important take-away from DNV classification is the limitation of allowable annual leakage rates, where annual leakage rate should be below 10 % of total system charge. DNV also currently prohibits the use of A3 highly flammable refrigerants onboard marine vessels due to safety concerns, making it implementation impossible for conventional cryogenic enhanced ORCs. Hence, the non-flammable and mildly flammable novelty of this project presents an opportunity for marine-based applications.

Lloyd's register, a United Kingdom-based marine classification society, have also implemented recommendations for maritime hydrofluorocarbon utilisation, similar to DNV. They also prohibit the use of A3 flammable refrigerants, again limiting hydrocarbon-based cryogenic ORC applications within the marine sector [165] [166]. The main difference between the Lloyd's register and the DNV classification societies recommendations for onboard hydrofluorocarbon utilisation stems from the environmental impact of chosen refrigerants and the allowable annual leakage rates. The Lloyd's register provides stricter recommendations, providing the classification 'natural' to refrigerants with a GWP below 1950 and limiting maximum annual refrigerant leaks to less than 3 % of the total system capacity.

4.4.3 Working fluid selection

The above discussed regulations and recommendations provide a selection criteria regarding environmental impact and safety of hydrofluorocarbons which only forms part of the screening process for cryogenic enhanced ORC working fluid selection. The overall working fluid selection criteria during the ORC design procedure requires a multi-faceted approach, considering a combination of thermophysical, environmental, and safety

factors. These factors include the boiling and critical temperatures, ODP and GWP, toxicity and flammability, and fluid densities. All these factors contribute to the overall goal of achieving a high multi-objective balance between power generation, efficiencies, and overall system performance [167] [90] [168].

Specifically for cryogenic enhanced ORCs, the working fluid boiling temperatures should be well below 0 °C, and the lower the boiling temperature, the more cryogenic energy may be utilised. Since one of the novelties of this project is the implementation of low flammability refrigerants, only A1 and A2L hydrofluorocarbons with a saturation temperature below -20 °C were chosen to maximise cryogenic energy reutilisation. According to the ASHRAE fluid safety index [151], A1 and A2L refrigerants are both non-toxic, with A1 being non-flammable and A2L being mildly flammable. Yet, the mildly flammable nature of A2L refrigerants is often misconstrued, as extensive laboratory testing has revealed that they have a high flammability limit (300 g/m^3) and have difficulty igniting even under direct contact with naked flames. Additionally, they have low flame and burning velocities, and often self-extinguish [169] [170]. Hence, proper ventilation and leak prevention protocols would almost eliminate the risk of ignition [171] [172] [173]. Since marine classification societies only present recommendations without a legal basis, it was decided that the working fluid selection would follow EU regulations regarding GWP, hence only refrigerants below 2500 GWP were selected.

Table 4.4 presents the proposed working fluids for the numerical study of the cryogenic enhanced ORC. The Organic Rankine Cycle performance is based on the expansion power produced by the expander due to a pressure differential, which increases with a low condensation pressure. Hence, a control loop was implemented into the simulation tool which controlled and adjusted the flow rate of the liquid nitrogen flowing through the condenser such that the working fluid would always condense near atmospheric pressure. Hence, the condensation pressure of the working fluids was always maintained between $1.01325\ barA \leq P_{cond} \leq 1.02\ barA$. This limit of condensation pressure also ensured that the maximum cryogenic energy was utilised, as a higher condensation pressure also leads to a higher working fluid saturation temperature.

Table 4.4: Properties of working fluid selected for the numerical model [173] [43]:

Working fluid	GWP	ASHRE A Safety group	Boiling point at 1atm (°C)	Critical temperature (°C)	Molar mass (g/mol)	Liquid density at 25 °C (kg/m^3)	Composition	Mixture Ratio (by weight)
R407C	1774	A1	-43.63	86.19	86.2	1134	R32/R125/R134a	0.23/0.25/0.52
R410a	2088	A1	-51.44	71.34	72.59	1062	R32/R125	0.50/0.50
R450A	605	A1	-23.36	104.5	108.7	1177.3	R134a/R1234ze	0.42/0.58
R452B	698	A2L	-50.67	77.1	63.53	993.5	R125/R1234y/R32	0.7/0.26/0.67
R454C	148	A2L	-45.56	85.67	90.78	1042.4	R32/R1234yf	0.215/0.785
R455a	148	A2L	-52.02	85.61	87.45	1033.4	R1234yf/R32/CO2	0.755/0.215/0.03

The chosen refrigerants were conformant with current regulations, with five refrigerants achieving the DNV and Lloyd's register classification of 'clean' and 'natural', respectively. R410a was the only refrigerant not within the classification society GWP limitations yet was chosen for both the experimental and numerical study due its wide utilisation and high efficiency within the refrigeration industry. Specifically for the experimental study, the wide availability and low cost also played a significant factor. R450A was the only refrigerant with a saturation temperature higher than – 40 °C, severely limiting its potential for cryogenic energy reutilisation. Yet, R450A provided the flexibility to adapt to constantly changing global greenhouse gas regulations, as it has the lowest GWP within the non-flammable category. Hence, the chosen refrigerants provide flexibility in application and would meet the harshest regulatory requirements. It is pertinent to note that while all chosen low-flammability hydrofluorocarbon working fluids are currently permitted till 2025, only R450A, R452B, R454C, and R455A would be permitted beyond 2032, based on new EU regulations regarding F-gas utilisation.

4.5 Energy and Exergy balance

This section presents the thermodynamic model of the dual waste thermal and cryogenic energy reutilisation ORC system and applies to both the experimental methodology and the dynamic numerical model. The cryogenic enhanced ORC thermodynamic model was

based on a controlled volume, hence the mass, energy, and exergy conservation equations applied as presented below [174] [175]:

$$\sum \dot{m}_{in} = \sum \dot{m}_{out} \tag{4.35}$$

$$\dot{Q} + \sum \dot{m}_{in} h_{in} = \dot{W} + \sum \dot{m}_{out} h_{out} \tag{4.36}$$

$$\dot{E_Q} + \sum \dot{m}_{in} e_{in} = \dot{E_D} + \dot{E_W} + \sum \dot{m}_{out} e_{out} \tag{4.37}$$

$$\dot{E_Q} = \sum \dot{Q} \times (1 - \frac{T_O}{T}) \tag{4.38}$$

$$\dot{E_w} = \dot{W} \tag{4.39}$$

Where:

- $\sum \dot{m}_{in} h_{in}$ and $\sum \dot{m}_{in} e_{in}$ represented the system energy and exergy input, respectively.
- $\sum \dot{m}_{out} h_{out}$ and $\sum \dot{m}_{out} e_{out}$ represented the system energy and exergy output, respectively.
- $\dot{Q}$ and $\dot{E_Q}$ denoted the rate of heat transfer and heat transfer exergy rate, respectively.
- $\dot{W}$ and $\dot{E_W}$ denoted the mechanical work output and the rate of exergy transfer due to mechanical work, respectively.
- $\dot{E_D}$ represented the exergy destruction rate.
- T_O was the reference state temperature, set at 293.15 K. The ambient pressure was set to 1.013 bar.

4.5.1 Energy model

The heat energy rejected by the heating medium to the working fluid in the evaporator, causing the working fluid to vaporise and super-heat, was regarded as the system heat energy input (Q_{evap}):

$$Q_{evap} = \dot{m}_{WF} \times (h_3 - h_2) \tag{4.40}$$

Where, $\dot{m}_{WF}(\frac{kg}{s})$, h_2 $(\frac{kJ}{kg})$, and h_3 $(\frac{kJ}{kg})$ represented the mass flow rate, evaporator inlet specific enthalpy, and evaporator outlet specific enthalpy of the working fluid, respectively.

The energy difference between the expander inlet and outlet was defined as the expander isentropic work output ($W_{exp,is}$):

$$W_{exp,is} = \dot{m}_{WF} \times (h_3 - h_4) \tag{4.41}$$

Where the specific enthalpies at the expander inlet and outlet were denoted by h_3 $(\frac{kJ}{kg})$ and h_4 $(\frac{kJ}{kg})$, respectively.

The expander efficiency (η_{exp}) was defined as:

$$\eta_{exp} = \frac{W_{exp,a}}{W_{exp,is}} \tag{4.42}$$

Where $W_{exp,a}$ denoted the actual expander work. In the numerical model, the simulation tool was used to calculate the expander actual work directly by application of load that maintained expander rotational speed within optimal maximum range (3600 rpm). In the experimental analysis, the expander actual work was calculated using:

$$W_{exp,a} = \frac{Rotational\ speed\ x\ Torque\ x\ 2\pi}{60} \tag{4.43}$$

The pump isentropic energy consumption ($W_{Pump,is}$) was defined as:

$$W_{Pump,is} = \dot{m}_{WF} \times (h_2 - h_1) \tag{4.44}$$

Where the specific enthalpies at the pump inlet and outlet were denoted by $h_1\ (\frac{kJ}{kg})\ and\ h_2\ (\frac{kJ}{kg})$, respectively.

The pump efficiency (η_{pump}) was defined as:

$$\eta_{pump} = \frac{W_{pump,a}}{W_{pump,is}} \tag{4.45}$$

Where $W_{pump,a}$ denoted the actual pump work. The simulation tool depicted the pump power consumption, whereas in the experimental analysis, the pump drive was used to display the actual pump electrical power consumption.

The heat rejected by the working fluid to the cryogenic cooling medium, inducing condensation, in the condenser (Q_{cond}) was defined as:

$$Q_{cond} = \dot{m}_{WF} \times (h_4 - h_5) \tag{4.46}$$

Where the specific enthalpies at the condenser inlet and outlet were denoted by $h_4\ (\frac{kJ}{kg})\ and\ h_5\ (\frac{kJ}{kg})$, respectively.

The energy absorbed by the liquid nitrogen (Q_{LN_2}) was defined as:

$$Q_{LN_2} = \dot{m}_{LN_2} \times (h_7 - h_6) \tag{4.47}$$

Where, $h_6\ (\frac{kJ}{kg})$ denoted the liquid nitrogen condenser inlet specific enthalpy and $h_7\ (\frac{kJ}{kg})$ denoted the liquid nitrogen condenser outlet specific enthalpy.

4.5.2 Exergy model

For the exergy model, it was first imperative to calculate the exergy at each state point within the system (E_{x_i}):

$$E_{x_i} = \dot{m}_i \times [(h_i - h_0) - T_0(s_i - s_0)] \tag{4.48}$$

Where:

- h_i $\left(\frac{kJ}{kg}\right)$ and h_o $\left(\frac{kJ}{kg}\right)$ were the specific enthalpies at the specific state points and reference point at the dead-state temperature (T_0) of 293.15 K, respectively.
- $s_i(\frac{kJ}{kgK})$ and $s_o(\frac{kJ}{kgK})$ were the specific entropies at the specific state points and reference point at the dead-state temperature (T_0) of 293.15 K, respectively.

The system cold exergy input ($\Delta \dot{E}_{x,LN2}$) was defined as:

$$\Delta \dot{E}_{x,LN2} = E_{x_7} - E_{x_6} \tag{4.49}$$

Where, E_{x_6} denoted the condenser inlet liquid nitrogen exergy and E_{x_7} denoted the condenser outlet liquid nitrogen outlet exergy.

The change in fuel exergy between the input and output of each individual component of the system denoted the measure of irreversibility, or exergy destruction (I), and was calculated using:

$$I_{evap} = \left(E_{x_8} - E_{x_9}\right) + (E_{x_2} - E_{x_3}) \tag{4.50}$$

$$I_{cond} = \left(E_{x_4} - E_{x_5}\right) + (E_{x_6} - E_{x_7}) \tag{4.51}$$

$$I_{pump} = (E_{x_1} - E_{x_2}) + W_{pump} \tag{4.52}$$

$$I_{exp} = (E_{x_3} - E_{x_4}) - W_{exp} \tag{4.53}$$

$$I_{total} = I_{evap} + I_{cond} + I_{pump} + I_{exp} \tag{4.54}$$

The ratio of the individual component exergy to the overall system exergy destruction denoted the exergy destruction ratio (I_{DR}) and was calculated using:

$$I_{DR,i} = \frac{I_i}{I_{total}} \tag{4.55}$$

4.5.3 Key performance indicators

Several key performance indicators were identified once all state and individual component energy and exergy points were calculated.

The useful work done by the system is denoted by the specific net-work output (W_{net}):

$$W_{net} = W_{exp} - W_{pump} \tag{4.56}$$

The system thermal efficiency (η_{th}) was defined as:

$$\eta_{th} = \frac{W_{exp} - W_{pump}}{Q_{eva}} \tag{4.57}$$

Cryogenic enhanced ORCs differentiate from traditional ORCs through the utilisation of ultra-low temperature fluid regasification energy in the condenser. Hence, cryogenic energy and exergy efficiency was of paramount importance to fully realise the potential of cryogenic ORCs. Cryogenic energy and exergy efficiency calculations disregard the energy and exergy inputs in the evaporator, and only the condenser energy and exergy are factored in the cryogenic efficiency calculations. This method of factoring only the cryogenic energy and exergy rejected by the working fluid for cryogenic fuel regasification was utilised by multiple researchers to gauge a better understanding of cryogenic enhanced ORCs [105] [176] [74]. The system cryogenic energy ($\eta_{cryogenic}$) and exergy efficiencies (η_{ex}) were calculated using:

$$\eta_{cryogenic} = \frac{W_{exp} - W_{pump}}{Q_{cond}} \tag{4.58}$$

$$\eta_{ex} = \frac{W_{exp} - W_{pump}}{\dot{\Delta E}_{LN_2}} \tag{4.59}$$

The heat exchanger effectiveness is the ratio of the heat transferred from the heating or cooling medium to the working fluid and calculated as:

$$\varepsilon_{evaporator} = \frac{\dot{m}_{WF}.\Delta\, h_{refrigerant}}{\dot{m}_{water}.\Delta\, h_{hot\ water}} \tag{4.60}$$

$$\varepsilon_{condenser} = \frac{\dot{m}_{WF}.\Delta\, h_{refrigerant}}{\dot{m}_{LN2}.\Delta\, h_{LN2}} \tag{4.61}$$

4.6 Summary

This chapter described the development of the dynamic numerical model for the cryogenic enhanced Organic Rankine Cycle system utilising low flammability hydrofluorocarbon working fluids for simultaneous reutilisation of thermal and cryogenic waste energy. The dynamic numerical model was developed in the professional modelling software, Siemens Amesim. A complete system sketch and individual component modelling techniques were presented, considering advanced two-phase flow correlations for an accurate prediction of component- and system-level thermo-fluid performance. Each loop was modelled based on the experimental methodology. The heating loop utilised water as the heating medium, while the cooling loop utilised liquid nitrogen as the cryogenic cooling medium. Both the heating and the cooling loops were modelled as open-loop systems. The ORC loop was modelled as a closed-loop system, capable of utilising multiple cryogenic working fluids without requiring modifications. Each component and associated piping was modelled based on the developed experimental setup described in Chapter 3, which ensured the real-world applicability of the dynamic numerical model. The limitations of the model were identified as the inability of achieving a perfectly insulated system in real-world applications and the variation in atmospheric conditions. Environmental regulations-, safety-, and performance-based selection criteria was adopted and presented for the cryogenic working fluids. Justification was provided regarding the safety implications of mildly flammable refrigerants. The thermodynamic model was presented, which was used to gauge system performance for both the experimental methodology described in

Chapter 3 and the dynamic numerical model. Performance metrics were identified with special considerations for ultra-low temperature cryogenic enhanced ORCs.

Chapter 5. Experimental Analysis

5.1 Introduction

In this chapter, an experimental parametric energy and exergy analysis is presented for the cryogenic enhanced Organic Rankine Cycle utilising low flammability hydrofluorocarbon as the working fluid. R410A, non-flammable hydrofluorocarbon, was utilised as the working fluid, and liquid nitrogen was utilised as the cryogenic fuel surrogate to mimic the cryogenic regasification exergy. The system performance was analysed at varied working fluid mass flow rates and different evaporation temperatures. Different correlations were revealed between the heat transfer capability and the mass flow rate of the working fluid. One of the most important findings exhibited the operational flexibility provided by the cryogenic enhanced ORC to the downstream end-use systems utilising the cryogenic fuels, which had a direct correlation with the evaporation temperatures and working fluid mass flow rates of the cryogenic enhanced ORC. Heat exchanger effectiveness analysis was conducted to identify the operational parameters to achieve efficient heat transfer. The experimental analysis was utilised to validate the dynamic numerical model presented in Chapter 4. Finally, the performance of the hydrofluorocarbon working fluid was pitted against traditional hydrocarbon working fluid-based cryogenic enhanced ORC found in literature.

The results presented in this chapter are under review in the peer-reviewed Elsevier journal *Applied Energy* under the title “Experimental investigation of non-flammable hydrofluorocarbons for cryogenic-enhanced Organic Rankine Cycles”.

5.2 Experimental procedure

R410A is a cryogenic non-flammable hydrofluorocarbon working fluid, having a boiling temperature of -51.43 °C at atmospheric pressure and a pressure of 14.43 bar at 20 °C

[43]. To avoid the formation of acid in the system due to working fluid interaction with water vapor, the experimental procedure started with inducing a deep vacuum within the system. After the deep vacuum was achieved, 9 kg of the liquid/gas mixture working fluid was charged into the system through the charging valve. Since the numerical model was based on the exact same components and pipework utilised in the experimental setup, hence having the same fixed volume across them, it accurately predicted the working fluid charge. R410A is stored as a high-pressure liquid, which allowed the working fluid to be charged into the system without requiring additional induced flow. Once the working fluid was charged, the system could technically run due to adequate liquid working fluid supply to pump. However, since the pump was a positive displacement pressure inducer and the working fluid pressure at the pump inlet was high, initiating flow through pump rotation would have led to extremely high pressures at the pump outlet, compromising the integrity of the pipework and components. Furthermore, the cryogenic component of the ORC would not have been achieved, as the working fluid condensation temperature would be atmospheric temperature, due to limitations posed by the maximum achievable pressure ratio of the expander.

To achieve cryogenic condensation temperatures, liquid nitrogen flow was introduced into the condenser, subsequently lowering the condensation pressure. The introduction of liquid nitrogen started to condense the working fluid in the condenser, causing it to accumulate in the liquid receiver, while the high-pressure working fluid kept forcing its way into the condenser for further condensation. Once the condensed cryogenic liquid working fluid reached its normal boiling point at the pump inlet, observed through the temperature and pressure transducers, the system was started by providing power and fixed rotational speed to the pump, initiating flow, through the variable frequency drive. The water heater was then started to increase the evaporation temperature by setting the required temperature value through the digital temperature control display.

5.3 Working conditions

The effects of increasing evaporation temperatures and varied working fluid mass flow rates were studied on the system performance. For each evaporation temperature value, the system was allowed to stabilise, and the flow rates were varied between 10 – 16 g/s. This was achieved by increasing the pump rotational speed based on the manufacturer performance curves, displayed in Figure 3.4 in Chapter 3. Table 5.1 displays the set and tested operational parameters utilised during the experimental procedure. Due to high liquid nitrogen acquisition delays, each set of evaporation temperature and flow rate values were allowed a maximum of 120 seconds to stabilise, while the numerical analysis conducted in *Chapter 6: Dynamic Numerical Model Analysis* accounts for 4000 seconds of steady-state operation. The stability criteria was determined based on the total amount of liquid nitrogen available (180 L), and the total number of test cases (52). Initially, 10 minutes were required to decrease the condensation temperature below -45 °C. Hence, the experiment was run for a total of approximately two hours, which reduced the liquid nitrogen level to below 5 %, at a flow rate of approximately 1.5 lpm. Three separate tests were conducted on different days over a period of 3 weeks, one test each week, and the best results were selected for this study. In terms of each individual experimental test value, three values were recorded, and the average was used as the final experimental value. Hence, each tested parameter tabulated in Table 5.1 had 156 values, 3 for each of the 52 test cases. The lower limit temperature values corresponded to the lower limit pressure values and the higher limit temperature values corresponded to the higher limit pressure values.

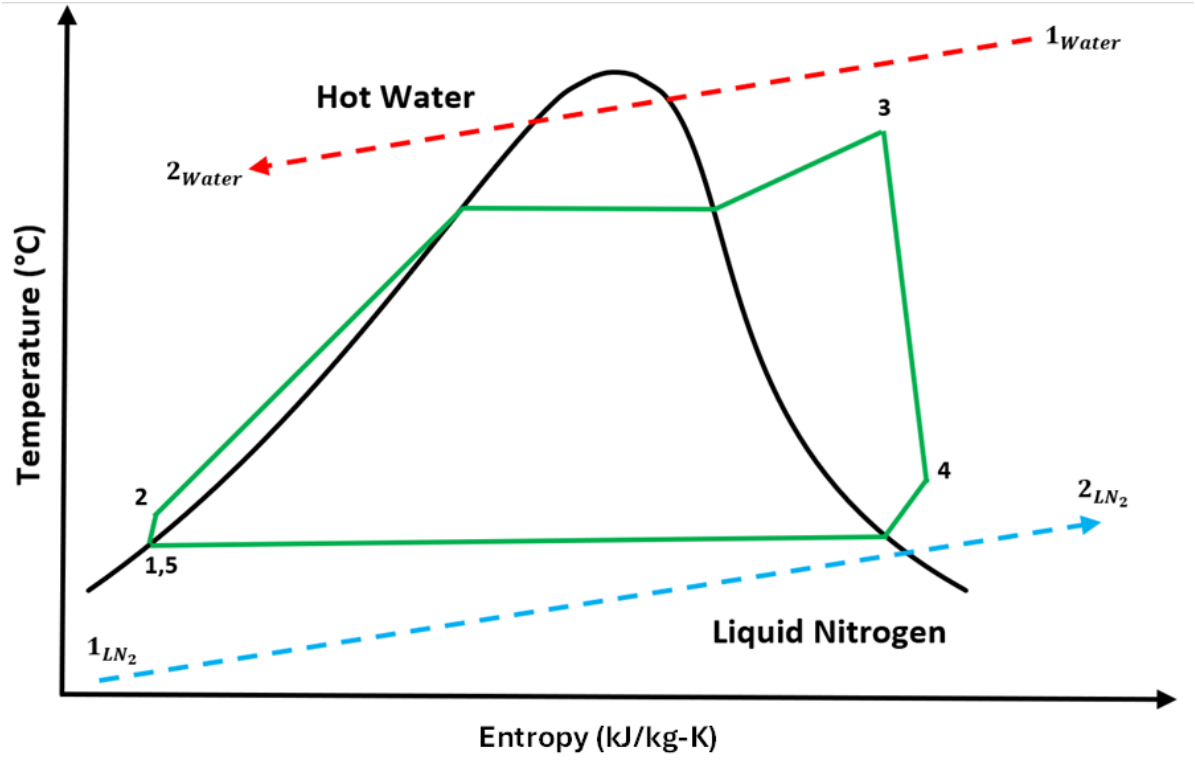

Figure 5.1: T-s diagram of the cryogenic enhanced ORC system using R410A experiment

The temperature-entropy (T-s) diagram of the cryogenic enhanced ORC utilising R410A as the non-flammable working fluid medium is illustrated in Figure 5.1. The process labels are the same as in Figure 3.1 in Chapter 3. The pressure inducing process of the pump was indicated by process 1-2, and the isobaric heat addition from the hot water to R410A in the evaporator was designated by process 2-3. Here, R410A initially absorbed the heat to reach the saturation temperature, and continued to absorb the heat at the saturation temperature until the latent heat of vaporisation was absorbed, before beginning the superheating process. The expansion of R410A through the scroll expander was indicated by process 3-4. The condensation of the expanded R410A vapour was indicated by process 4-5, where R410A rejected the heat to the liquid nitrogen to transition back into sub-cooled liquid phase.

Table 5.1 Cryogenic enhanced ORC experimental operational parameters

Parameter	Range	Source

Working fluid	R410A	Set
Water temperature	15 to 75 °C	Set
Pump rotational speed	900 to 1200 rpm	Set
Water flow rate	13 lpm	Set
Liquid nitrogen flow rate	20 to 30 g/s	Set
T1	-98 to -88 °C	Tested
T2	-96 to -79 °C	Tested
T3	15.1 to 75.8 °C	Tested
T4	0 to 28 °C	Tested
T5	-98 to -89 °C	Tested
$T1_{LN2}$	-182 to -176 °C	Tested
$T2_{LN2}$	-11 to 5 °C	Tested
$T1_{Water}$	32 to 87 °C	Tested
$T2_{Water}$	16 to 71 °C	Tested
P1	1.34 to 3.39 bar	Tested
P2	5.97 to 9.42 bar	Tested
P3	5.81 to 9.15 bar	Tested
P4	1.49 to 4.27 bar	Tested
P5	1.36 to 4.03 bar	Tested
$P1_{LN2}$	2.96 to 5.87 bar	Tested
$P2_{LN2}$	1.57 to 1.98 bar	Tested
$P1_{Water}$	1.33 to 1.47 bar	Tested
$P2_{Water}$	1.29 to 1.4 bar	Tested
$\dot{m}_{W.F}$	9.97 to 16.31 g/s	Tested

$\dot{m}_{W.F,\ LN2}$	0.0203 to 0.031 g/s	Tested
$\dot{m}_{W.F,\ Water}$	0.206 to 0.221 g/s	Tested
P_{atm}	1.013 bar	Tested
T_{atm}	11 to 19 °C	Tested

5.4 Key Performance Indicators

Figure 5.2 illustrates the effect of increasing evaporation temperature at different working fluid flow rates on the net-work output of the system. The effect of mass flow rate variation was clearly evident, with higher mass flow rates providing a higher net-work output. The rise in system net-work output as a result of increasing working fluid mass flow rate stemmed from the upsurge in expander rotational speed relative to the pump power consumption. An increase in mass flow rate only slightly increased the pump power consumption, whereas the expander rotational speed was significantly increased, subsequently providing a high net-work output. For example, at the highest tested evaporation temperature of 75 °C, the net-work output increased by 88 %, from 266.7 W to 501.44 W when the mass flow rate increased from 10 g/s to 16 g/s.

In terms of increasing evaporation temperatures, similar trends were observed across all the tested mass flow rates, such that the net-work output of the system steadily increased. For example, at a mass flow rate of 16 g/s, the net-work output increased by 561.88 %, when the evaporation temperature increased from 20 °C to 75 °C, as illustrated in Figure 5.2. The increase in evaporation temperatures resulted in the working fluid attaining a higher degree of superheat, increasing its enthalpic energy content, which led to an increase in the expansion work output of the expander. Hence, the increase in evaporation temperatures coupled with an increase in working fluid mass flow rates provided the optimum net-work output of the system. In addition to higher expander rotational speed and higher degree of superheat, higher flow rates at higher evaporation temperatures allowed the working fluid to better absorb the available sensible heat from

the hot water, which led to an overall increase in system performance. In simple terms, more energy was absorbed by the working fluid by increasing its mass flow rate, while the flow rate of the heat source remained constant. This was also concluded by Alimoradi [193] and Shahrul et al. [194] in their study regarding heat exchanger effectiveness.

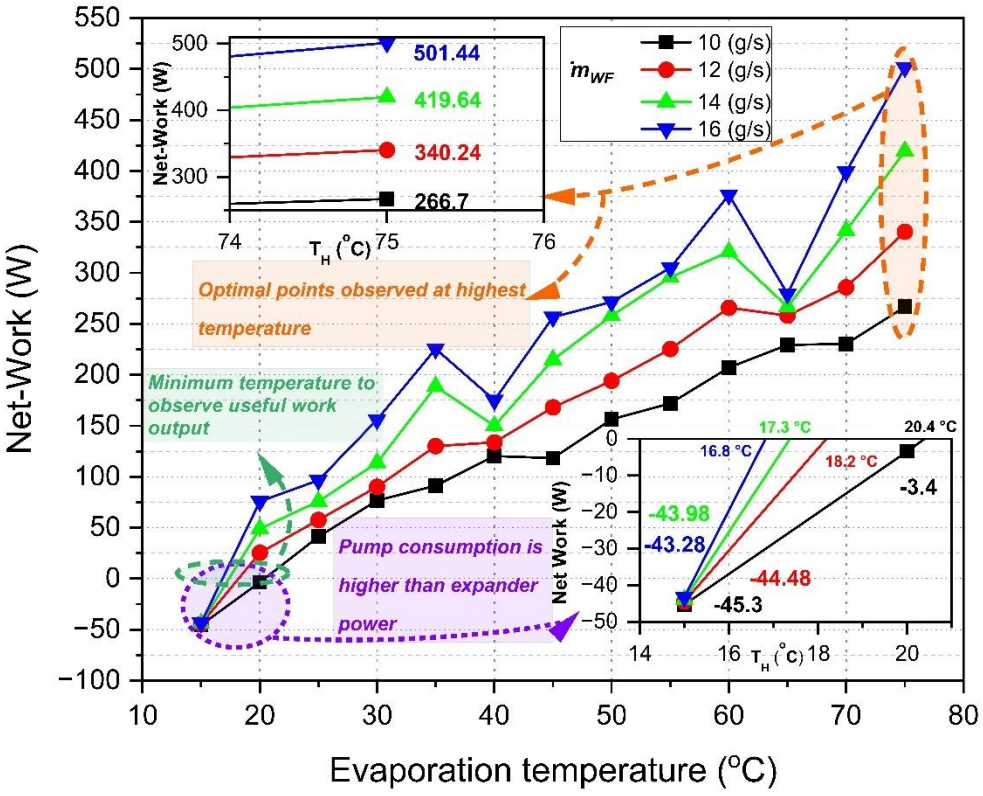

Figure 5.2: Net-work output of the cryogenic enhanced ORC experimental test rig

A negative net-work output was observed below a certain evaporation temperature for each specific working fluid mass flow rate, which indicated that the pump power consumption was higher than the work output provided by the expander, displayed at the bottom right corner of Figure 5.2, Figure 5.3, Figure 5.5, and Figure 5.6. For example, at 15 °C evaporation temperature, a net-work output of -45.3 W, -44.48 W, -43.98 W, and -43.28 W was observed at working fluid mass flow rates of 10 g/s, 12 g/s, 14 g/s, and 16 g/s, respectively. Hence, the rotation of the expander was being driven by the pressure differential at the expander inlet and outlet, and the thermal energy content of the working fluid was not enough to provide any useful work output. It is therefore recommended that each cryogenic enhanced ORC system be thoroughly tested to identify the minimum evaporation temperature point. For example, the minimum evaporation temperatures were observed to be 16.8 °C, 17.3 °C, 18.2 °C, and 20.4 °C,

corresponding to the working fluid mass flow rates of 10 g/s, 12 g/s, 14 g/s, and 16 g/s, respectively. Consequently, thermal efficiency, cryogenic energy efficiency, and exergy efficiency, along with the net-work output, were observed to be negative at 15 °C, as illustrated in Figure 5.2, Figure 5.3, Figure 5.5, and Figure 5.6.

Figure 5.3 illustrates the effect of increasing evaporation temperatures at varying working fluid mass flow rates on the thermal efficiency performance of the system. Higher thermal efficiency was observed, at the same evaporation temperatures, for higher working fluid mass flow rates. For example, at the evaporation temperature of 75 °C, a thermal efficiency (Equation 4.57) of 6.25 %, 6.65 %, 6.99 %, and 7.29 % was observed at working fluid mass flow rates of 10 g/s, 12 g/s, 14 g/s, and 16 g/s, respectively. The higher thermal efficiency at a specific evaporation temperature occurred due to the working fluid ability to absorb the available thermal energy from the heat source. The thermal energy content of the waste heat source remained the same at specific evaporation temperatures, due to constant heat source flow rates, but the ability of thermal heat absorption of the working fluid increased at a higher flow rate. Subsequently, the heat absorption capability of the working fluid increased by 16.64 % when the working fluid mass flow rate increased from 10 g/s to 16 g/s. The heat absorption capability is simply the increase in heat flow between the hot and cold fluid due to the increase in heat exchanger effectiveness while the flow rate of the hot water remains constant and refrigerant flow rate increases, as per Equation 4.60 and Equation 4.61.

In terms of the effect on thermal efficiency due to increasing evaporation temperatures (T3), similar trends were observed as in the case of the net-work output, such that the thermal efficiency steadily increased due to an increase in evaporation temperatures, resulting from an increase in the degree of superheat of the working fluid. Hence, in terms of energetic system performance, system optimisation routes should identify the optimal evaporation temperatures and mass flow rates, and observations conducted in this study indicate higher evaporation temperatures and working fluid mass flow rates would lead to an overall increase in energetic system performance.

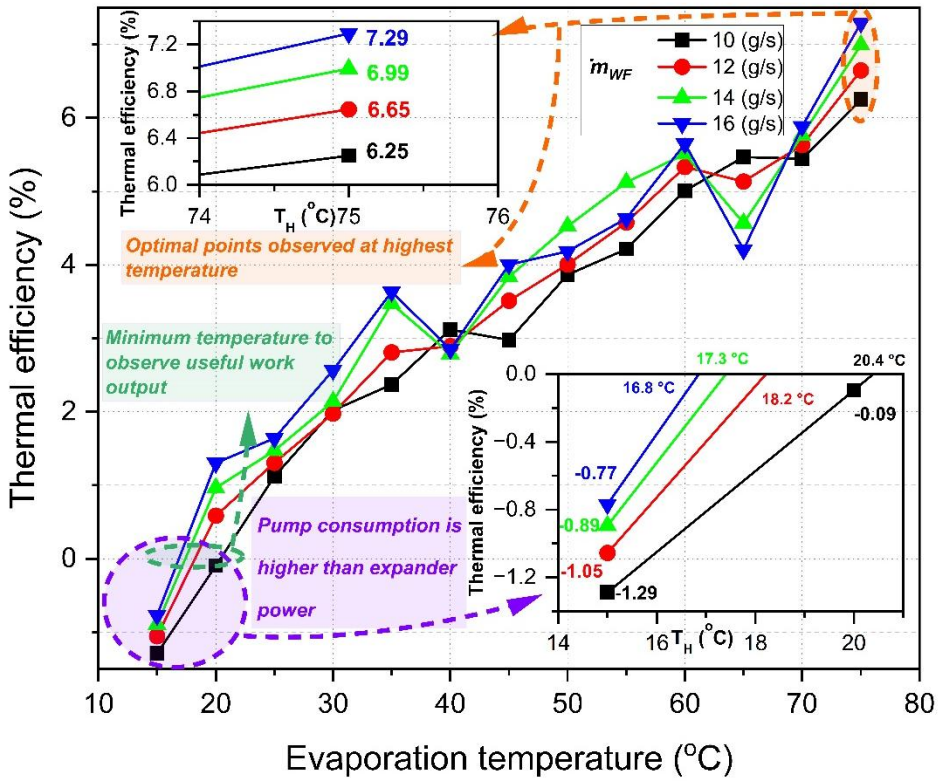

Figure 5.3: Thermal efficiency of the cryogenic enhanced ORC experimental test rig

Table 5.2 provides a comparison of the ultra-low temperature cryogenic enhanced ORC with the normal non-cryogenic experimental ORC systems found in literature. It was observed that the cryogenic enhanced ORC designed in this study provides a superior performance at a lower heat source temperature and lower working fluid mass flow rates. If the mass flow rate and the evaporation temperature in this experimental study were to be increased, based on the trends in Figures 5.2, 5.3, 5.5, and 5.6, the efficiency and net-work output would also increase, significantly surpassing the non-cryogenic ORCs.

Table 5.2: Comparison of experimental cryogenic enhanced ORC developed in this study and non-cryogenic ORCs found in literature.

Reference	Configuration	Working fluid	Evaporation temperature (°C)	Heat sink temperature (°C)	Flow rate (kg/s)	Key Performance Indicators	
						Net-work	Thermal efficiency

2019 [177]	Simple ORC	R1233zd (E)	120	23	0.045	0.325 kW	4.7 %
2015 [178]	Recuperative ORC	R245fa	110	20	0.005	0.28 kW	3.2 %
2012 [179]	Simple ORC	R245fa	85	37	2.56	31.2 kW	5.66 %
2016 [180]	Simple ORC	R1233zd (E)	120	30	0.04	0.312 kW	5.1 %
2015 [181]	Simple ORC	R245fa	100	26.8	0.052	1.17 kW	9.2 %
2017 [182]	Simple ORC	R134a	85	16	0.132	1.2 kW	4.4 %
2020 [183]	Recuperative ORC	R245fa	165	15	0.125	2.53 kW	7.3 %
This study	Simple ORC	R410a	75	- 182	0.01 – 0.016	0.501 kW	7.29 %

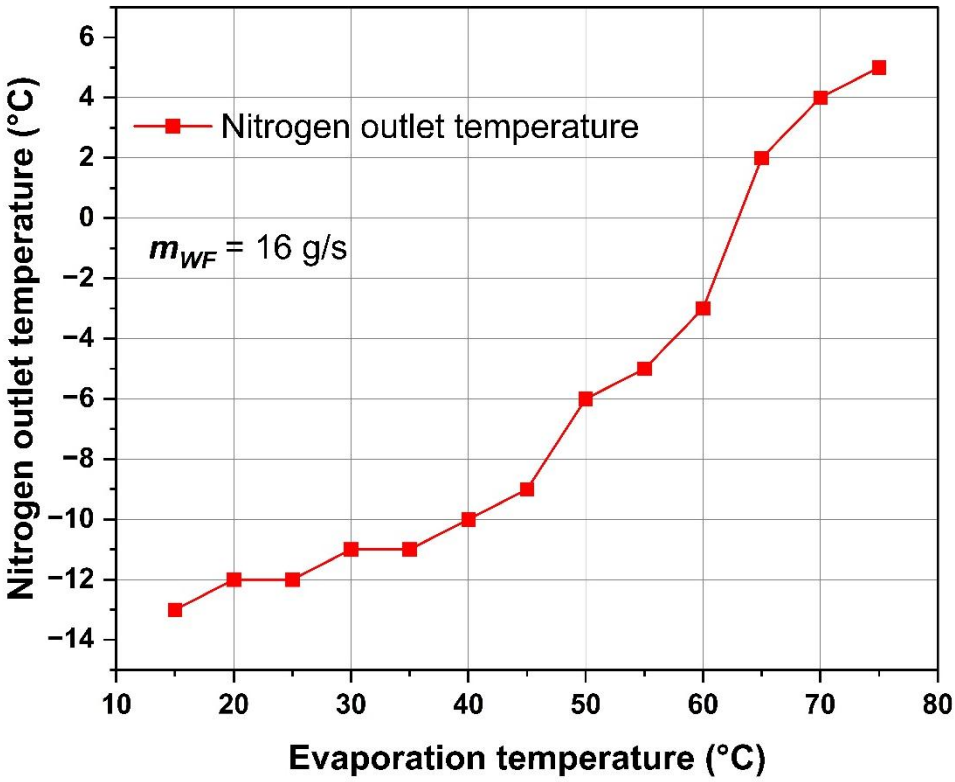

Figure 5.4: Variation of nitrogen exhaust temperature with evaporation temperature

An astute observation was made that the temperature of the gaseous nitrogen at the condenser outlet was directly linked to the ORC evaporation temperature, such that higher evaporation temperatures led to higher gaseous nitrogen temperatures, as illustrated in Figure 5.4. This exhibited the flexibility of the cryogenic enhanced ORC system, which could provide variable cryogenic fuel conditions, dependant on the end-use requirements. Hence, through extensive and sustained operational parameter sensitivity analysis, it is possible to provide favourable cryogenic fuel regasification parameters, as required by the end-use applications, such as combustion engines and fuel cells. According to Pimm et al. [184], hydrogen fuel consumption could be significantly reduced by preheating prior to combustion. They demonstrated that preheating of hydrogen for industrial burners could provide fuel savings of up to 20 %, and cost savings of up to 8 % if the hydrogen was preheated to 500 °C. Yang et al. [185] corroborated this finding by concluding that preheating of hydrogen leads to a better flame stablisation and increases the combustion reaction rates. Similarly, Luo et al. [186] and Uzun et al. [187] investigated the efficacy of preheating the hydrogen before introduction into a PEMFC and concluded that preheating of hydrogen should be conducted to prevent cold start, and the system performance of the PEMFC significantly increased as a result of preheating, with Ref. [187] reporting a performance enhancement of 9.4 % in the PEMFC by preheating the inlet hydrogen to 50 °C, compared to cold start at -10 °C. Similar observations were made in literature for ammonia combustion and fuel cell cold start operations [188] [189]. Ammonia is notorious for being inherently difficult to ignite, and according to Erdemir and Dincer [188], high temperature ammonia intake through preheating can enhance combustion reactions and aid in autoignition. Chen et al. [190] performed a flame study on ammonia combustion and concluded that with induced increasing preheating temperatures, the concentration of unburned ammonia can be significantly reduced along with the nitrogen oxide emissions. They reported that the concentration of unburnt ammonia can be reduced below 0.1 mg/m^3 and nitrogen oxide emissions below 8.38 mg/m^3 by preheating ammonia to 500 °C, compared to 5 mg/m^3 and 21.02 mg/m^3 at 320 °C. Nie et al. [191] reported that by preheating ammonia before fuel cell operation can increase the performance by 6.29 %, by inducing ammonia oxidation. Hence, by increasing the evaporation temperatures of the cryogenic enhanced ORC system and matching the low flammability ORC working fluid and cryogenic heat

sink mass flow rates, the cryogenic fuels can be preheated in addition to being regasified, while still providing sufficient condensation cooling to the ORC working fluid. Therefore, cryogenic enhanced ORCs have the potential of providing an inherent benefit to the overall balance of plant for low-carbon cryogenic fuel utilisation through multiple avenues, such as through providing additional work output through dual waste thermal and waste cryogenic energy reutilisation, and preheating the fuels before end-use applications, significantly increasing the overall balance of plant efficiency.

Figure 5.5 illustrates the effect on the cryogenic energy efficiency due to increasing evaporation temperatures and working fluid mass flow rates. Cryogenic energy efficiency is a performance indicator used specifically for cryogenic enhanced ORCs [99] [105] [93] [75], where the system performance is judged based on the ratio of system net-work output to the heat rejected by the working fluid to the cryogenic cold source in the condenser. It provides a measure of the focal point, regasification of cryogenic fuels, of cryogenic enhanced ORCs. It was observed that an increase in evaporation temperatures led to an increase in the cryogenic energy efficiency. This resulted from the increase in the expander outlet temperatures, which steadily increased as the evaporation temperature, or expander inlet temperature, increased. Hence, more thermal energy was available at the expander outlet, which had to be rejected to the cryogenic liquid nitrogen source. However, the increase in the amount of heat rejected to the cryogenic source was lower than the increase in the net-work output, hence an increase in cryogenic energy efficiency was observed. The highest cryogenic energy efficiency was observed at 75 °C, recording 6.58 %, 6.79 %, 7.36 %, and 7.67 % at working fluid mass flow rates of 10 g/s, 12 g/s, 14 g/s, and 16 g/s, respectively. Similarly to the net-work output and the thermal efficiency, a negative cryogenic energy efficiency was observed below specific evaporation temperatures, where the pump power consumption was higher than the expander work output. The cryogenic energy efficiency was observed to be higher than the thermal efficiency, which was expected due to the higher heat load at the evaporator side, based on the governing equations 4.57 and 4.58.

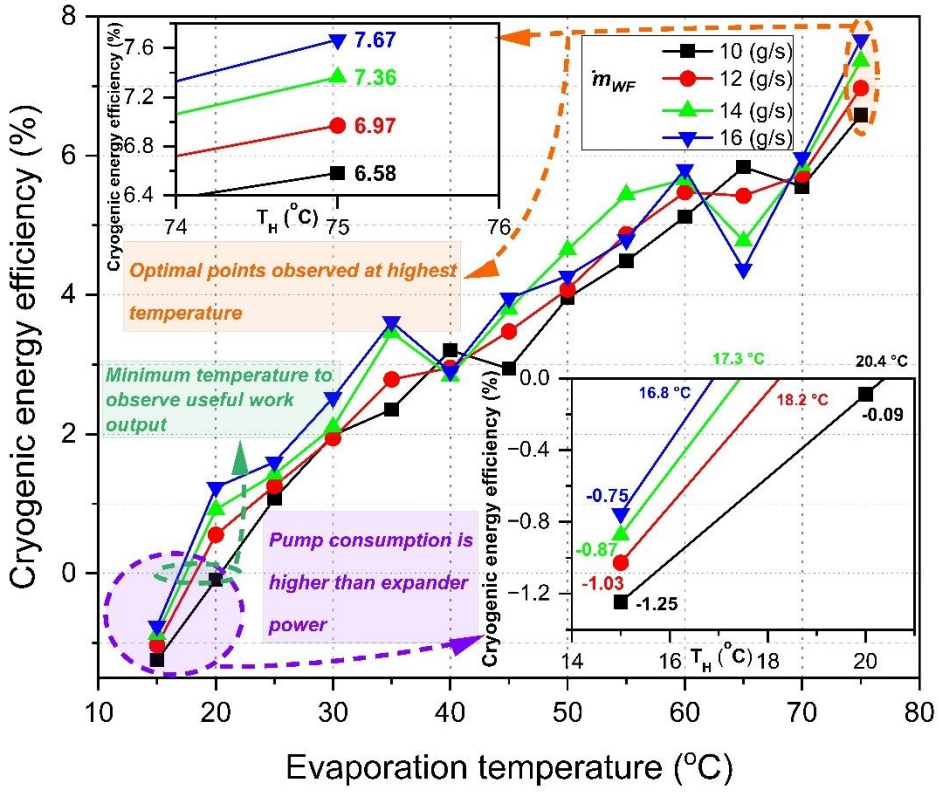

Figure 5.5: Cryogenic energy efficiency of the cryogenic enhanced ORC experimental test rig

Figure 5.6 depicts the effect of increasing evaporation temperatures and mass flow rates on the cryogenic exergy efficiency. Exergy efficiency usually relates to the ratio of the useful net-work output of the system to the total exergy input into the system [192]. However, in the context of cryogenic enhanced ORCs, the most important parameter is the large temperature difference between the heat source and the cryogenic heat sink, creating a much higher temperature gradient, and therefore higher Carnot efficiency, leading to cryogenic fuel regasification. In this context, the heat source exergy is excluded from the definition of exergy efficiency and only the cryogenic exergy input into the condenser is considered, henceforth known as the cryogenic exergy efficiency, defined by *Equation 4.59* in *Chapter 4: Dynamic Numerical Model*.

Similar trends were observed as the energy analysis, where higher mass flow rates provided a better system cryogenic exergy efficiency, and an increasing trend was observed with increasing evaporation temperatures. In terms of higher working fluid mass flow rates, it was evident from Figure 5.2 that the working fluid net-work output increased. Additionally, the rate of heat rejection to the cryogenic source also increased,

but at a lower rate than the increase in the net-work output. The highest cryogenic exergy efficiency was recorded at an evaporation temperature of 75 °C, achieving 4.41 %, 5.66 %, 6.98 %, and 8.38 % at working fluid flow rates of 10 g/s, 12 g/s, 14 g/s, and 16 g/s, respectively. All KPIs discussed across Figure 5.2, Figure 5.3, Figure 5.5, and Figure 5.6 exhibited negative values below a specific evaporation temperature, highlighting the importance of parametric sensitivity analysis to determine optimal system performance parameters. The cryogenic exergy performance provided a better understanding of the state of the cryogenic fuel, which is quintessential when taking a holistic system integration approach towards cryogenic low-carbon fuel dissemination within the current energy infrastructure. Therefore, a complete system analysis for cryogenic enhanced ORCs should include both energy and exergy objective parameters. This would allow the entire balance of plant integration and optimisation to be carried out, from storage to end-use applications, with the cryogenic enhanced ORC acting as an energy efficiency increment and operational flexibility device. The cryogenic ORC would then essentially serve a dual purpose by providing additional work output through waste energy reutilisation and providing cryogenic fuel regasification. Additionally, the fuel regasification component could be optimised based on end-use requirements, providing much needed preheating in applications where cold starts may negatively impact system performance and lifetime.

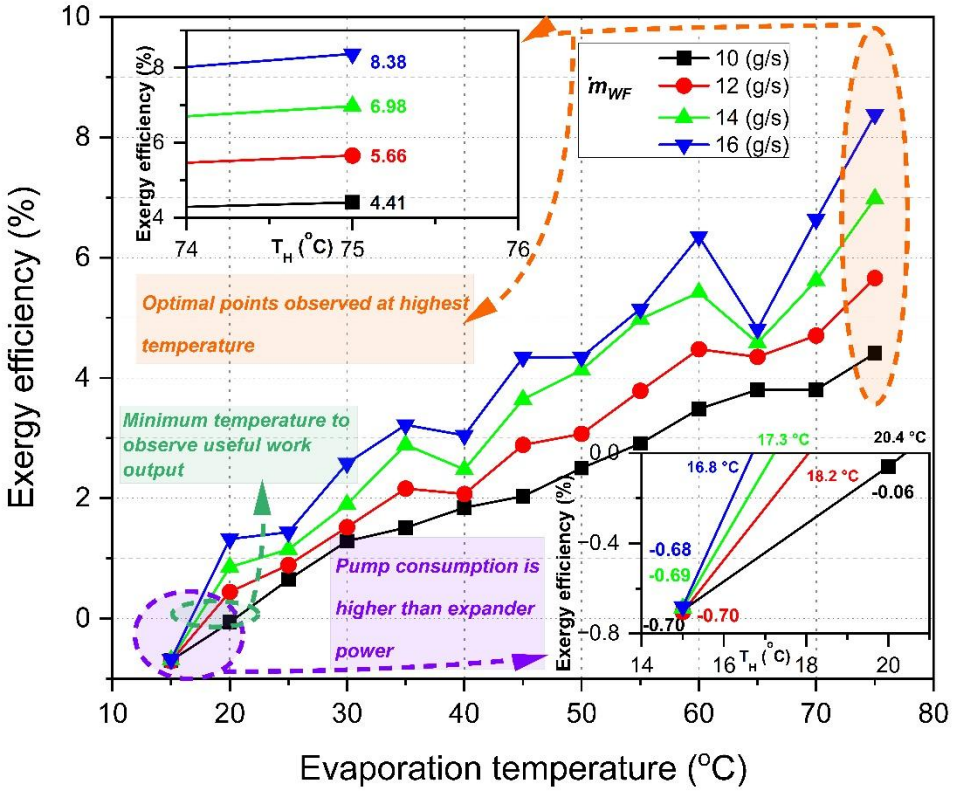

Figure 5.6: Cryogenic exergy efficiency of the cryogenic enhanced ORC experimental test rig

The anomalies observed in Figure 5.2, Figure 5.3, Figure 5.5, and Figure 5.6 at evaporation temperatures of 40 °C and 65 °C were in part attributed to random errors. However, additional scrutiny revealed that the system required a longer time to achieve steady-state operation, as evident from the analysis conducted in *Chapter 6: Dynamic Numerical Model Analysis*, where the model was allowed 4000 seconds to achieve steady-state operation. It is entirely plausible to suggest these data points suffered from thermal shock, where the water heater required additional time to provide the required energy and the expander required additional time to stabilise to account for increased flow rate and temperature, for a sustained linear increasing trend in performance.

A heat exchanger effectiveness analysis (Equation 4.60 and 4.61) was carried out based on increasing evaporation temperatures and working fluid mass flow rates, illustrated in Figure 5.7. It was clearly evident that the mass flow rate played a significant role in deciding the heat exchanger effectiveness. This stemmed from the fact that higher mass

flow rates in heat exchangers with parallel flow configurations led to increased heat transfer rates between the hot and the cold fluids. In simple terms, more energy was absorbed or rejected by the working fluid by increasing its mass flow rate, while the flow rate of the heat source or cryogenic source remained constant. Alimoradi [193] and Shahrul et al. [194] arrived at a similar conclusion regarding heat exchanger effectiveness and mass flow rate variation. Comparing the effectiveness of the evaporator and the condenser at the same mass flow rates revealed that for low evaporation temperatures, the condenser exhibited a higher effectiveness, while at higher temperatures, the evaporator exhibited higher effectiveness. For example, at a mass flow rate of 10 g/s and evaporation temperature of 15 °C, the evaporator effectiveness was 55.71 % and the condenser effectiveness was 59.59 %. Here, the heat source temperature was 32 °C and the heat sink temperature was -182 °C, and much of the thermal and cryogenic energy was left unutilised. Conversely, at an evaporation temperature of 75 °C at the same mass flow rate, the evaporator effectiveness was 76.59 % and the condenser effectiveness was 63.76 %. The rationale originated from the fact that condensation and evaporation were both occurring in the condenser. The latent heat of vaporisation of the liquid nitrogen, as it changed phase from liquid to vapor, and the latent heat of condensation of the working fluid, as it changed phase from vapor to liquid, were being absorbed and rejected simultaneously. On the other hand, only the latent heat of vaporisation was being absorbed by the working fluid in the evaporator, in addition to the sensible heat from the heat source to induce superheating. Initially, at low evaporation temperatures, the rate of latent heat of vaporisation and condensation in the condenser was greater than the degree of superheating and latent heat of vaporisation in the evaporator, hence the condenser exhibited higher effectiveness due to higher rate of heat transfer. However, as the evaporation temperature increased, the increase in degree of superheat led to the working fluid entering supercritical state and increased the rate of heat transfer. Therefore, the rate of effectiveness for the evaporator rose sharply, while the rate of effectiveness for the condenser exhibited stagnated growth. The maximum evaporator and condenser effectiveness of 99.1 % and 99.35 %, respectively, was observed at the mass flow rate 16 g/s and evaporation temperature of 75 °C. This translated to an increase of 77.89 % and 66.72 % for the evaporator and condenser, respectively, up from 55.71 % and 59.59 % at a working fluid mass flow rate of 10 g/s and evaporation temperature of 15 °C.

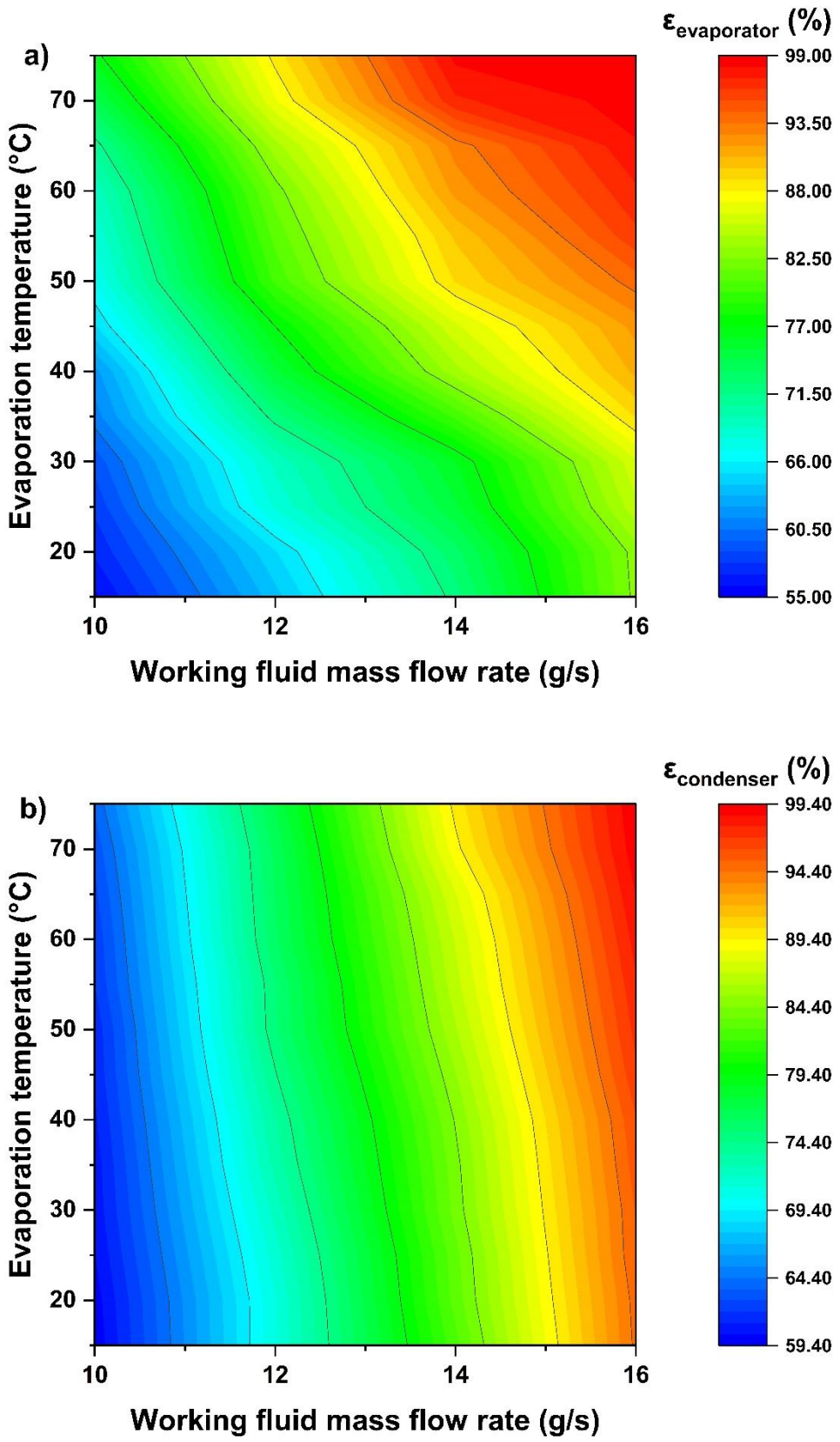

Figure 5.7: Heat exchanger effectiveness of the cryogenic enhanced ORC experimental test rig: a) Evaporator; b) Condenser

5.5 Exergy destruction analysis

Figure 5.8 illustrates the effect on exergy destruction in each individual component, at varied working fluid mass flow rates, with increasing evaporation temperatures. The general trend was that the exergy destruction was lower at lower mass flow rates, and higher at higher mass flow rates. For example, at the evaporation temperature of 75 °C, the exergy destruction increased by 53.88 %, 51.63 %, 37.46 %, and 12.6 % for the pump, evaporator, expander, and condenser, respectively, when the working fluid mass flow rate increased from 10 g/s to 16 g/s. The pump exhibited the highest rate of increase in exergy destruction rates with increasing working fluid mass flow rates, which was expected as higher input power was required to increase the rotational speed of the pump. In terms of the evaporator, an increase in working fluid mass flow rates led to an increase in the exergy heat transfer rates between the working fluid and the heat source, which caused the increased exergy destruction rates as the working fluid had less time to change phase from sub-cooled liquid to superheated vapour at higher mass flow rates. With increased mass flow rates, the rotational speed of the expander increased, causing an upsurge of power generated by the expander, which, according to equation 4.53, should cause a lower exergy destruction. However, the exergy difference between the expander inlet and outlet increased, due to higher rates of heat transfer in the evaporator, which caused the higher exergy destruction rates. Hence, the rate of increase in the power produced by the expander was slightly less than the rate of increase of exergy at the expander inlet. It was evident that the condenser exhibited the lowest increase in exergy destruction rate with increasing working fluid flow rate. The difference between the condenser and the evaporator exergy destruction rates based on increasing mass flow rates lies in the fact that the working fluid density decreases in the evaporator, while it increases in the condenser. Hence, lower density and higher mass flow rate increases the rate of exergy destruction.

In terms of the overall component exergy destruction, the pump exhibited the lowest exergy destruction, followed by the expander and evaporator, while the highest exergy destruction was revealed in the condenser. For example, at an evaporation temperature of 50 °C and working fluid mass flow rate of 16 g/s, the exergy destruction rates were 0.096

kW, 0.78 kW, 0.36 kW, and 6.2 kW for the pump, evaporator, expander, and condenser, respectively. Low exergy destruction in the pump was expected, as the working fluid was undergoing minimal heat transfer (only heat losses to the environment), and most of the exergy destruction resulted from the pump input power. In the expander, the majority of the exergy destruction occurred due to working fluid expansion, effectively reducing the pressure and the temperature to produce mechanical power. In the evaporator, the working fluid changed phase to superheated vapor, while the hot water remained in liquid phase, hence increasing the exergy heat transfer and leading to higher exergy destruction rates than the pump and expander. Conversely, in the condenser, the working fluid changed phase from superheated low-pressure vapor to sub-cooled liquid, rejecting the latent heat of condensation, while the liquid nitrogen absorbed the latent heat of vaporisation as it changed phase from liquid to vapour. Therein lies the explanation of the differences in the exergy destruction rates of the evaporator and the condenser. The latent heat of vaporisation and condensation, in the condenser, was of higher quality than the latent heat of vaporisation and sensible heat in the evaporator, which was why the condenser exhibited the highest rate of exergy destruction. For example, the condenser had an exergy destruction rate of 6.71 kW at an evaporation temperature of 75 °C and working fluid mass flow rate of 16 g/s, compared to the evaporator, which exhibited an exergy destruction rate of 0.86 kW. Additionally, the working fluid temperature increase in the evaporator, from sub-cooled liquid to superheated vapor, was always higher than the working fluid temperature decrease in the condenser, from low-pressure superheated vapor to sub-cooled liquid. However, the hot water underwent a relatively minor temperature differential compared to the liquid nitrogen, which was another major cause of higher exergy destruction in the condenser.

In terms of the evaporation temperature, it was noticed that the exergy destruction increased linearly with increasing evaporation temperatures. For example, at working fluid mass flow rate of 16 g/s, the exergy destruction increased by 43.29 %, 26.31 %, 19.4 %, and 25.09 %, for the pump, evaporator, expander, and condenser, respectively, when the evaporation temperature increased from 15 °C to 75 °C. In terms of the pump and the expander, the exergy destruction rates should be relatively constant based on the results of the numerical model, *Chapter 6: Dynamic Numerical Model Analysis*. However,

in real-world conditions, heat losses to the environment cannot be discounted. In the case of the pump, the pump variable frequency drive displayed the pump power, while also consuming power itself for the display. In terms of the expander, increased rotational speed due to higher evaporation temperatures would result in higher frictional losses in the expander shaft, resulting in exergy losses. In terms of the evaporator, increasing evaporation temperatures required the degree of superheat to be increased, leading to an increase in exergy destruction rates. For the condenser, this led to increased working fluid temperatures at the inlet, which required a higher heat rejection to the cryogenic heat sink medium, which increased the rate of exergy destruction in the condenser.

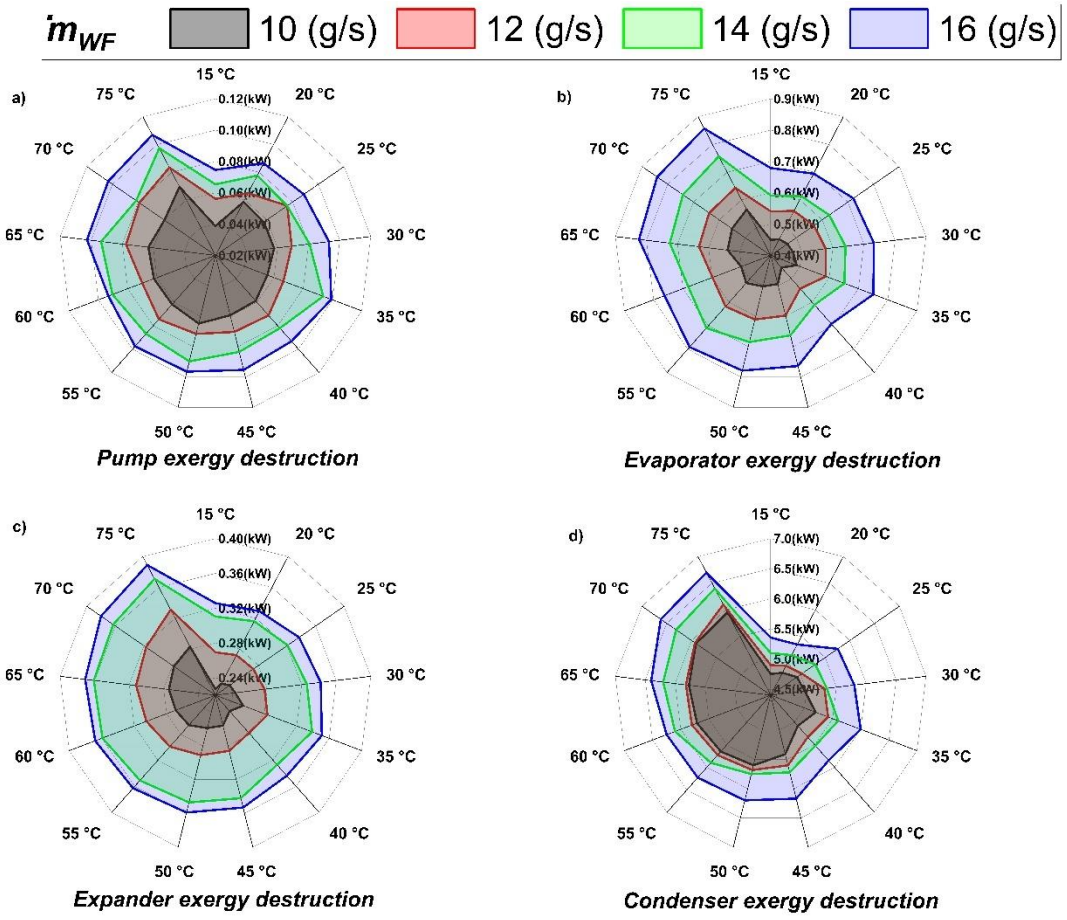

Figure 5.8: Individual component exergy destruction of the cryogenic enhanced ORC experimental test rig: a) Pump; b) Evaporator; c) Expander; d) Condenser

Figure 5.9 and Figure 5.10 illustrate the exergy destruction rates and exergy destruction ratios, respectively, at the highest heat exchanger performance (above 80 %). From Figure

5.7, this was achieved at a working fluid mass flow rate of 16 g/s. The condenser exhibited the highest exergy destruction, due to the highest temperature differential between the heat exchange fluids and accounted for more than 80 % of the total system exergy destruction. The pump exhibited the lowest exergy destruction rates as practically no heat exchange occurred, and most of the exergy destruction was accounted for by the input power to induce flow.

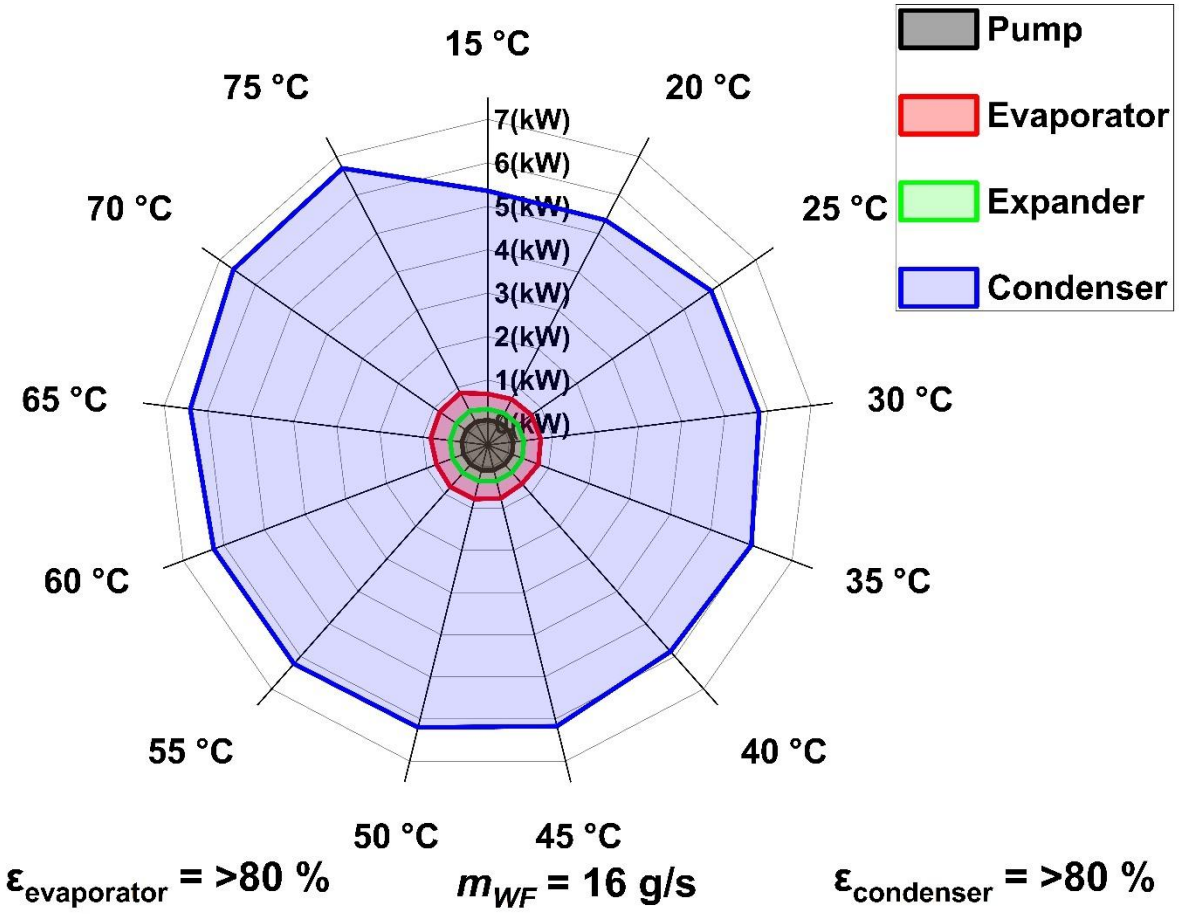

Figure 5.9: Cryogenic ORC exergy destruction rate at high heat exchanger effectiveness

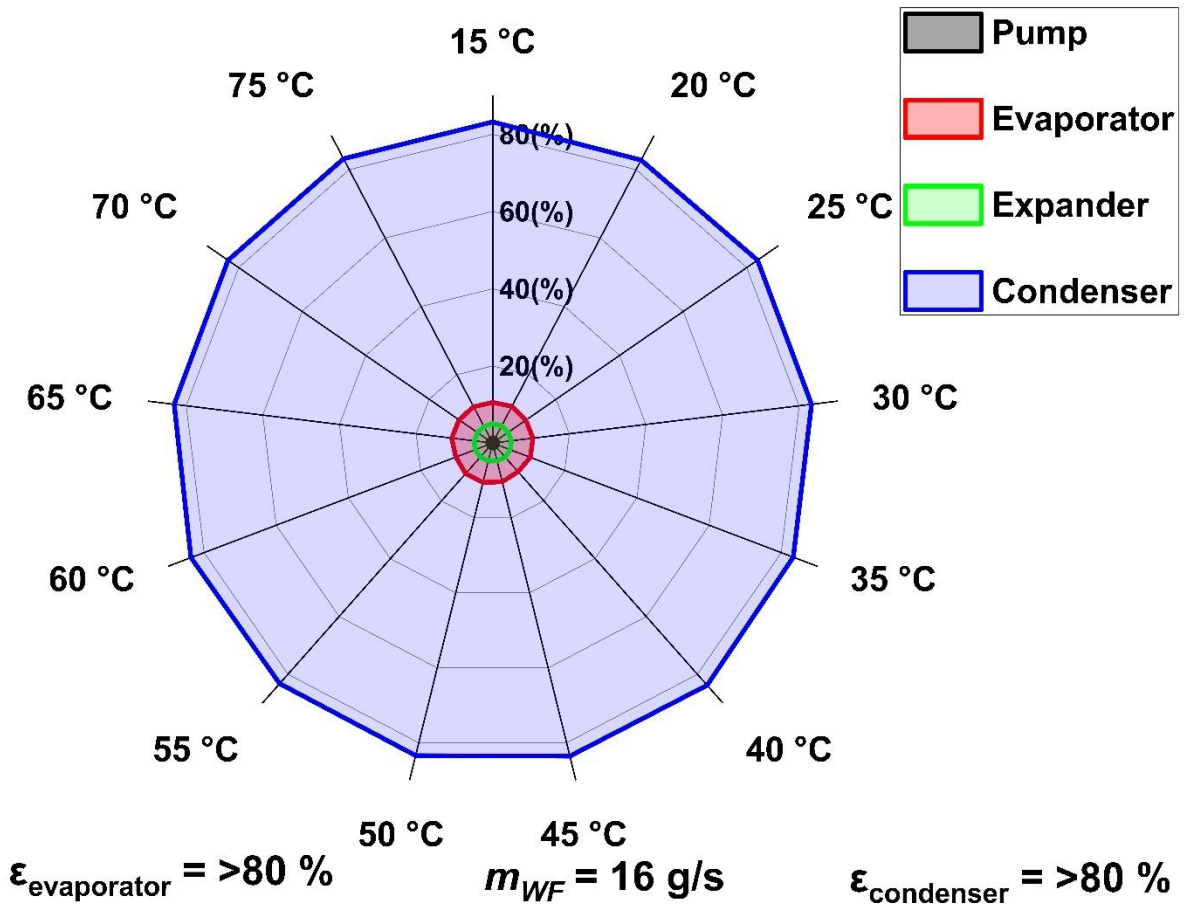

Figure 5.10: Cryogenic ORC exergy destruction rate at high heat exchanger effectiveness

The individual component exergy destruction ratios are illustrated in Figure 5.11. Since the rates of exergy destruction increase, compared to the evaporator and condenser, for the pump and the expander were minimal, the exergy destruction ratios decreased with increasing evaporation temperatures. For example, the exergy destruction of the pump and expander increased from 0.065 kW and 0.31 kW to 0.097 kW and 0.37 kW, respectively, when the evaporation temperature increased from 15 °C to 75 °C at a working fluid mass flow rate of 14 g/s. Conversely, the exergy destruction of the evaporator and condenser increased from 0.59 kW and 5.1 kW to 0.75 kW and 6.4 kW, respectively. Hence, only the evaporator exhibited increased exergy destruction ratios with increased evaporation temperatures. In terms of the condenser, the exergy destruction ratios decreased with increasing mass flow rates, since the proportion of evaporator exergy destruction in the total system exergy destruction increased at a higher rate than the condenser. Interestingly, as the mass flow rates increased, the exergy

destruction ratios in the condenser decreased, due to higher proportion of evaporator exergy destruction.

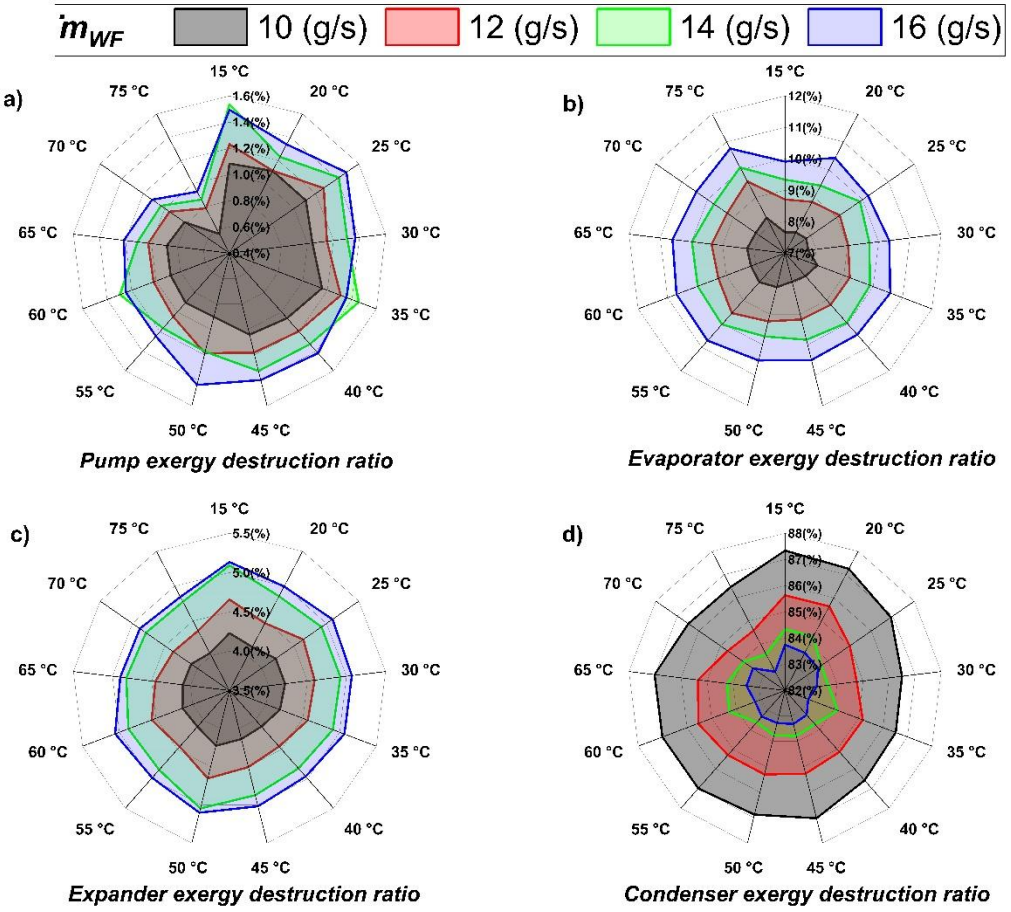

Figure 5.11: Individual component exergy destruction ratios of the cryogenic enhanced ORC experimental test rig: a) Pump; b) Evaporator; c) Expander; d) Condenser

5.6 Measurement accuracy

The uncertainty in individual sensor readings (U_{total}) was calculated using the root square sum of the random errors (U_{random}) and the systematic errors ($U_{systematic}$) as follows [195] [196]:

$$U_{total} = \sqrt{(U_{random}^2 + U_{systematic}^2)} \quad (5.1)$$

$$U_{random}^2 = t_{(N-1),95\%} \times S_x \quad (5.2)$$

The systematic errors were obtained from the manufacturer calibration sheets.

Where $t_{(N-1),95\%}$ represents the 95th percentile confidence interval student distribution factor and S_x is the mean deviation, represented by:

$$S_x = \left(\frac{\sum_{i=1} N\,(x_i - \bar{x}_i)^2}{N \times (N-1)}\right)^{0.5} \tag{5.3}$$

Where, N was the number of sample points, x_i was the calibration sample point, and $\bar{x}_i$ was the fitted trendline at point i.

The error propagation (U_y) to the objective functions was then calculated using:

$$U_y = \left(\frac{\sum_{i=1} N\,(\frac{\delta y}{\delta x_i} U_{x_i})^2}{N \times (N-1)}\right)^{0.5} \tag{5.4}$$

$$y = f(x_1, \ldots, x_n) \tag{5.5}$$

Where y was the output to the function f with n number of input variables x, $\frac{\delta y}{\delta x_i}$ was the partial differential of y with respect to x_i, and U_{x_i} was the uncertainty of variable x_i.

The individual reading and the key performance indicator calculation uncertainty propagation is tabulated in Table 5.3.

Table 5.3: Experiment uncertainty analysis

Sensor	Random error	Systematic error	Total error
Temperature sensors	± 0.342 °C	± 0.5 °C	± 0.842 °C
Pressure sensors	± 0.052 bar	± 0.1 bar	± 0.152 bar
Working fluid flow meter	0.0000012 kg/s	0.00004 kg/s	0.0000412 kg/s
Liquid nitrogen flow meter	0.000027 kg/s	0.00015 kg/s	0.000177 kg/s
Water flow meter	0.00112 kg/s	0.004 kg/s	0.00512 kg/s

Torque sensor	0.007 N.m	0.015 N.m	0.022 N.m
Uncertainty propagation			
Net-work output		± 3.21 W	
Thermal efficiency		0.68 %	
Cryogenic energy efficiency		0.68 %	
Exergy efficiency		0.81 %	

5.7 Numerical model validation

The validation of the experimental setup was conducted by comparing the transient region, up to 120 seconds, of the dynamic numerical model.

Figure 5.12 illustrates the validation of the dynamic numerical model based on the experimental rig. The KPIs conformed to within 4.49 % error range. It is important to note that the simulation results presented in *Chapter 6: Dynamic Numerical Model* are steady-state, and the run time was 4000 seconds. However, due to limited availability of liquid nitrogen supply, the experiment conditions were transient, and each set of experimental operational parameters was given a maximum of 2 minutes to stabilise. Hence, the transient region of the dynamic numerical model was chosen for the validation. The steady-state results for the numerical model analysis have been presented in Section 6.3.

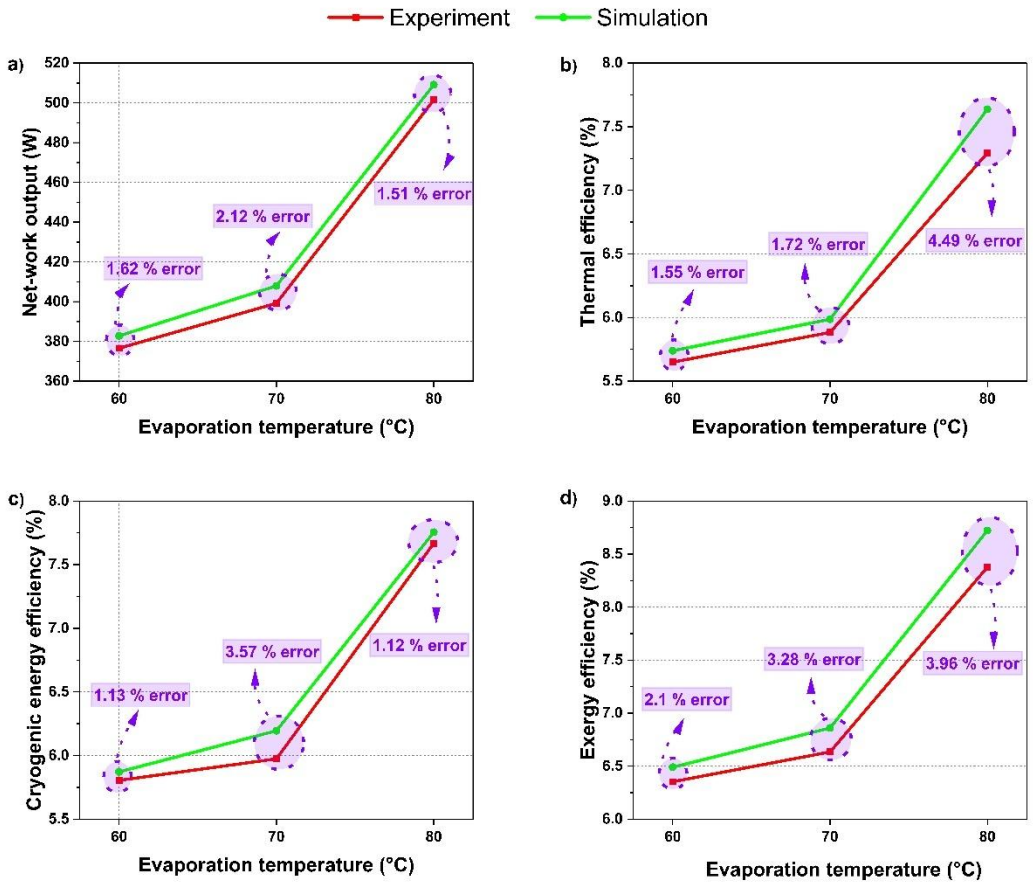

Figure 5.12: Numerical model validation of the cryogenic enhanced ORC at 16 g/s: a) Net-work output; b) Thermal efficiency; c) Cryogenic energy efficiency; d) Exergy efficiency

The validation of the exergy analysis is tabulated in Table 5.4. A slightly higher exergy destruction was noticed in the experimental analysis when compared to the numerical model analysis for the pump and the evaporator. This was due to the fact that the modelling software, Siemens Amesim [155], considered a perfectly insulated system, with no considerations for environmental losses. The experimental testing rig was insulated using high-quality cryogenic insulation. However, in the case of the pump and the evaporator, their circular geometry prevented them from being fully covered by the insulation. Hence, exergy destruction was higher for the pump and the evaporator. In terms of the expander and the condenser, the exergy destruction was slightly lower than the dynamic numerical model. This can be accounted to the changing atmospheric conditions and slight elevation pressure drops, which could not be accounted for in the numerical model. The dead-state temperature was set at 20 °C in the numerical model

analysis, whereas the atmospheric temperature during the experiments varied between 12 °C to 14 °C. The pressure drops also played an important role, as lower pressure at expander and condenser inlet led to lower working fluid enthalpy, hence reducing the overall exergy destruction in those components. The total system exergy destruction was within a 3.93 % error.

Table 5.4: Exergy destruction validation analysis

Evaporation temperature (°C)	Experimental results	Numerical model results	Deviation (%)
Pump exergy destruction (W)			
60	93.1	85.70	-8.62
70	88.69	82.04	-8.10
80	74.62	73.28	-1.82
Evaporation exergy destruction (W)			
60	763	594.38	-28.36
70	841	671.56	-25.23
80	857.71	791.43	-8.37
Expander exergy destruction (W)			
60	368	376.01	2.13
70	380	396.62	4.19
80	389	406.86	4.39
Condenser exergy destruction (W)			
60	6251	6724.89	7.04
70	6625	6781.91	2.31
80	6707	6871.27	2.39
Total exergy destruction (W)			

60	7475.1	7780.99	3.93
70	7934.69	7932.14	-0.03
80	8028.33	8142.85	1.40

A quick comparison of the key performance indicators, at specific evaporation temperatures, between *Chapter 5: Experimental Analysis* and *Chapter 6: Dynamic Numerical Model Analysis* revealed the importance of achieving steady-state system operation through sustained attainment of steady-state operational parameters, where the steady-state numerical model performance indicators perform better than the transient experimental setup. This also brought to light the importance of temporal steady-state operation enhancement, where the system performance steadily increased as the operational parameters achieved steady-state, until it reached the maximum achievable system performance plateau. Indeed, this was one of the key contributing factors while deciding the development of a novel dynamic model rather than the simple steady-state model, which would not be able to predict transient behaviour accurately and cannot account for working fluid charge quantity or initial charging conditions.

5.8 Performance comparison

To understand the performance of non-flammable hydrofluorocarbon working fluids for cryogenic enhanced ORCs, a comparative analysis was conducted against the only other experimental study on cryogenic enhanced ORCs by Ref. [105]. They utilised propane as the working fluid, which is a hydrocarbon and extremely flammable. The thermophysical properties of R410A, the working fluid utilised in this study, and propane are listed in Table 5.5. The safety advantage of this study was clearly evident, as R410A is classed as an A1 fluid in the ASHRAE safety index [151], whereas propane is classed as an A3 fluid. The highly flammable and explosive nature of propane would limit its applicability in space constrained and severe applications, where health and safety risks would outweigh the system performance metrics.

Table 5.5: Working fluid thermophysical properties comparison between this experimental study and Tian et al. [105]. The property data was obtained from REFPROP [43].

Working fluid comparison		
Property	**R410A**	**Propane**
Normal boiling temperature (°C)	-51.44	-42.04
GWP	2088	5
ODP	0	0
Melting temperature (°C)	-155	-187.69
Critical temperature (°C)	71.34	96.67
Molar mass (g/mol)	72.59	44.09
Liquid density (kg/m^3)	1062	492.08
Liquid / vapour thermal conductivity at 25 °C (mW/m-K)	94.527 / 15.67	93.621 / 18.97
Liquid / vapour specific heat capacity at 25 °C (kJ/kg-K)	1.6579 / 1.4455	2.7367 / 2.0724
ASHRAE safety group	A1 (non-flammable)	A3 (highly flammable)

Figure 5.13 illustrates the comparative analysis of the KPIs between this experimental study and the study conducted by Tian et al. [105]. In terms of the net-work, it was observed that the performance was comparable to the work of Ref. [105]. Initially, propane outperformed R410A, showing a higher increase in performance as the evaporation temperature increased. However, there was a decline in performance noticed at 40 °C for propane. This was because the condensation pressure was much higher than the atmospheric pressure in the works of Ref. [105], leading to a decline in performance. The slight increase in the net-work performance of propane stems from the lower molar mass, as the ORC is a closed loop system with a fixed volume. Hence, a

higher molar mass results in lower moles on a mass-basis, which is explained in detail in *Section 6.2.1* of *Chapter 6: Dynamic Numerical Model Analysis*. The decrease in performance at 40 °C for R410A in this study was explained in Section 5.3, due to insufficient time to reach steady-state conditions. In terms of the thermal efficiency, R410A outperformed propane, due to a lower critical temperature. Hence, R410A required less energy input to achieve the same evaporation temperature, as compared to propane. The cryogenic energy efficiency exhibited major variations, and propane outperformed R410A. However, the reason for this can be ascertained by the operational parameters utilised in the works of Ref. [105]. The condensation pressure of propane reached 6.7 bars, and the corresponding condensation temperature was 8.9 °C. On the other hand, the condensation pressure in this study ranged from 1.2 to 1.6 bars, and the corresponding condensation temperatures were – 98 °C to - 89 °C. The differences in condensation pressures and temperatures also led to a higher cryogenic exergy efficiency for propane. Additionally, the liquid nitrogen utilised by Tian et al. [105] was at a pressure of 6.8 to 7.2 bars, which resulted in lower exergy destruction in the condenser. In this study, the liquid nitrogen pressure ranged between 1.5 to 2.5 bars, resulting in a much higher exergy destruction rate. However, it must be noted that in the works of Tian et al. [105], the liquid nitrogen still had a lot of cryogenic exergy unutilised, and would require an additional heat exchanger to bring the cryogenic fuel to atmospheric conditions. On the other hand, the current experimental study achieved complete fuel regasification, and no further heating was required to enable the nitrogen exhaust to reach atmospheric temperature.

The comparative analysis proved that hydrofluorocarbons for cryogenic enhanced ORCs can compete with hydrocarbons, while providing the additional safety aspect of low flammability. To achieve a shift from hydrocarbons to hydrofluorocarbons as working fluids for cryogenic fuel regasification through cryogenic enhanced ORCs, detailed operational parameter analysis to achieve objective parameter optimisation is necessary.

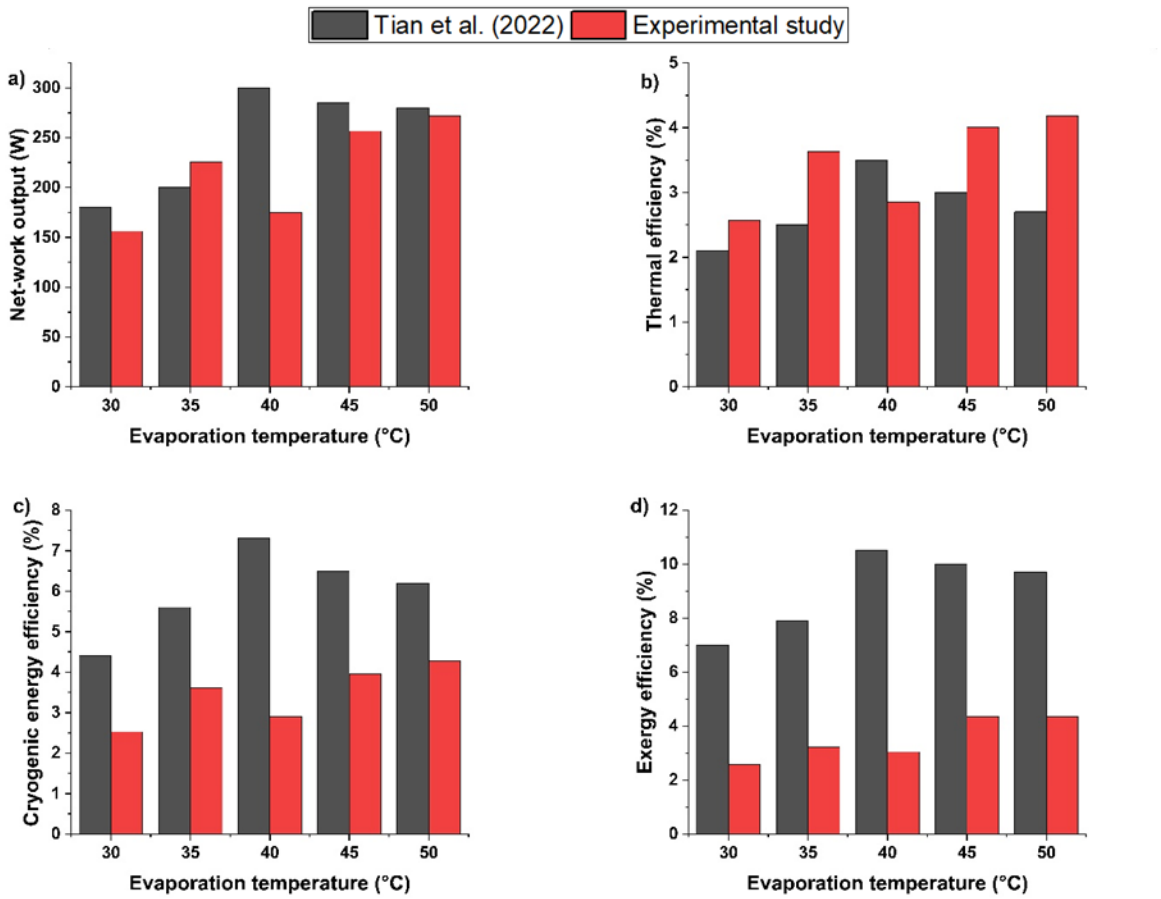

Figure 5.13: Performance comparison with literature [105]: a) Net-work output; b) Thermal efficiency; c) Cryogenic energy efficiency; d) Exergy efficiency

5.9 Summary

This chapter presented the experimental investigation of low flammability hydrofluorocarbon working fluids for cryogenic energy reutilisation using Organic Rankine Cycles. R410A was utilised as the cryogenic non-flammable working fluid, and liquid nitrogen was utilised as the cryogenic energy source. A detailed energy and exergy performance analysis was conducted by varying the system operational parameters to maximise the key performance indicators. The parametric analysis conducted involved the variation of the working fluid mass flow rate between 10 to 16 g/s, while the evaporation temperature was varied between 15 °C to 75 °C. A heat exchanger effectiveness analysis was performed to understand the heat transfer efficiency at

different operational parameters. The dynamic numerical model was validated through the experimental analysis, and the current experimental study was pitted against literature to understand the feasibility of utilising low flammability hydrofluorocarbons over the traditional highly flammable hydrocarbons as working fluids for cryogenic enhanced ORCs. The main findings of the experimental investigation are summarised as follows:

1. The working fluid mass flow rate and the evaporation temperature had a direct correlation with the system key performance indicators. There exists an evaporation temperature limit, different for each working fluid mass flow rate, below which the expander rotation is facilitated by the pump pressure differential. Hence, the parametric analysis enables identification of critical points above which the system can provide useful work. Higher working fluid mass flow rates and higher evaporation temperatures lead to better heat transfer rates, observed through the heat exchanger effectiveness analysis, and increasing degree of superheat, which enhances system performance. The system achieved a maximum net-work output, thermal efficiency, cryogenic energy efficiency, and cryogenic exergy efficiency of 501.44 W, 7.29 %, 7.67 %, and 8.38 %, respectively.

2. The gaseous nitrogen exhaust temperature was directly dependent on the evaporation temperature. Hence, in terms of balance of plant integration, the cryogenic ORC could provide operational flexibility downstream. The cryogenic fuel regasification and preheating could add to the overall balance of plant efficiency, where several hydrogen end-use technologies, such as fuel cells and combustion engines, require the fuel to be preheated to prevent cold starts. Therefore, in addition to additional useful work output through the reutilisation of the waste thermal and cryogenic energy, the cryogenic enhanced ORC's operational parameters would provide flexibility to downstream system applications, achieving holistic system integration.

3. The individual component exergy destruction rates were directly dependant on the working fluid mass flow rates and evaporation temperatures. The pump exhibited the lowest overall exergy destruction, while the condenser presented with the highest exergy destruction. This is because there was no heat exchange occurring in the pump, and all the exergy destruction was attributed to the increase in pump power consumption and

environmental heat losses. The implications of the large temperature difference between the cryogenic cooling medium and the ORC working fluid, pressure drop, due to simultaneous phase-change of the heat transfer fluids, and heat loss to the environment resulted in the condenser exhibiting the highest exergy destruction rates and occupying the bulk proportion of the total system exergy destruction.

4. The dynamic numerical model was validation through the experimental analysis, using the transient region. The results proved that the dynamic numerical model was valid, with the KPIs presenting within a maximum error range of 4.49 %. In terms of the exergy destruction validation, the evaporator and the pump exhibited slightly higher variations, which were attributed to insufficient insulation and environmental heat losses. The overall system exergy destruction rates were within a maximum error range of 3.93 %. Small errors were expected because of the changing environmental conditions during the experimental analysis.

5. A comparative analysis was conducted between this experimental study utilising low flammability hydrofluorocarbon working fluids and the study conducted by Tian et al. [105] using propane. The variations in performance between this experimental study and Ref. [105] were due to the high condensation pressure and temperatures and high-pressure liquid nitrogen utilised in Tian et al.'s [105] study, leading to a lot of the high-quality cryogenic energy being unutilised. Additionally, hydrocarbons present with lower molar masses than low flammability hydrofluorocarbons, which results in a slight performance enhancement for the hydrocarbon working fluids. The results indicated that low flammability hydrofluorocarbons can compete with traditional hydrocarbon working fluids for cryogenic enhanced ORC but require extensive operational parameter search for objective function optimisation.

Table 5.6: Summary of best system performance for cryogenic-enhanced ORC experiment

Parameter	Value
Net-Work Output	501.44 W
Thermal Efficiency	7.29 %
Cryogenic Energy Efficiency	7.67 %
Cryogenic Exergy Efficiency	8.38 %

The isentropic efficiencies of the expander and the pump, along with the pressure ratio, are presented in Figure 5.14. In the case of the pump, relatively little change is seen in the isentropic efficiency. In the case of the expander, the isentropic efficiency is low for 15 °C, which was expected as the net-work output and the pressure ratio was low. The expander efficiency hovered between 60 – 85 %. The pressure ratio also remained relatively unaffected, between 3 – 4. Hence, constant values for the pump and expander isentropic efficiencies of 80 % were applied to the dynamic numerical model, presented in Chapter 4. Table 5.7 presents the detailed operational parameters at 70 °C and 16 g/s at each state of the cycle.

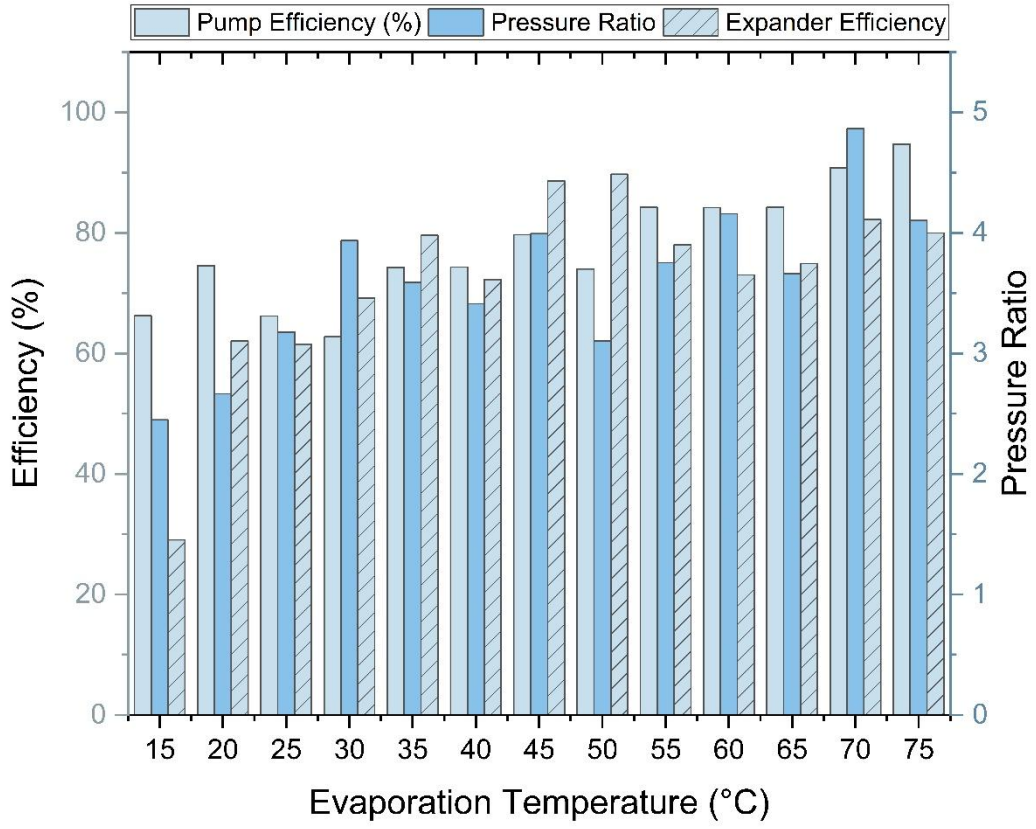

Figure 5.14: Pump efficiency, expander efficiency, and pressure ratio of the experimental rig.

Table 5.7: State points at 70 °C evaporation temperature and 16 g/s working fluid mass flow rate.

Parameter	Range	Source
Working fluid	R410A	Set
Water temperature	70 °C	Set

Pump rotational speed	1200 rpm	Set
Water flow rate	13 lpm	Set
Liquid nitrogen flow rate	28 g/s	Set
T1	-98 °C	Tested
T2	-93 °C	Tested
T3	70.4 °C	Tested
T4	28 °C	Tested
T5	-98 °C	Tested
$T1_{LN2}$	-181 °C	Tested
$T2_{LN2}$	5 °C	Tested
$T1_{Water}$	84 °C	Tested
$T2_{Water}$	76 °C	Tested
P1	2.28 bar	Tested
P2	7.04 bar	Tested
P3	6.7 bar	Tested
P4	2.39 bar	Tested
P5	2.15 bar	Tested
$P1_{LN2}$	3.7 bar	Tested
$P2_{LN2}$	1.71 bar	Tested
$P1_{Water}$	1.39 bar	Tested
$P2_{Water}$	1.32 bar	Tested
$\dot{m}_{W.F}$	16.11 g/s	Tested
$\dot{m}_{W.F,\ LN2}$	28 g/s	Tested
$\dot{m}_{W.F,\ Water}$	0.21 g/s	Tested

The dynamic experiment results are depicted in Figure 5.15.

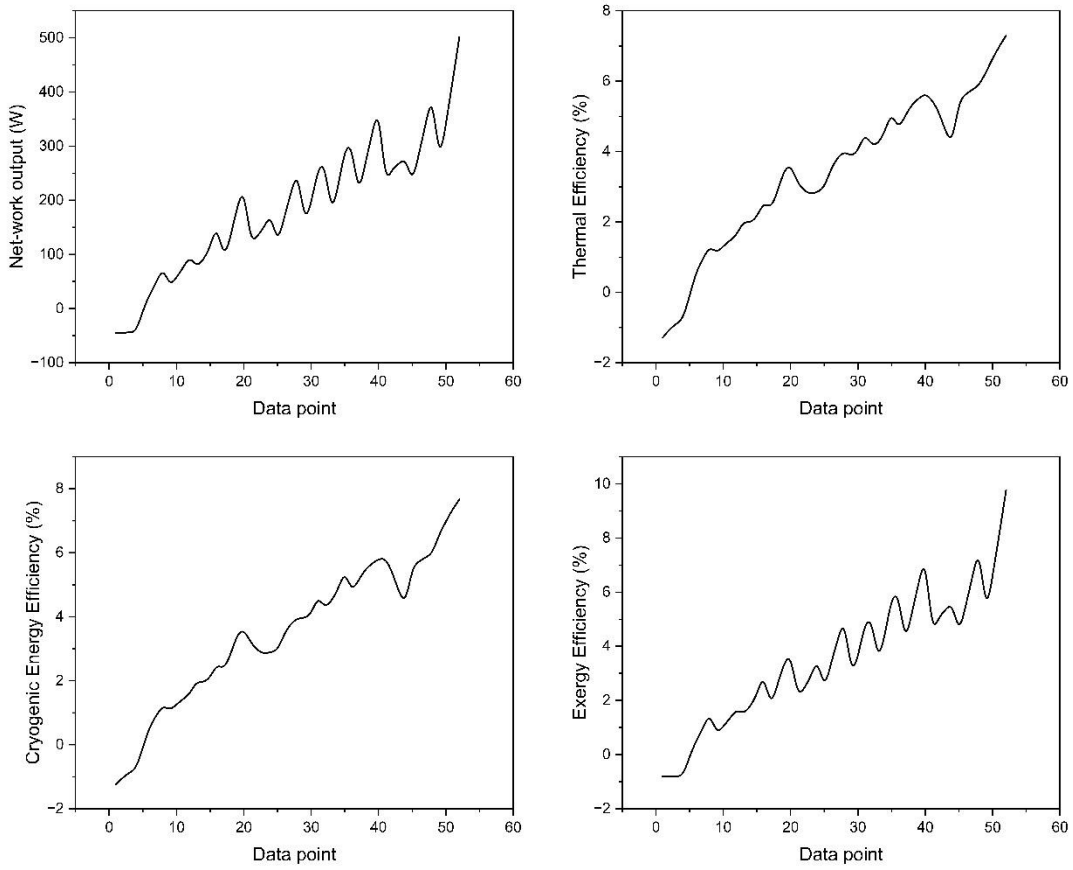

Figure 5.15: Dynamic experiment results.

Chapter 6. Dynamic Numerical Model Analysis

6.1 Introduction

In this chapter, multi-parameter sensitivity analysis was carried out using the advanced dynamic numerical model developed in *Chapter 4: Dynamic Numerical Model*. Firstly, the evaporation temperature sensitivity analysis was conducted, and the effect on system key performance indicators and individual component exergy destruction was gauged. Correlations were determined based on the results as a function of the thermophysical properties of each individual low flammability hydrofluorocarbon working fluid. Secondly, based on the gaps identified in Chapter 2 and presented in Figure 1.4, for the first time for cryogenic enhanced Organic Rankine Cycles, a system charge sensitivity analysis was conducted to determine the effect on energy and exergy performance metrics and identification of failure modes was elucidated through under- or over-charging of the closed-loop cryogenic enhanced ORC system. Lastly, a preliminary scale-up model of the cryogenic enhanced ORC was pitted against a marine auxiliary diesel engine to determine environmental feasibility based on current regulations and recommendations put forward by the International Maritime Organisation. It was revealed that low flammability hydrofluorocarbons are feasible alternatives to hydrocarbon working fluids for cryogenic enhanced ORCs, especially in critical limited space applications, but comprehensive multi-parameter studies encompassing the effects on system performance and environment are required. The results and analysis presented in this chapter have been conducted based on the steady-state results from the numerical modelling. The following KPIs were evaluated in this chapter: Net-Work Output, Thermal Efficiency, Cryogenic Energy Efficiency, and Cryogenic Exergy Efficiency. The KPIs were evaluated against varying evaporation temperature and system charge. A component exergy analysis was also conducted.

The results presented in this chapter have been published in the Elsevier journal *"Energy"* under the title *"Cryogenic energy assisted power generation utilizing low flammability refrigerants" [99]*. The digital identifier is https://doi.org/10.1016/j.energy.2024.132770.

6.2 Transient system response

The transient system response is illustrated in Figure 6.1. It was observed that the system required between 1500 seconds and 2000 seconds to stabilise. Initially, the net-work output was negative, due to the pump driving the expander to produce power. Consequently, all key performance indicators exhibited negative values. Eventually, the heat transfer between the working fluids and the heating medium increased the energy and exergy content of the working fluids, which resulted in increasing expander output. The fluctuations exhibited by the system during initialisation resulted from the working fluid being charged at high-pressure (to mimic atmospheric temperature conditions), and subsequently undergoing rapid evaporation and condensation in the evaporator and condenser, respectively. Hence, the working fluid had to undergo a few cycles in the system before achieving steady state. This meant that the temperature at the pump inlet and outlet initially started at atmospheric temperature conditions (20 °C) at a pressure of 14.5 bars. To achieve cryogenic conditions, the working fluid required multiple cycles of condensation through the liquid nitrogen, which resulted in the fluctuations in pressures and temperatures in the liquid receiver. Consequently, the key performance indicators all fluctuated until the cycle achieved steady state through sustained condensation. The dynamic cycle conditions enabled the system charge to be correctly predicted and allowed a timeframe on when steady state operation may be expected. Additionally, it helped evaluate the cryogenic exergy (and the time), during the experimental analysis, required before the pump could be started, hence preventing high-pressure operation and pump cavitation. Therefore, it was observed that liquid nitrogen flow through the condenser should be started prior to pump operation to allow for cryogenic conditions through rapid condensation and subsequent liquid receiver pressure reduction.

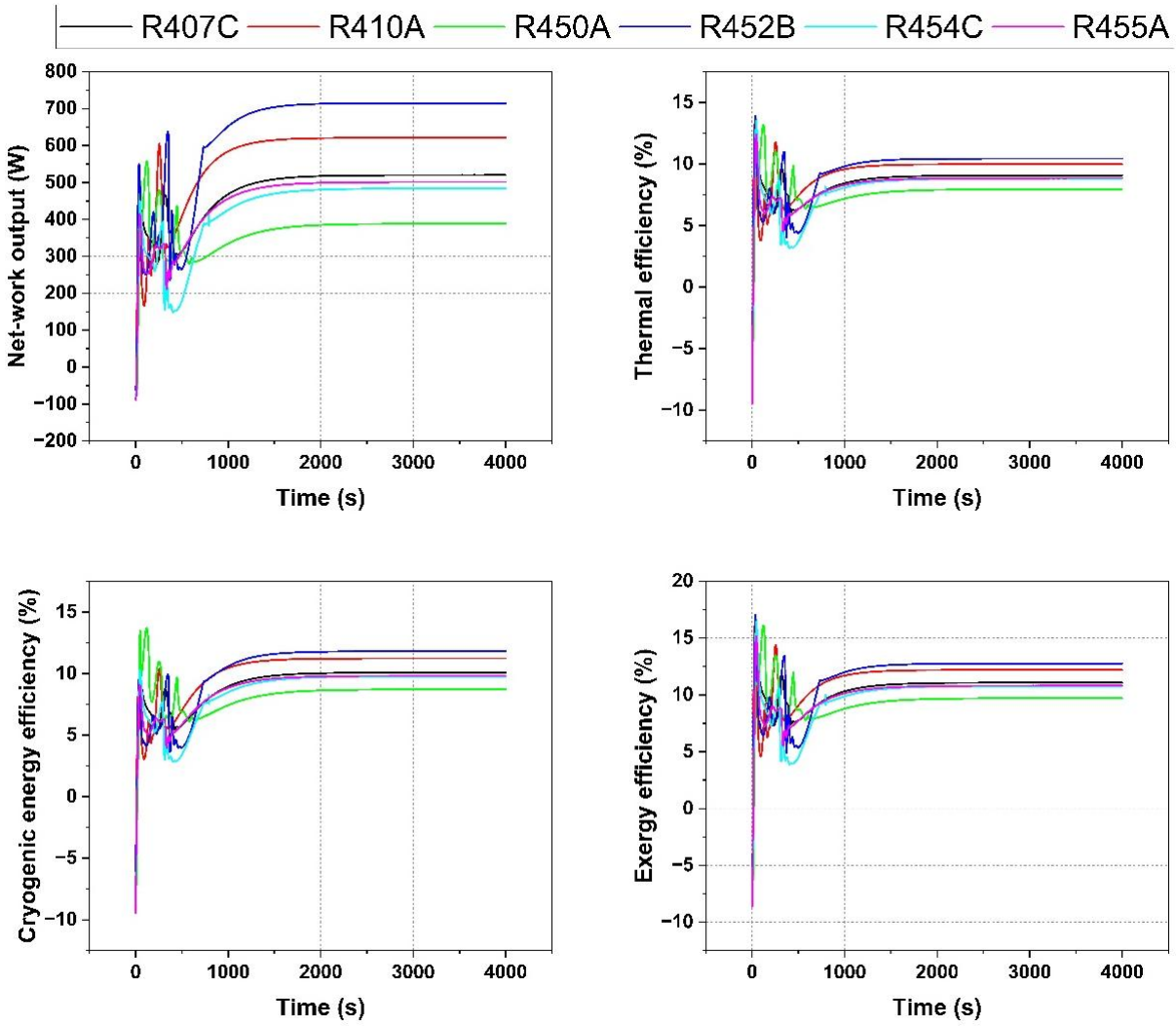

Figure 6.1: Dynamic KPI response of the low-flammability cryogenic enhanced ORC

6.3. Parametric optimisation

A comprehensive parametric study was conducted to determine the influence of the evaporation temperature and system charge variation on the key performance indicators, defined in *Chapter 4: Dynamic Numerical Model*, and the individual component exergy destruction. Initially, the evaporation temperature was varied between 70 °C to 110 °C for all working fluids. To understand if the performance trends upheld at the higher limits of the low-grade waste heat temperature range (up to 200 °C [197] [198]), a further analysis was conducted using R410A as the working fluid. The system charge was varied from +30 % to -30 % of the system charge determined in *Section 4.3.6* of *Chapter 4: Dynamic*

Numerical Model. The T-s diagrams of the working fluids are illustrated in Figure 6.2, and the thermophysical properties are tabulated in Table 6.1 (Also presented in Table 4.4 in Chapter 4). In the T-s diagram, the highest temperature in the cycle, at point 3, corresponded to the evaporation temperature of 110 °C. All the tested working fluids were wet fluids, based on the negative slope of the T-s diagram [199]. From the cycle diagram, it was clear that the degree of superheat for some working fluids, such as R410A and R452B was higher than the rest, which resulted in a better system performance. For some working fluids, such as R450A and R454C, the slope was very steep, which resulted in the expansion process closely following the saturation curve, inhibiting expansion efficiency and power generation. The parametric study involves the KPIs defined in Equations 4.56 – 4.59 in Section 4.5.3.

Table 6.1: Properties of working fluid selected for the numerical model [173] [43]**:**

Working fluid	GWP	ASHRE A Safety group	Boiling point at 1atm (°C)	Critical temperature (°C)	Molar mass (g/mol)	Liquid density at 25 °C (kg/m^3)	Composition	Mixture Ratio (by weight)
R407C	1774	A1	-43.63	86.19	86.2	1134	R32/R125/R134a	0.23/0.25/0.52
R410a	2088	A1	-51.44	71.34	72.59	1062	R32/R125	0.50/0.50
R450A	605	A1	-23.36	104.5	108.7	1177.3	R134a/R1234ze	0.42/0.58
R452B	698	A2L	-50.67	77.1	63.53	993.5	R125/R1234y/ R32	0.7/0.26/0.67
R454C	148	A2L	-45.56	85.67	90.78	1042.4	R32/R1234yf	0.215/0.785
R455a	148	A2L	-52.02	85.61	87.45	1033.4	R1234yf/R32/ CO2	0.755/0.215/0.03

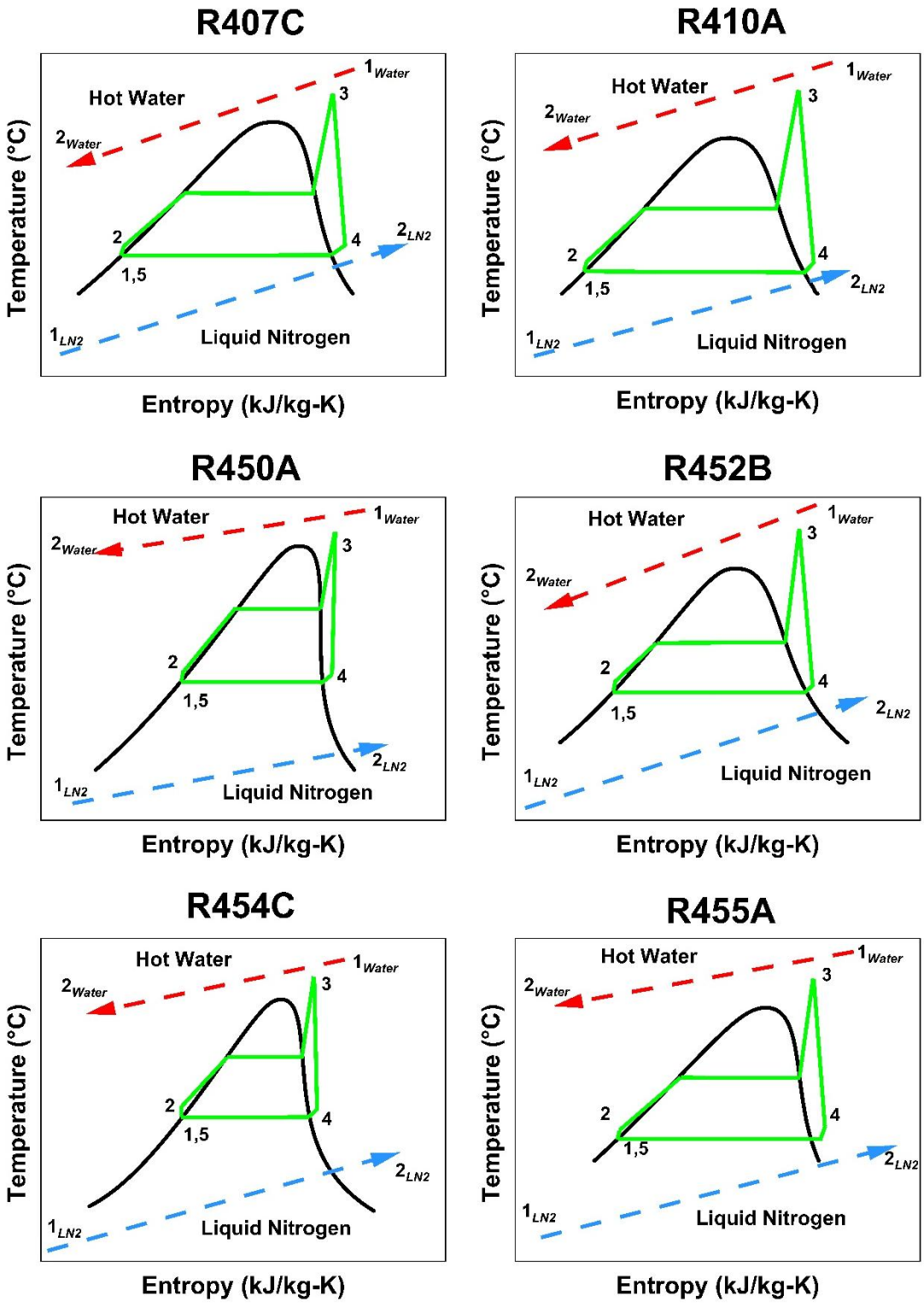

Figure 6.2: T-s diagrams of the low flammability working fluids for cryogenic ORC. Here, point 3 corresponds to the evaporation temperature of 110 °C (control variable) for all working fluids. Point 1 and point 5 correspond to the boiling temperature at the pump inlet near atmospheric pressure conditions, different for each working fluid (floating variable). The control strategy employed in the cooling loop (as

described in Section 4.4.3 in Chapter 4) ensured that the working fluid did not go below the atmospheric pressure by adjusting the liquid nitrogen flow rate.

6.3.1 Evaporation temperature

Figure 6.3 illustrates the effect of the evaporation temperature, as the objective parameter, sensitivity analysis on the key performance indicators. All four key performance indicators, namely the net-work output, thermal efficiency, cryogenic efficiency, and exergy efficiency linearly increase with an increase in the heat source temperature. This system performance enhancement can be attributed to the higher rate of heat absorption by the working fluids as a result of increasing evaporation temperatures and increasing degrees of superheat, subsequently resulting in higher net-work output from the expander due to an increase in working fluid enthalpy difference across the evaporator.

The numerical results of the evaporation temperature sensitivity analysis have been tabulated in Table 6.2. The worst performing hydrofluorocarbon working fluid was R450A, exhibiting a net-work output of 329.37 W at 70 °C and 388.25 W at 110 °C. The highest system performance was exhibited by R452B, which demonstrated a net-work output of 603.29 W at 70 °C and 714.73 W at 110 °C. A deep-dive into the thermophysical properties of the working fluids, tabulated in Table 4.4 in Chapter 4 and Table 6.1, revealed the influence of individual fluid properties on the system performance. The key performance indicators of each working fluid exhibited inverse functionality with the molar mass of the fluid, such that a higher molar mass led to a decreased system performance. This inverse functionality of the molar mass with system performance can be attributed to the controlled volume of the cryogenic enhanced ORC system. Closed ORC systems have a fixed volume and hence may only contain a specific amount of working fluid charge, depending on the working fluid density. This led to a lower number of moles on a mass-basis for working fluids with a higher molar mass, subsequently affecting the working fluid capacity for endothermic heat absorption from the heat source, which directly affected the system performance due to lower volumetric and thermal expansion ratios. For example, R407C, R410A, R450A, R452B, R454C, and R455A have a

molar mass of 86.2 g/mol, 72.59 g/mol, 108.7 g/mol, 63.53 g/mol, 90.78 g/mol, 87.45 g/mol, respectively. This translates to 0.0116 mol/g, 0.0138 mol/g, 0.0092 mol/g, 0.0157 mol/g, 0.011 mol/g, and 0.0114 mol/g, respectively. Figure 6.3 clearly demonstrates the direct correlation between the number of moles on a mass-basis and the system performance. Hence, R452B, having the highest number of moles and lowest molar mass, exhibited the best system performance, and R450A, having the lowest number of moles and highest molar mass, exhibited the worst system performance.

The rate of increase in system performance for each individual working fluid, as the evaporation temperature increased, is illustrated in Figure 6.3. For some working fluids, the gradient of the graph increased sharply, while others demonstrated stagnated growth. Specifically for the energy efficiencies, namely the thermal efficiency and the cryogenic efficiency, the rate of performance increase with increasing evaporation temperature for each individual working fluid can be attributed to the critical temperatures of the working fluids, tabulated in Table 6.1. For the thermal efficiency and the cryogenic energy efficiency, the steepest gradient was demonstrated by R452B, followed by R410A, R407, R455A, and R454C, with R450A exhibiting the shallowest growth in both thermal and cryogenic energy efficiency. Close examination of the critical temperatures of each working fluid exhibited the same pattern, except for R410A and R452B, such that the lowest critical temperature working fluid had the steepest rise in energy efficiency performances. This inverse relation between the critical temperature and the rise in energy efficiency performance, with increasing evaporation temperature, of each working fluid can be attributed to the difference between the critical and evaporation temperatures. For example, at the evaporation temperature of 70 °C for R452B, the thermal and cryogenic efficiencies were 9.72 % and 10.9 %, respectively, with the critical temperature being 77.1 °C, translating to a difference of -7.1 °C. When the evaporation temperature increased to 110 °C, the thermal and cryogenic efficiencies increased to 10.44 % and 11.81 %, respectively, exhibiting an increase of 7.36 % and 8.32 %, respectively, while the difference between the critical and evaporation temperatures increased to 32.9 °C. Alternatively, for R450A, at the evaporation temperature of 70 °C, the critical and evaporation temperature difference was -34.5 °C, increasing to 5.5 °C at the evaporation temperature of 110 °C. Hence, a small rise of 1.81 % and 2.15 % was

seen in the thermal and cryogenic efficiency, respectively. Hence, a higher positive difference between the evaporation temperature and the critical temperature leads to a better thermal and cryogenic energy performance. In terms of the cryogenic energy performance, benchmarks can be obtained from the studies presented in Table 2.2, and Section 5.8.

In terms of R410A and R452B, a steeper rise was observed for R452B, although R410A has a lower critical temperature. R452B has an 8 % higher critical temperature than R410A, yet it exhibits a steeper performance gradient with increasing evaporation temperatures, due to having a 15 % lower molar mass. This revealed that overdependence on one thermophysical property cannot be relied on for system performance analysis, and a holistic approach across multiple thermophysical properties is necessary during system performance correlation analysis. Interestingly, the exergy efficiency increased with the rise in evaporation temperatures, indicating that the increase in the system net-work output was greater than the total exergy destruction of the condenser. However, for exergy efficiency analysis, it is imperative to conduct a comprehensive individual component exergy destruction analysis to determine the exergy correlations.

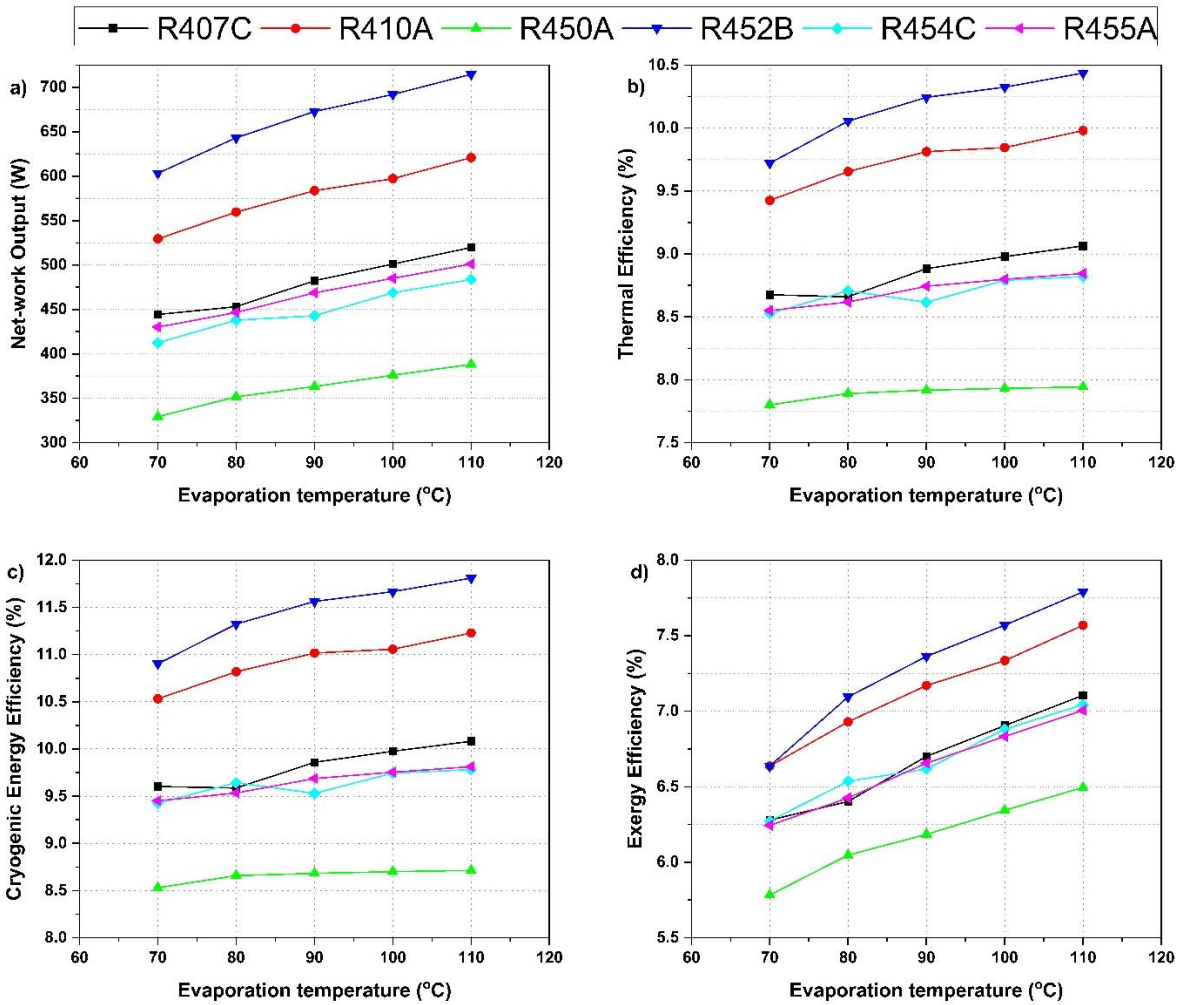

Figure 6.3: Evaporation temperature sensitivity analysis effect on key performance indicators: a) net-work output; b) thermal efficiency; c) cryogenic energy efficiency; d) exergy efficiency. The mass flow rate is 16 g/s and the condensing temperature ranges between -90 to -98 °C.

Table 6.2: Tabulation of evaporation temperature sensitivity effect on key performance indicators. The percent change is the increase in performance from 70 to 110 °C.

	Evaporation temperature (°C)					
Fluid	**70**	**80**	**90**	**100**	**110**	**Percent change (%)**
	Net-work output (W)					
R407C	444.38	453.15	482.43	501.18	519.75	16.96
R410A	529.40	559.61	583.73	597.19	620.93	17.29
R450A	329.37	351.70	363.30	375.99	388.25	17.87

R452B	603.29	643.32	672.76	691.99	714.73	18.47
R454C	412.53	437.98	443.04	468.87	483.77	17.26
R455A	430.24	446.67	468.70	485.05	501.11	16.47
Thermal Efficiency (%)						
R407C	8.68	8.66	8.88	8.98	9.06	4.47
R410A	9.43	9.65	9.81	9.84	9.98	5.89
R450A	7.80	7.89	7.92	7.93	7.94	1.81
R452B	9.72	10.06	10.24	10.33	10.44	7.36
R454C	8.53	8.71	8.62	8.79	8.82	3.43
R455A	8.55	8.62	8.74	8.80	8.84	3.43
Cryogenic energy efficiency (%)						
R407C	9.60	9.59	9.86	9.98	10.08	4.98
R410A	10.53	10.82	11.02	11.06	11.23	6.62
R450A	8.53	8.66	8.68	8.70	8.71	2.15
R452B	10.90	11.32	11.56	11.67	11.81	8.32
R454C	9.42	9.64	9.53	9.74	9.78	3.77
R455A	9.45	9.53	9.69	9.75	9.81	3.80
Exergy efficiency (%)						
R407C	6.28	6.40	6.70	6.91	7.11	13.16
R410A	6.64	6.93	7.17	7.34	7.57	14.05
R450A	5.78	6.05	6.18	6.34	6.50	12.32
R452B	6.64	7.09	7.36	7.57	7.79	17.37
R454C	6.27	6.54	6.62	6.88	7.04	12.28
R455A	6.24	6.43	6.66	6.83	7.01	12.17

Figure 6.4 illustrates the exergy destruction of the individual main components of the cryogenic enhanced ORC system, namely the pump, evaporator, expander, and condenser. The exergy destruction rates for the pump and the expander remained relatively unchanged, and the reason can be ascertained from the selection and modelling of these devices, described in *Chapter 3: Methodology* and *Chapter 4: Dynamic Numerical Model*. The rotary vane pump and the scroll expander are fixed

volumetric devices and hence were uninfluenced by the temperature difference arising from the increase in evaporation temperatures. For exergy destruction to increase, based on Equation 4.48, the enthalpy and entropy difference entering and exiting the component should increase. In terms of the pump, the inlet temperature was based on the working fluid boiling temperature, which remained relatively constant, based on the condensation pressure limit of $1.01325\ barA \leq P_{cond} \leq 1.02\ barA$, irrespective of the evaporation temperature. In terms of the expander, which has a fixed volumetric ratio, the temperature difference between the inlet and outlet of the expander remained relatively unchanged, regardless of the evaporation temperature. The slight increase in the exergy destruction rates of the pump and expander can be attributed to the slightly varying condensation pressures, due to the dynamic nature of the numerical model.

The highest rate of increase in the exergy destruction rates, with increasing evaporation temperatures, was observed in the evaporator. From Figure 4.3, Chapter 4, it was seen that the condensation temperatures were relatively unaffected by the evaporation temperatures. Hence, the working fluid temperature at the evaporator inlet remained similar to the boiling points of the working fluids, albeit at a higher pressure, resulting in sub-cooled fluid entering the evaporator. Therefore, the increase in evaporation temperatures led to an increase in the degree of superheat of the working fluids, which caused the increase in the exergy destruction rates in the evaporator. The condenser exhibited the highest exergy destruction out of all the individual components, due to the highest temperature difference between the heat exchange fluids. The expander outlet temperature is directly dependent on the evaporation temperature and linearly increased with the increase in evaporation temperatures. Hence, the exergy destruction in the condenser also linearly increased with the increase in evaporation temperatures, although the rate of increase was not to the extent as that in the evaporator, since the expander utilised most of the thermal and mechanical exergy of the working fluid. Additionally, both the cooling fluid and the working fluid underwent phase change in the condenser, the liquid nitrogen changed phase from liquid to vapor and the working fluid changed phase from vapor to liquid, whereas in the evaporator only the working fluid changed phase from liquid to vapor. This was one of the main reasons for the high exergy destruction observed in the condenser. In summation, the condenser's majority

proportion of the total system exergy destruction was due to the large temperature difference between the heat exchange fluids and the pressure drop across the condenser. For R452B, the exergy destruction increased from 612.29 W to 1145.62 W in the evaporator, and 7606.38 W to 7889.19 W in the condenser, and increase of 87.1 % and 3.72 %, respectively. The exergy destruction of each individual component is displayed in Figure 6.4 and tabulated in Table 6.3. From Figure 6.3, the exergy efficiency increased with increasing evaporation temperature, due to the increase in net-work output being higher than the exergy destruction rate in the condenser. For cryogenic enhanced ORCs, only the cold exergy is utilised as the exergy input to the system for the exergy efficiency evaluation [105] [176], as shown in Equation 4.59.

Figure 6.5 illustrates the effect of increasing evaporation temperatures on the exergy destruction ratios. Since the system overall exergy destruction increased with the increase in evaporation temperatures, the exergy destruction ratios decreased in all components except the evaporator, since it had the highest individual rate of exergy destruction. Hence, it can be deduced that the highest exergy destruction will always occur in the condenser, and the highest rate of exergy destruction increase will always occur in the evaporator.

Table 6.3: Tabulation of evaporation temperature sensitivity effect on exergy destruction. The percent change is the increase in performance from 70 to 110 °C

Evaporation temperature (°C)						
Fluid	**70**	**80**	**90**	**100**	**110**	**Percent change (%)**
Pump (W)						
R407C	6.00	6.07	6.21	6.30	6.38	6.35
R410A	6.96	7.10	7.21	7.28	7.38	6.12
R450A	4.97	4.85	5.17	5.24	5.32	6.86
R452B	8.09	8.06	8.20	8.29	8.40	3.78
R454C	6.25	6.40	6.46	6.58	6.66	6.60
R455A	6.49	6.60	6.72	6.81	6.90	6.28
Evaporator (W)						

R407C	484.34	584.11	705.92	812.18	915.75	89.07
R410A	658.70	791.43	914.36	1023.49	1140.27	73.11
R450A	216.38	328.24	414.13	503.05	586.20	170.91
R452B	612.29	754.58	892.92	1020.35	1145.62	87.10
R454C	491.77	602.56	692.04	799.64	893.42	81.67
R455A	555.92	660.95	772.74	874.13	972.56	74.95
Expander (W)						
R407C	321.97	318.34	329.82	333.88	337.73	4.90
R410A	396.55	406.86	413.11	410.86	416.60	5.06
R450A	232.94	239.28	240.62	242.35	244.21	4.84
R452B	468.95	482.59	489.97	488.73	491.38	4.78
R454C	293.78	303.51	297.89	307.80	309.77	5.45
R455A	307.87	310.55	316.95	319.64	322.15	4.64
Condenser						
R407C	6229.53	6270.88	6383.98	6460.60	6538.55	4.96
R410A	6782.01	6871.27	6942.58	6983.09	7057.30	4.06
R450A	5286.23	5425.78	5507.60	5591.08	5673.39	7.32
R452B	7606.38	7715.52	7789.26	7831.37	7889.19	3.72
R454C	5784.60	5901.13	5952.54	6069.50	6154.94	6.40
R455A	6001.26	6082.66	6182.70	6265.19	6349.16	5.80

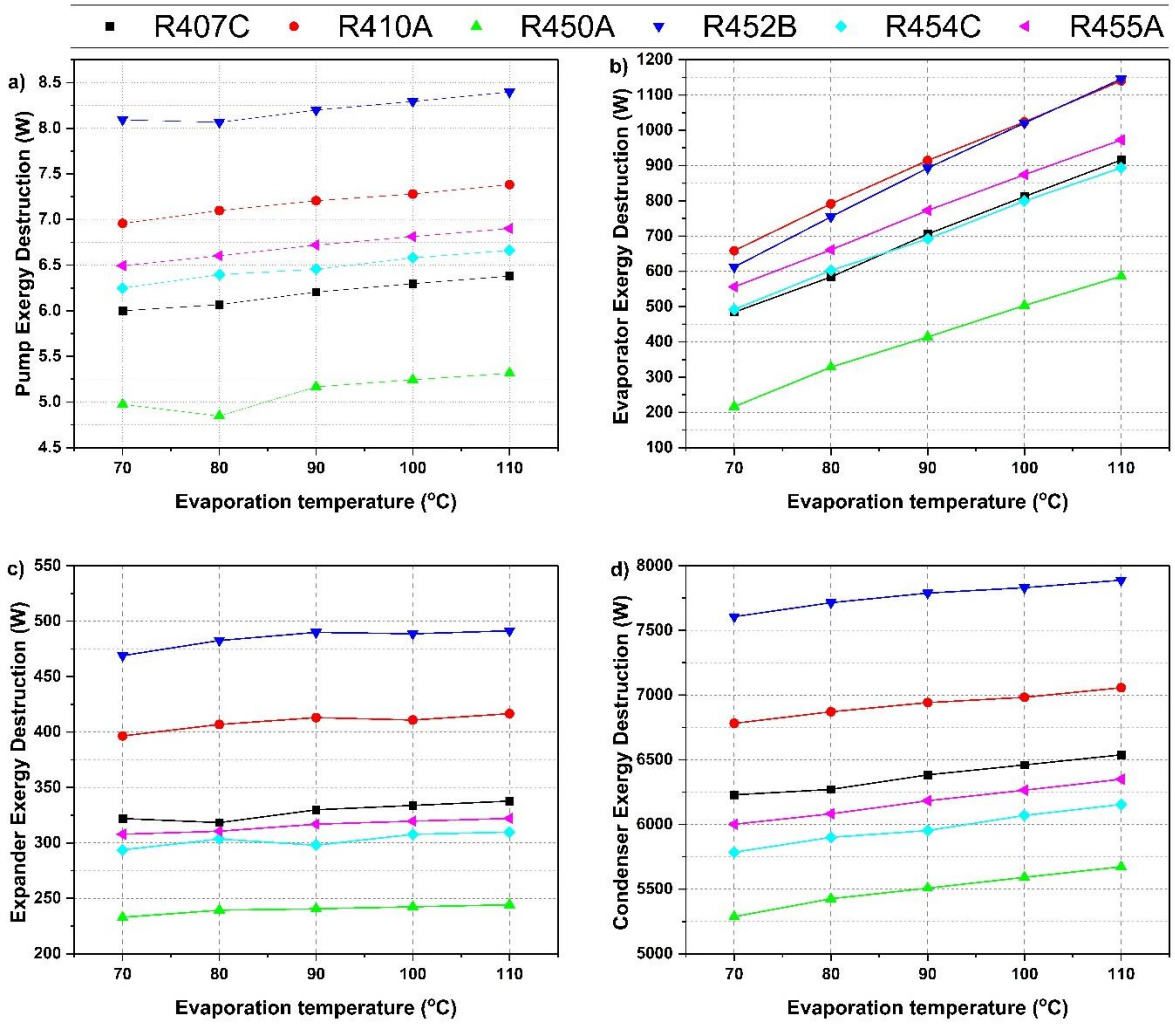

Figure 6.4: Evaporation temperature sensitivity analysis effect on exergy destruction: a) pump; b) evaporator; c) expander; d) condenser

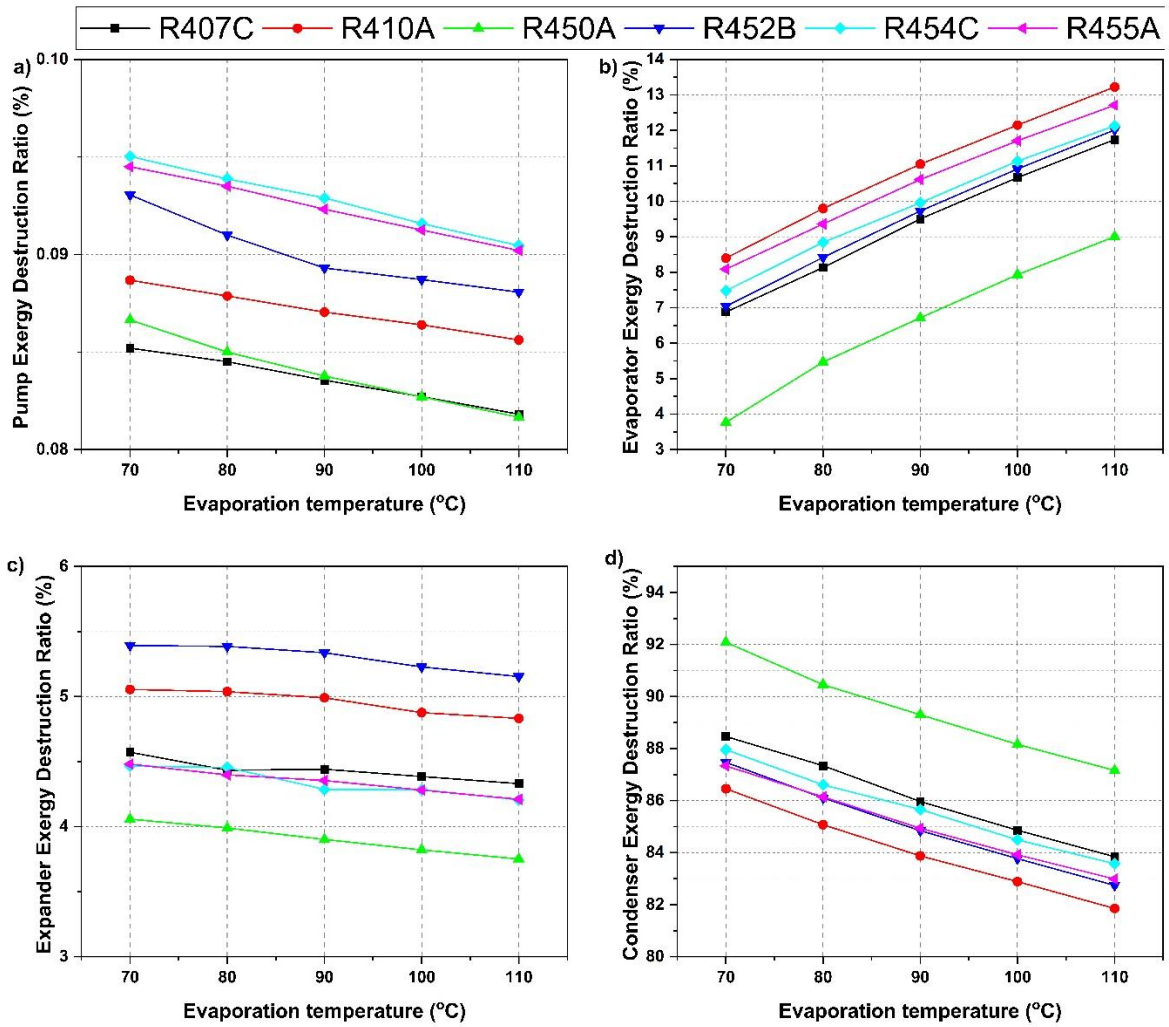

Figure 6.5: Evaporation temperature sensitivity analysis effect on exergy destruction ratios: a) pump; b) evaporator; c) expander; d) condenser

To understand if the system key performance indicators would exhibit similar trends at higher temperatures, up to 200 °C which is the upper limit of low grade waste heat [197] [198], the heat source was changed to marine engine lubrication oil. The evaporation temperature sensitivity effect on the key performance indicators, using R410A as the working fluid, is illustrated in Figure 6.6. Similar trends were observed in that the system performance increased linearly with the increase in evaporation temperatures. Thus, the novelty of low flammability cryogenic enhanced ORCs is further strengthened, as they can flexibly utilise a wide range of waste heat temperatures.

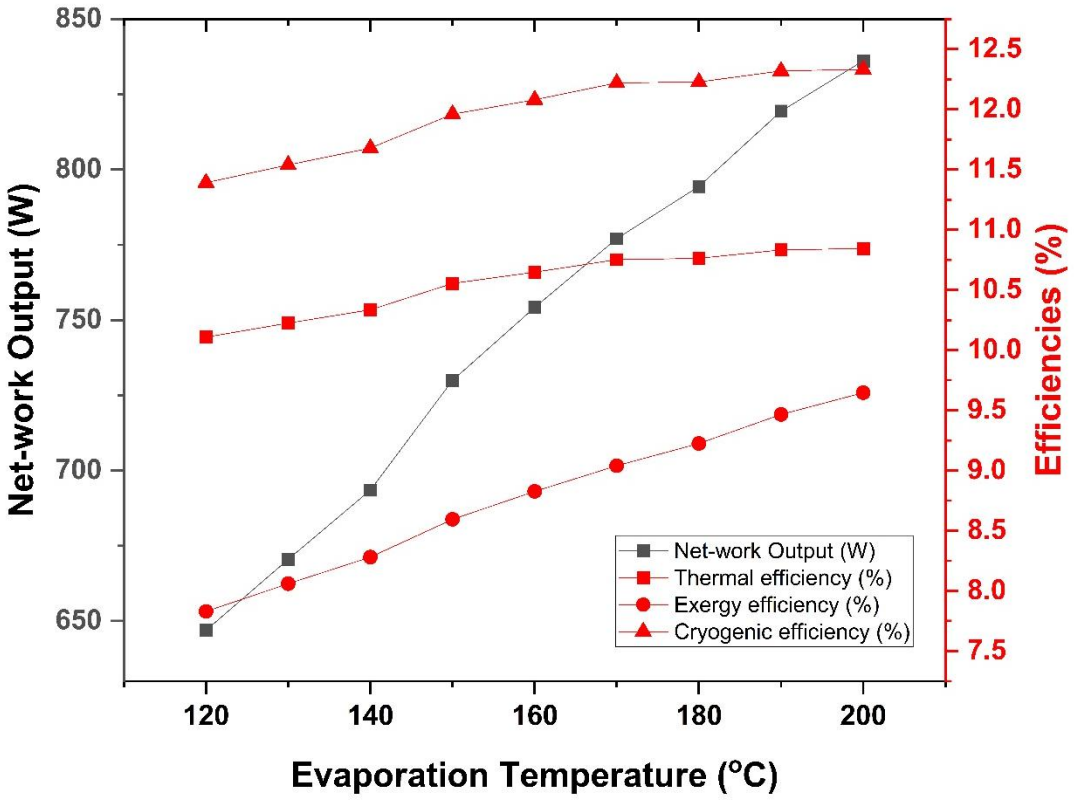

Figure 6.6: Evaporation temperature sensitivity analysis using R410A, encompassing upper limit of low-grade waste heat source

6.3.2. System charge

The extensive literature review conducted in *Chapter 2: Literature Review* revealed that none of the studies conducted on cryogenic enhanced ORC systems researched the influence of system charge on the key performance indicators [99] [105] [176] [75] [200] [201]. Since closed-loop ORC systems have a fixed volume, system charge quantity would influence the condensation pressures and temperatures, subsequently having implications for the key performance indicators. Hence, a system charge quantity analysis was conducted to observe the ramifications of under- and over-charging of a cryogenic enhanced ORC system.

Figure 6.7 illustrates the system charge quantity sensitivity effect on the key performance indicators, where the evaporation temperature was kept constant at 110 °C across all working fluids. The baseline system charge was denoted by '0' and referred to the system

charge determined during the evaporation temperature sensitivity analysis, as defined in *Section 4.3.6* of *Chapter 4: Dynamic Numerical Model*. It was observed that overcharging the system led to a drastic decrease in the key performance indicators. For some working fluids, a steep decline in system performance was noted, while others exhibited a gradual performance decline. Close observation of Table 4.4 and Table 6.1 revealed that a direct correlation could be established based on the working fluid densities. Since the ORC is a closed-loop system with a fixed volume, working fluids with high densities were seen to tolerate overcharging, up to 20 %, with slight performance reduction. On the other hand, working fluids with low densities displayed an immediate reduction in all key performance indicators, even at a slight overcharging of 10 %. Hence, low density working fluids are more sensitive to overcharging, and require robust calculations to determine the proper system charge. In terms of drastic system overcharging, all working fluids exhibited decreased system performance, and the reason can be attributed to the liquid receiver. Liquid receiver overfilling caused the condensation pressures to rise, subsequently increasing the condensation temperatures. This increased the input power to the system through the pump, which reduced the overall system net-work output. Once the liquid receiver was overfilled, since the pump inlet could only handle a specific flow based on pump displacement, the remaining liquid working fluid started to flood the condenser, effectively reducing the heat exchange area and thereby, reducing system performance. The high-density working fluids, namely R407C, R410A, and R450A, tolerated overcharging to a degree, while the low-density working fluids, namely R452B, R454C, and R450A, exhibited immediate system performance decline. Overcharging also resulted in drastically high system pressures, since the pump was a positive displacement pump, compromised the strength integrity of the system, and should be avoided at all costs. The effect of system charge variation on key performance indicators has been tabulated in Table 6.4.

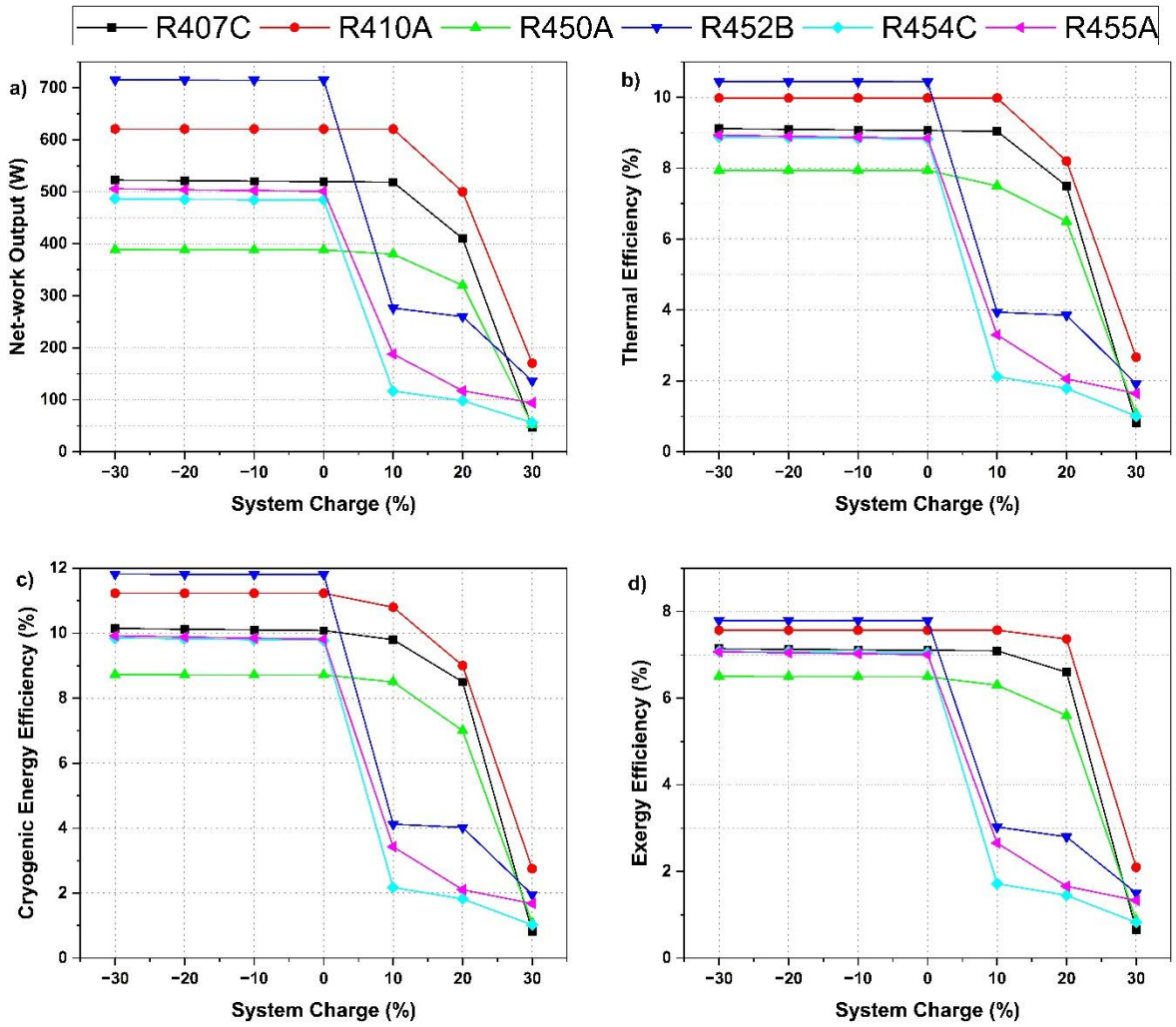

Figure 6.7: System charge sensitivity analysis effect on key performance indicators: a) net-work output; b) thermal efficiency; c) cryogenic energy efficiency; d) exergy efficiency.

Table 6.4: Effect of system charge variation on system key performance indicators

	System charge (%)							
Fluids	**-30**	**-20**	**-10**	**0**	**10**	**20**	**30**	**Baseline shift (%)**
	Net-work output (W)							
R407C	522.51	521.56	520.62	519.75	518.53	136.96	47.37	-90.89
R410A	620.97	620.96	620.94	620.93	620.88	599.19	170.35	-72.57
R450A	388.46	388.30	388.24	388.25	152.64	140.74	51.80	-86.66
R452B	715.11	714.98	714.82	714.73	276.31	270.27	136.53	-80.90

R454C	486.66	485.63	484.63	483.77	116.71	98.37	55.85	-88.46
R455A	505.73	504.11	502.55	501.11	187.87	117.26	94.13	-81.22
Thermal efficiency (%)								
R407C	9.12	9.10	9.08	9.06	9.04	2.36	0.81	-91.10
R410A	9.98	9.98	9.98	9.98	9.98	9.63	2.67	-73.27
R450A	7.95	7.94	7.94	7.94	3.15	2.90	1.07	-86.58
R452B	10.44	10.44	10.44	10.44	3.94	3.85	1.91	-81.66
R454C	8.88	8.86	8.84	8.82	2.12	1.79	1.01	-88.57
R455A	8.93	8.90	8.87	8.84	3.30	2.06	1.65	-81.38
Cryogenic energy efficiency (%)								
R407C	10.15	10.12	10.10	10.08	10.05	2.42	0.81	-91.93
R410A	11.23	11.23	11.23	11.23	11.23	10.77	2.75	-75.51
R450A	8.72	8.72	8.71	8.71	3.26	3.00	1.08	-87.62
R452B	11.82	11.82	11.81	11.81	4.12	4.02	1.96	-83.44
R454C	9.85	9.83	9.80	9.78	2.17	1.82	1.02	-89.57
R455A	9.92	9.88	9.85	9.81	3.43	2.10	1.68	-82.91
Exergy efficiency (%)								
R407C	7.14	7.13	7.12	7.11	7.09	1.89	0.66	-90.76
R410A	7.57	7.57	7.57	7.57	7.57	7.37	2.10	-72.30
R450A	6.50	6.50	6.50	6.50	2.57	2.38	0.88	-86.51
R452B	7.79	7.79	7.79	7.79	3.03	2.96	1.50	-80.72
R454C	7.09	7.07	7.06	7.04	1.72	1.45	0.82	-88.30
R455A	7.07	7.05	7.03	7.01	2.66	1.66	1.33	-80.99

Figure 6.8 illustrates the system charge sensitivity effect on the exergy performances of the system individual components. The exergy destruction in all components was observed because of overcharging, apart from the condenser. In terms of the pump, overcharging resulted in increased pressure in the liquid receiver, which in turn increased the pump inlet pressures and temperatures, hence decreasing the temperature gradient with the dead state temperature. The pump outlet temperature was also increased, and hence the temperature difference between the heat source and the working fluid

decreased, leading to decreased exergy destruction in the evaporator. With an increase in pump inlet pressure, the working fluid flow rate also increased, which resulted in a lower exergy destruction in the expander. However, for the condenser, since the overcharged liquid working fluid back propagated to the condenser and caused reduction in heat exchange area, an increased exergy destruction was observed. The exergy destruction ratios for each individual component are illustrated in Figure 6.9.

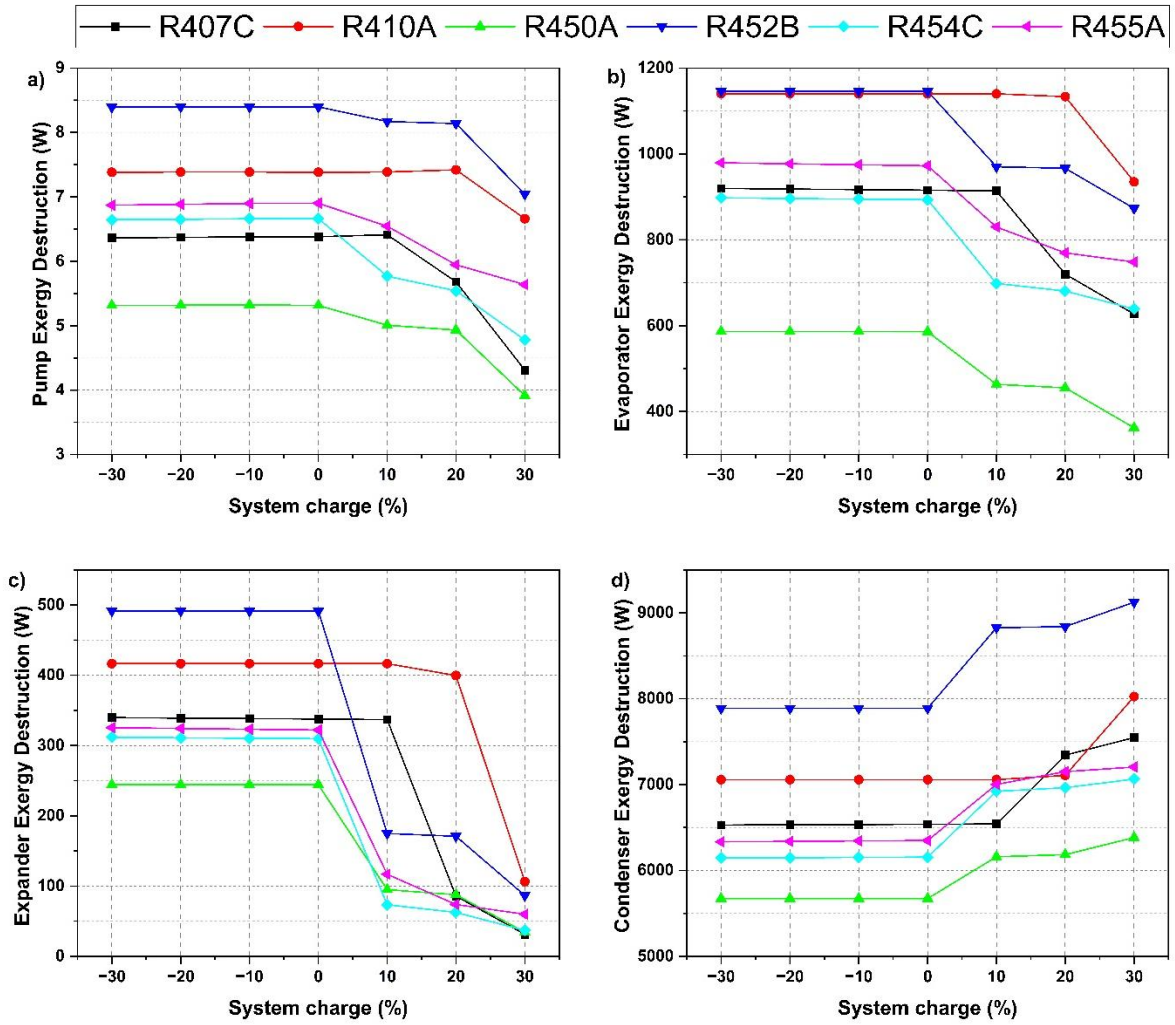

Figure 6.8: System charge quantity sensitivity analysis effect on exergy destruction: a) pump; b) evaporator; c) expander; d) condenser

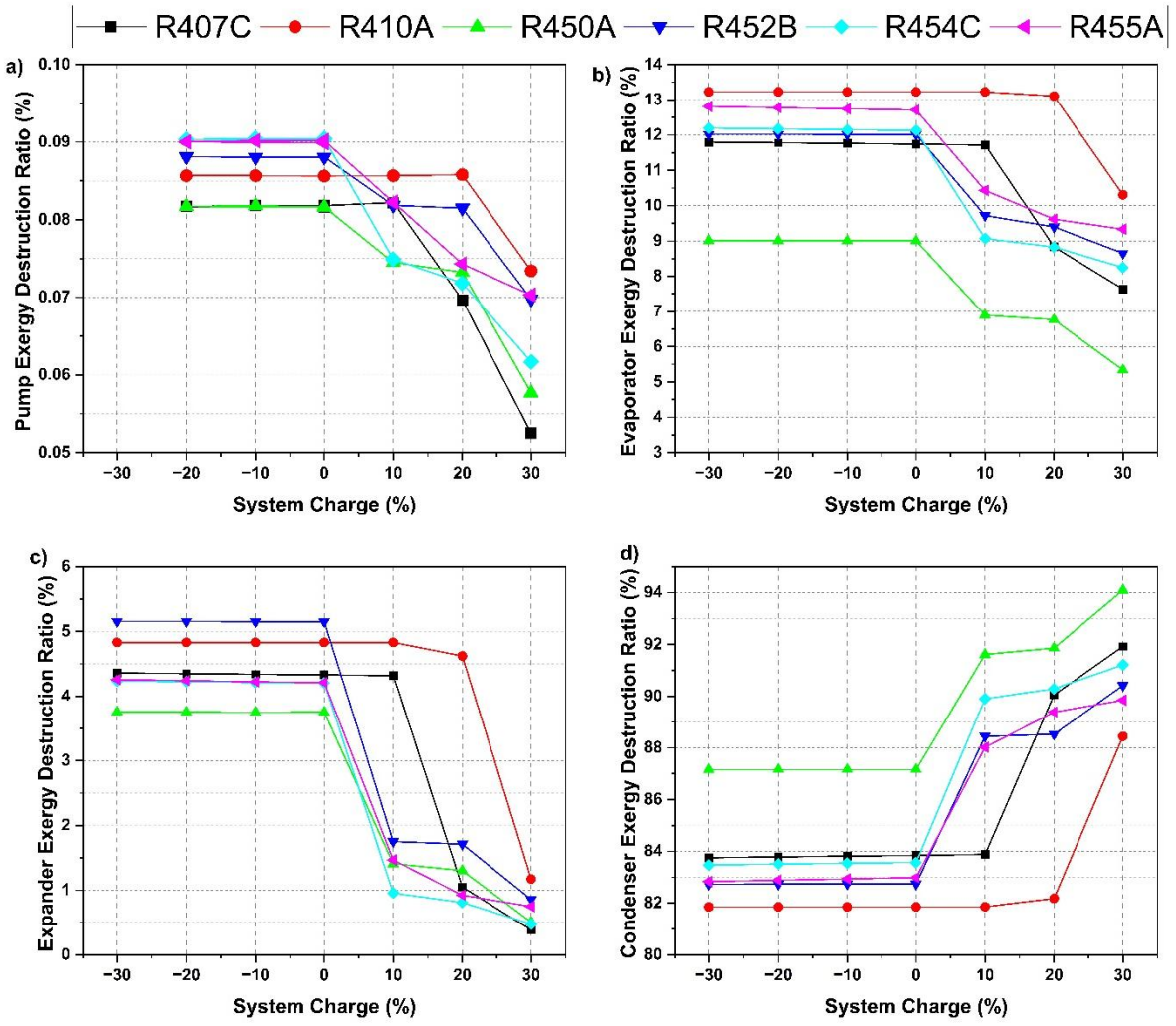

Figure 6.9: System charge quantity sensitivity analysis effect on exergy destruction ratios: a) pump; b) evaporator; c) expander; d) condenser

In terms of system undercharging, it was observed that the system performance remained unaffected up to a 30 % reduction in system charge quantity, as illustrated in Figure 6.7, Figure 6.8, and Figure 6.9. Cao et al. [202] and Dickes et al. [153] performed a system charge study on their ORC system and noted that the system performance was unaffected up to a reduction of 32.5 % in system charge quantity, using R245fa and the working fluid. However, their study focused on non-cryogenic ORCs. Hence, a system failure analysis was conducted to determine the charge quantity at which each individual working fluid system would suffer mass insufficiency, as illustrated in Figure 6.10.

It was observed that the working fluids with higher densities, such as R407C, R410A, and R450A, failed at a lower Mass-to-Volume Ratio (MVR), compared to their low-density counterparts. The working fluids utilised in this study were all cryogenic low boiling

temperature fluids, and hence would form a vapour-liquid mixture in the liquid receiver. The liquid receiver was designed such that the outlet would be lower than the vapour-liquid level, so that the pump would always have a liquid supply, as described in *Chapter 4: Dynamic Numerical Model*. Continuously decreasing the system charge reduced the liquid level in the liquid receiver, and at a specific point, pump cavitation would occur as vapor starts to enter the pump. Further reduction in working fluid charge would result in dry running of the pump, which would severely damage the pump and lead to catastrophic system failure. Therefore, higher density working fluids failed quicker than lower density working fluids, as they required less system charge. For example, R407C failed after 105 seconds, having a density of 1134 kg/m^3, while R452B failed after 115 seconds, having a density of 993.5 kg/m^3. The most important takeaway from the system charge sensitivity analysis is that correct system charge determination is an important aspect of cryogenic enhanced ORC design, and under- or over-charging could lead to catastrophic failure or severely diminished system performance.

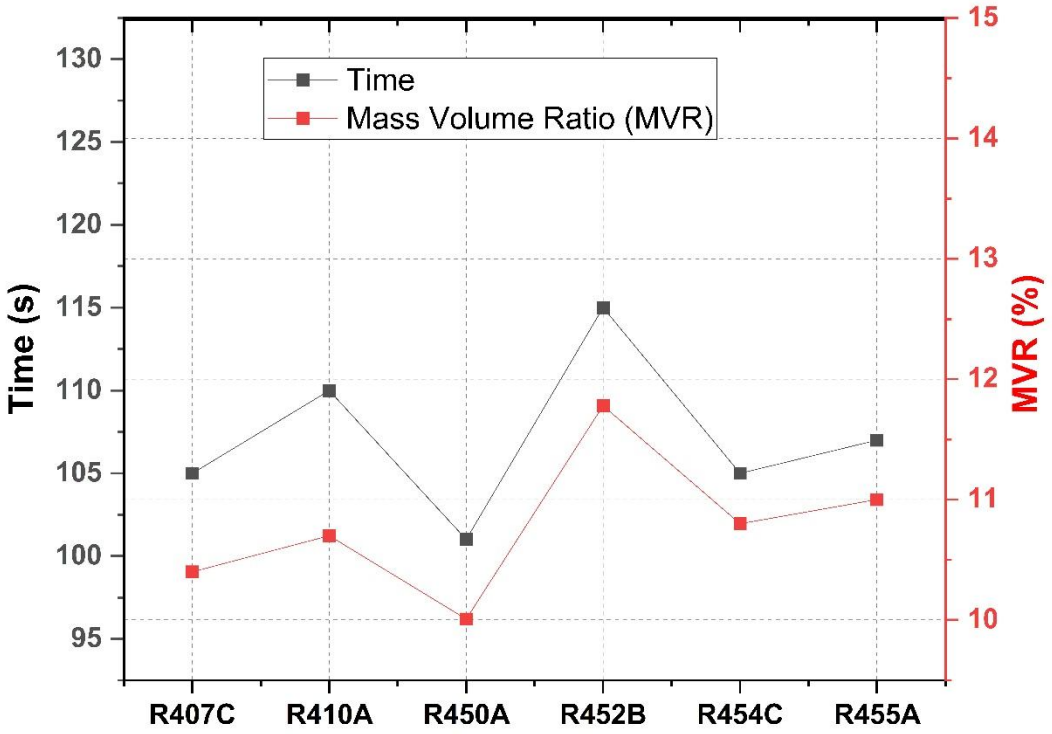

Figure 6.10: Critical system failure due to undercharging

6.4. GHG emission reduction potential

Hydrocarbons as working fluids for cryogenic enhanced ORCs are primarily preferred due to their low Global Warming Potential (GWP). However, their flammability risk cannot be overlooked, and hence low flammability hydrofluorocarbon working fluids are suggested in this study. Since hydrofluorocarbons are generally emission intensive, it was equally imperative to understand their GHG impact. In this section, the micro-scale ORC was scaled-up as a replacement for a marine auxiliary engine powertrain, with a power rating of 1.2 MW. The ship and route details can be found in the author's published paper [15], as well as the baseline emissions from the marine diesel auxiliary engine. Equation 6.1 was used to calculate the environmental impact of the cryogenic enhanced ORC:

$$GHG = M_{wf} \times \varphi_{ALR} \times GWP \times LT + M_{wf} \times \varphi_{EOL} \times GWP \quad (6.1)$$

Where, M_{wf} was the working fluid system charge quantity, φ_{ALR} was the maximum allowable annual leakage, φ_{EOL} was the end-of-life leakage rate, and LT was the ORC system lifespan.

A simple methodology was employed to scale up the micro-scale ORC to the large marine vessel ORC. The specific mass of the working fluids, on a per kW basis, was calculated, and then multiplied by 1200 kW to determine the overall system charge quantity. Based on the regulations defined in *Section 4.4 of Chapter 4: Dynamic Numerical Model*, two scenarios were selected. The first scenario considered the Lloyds Register marine classification society regulations requiring annual hydrofluorocarbon leakage rates to be kept under 3 % [165] [166]. The second scenario was based on the DNV marine classification society regulations, limiting the maximum hydrofluorocarbon leakage to 10 % annually [165] [166]. Hence, φ_{ALR} was set as 3 % for the Lloyds register scenario and 10 % for the DNV scenario in Equation 6.1. In both cases, the end-of-life leakage rate was set at 15 % [203]. The lifespan of the ORC was set to the typical lifespan of a marine diesel engine, which is 25 years [15] [204].

Figure 6.11 illustrates the environmental impact of the direct emissions, through leakage, of the low flammability hydrofluorocarbon working fluids proposed in this study. It was clear from the analysis that the annual leakage rates were defining factors in hydrofluorocarbon emission potential, and the Lloyds register scenario exhibited lower emissions than the DNV scenario, since it enforced a rigorous leak prevention target. High GWP hydrofluorocarbons have long since been considered as emission intensive, and regulations have constantly evolved limiting or banning their usage [162] [161]. However, this study clearly indicates that the refrigerants under 2100 GWP offer significant emission reduction potential over traditional marine diesel engines, if strict leak prevention protocols are employed. For example, implementation of the Lloyds register scenario could provide emission reductions of up to 96 % using R455A, while the DNV scenario would provide 87 % reductions for the same working fluid. The key to the commercialisation and implementation of cryogenic enhanced ORCs would require a global certification requirement from the IMO, similar to the sulphur and nitrogen oxide emissions [27]. The feasibility of utilising low flammability hydrofluorocarbons over hydrocarbons as working fluids for cryogenic enhanced ORCs is therefore reiterated, providing significant emission reduction potential, while also eliminating the flammability risk posed by hydrocarbons. However, a generalised criterion must be defined during the working fluid selection process, taking into account global certification and regulatory requirements, while not compromising on system performance.

Considering the aforementioned multi-parameter and multi-objective analysis, different correlations were determined based on individual thermophysical fluid properties, requiring each cryogenic enhanced ORC system utilising low flammability hydrofluorocarbons to be carefully evaluated. While extensive evaluation and system performance enhancement techniques have been employed, it was clear from the proof-of-concept analysis that low flammability hydrofluorocarbons were indeed competitive with hydrocarbon working fluids and provided a much-required aspect of safety in space-constrained applications where fire and explosion risks would prove to be catastrophic.

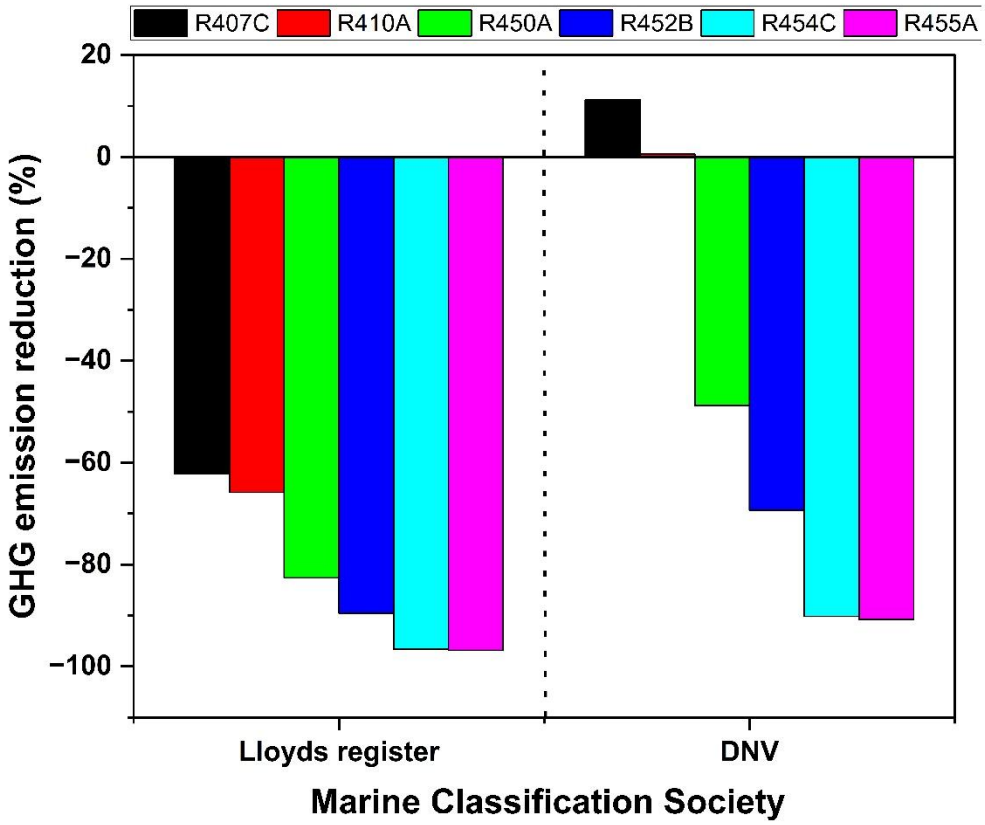

Figure 6.11: Low flammability hydrofluorocarbon direct leakage emissions

6.5 Static Model

A static model of the cryogenic-enhanced ORC was developed, using R410A as the working fluid. The static model was developed in MATLAB, connected with REFPROP, to ascertain the feasibility of a scaled up cryogenic-enhanced ORC utilising low flammability hydrofluorocarbon working fluids. The input parameters of the static model are tabulated in Table 6.5. The input parameters were modelled based on the works of Ref. [75]. The same thermodynamic modelling equations were used as described in Section 4.5. LNG (methane) was used as the cryogenic fluid. Based on the results of the simple static model, compared to the references in Table 2.2, it is feasible to suggest that the cryogenic-enhanced ORC utilising low flammability hydrofluorocarbon working fluids can be competitive with cryogenic-enhanced ORC utilising hydrocarbon working fluids. Further details on the static model can be found in the authors published works “Dual utilization of waste thermal and cryogenic energy onboard an LNG fuelled marine vessel

using ORC technology" - Proceedings of International Conference Royal Institution of Naval Architects".

Table 6.5: Input parameters for the static model

Parameter	Value
Exhaust gas flow rate	10.44 kg/s
Exhaust gas temperature	400 °C
Methane flow rate	0.875 kg/s
Methane inlet temperature	-133 °C
LNG inlet outlet	27 °C
Working fluid	R410A
Working fluid flow rate	1.133 kg/s
Evaporation temperature	300 °C
Evaporation pressure	1.1 bar
Condensation pressure	15 bar
Condensation temperature	- 51 °C
Heat exchanger effectiveness	0.8
Pump efficiency	0.8
Expander efficiency	0.8

Table 6.6: Thermodynamic state properties for the static model

State	T (°C)	P (bar)	Flow rate (kg/s)	Fluid	Enthalpy (kJ/kg)
1 (Pump Inlet)	-51	1.1	1.133	R410A	126.95
2 (Pump Outlet)	-50	15	1.133	R410A	128.82
3 (Evaporator Outlet)	300	15	1.133	R410A	732.82
4 (Expander Outlet)	150	1.1	1.133	R410A	573.4
5 (LNG Inlet)	-138	5	0.875	Methane	84.788
6 (LNG Outlet)	27	5	0.875	Methane	910.56
7 ((Exhaust Inlet)	400	1.3	10.44	LNG Exhaust	-
9 (Exhaust Outlet)	284	1.3	10.44	LNG Exhaust	-

Table 6.7 KPIs of the static model

Key Performance Indicator	Value
Net-work output	144.5 kW
Thermal efficiency	22.57 %
Cryogenic energy efficiency	32.36 %

6.6 Summary

In this chapter, a detailed multi-parameter and multi-objective feasibility analysis was conducted based on the advanced dynamic numerical model of the dual waste thermal and cryogenic energy reutilisation Organic Rankine Cycle system utilising low flammability hydrofluorocarbon working fluids, described in *Chapter 4*. The parametric analysis firstly considered the effect of variation of evaporation temperatures on the system key performance indicators, namely the net-work output, thermal efficiency, cryogenic energy efficiency, and the exergy efficiency. Individual component exergy destruction analysis was also conducted to fully realise the feasibility of low flammability hydrofluorocarbon working fluids. For the first time for cryogenic enhanced ORCs, a system charge sensitivity analysis was conducted to examine the system energy and exergy behaviours, and modes of system critical failure due to mass insufficiency were determined. Different regulatory-based environmental analysis approaches were undertaken to understand the greenhouse gas emission reduction potential of these low flammability hydrofluorocarbon working fluids when pitted against traditional diesel-fuelled marine auxiliary engines. The summary of the main conclusions of this chapter are presented below:

1. Thermophysical properties played a decisive role in defining the system performance for each individual working fluid. It was noted that the highest individual system performance at a specific evaporation temperature and rate of increase of system performance with increasing evaporation temperature exhibited an inverse correlation with the molar mass, critical temperature, and fluid density. For example, R452B had the lowest molar mass, second lowest critical temperature, and lowest density and displayed the highest system

performance. On the other hand, R450A, had the highest aforementioned thermophysical property values, and exhibited the lowest performance. Similar trends were observed for the rate of increase of key performance indicators with rising evaporation temperatures. However, over-generalisation and over-dependence on one thermophysical property to determine performance correlations proved to be disadvantageous. For example, R452B exhibited the highest performance, yet R410A had a lower critical temperature. Considering different thermophysical properties in tandem helped identify correlations for performance enhancement and reduced anomalies. It was observed that low flammability hydrofluorocarbons can viably compete with hydrocarbons, especially if safety is of paramount concern. Consideration of the key performance indicators, exergy analysis, and environmental evaluation indicated R452B as the best working fluid, providing a maximum net-work output, thermal efficiency, cryogenic energy efficiency, exergy efficiency, and GHG emission reduction of 714.73 W, 10.44 %, 11.81 %, 7.79 %, and 90 %, respectively

2. The highest system exergy destruction was always observed in the condenser, regardless of the evaporation temperatures. Even though the evaporator rate of exergy destruction was the highest with increasing evaporation temperatures, the overall exergy destruction ratios indicated the rate of increase was overall inconsequential relative to the condenser exergy destruction. Additionally, it was noticed that similar trends in energy and exergy performance were observed at higher evaporation temperatures, indicating linearity and cementing the feasibility of low flammability hydrofluorocarbons in the utilisation of a wide range of low-grade waste heat temperatures.
3. A sudden decrease in system key performance indicators was observed for low-density working fluids, while high-density working fluids exhibited slight performance detriments for slight overcharging, but ultimately reached the same low performance for severe overcharging. The reason for the rate of performance decrease dependant on density was associated to the fixed volume of the closed-loop ORC system, where high-density working fluids occupied less space and hence could withstand slight overcharging. In any case, overcharging effect on system performance was noticed to be disadvantageous, and correlated to the

increase in condensation pressures due to liquid receiver overfilling, consequently flooding the condenser with liquid working fluid, effectively reducing condenser heat exchange area and causing increased exergy destruction, while simultaneously increasing pump power consumption.

4. System performance was observed to be unaffected by undercharging up to a 30 % mass to volume ratio, whereby the vapor-liquid interface remained higher than the liquid receiver outlet port, hence ensuring constant liquid working fluid supply to the pump. Further undercharging resulted in the vapor-liquid interface falling below the outlet liquid receiver port, resulting in pump cavitation phenomena. Additional undercharging would result in critical system failure, as mass insufficiency would cause the pump to run dry. Hence, correct system charge determination, dependant on fixed volume and individual working fluid density, is an integral part of cryogenic ORC design parameters.
5. Regulation-based environmental analysis indicated the dependence on annual leak prevention allowances and protocols. Stringent leak prevention practices allowed for fluids up to GWP 2100, while laxed leak prevention regulation permitted only fluids with up to GWP 700 to be environmentally viable. Stringiest Lloyds Register regulations achieved 65 % emission reduction with the highest GWP refrigerant, R410A with GWP 2088, while laxed DNV regulations provided with a maximum of 87 % emission reduction with the most emission friendly working fluid, R455A with 148 GWP. The need for global marine standardisation regarding leakage allowances was identified.

Chapter 7. Conclusions and future work

The aim of this PhD research was to numerically and experimentally investigate the cryogenic-enhanced Organic Rankine Cycle for dual reutilisation of waste thermal energy and waste cryogenic energy through utilisation of low flammability hydrofluorocarbon working fluids as an alternative to traditional hydrocarbon working fluids onboard marine vessels. The previous chapters discussed the development of the dynamic numerical model and experimental testing rig of the cryogenic-enhanced ORC, analysing the system performance and identifying the key system operational parameters. Through the parametric optimisation, system key performance indicators were optimised from a first and second law efficiency perspective. This chapter summarises the most important conclusions derived from the current research and suggests avenues for further studies.

7.1 Conclusions

- An extensive literature review revealed that studies surrounding cryogenic energy reutilisation for power generation applications using Organic Rankine Cycles consist primarily of steady-state numerical modelling techniques. None of the studies in literature considered dynamic modelling techniques, completely disregarding the effect of system charge and initial charging conditions on the overall system performance. This exposed a lack of consideration of two-phase fluid thermophysical properties during transient operation, and an inability to correctly predict working fluid charge. Additionally, the literature review identified the lack of experimental studies regarding cryogenic-enhanced ORCs for dual reutilisation of waste thermal and cryogenic energy. Finally, all the studies conducted in literature on cryogenic-enhanced ORCs only considered highly flammable hydrocarbons as the working fluids.

- To address the gaps in knowledge detailed above, a novel dynamic numerical model of a cryogenic-enhanced ORC was developed, considering working fluid initial charging conditions, based on real-world component data obtained from manufacturers. The dynamic numerical model incorporated low flammability hydrofluorocarbons as working fluids to address the safety issue posed by flammable hydrocarbon working fluids. Finally, an experimental testing rig of the cryogenic-enhanced ORC was developed and tested with one of the identified low flammability hydrofluorocarbon working fluid. The numerical model was validated through the experiment, and the KPIs conformed to within 4.49 % error range.

- The low flammability hydrofluorocarbon working fluid selection was undertaken from a thermophysical property and regulatory standpoint. It was identified that current regulatory barriers prohibit the utilisation of hydrofluorocarbons that have a global warming potential above 2500. Marine classification societies, such as the Lloyds Register and the DNV, were found to have imposed restrictions on the maximum allowable annual leakage rates. Based on the regulations and recommendations, six low flammability hydrofluorocarbon working fluids, namely R407C, R410A, R450A, R452B, R454C, and R455A were selected as the working fluids for the numerical study. The different hydrofluorocarbon working fluids were evaluated based on the first and second law efficiencies, and system charge effect, for the first time, on the performance metrics was also studied. Thus, the marine classification regulation consideration provided useful insights into GHG emission analysis and revealed that current flammable hydrocarbon working fluid-based cryogenic-enhanced ORCs, if at-scale prototypes were available, would not be allowed onboard marine vessels due to safety concerns.

- The results of the dynamic numerical model revealed that the system performance was influenced significantly by the thermophysical properties of the working fluids. Fluids with lower molar mass, critical temperature, and density exhibited superior performance metrics compared to those with higher values. R452B, the best performing working fluid, achieved a net-work output, thermal

efficiency, cryogenic energy efficiency, and exergy efficiency of 714.73 W, 10.44 %, 11.81 %, 7.79 %, respectively, while R450A, the worst performing working fluid, exhibited system performance of 388.25 W, 7.94 %, 8.71 %, and 6.5 %, respectively. Hence, thermophysical properties should always be analysed during cryogenic-enhanced ORC working fluid selection process.

- A detailed exergy analysis revealed that individual component exergy destruction rates were influenced significantly by working fluid mass flow rate and evaporation temperature. The pump exhibited minimal exergy destruction due to negligible heat exchange, exhibiting a maximum experimental exergy destruction proportion of 1.55 % using R410A, and most of the exergy destruction was attributed to the pump power consumption. The condenser consistently exhibited the highest exergy destruction rates across all evaporation temperatures for all working fluids, dominating the system's overall exergy losses. Although evaporator exergy destruction increased at a higher rate with increasing evaporation temperatures, increasing from 7 % to 12 % when the evaporation temperature increased from 70 °C to 110 °C for R452B, its contribution remained secondary to the condenser. Across all tested working fluids and evaporation temperatures, the condenser's exergy destruction proportion, in relation to the overall system exergy destruction rate, remained greater than 80 %. This is attributed to the large temperature gradients, simultaneous phase changes, and environmental heat losses. In the dynamic numerical study, the condenser accounted for 87.63 % of the total exergy destruction, using R452B at 70 °C, while in the experimental study using R410A as the working fluid, the condenser retained 86.64 % of the total exergy destruction proportion, at a mass flow rate and evaporation temperature of 10 g/s and 75 °C, respectively.

- Higher mass flow rates and evaporation temperatures were found to enhance heat transfer rates, degree of superheat, and overall system efficiency. Key minimum evaporation temperature thresholds, specific to each mass flow rate, were identified, below which pump pressure differential supported expander rotation, leading to negative system performance metrics. Hence, it is concluded that the evaporation temperature be kept above the identified thresholds to obtain useful

net-work output. A maximum experimental system performance, using R410A, of 501.44 W, 7.29%, 7.67%, and 8.38% were achieved for the net-work output, thermal efficiency, cryogenic energy efficiency, and exergy efficiency, respectively, at the highest working fluid mass flow rate of 16 g/s and evaporation temperature of 75 °C, emphasising the importance of parametric optimisation in improving system performance. The cryogenic-enhanced prototype developed in this study outperformed its counterpart non-cryogenic ORC prototypes found in literature, achieving higher system performance metrics at lower mass flow rates and heat source temperatures, evidenced by Table 5.2.

- The comparative analysis of the prototype cryogenic-enhanced ORC, utilising non flammability hydrofluorocarbon working fluid R410A, developed in this study and the prototype developed by Tian et al. [105], utilising highly flammable hydrocarbon propane as the working fluid, revealed that low flammability hydrofluorocarbon working fluids can compete with traditional hydrocarbon working fluids for cryogenic-enhanced ORCs. At a heat source temperature of 50 °C, Ref. [105]'s prototype system achieved a net-work and thermal efficiency of 281 W and 2.7 %, respectively, while the prototype in this study achieved 271.6 W and 4.18 %, respectively. The differences in the cryogenic energy and exergy performances were revealed to be caused by the high condensation temperatures in Ref. [105]'s study, up to 8.9 °C compared to -88 °C in this study. This resulted in the cryogenic medium retaining much of the high-quality cryogenic exergy, evidenced by the cryogenic medium condenser outlet exhaust temperature of -38.9 °C compared to 11 °C in this study, and, hence, requiring additional heating. These results verified the viability of low flammability hydrofluorocarbon working fluids for cryogenic-enhanced ORCs while addressing safety concerns effectively.

- The exhaust temperature of the regasified cryogenic fuel exhibited a direct dependency on the evaporation temperature, underscoring the cryogenic ORC's potential for operational flexibility in downstream applications. Through the experimental analysis, it was revealed that the exhaust temperature of the cryogenic cooling medium at the condenser outlet increased from -13 °C to 5 °C

as the ORC working fluid evaporation temperature increased from 15 °C to 75 °C. Literature search revealed the importance of preheating of cryogenic fuels, such as hydrogen and ammonia, for end-use application enhancement. Thus, the cryogenic-enhanced ORC provides valuable preheating opportunities contributing to comprehensive system integration by leveraging waste thermal and cryogenic energy reutilisation for power generation applications. The results suggest that at higher heat source temperatures, the preheating of the regasified cryogenic fuel can be intensified, thus leading to increasingly efficient holistic system integration of the cryogenic-enhanced ORC.

- Variations in system charge had distinct impacts on performance, influenced by the fixed volume of the ORC system and the density of the working fluids. Overcharging, especially in low-density fluids, led to reduced heat exchange efficiency, increased pump power consumption, and elevated exergy destruction due to liquid receiver overfilling. It was revealed that high density working fluids, such as R410A, could tolerate slight overcharging, up to 10 %, whereas low density working fluids, such as R452B, suffer immediate performance detriments. R410A, when overcharged by 20 %, exhibited a net-work decrease of 16.67 %, while R452B, at 10 % overcharging, showed a 47.18 % decrease in net-work output. Undercharging, up to -30 %, had negligible effects on system performance but further undercharging eventually caused pump cavitation and critical system failure as the liquid supply to the pump diminished. These findings emphasised the importance of precise charge determination based on the fixed ORC system volume and fluid properties. Combined with the higher performance of low-density hydrofluorocarbon working fluids, it is concluded that system charge identification should be included as a priority during cryogenic-enhanced ORC design process.
- The environmental viability of working fluids was contingent on leak prevention practices and global warming potential (GWP) limits. Strict protocols, the Lloyds Register scenario, only allowed annual hydrofluorocarbon leakage rates of 3 %, while more lenient regulations, the DNV scenario, allowed annual leakage rates of

10 %. Analysis revealed that stringent Lloyd's Register standards reduced emissions by 65% for high-GWP fluids like R410A, whereas relaxed DNV standards achieved up to 87% reductions with low-GWP fluids like R455A. These findings highlighted the necessity for global regulatory alignment and standardisation to ensure consistent emission reduction metrics.

This research brings together the increasingly important theme of system integration and energy efficiency enhancement of cryogenic liquid low-carbon fuels by integrating cryogenic-enhanced ORCs with low flammability HFCs to enhance safety while not compromising on system performance. This study presents as an important factor during alternative fuel system integration, providing avenues for maximising balance of plant efficiency while furthering the decarbonisation goals. Hence, cryogenic-enhanced ORCs could serve as an energy efficiency device towards the ultimate goal of Net Zero by 2050, as stated by the IMO.

7.2 Future work

Based on the numerical and experimental investigations in this research, the following future research avenues could be explored:

- The validated dynamic numerical model should be integrated with advanced AI and machine learning algorithms to employ a simultaneous multi-parameter and multi-objective paradigm for low flammability hydrofluorocarbon working fluids for cryogenic-enhanced ORCs. This would enable optimal design approach towards prototype sizing and development.
- Advanced performance prediction digital twin of the cryogenic-enhanced ORC should be developed, linked to the experimental test rig, through feedback loops and Artificial Neural Network. This would facilitate the upscaling of the prototype system without requiring the need for complex thermodynamic calculations, while also providing real-time input optimisation of system operation parameters to the system.

- Further studies to gauge the feasibility of balance of plant integration and system enhancement of cryogenic-enhanced ORCs for various applications, such as marine applications, refuelling stations, power generation plants etc., should be conducted.

These further research avenues would address the limitations of this study such as multi-objective optimisation and component sizing through AI applicability rather than traditional calculation-based system design.

References

1. UK P. Climate change act 2008. London, UK. 2008.
2. UK P. The Climate Change Act 2008 (2050 Target Amendment) Order 2019. 2019.
3. Agreement P, editor Paris agreement. report of the conference of the parties to the United Nations framework convention on climate change (21st session, 2015: Paris) Retrived December; 2015: HeinOnline.
4. Government H. The ten point plan for a green industrial revolution. Tech rep. 2020.
5. DESNZ. 2022 UK Greenhouse Gas Emissions Final Figures 2024 [Available from: https://assets.publishing.service.gov.uk/media/65c0d15863a23d0013c821e9/2022-final-greenhouse-gas-emissions-statistical-release.pdf.
6. DESNZ. Energy Trends UK, January to March 2024 2024 [Available from: https://assets.publishing.service.gov.uk/media/667c1741aec8650b10090082/Energy_Trends_June_2024.pdf.
7. GOV.UK. Government sets out path to zero emission vehicles by 2035 2023 [Available from: https://www.gov.uk/government/news/government-sets-out-path-to-zero-emission-vehicles-by-2035.
8. Committee CC. The sixth carbon budget: the UK's path to net zero. 2020.
9. Deniz C, Zincir B. Environmental and economical assessment of alternative marine fuels. Journal of Cleaner Production. 2016;113:438-49.
10. Ampah JD, Yusuf AA, Afrane S, Jin C, Liu H. Reviewing two decades of cleaner alternative marine fuels: Towards IMO's decarbonization of the maritime transport sector. Journal of Cleaner Production. 2021;320:128871.
11. Faber J, Hanayama S, Zhang S, Pereda P, Comer B, Hauerhof E, et al. Reduction of GHG emissions from ships—Fourth IMO GHG study 2020—Final report. IMO MEPC. 2020;75(7):15.
12. IMO. Adoption of the initial IMO strategy on reduction of GHG emissions from ships and existing IMO activity related to reducing GHG emissions in the shipping sector. IMO London; 2018.

13. Goulielmos AM. The Initial 40 Years of the EC Maritime Policy, Part I: 1957-1997: Is EU-27 Maritime Industry “Fit for 55”? Modern Economy. 2022;13(2):159-85.
14. Comer B, Osipova L. Accounting for well-to-wake carbon dioxide equivalent emissions in maritime transportation climate policies. The International Council on Clean Transportation (ICCT): Washington, DC, USA. 2021.
15. Farrukh S, Li M, Kouris GD, Wu D, Dearn K, Yerasimou Z, et al. Pathways to Decarbonization of Deep-Sea Shipping: An Aframax Case Study. Energies. 2023;16(22):7640.
16. Kersey J, Popovich ND, Phadke AA. Rapid battery cost declines accelerate the prospects of all-electric interregional container shipping. Nature Energy. 2022;7(7):664-74.
17. Minnehan JJ, Pratt JW. Practical application limits of fuel cells and batteries for zero emission vessels. Sandia National Lab.(SNL-NM), Albuquerque, NM (United States); 2017.
18. Balcombe P, Brierley J, Lewis C, Skatvedt L, Speirs J, Hawkes A, et al. How to decarbonise international shipping: Options for fuels, technologies and policies. Energy conversion management. 2019;182:72-88.
19. Mukherjee A, Bruijnincx P, Junginger M. A perspective on biofuels use and CCS for GHG mitigation in the marine sector. Iscience. 2020;23(11):101758.
20. Ammar NR. An environmental and economic analysis of methanol fuel for a cellular container ship. Transportation Research Part D: Transport and Environment. 2019;69:66-76.
21. Radonja R, Bebić D, Glujić D. Methanol and ethanol as alternative fuels for shipping. Promet-Traffic&Transportation. 2019;31(3):321-7.
22. Liu M, Li C, Koh EK, Ang Z, Lam JSL, editors. Is methanol a future marine fuel for shipping? Journal of Physics: Conference Series; 2019: IOP Publishing.
23. Svanberg M, Ellis J, Lundgren J, Landälv IJR, Reviews SE. Renewable methanol as a fuel for the shipping industry. Renewable Sustainable Energy Reviews. 2018;94:1217-28.
24. Bernatik A, Senovsky P, Pitt M. LNG as a potential alternative fuel–safety and security of storage facilities. Journal of loss prevention in the process industries. 2011;24(1):19-24.

25. Burel F, Taccani R, Zuliani N. Improving sustainability of maritime transport through utilization of Liquefied Natural Gas (LNG) for propulsion. Energy. 2013;57:412-20.

26. Statista. Number of liquefied natural gas storage vessels worldwide from 2010 to 2023 2024 [Available from: https://www.statista.com/statistics/468412/global-lng-tanker-fleet/#:~:text=The%20global%20liquefied%20natural%20gas,2011%2C%20figures%20have%20steadily%20increased.

27. Net D. IMO Marine Engine Regulations 2018 [Available from: https://www.dieselnet.com/standards/inter/imo.php.

28. Yoo B-Y. Economic assessment of liquefied natural gas (LNG) as a marine fuel for CO2 carriers compared to marine gas oil (MGO). Energy. 2017;121:772-80.

29. Balcombe P, Staffell I, Kerdan IG, Speirs JF, Brandon NP, Hawkes AD. How can LNG-fuelled ships meet decarbonisation targets? An environmental and economic analysis. Energy. 2021;227:120462.

30. Hwang S, Jeong B, Jung K, Kim M, Zhou P. Life cycle assessment of LNG fueled vessel in domestic services. Journal of Marine Science Engineering. 2019;7(10):359.

31. DESNZ. UK Hydrogen Strategy 2021 [Available from: https://assets.publishing.service.gov.uk/media/64c7e8bad8b1a70011b05e38/UK-Hydrogen-Strategy_web.pdf.

32. Teoh YH, How HG, Le TD, Nguyen HT, Loo DL, Rashid T, et al. A review on production and implementation of hydrogen as a green fuel in internal combustion engines. Fuel. 2023;333:126525.

33. Aminudin M, Kamarudin S, Lim B, Majilan E, Masdar M, Shaari N. An overview: Current progress on hydrogen fuel cell vehicles. International Journal of Hydrogen Energy. 2023;48(11):4371-88.

34. Sun Z, Hong J, Zhang T, Sun B, Yang B, Lu L, et al. Hydrogen engine operation strategies: recent progress, industrialization challenges, and perspectives. International Journal of Hydrogen Energy. 2023;48(1):366-92.

35. DNV. Energy transition outlook 2019: Maritime forecast to 2050. 2020.

36. Giddey S, Badwal S, Munnings C, Dolan M. Ammonia as a renewable energy transportation media. ACS Sustainable Chemistry & Engineering. 2017;5(11):10231-9.

37. Zhang Y, Zhao N, Li M, Xu Z, Wu D, Hillmansen S, et al. A techno-economic analysis of ammonia-fuelled powertrain systems for rail freight. Transportation Research Part D: Transport and Environment. 2023;119:103739.

38. Pospíšil J, Charvát P, Arsenyeva O, Klimeš L, Špiláček M, Klemeš JJ. Energy demand of liquefaction and regasification of natural gas and the potential of LNG for operative thermal energy storage. Renewable and Sustainable Energy Reviews. 2019;99:1-15.

39. Cardella U, Decker L, Klein H. Roadmap to economically viable hydrogen liquefaction. International Journal of Hydrogen Energy. 2017;42(19):13329-38.

40. Al-Breiki M, Bicer Y. Technical assessment of liquefied natural gas, ammonia and methanol for overseas energy transport based on energy and exergy analyses. International journal of hydrogen energy. 2020;45(60):34927-37.

41. Song Q, Tinoco RR, Yang H, Yang Q, Jiang H, Chen Y, et al. A comparative study on energy efficiency of the maritime supply chains for liquefied hydrogen, ammonia, methanol and natural gas. Carbon Capture Science & Technology. 2022;4:100056.

42. Shukuya M. Exergy concept and its application to the built environment. Building and Environment. 2009;44(7):1545-50.

43. Lemmon EW, Bell IH, Huber M, McLinden M. NIST standard reference database 23: reference fluid thermodynamic and transport properties-REFPROP, Version 10.0, National Institute of Standards and Technology. Standard Reference Data Program, Gaithersburg. 2018.

44. Farrukh S, Wu D, Al-Dadah R, Gao W, Wang Z. A review of integrated cryogenic energy assisted power generation systems and desalination technologies. Applied Thermal Engineering. 2022:119836.

45. Wang F, Wang L, Zhang H, Xia L, Miao H, Yuan J. Design and optimization of hydrogen production by solid oxide electrolyzer with marine engine waste heat recovery and ORC cycle. Energy Conversion and Management. 2021;229:113775.

46. Baroutaji A, Arjunan A, Ramadan M, Robinson J, Alaswad A, Abdelkareem MA, et al. Advancements and prospects of thermal management and waste heat recovery of PEMFC. International Journal of Thermofluids. 2021;9:100064.

47. Wilberforce T, Olabi A, Muhammad I, Alaswad A, Sayed ET, Abo-Khalil AG, et al. Recovery of waste heat from proton exchange membrane fuel cells–A review. International Journal of Hydrogen Energy. 2024;52:933-72.

48. Lion S, Vlaskos I, Taccani R. A review of emissions reduction technologies for low and medium speed marine Diesel engines and their potential for waste heat recovery. Energy Conversion and Management. 2020;207:112553.

49. Wang S, Li Y, Fu J, Liu J, Dong H, Tong J. Quantitative investigation of the effects of EGR strategies on performance, cycle-to-cycle variations and emissions characteristics of a higher compression ratio and heavy-duty NGSI engine fueled with 99% methane content. Fuel. 2020;263:116736.

50. Long Y, Li G, Zhang Z, Liang J. Application of reformed exhaust gas recirculation on marine LNG engines for NOx emission control. Fuel. 2021;291:120114.

51. Bosma P, Nagelvoort RK, editors. Liquefaction technology; developments through history. Proceedings of the 1st annual gas processing symposium; 2009: Elsevier.

52. Griepentrog H, Sackarendt P, editors. Vaporization of LNG with closed-cycle gas turbines. Turbo Expo: Power for Land, Sea, and Air; 1976: American Society of Mechanical Engineers.

53. Krey G. Utilization of the cold by LNG vaporization with closed-cycle gas turbine. Journal of Engineering for gas turbines and power. 1980.

54. Angelino G. The use of liquid natural gas as heat sink for power cycles. Journal of Engineering for gas turbines and power. 1978.

55. Karashima N, Akutsu T, editors. Development of LNG cryogenic power generation plant. Proc, Intersoc Energy Convers Eng Conf;(United States); 1982: The Tokyo Electric Power Co., Inc., Tokyo.

56. K. K. LNG cold energy for power generation plants. Turbo Machine. 1983.

57. Wu D, Tsougranis E-L. LNG Cryogenic Energy Technologies. Advances in Energy Research: Nova Science Publishers; 2020.

58. H. A. Expansion turbines for LNG cold energy driven power generation. Turbo Machine. 1987.

59. Kanagawa T. Japan's LNG utilization and environmental efforts. The Japan Gas Association: Tokyo, Japan. 2008.

60. Najjar Y. A cryogenic gas turbine engine using hydrogen for waste heat recovery and regasification of LNG. International journal of hydrogen energy. 1991;16(2):129-34.
61. Najjar YS, Zaamout MS. Cryogenic power conversion with regasification of LNG in a gas turbine plant. Energy Conversion & Management. 1993;34(4).
62. Uchiyama Y, Hirayama S, Sato T. Liquid air energy storage gasturbine power generation system.; Hiqh efficiency power generation system utilizing liquid natural gas refrigerstion. Ekitai kuki chozo gas turbine hatsuden system.; LNG reinetsu wo riyoshita kokoritsu hatsuden system. Enerugi, Shigen. 1991;12(6).
63. Wong W. LNG power recovery. Proceedings of the Institution of Mechanical Engineers, Part A: Journal of Power and Energy. 1994;208(1):3-12.
64. Chiesa P, editor LNG receiving terminal associated with gas cycle power plants. The 42nd ASME International Gas Turbine & Aeroengine Congress and Exposition; 1997.
65. Bisio G, Pisoni C. Thermodynamic analysis of solar energy utilization combined with the exploitation of the LNG physical exergy. Journal of solar energy engineering. 1995.
66. Hisazumi Y, Yamasaki Y, Sugiyama S. Proposal for a high efficiency LNG power-generation system utilizing waste heat from the combined cycle. Applied Energy. 1998;60(3):169-82.
67. Liu H, You L. Characteristics and applications of the cold heat exergy of liquefied natural gas. Energy conversion & management. 1999;40(14):1515-25.
68. Xue F, Chen Y, Ju Y. A review of cryogenic power generation cycles with liquefied natural gas cold energy utilization. Frontiers in Energy. 2016;10(3):363-74.
69. Franco A, Giovannini C. Optimal design of direct expansion systems for electricity production by LNG cold energy recovery. Energy. 2023;280:128173.
70. Franco A, Casarosa C. Thermodynamic analysis of direct expansion configurations for electricity production by LNG cold energy recovery. Applied Thermal Engineering. 2015;78:649-57.
71. Tsatsaronis G, Morosuk T. Advanced exergetic analysis of a novel system for generating electricity and vaporizing liquefied natural gas. Energy. 2010;35(2):820-9.
72. Gómez MR, Garcia RF, Gómez JR, Carril JC. Review of thermal cycles exploiting the exergy of liquefied natural gas in the regasification process. Renewable and Sustainable Energy Reviews. 2014;38:781-95.

73. Tian Z, Yue Y, Gu B, Gao W, Zhang Y. Thermo-economic analysis and optimization of a combined Organic Rankine Cycle (ORC) system with LNG cold energy and waste heat recovery of dual-fuel marine engine. International Journal of Energy Research. 2020;44(13):9974-94.
74. He T, Ma H, Ma J, Mao N, Liu Z. Effects of cooling and heating sources properties and working fluid selection on cryogenic organic Rankine cycle for LNG cold energy utilization. Energy Conversion and Management. 2021;247:114706.
75. Tsougranis EL, Wu D. A feasibility study of Organic Rankine Cycle (ORC) power generation using thermal and cryogenic waste energy on board an LNG passenger vessel. International Journal of Energy Research. 2018;42(9):3121-42.
76. Sun Z, Wang S, Xu F, He W. Multi-parameter optimization and fluid selection guidance of a two-stage organic Rankine cycle utilizing LNG cold energy and low grade heat. Energy Procedia. 2017;142:1222-9.
77. Mahmoudi A, Fazli M, Morad M. A recent review of waste heat recovery by Organic Rankine Cycle. Applied Thermal Engineering. 2018;143:660-75.
78. Rao W-J, Zhao L-J, Liu C, Zhang M-G. A combined cycle utilizing LNG and low-temperature solar energy. Applied thermal engineering. 2013;60(1-2):51-60.
79. Liu Y, Guo K, editors. Efficiency of power generation by LNG cold energy. 2010 Asia-Pacific Power and Energy Engineering Conference; 2010: IEEE.
80. Liu Y, Guo K. A novel cryogenic power cycle for LNG cold energy recovery. Energy. 2011;36(5):2828-33.
81. Sun Z, Lai J, Wang S, Wang T. Thermodynamic optimization and comparative study of different ORC configurations utilizing the exergies of LNG and low grade heat of different temperatures. Energy. 2018;147:688-700.
82. Sun Z, Zhang H, Zhang T, Lin L, Lin K. Optimizations and comparison of three two-stage Rankine cycles under different heat source temperatures and NG distribution pressures. Energy Conversion & Management. 2020;209:112655.
83. Xue X, Guo C, Du X, Yang L, Yang Y. Thermodynamic analysis and optimization of a two-stage organic Rankine cycle for liquefied natural gas cryogenic exergy recovery. Energy. 2015;83:778-87.

84. Ghaebi H, Namin AS, Rostamzadeh H. Exergoeconomic optimization of a novel cascade Kalina/Kalina cycle using geothermal heat source and LNG cold energy recovery. Journal of Cleaner Production. 2018;189:279-96.
85. Choi I-H, Lee S, Seo Y, Chang D. Analysis and optimization of cascade Rankine cycle for liquefied natural gas cold energy recovery. Energy. 2013;61:179-95.
86. Nami H, Ertesvåg IS, Agromayor R, Riboldi L, Nord LO. Gas turbine exhaust gas heat recovery by organic Rankine cycles (ORC) for offshore combined heat and power applications-Energy and exergy analysis. Energy. 2018;165:1060-71.
87. Li P, Li J, Pei G, Munir A, Ji J. A cascade organic Rankine cycle power generation system using hybrid solar energy and liquefied natural gas. Solar Energy. 2016;127:136-46.
88. Bao J, Zhao L. A review of working fluid and expander selections for organic Rankine cycle. Renewable and sustainable energy reviews. 2013;24:325-42.
89. Linke P, Papadopoulos AI, Seferlis P. Systematic methods for working fluid selection and the design, integration and control of organic Rankine cycles—A review. Energies. 2015;8(6):4755-801.
90. Emadi MA, Chitgar N, Oyewunmi OA, Markides CN. Working-fluid selection and thermoeconomic optimisation of a combined cycle cogeneration dual-loop organic Rankine cycle (ORC) system for solid oxide fuel cell (SOFC) waste-heat recovery. Applied Energy. 2020;261:114384.
91. Sun H, Zhu H, Liu F, Ding H. Simulation and optimization of a novel Rankine power cycle for recovering cold energy from liquefied natural gas using a mixed working fluid. Energy. 2014;70:317-24.
92. Yu H, Kim D, Hu X, Gundersen T. Organic Rankine cycle with pure and mixed working fluids for LNG cold energy recovery. Chemical Engineering Transactions. 2019.
93. Kim K, Lee U, Kim C, Han C. Design and optimization of cascade organic Rankine cycle for recovering cryogenic energy from liquefied natural gas using binary working fluid. Energy. 2015;88:304-13.
94. Bao J, Lin Y, Zhang R, Zhang X, Zhang N, He G. Performance enhancement of two-stage condensation combined cycle for LNG cold energy recovery using zeotropic mixtures. Energy. 2018;157:588-98.

95. Tian Z, Zeng W, Gu B, Zhang Y, Yuan X. Energy, exergy, and economic (3E) analysis of an organic Rankine cycle using zeotropic mixtures based on marine engine waste heat and LNG cold energy. Energy Conversion & Management. 2021;228:113657.
96. Zhang J, Zhang H, Yang K, Yang F, Wang Z, Zhao G, et al. Performance analysis of regenerative organic Rankine cycle (RORC) using the pure working fluid and the zeotropic mixture over the whole operating range of a diesel engine. Energy conversion and management. 2014;84:282-94.
97. Song J, Gu C-w. Analysis of ORC (Organic Rankine Cycle) systems with pure hydrocarbons and mixtures of hydrocarbon and retardant for engine waste heat recovery. Applied Thermal Engineering. 2015;89:693-702.
98. Garg P, Kumar P, Srinivasan K, Dutta P. Evaluation of carbon dioxide blends with isopentane and propane as working fluids for organic Rankine cycles. Applied Thermal Engineering. 2013;52(2):439-48.
99. Farrukh S, Wu D, Taskin A, Dearn K. Cryogenic energy assisted power generation utilizing low flammability refrigerants. Energy. 2024;307:132770.
100. Lee Y, Kim J, Ahmed U, Kim C, Lee Y-W. Multi-objective optimization of Organic Rankine Cycle (ORC) design considering exergy efficiency and inherent safety for LNG cold energy utilization. Journal of Loss Prevention in the Process Industries. 2019;58:90-101.
101. Yuan T, Song C, Zhang R, Zhang X, Zhang N, Bao J. Energy and Economic Optimization of the Multistage Condensation Rankine Cycle That Utilizes LNG Cold Energy: Considerations on Working Fluids and Cycle Configurations. ACS Sustainable Chemistry & Engineering. 2019;7(15):13505-16.
102. Han F, Wang Z, Ji Y, Li W, Sunden B. Energy analysis and multi-objective optimization of waste heat and cold energy recovery process in LNG-fueled vessels based on a triple organic Rankine cycle. Energy Conversion & Management. 2019;195:561-72.
103. Mehrpooya M, Ashouri M, Mohammadi A. Thermoeconomic analysis and optimization of a regenerative two-stage organic Rankine cycle coupled with liquefied natural gas and solar energy. Energy. 2017;126:899-914.

104. Yi Li DW, Raya Al-Dadah, Wenzhong Gao. Mixtures of hydrocarbon refrigerant and fire retardant as working fluids for an Organic Rankine cycle system assisted with LNG cryogenic energy. International Conference on Applied Energy 2020.
105. Tian Z, Gan W, Qi Z, Tian M, Gao W. Experimental study of organic Rankine cycle with three-fluid recuperator for cryogenic cold energy recovery. Energy. 2022;242:122550.
106. Agazzani A, Massardo A, Korakianitis T. An assessment of the performance of closed cycles with and without heat rejection at cryogenic temperatures. Journal of Engineering for gas turbines and power. 1999.
107. Angelino G, Invernizzi CM. The role of real gas Brayton cycles for the use of liquid natural gas physical exergy. Applied Thermal Engineering. 2011;31(5):827-33.
108. Gómez MR, Garcia RF, Gómez JR, Carril JC. Thermodynamic analysis of a Brayton cycle and Rankine cycle arranged in series exploiting the cold exergy of LNG (liquefied natural gas). Energy. 2014;66:927-37.
109. Dispenza C, Dispenza G, La Rocca V, Panno G. Exergy recovery during LNG regasification: Electric energy production–Part one. Applied Thermal Engineering. 2009;29(2-3):380-7.
110. Dispenza C, Dispenza G, La Rocca V, Panno G. Exergy recovery during LNG regasification: electric energy production–part two. Applied thermal engineering. 2009;29(2-3):388-99.
111. Morosuk T, Tsatsaronis G. Comparative evaluation of LNG–based cogeneration systems using advanced exergetic analysis. Energy. 2011;36(6):3771-8.
112. Salimpour M, Zahedi M. Proposing a novel combined cycle for optimal exergy recovery of liquefied natural gas. Heat & Mass Transfer. 2012;48(8):1309-17.
113. Ma J, Song X, Zhang B, Mao N, He T. Optimal design of dual-stage combined cycles to recover LNG cold energy and low-temperature waste thermal energy for sustainable power generation. Energy Conversion and Management. 2022;269:116141.
114. Gómez MR, Garcia RF, Carril JC, Gómez JR. High efficiency power plant with liquefied natural gas cold energy utilization. Journal of the Energy Institute. 2014;87(1):59-68.

115. Cao Y, Ren J, Sang Y, Dai Y. Thermodynamic analysis and optimization of a gas turbine and cascade CO2 combined cycle. Energy Conversion & Management. 2017;144:193-204.
116. Cha S-H, Na S-I, Lee YH, Kim MS. Thermodynamic analysis of a gas turbine inlet air cooling and recovering system in gas turbine and CO2 combined cycle using cold energy from LNG terminal. Energy Conversion & Management. 2021;230:113802.
117. Moghimi M, Rashidzadeh S, Hosseinalipour SM, Khosravian M. Exergy and energy analysis of a novel power cycle utilizing the cold energy of liquefied natural gas. Heat & Mass Transfer. 2019;55(11):3327-42.
118. Shi X, Che D. Thermodynamic analysis of an LNG fuelled combined cycle power plant with waste heat recovery and utilization system. International journal of energy research. 2007;31(10):975-98.
119. She X, Zhang T, Cong L, Peng X, Li C, Luo Y, et al. Flexible integration of liquid air energy storage with liquefied natural gas regasification for power generation enhancement. Applied Energy. 2019;251:113355.
120. Kalina AI. Combined-cycle system with novel bottoming cycle. Journal of Engineering for gas turbines and power. 1984.
121. Wang J, Yan Z, Wang M, Dai Y. Thermodynamic analysis and optimization of an ammonia-water power system with LNG (liquefied natural gas) as its heat sink. Energy. 2013;50:513-22.
122. El-Sayed Y, Tribus M. A theoretical comparison of the Rankine and Kalina cycles. ASME publication AES. 1985;1:97-102.
123. Ibrahim MB, Kovach RM. A Kalina cycle application for power generation. Energy. 1993;18(9):961-9.
124. Marston CH, Hyre M. Gas turbine bottoming cycles: triple-pressure steam versus Kalina. Journal of Engineering for gas turbines and power. 1995.
125. Madhawa Hettiarachchi H, Golubovic M, Worek WM, Ikegami Y. The performance of the Kalina cycle system 11 (KCS-11) with low-temperature heat sources. Journal of energy resources technology. 2007.
126. Usvika R, Rifaldi M, Noor A. Energy and exergy analysis of kalina cycle system (KCS) 34 with mass fraction ammonia-water mixture variation. Journal of mechanical science and technology. 2009;23(7):1871-6.

127. Arslan O. Exergoeconomic evaluation of electricity generation by the medium temperature geothermal resources, using a Kalina cycle: Simav case study. International journal of thermal sciences. 2010;49(9):1866-73.
128. Arslan O. Power generation from medium temperature geothermal resources: ANN-based optimization of Kalina cycle system-34. Energy. 2011;36(5):2528-34.
129. Lolos P, Rogdakis E. A Kalina power cycle driven by renewable energy sources. Energy. 2009;34(4):457-64.
130. Shi X, Che D. A combined power cycle utilizing low-temperature waste heat and LNG cold energy. Energy conversion & management. 2009;50(3):567-75.
131. Kim KC, Ha JM, Kim KH. Exergy analysis of a combined power cycle using low-grade heat source and LNG cold energy. International Journal of Exergy. 2015;17(3):374-400.
132. Zhang L, Pan Z, Zhang Z, Shang L, Wen J, Chen S. Thermodynamic and Economic Analysis Between Organic Rankine Cycle and Kalina Cycle for Waste Heat Recovery From Steam-Assisted Gravity Drainage Process in Oilfield. Journal of Energy Resources Technology. 2018;140(12).
133. Abdolalipouradl M, Khalilarya S, Jafarmadar S. Exergoeconomic analysis of a novel integrated transcritical CO2 and Kalina 11 cycles from Sabalan geothermal power plant. Energy Conversion & Management. 2019;195:420-35.
134. Fang Z, Shang L, Pan Z, Yao X, Ma G, Zhang Z. Exergoeconomic analysis and optimization of a combined cooling, heating and power system based on organic Rankine and Kalina cycles using liquified natural gas cold energy. Energy Conversion & Management. 2021;238:114148.
135. Mosaffa A, Mokarram NH, Farshi LG. Thermoeconomic analysis of a new combination of ammonia/water power generation cycle with GT-MHR cycle and LNG cryogenic exergy. Applied Thermal Engineering. 2017;124:1343-53.
136. Li Y, Liu Y, Zhang G, Yang Y. Thermodynamic analysis of a novel combined cooling and power system utilizing liquefied natural gas (LNG) cryogenic energy and low-temperature waste heat. Energy. 2020;199:117479.
137. Ghorbani B, Ebrahimi A, Rooholamini S, Ziabasharhagh M. Pinch and exergy evaluation of Kalina/Rankine/gas/steam combined power cycles for tri-generation of

power, cooling and hot water using liquefied natural gas regasification. Energy Conversion & Management. 2020;223:113328.

138. Ghorbani B, Ebrahimi A, Ziabasharhagh M. Novel integrated CCHP system for generation of liquid methanol, power, cooling and liquid fuels using Kalina power cycle through liquefied natural gas regasification. Energy Conversion & Management. 2020;221:113151.

139. Parikhani T, Gholizadeh T, Ghaebi H, Sadat SMS, Sarabi M. Exergoeconomic optimization of a novel multigeneration system driven by geothermal heat source and liquefied natural gas cold energy recovery. Journal of cleaner production. 2019;209:550-71.

140. Ayou DS, Eveloy V. Integration of Municipal Air-Conditioning, Power, and Gas Supplies Using an LNG Cold Exergy-Assisted Kalina Cycle System. Energies. 2020;13(18):4599.

141. Ansarinasab H, Hajabdollahi H, Fatimah M. Life cycle assessment (LCA) of a novel geothermal-based multigeneration system using LNG cold energy-integration of Kalina cycle, stirling engine, desalination unit and magnetic refrigeration system. Energy. 2021;231:120888.

142. Ebrahimi A, Ghorbani B, Skandarzadeh F, Ziabasharhagh M. Introducing a novel liquid air cryogenic energy storage system using phase change material, solar parabolic trough collectors, and Kalina power cycle (process integration, pinch, and exergy analyses). Energy Conversion & Management. 2021;228:113653.

143. Abdolalipouradl M, Khalilarya S, Jafarmadar S. The thermodynamic analysis of new combined cycle using Sabalan geothermal wells and LNG cold energy. Amirkabir Journal of Mechanical Engineering. 2019;52(6):1413-28.

144. May M. SVM 1x100 2023 [Available from: https://marchmay.co.uk/pumps/svm-range/svm-1x100/.

145. Bowman E. Stainless Steel Heat Exchangers 2023 [Available from: https://ej-bowman.com/products/stainless-steel-heat-exchangers/.

146. Squared A. Scroll Expander 2023 [Available from: https://airsquared.com/products/scroll-expanders/e15h022a-sh/.

147. SWEP. B185 2020 [Available from: https://www.swep.net/products/b185/.

148. Danfoss. Vertical Liquid Receiver 160x345 5.7 litre 2023 [Available from: https://www.hrponline.co.uk/products/system-components/liquid-receivers/123277/liquid-receivers?c=1665.

149. TOOLTEMP. Water temperature control units TT-181 2023 [Available from: https://tool-temp.net/products/water-temperature-control-units/tt-181.html.

150. Cryogenics S. Cryostor 180 2023 [Available from: https://statebourne.info/product/cryostor-180/.

151. Kujak S. Flammability and new refrigerant options. ASHRAE Journal. 2017;59(5):16-23.

152. Lemmon EW, Huber ML, McLinden MOJNsrd. NIST reference fluid thermodynamic and transport properties–REFPROP. 2002;23:v7.

153. Dickes R, Dumont O, Lemort V. Experimental assessment of the fluid charge distribution in an organic Rankine cycle (ORC) power system. Applied Thermal Engineering. 2020;179:115689.

154. IOR. Designing out leaks: Design standards and practices. Institute of Refrigeration. 2015 [Available from: https://ior.org.uk/public/downloads/sLXdl/REAL%20Zero%20GN3_2015.pdf.

155. Software SDI. Simcenter Amesim 2020.1. 2020.

156. Gnielinski V. New equations for heat and mass transfer in turbulent pipe and channel flow. International chemical engineering. 1976;16(2):359-67.

157. Churchill SW. Comprehensive correlating equations for heat, mass and momentum transfer in fully developed flow in smooth tubes. Industrial & Engineering Chemistry Fundamentals. 1977;16(1):109-16.

158. Shah MM. A general correlation for heat transfer during film condensation inside pipes. International Journal of heat and mass transfer. 1979;22(4):547-56.

159. Chen JC. Correlation for boiling heat transfer to saturated fluids in convective flow. Industrial & engineering chemistry process design and development. 1966;5(3):322-9.

160. McAdams W. Vaporization inside horizontal tubes-II Benzene-oil mixtures. Trans ASME. 1949;39:39-48.

161. Protocol M. Montreal protocol on substances that deplete the ozone layer. Washington, DC: US Government Printing Office. 1987;26:128-36.

162. Breidenich C, Magraw D, Rowley A, Rubin JW. The Kyoto protocol to the United Nations framework convention on climate change. American Journal of International Law. 1998;92(2):315-31.
163. Regulation (Ec) No 842/2006 of the European Parliament and of the Council of 17 May 2006 on certain fluorinated greenhouse gases. , (2006).
164. Regulation (Eu) No 517/2014 of the European Parliament and of the Council of 16 April 2014 on fluorinated greenhouse gases and repealing Regulation (EC), No 842/2006. , (2014).
165. Hafner IA, Gabrielii C, Widell K. Refrigeration units in marine vessels: Alternatives to HCFCs and high GWP HFCs: Nordic Council of Ministers; 2019.
166. Álvarez Pardiñas Á, Gabrielii CH. Implementation of natural refrigerants on cruise ships. A review of rules and regulations from two Classification Societies. 2022.
167. White M, Oyewunmi O, Chatzopoulou M, Pantaleo A, Haslam A, Markides C. Computer-aided working-fluid design, thermodynamic optimisation and thermoeconomic assessment of ORC systems for waste-heat recovery. Energy. 2018;161:1181-98.
168. Fan W, Han Z, Li P, Jia Y. Analysis of the thermodynamic performance of the organic Rankine cycle (ORC) based on the characteristic parameters of the working fluid and criterion for working fluid selection. Energy Conversion and Management. 2020;211:112746.
169. Papas P, Verma P, Lord R, Burns L. Turbulent deflagrations of mildly flammable refrigerant-air mixtures. Journal of Loss Prevention in the Process Industries. 2019;61:255-61.
170. Kim DK, Sunderland PB. Viability of various sources to ignite A2L refrigerants. Energies. 2020;14(1):121.
171. Imamura T, Kamiya K, Sugawa O. Ignition hazard evaluation on A2L refrigerants in situations of service and maintenance. Journal of Loss Prevention in the Process Industries. 2015;36:553-61.
172. Davis S, Pagliaro J, Debold T, Van Wingerden M, Van Wingerden K. Flammability and explosion characteristics of mildly flammable refrigerants. Journal of Loss Prevention in the Process Industries. 2017;49:662-74.

173. Danfoss. A2L refrigerants in commercial refrigeration 2022 [Available from: https://www.danfoss.com/en-gb/about-danfoss/our-businesses/cooling/refrigerants-and-energy-efficiency/a2l-refrigerants-in-commercial-refrigeration/#:~:text=The%20lowest%20flammable%20concentration%20is,for%20an%20A3%20class%20refrigerant.

174. Nami H, Nemati A, Fard FJ. Conventional and advanced exergy analyses of a geothermal driven dual fluid organic Rankine cycle (ORC). Applied thermal engineering. 2017;122:59-70.

175. Yağlı H, Koç Y, Koç A, Görgülü A, Tandiroğlu A. Parametric optimization and exergetic analysis comparison of subcritical and supercritical organic Rankine cycle (ORC) for biogas fuelled combined heat and power (CHP) engine exhaust gas waste heat. Energy. 2016;111:923-32.

176. Tian Z, Chen X, Zhang Y, Gao W, Chen W, Peng H. Energy, conventional exergy and advanced exergy analysis of cryogenic recuperative organic rankine cycle. Energy. 2023;268:126648.

177. Eyerer S, Dawo F, Kaindl J, Wieland C, Spliethoff H. Experimental investigation of modern ORC working fluids R1224yd (Z) and R1233zd (E) as replacements for R245fa. Applied Energy. 2019;240:946-63.

178. Gao P, Jiang L, Wang L, Wang R, Song F. Simulation and experiments on an ORC system with different scroll expanders based on energy and exergy analysis. Applied Thermal Engineering. 2015;75:880-8.

179. Kang SH. Design and experimental study of ORC (organic Rankine cycle) and radial turbine using R245fa working fluid. Energy. 2012;41(1):514-24.

180. Eyerer S, Wieland C, Vandersickel A, Spliethoff H. Experimental study of an ORC (Organic Rankine Cycle) and analysis of R1233zd-E as a drop-in replacement for R245fa for low temperature heat utilization. Energy. 2016;103:660-71.

181. Galloni E, Fontana G, Staccone S. Design and experimental analysis of a mini ORC (organic Rankine cycle) power plant based on R245fa working fluid. Energy. 2015;90:768-75.

182. Bianchi M, Branchini L, De Pascale A, Orlandini V, Ottaviano S, Pinelli M, et al. Experimental performance of a micro-ORC energy system for low grade heat recovery. Energy Procedia. 2017;129:899-906.

183. Carraro G, Bori V, Lazzaretto A, Toniato G, Danieli P. Experimental investigation of an innovative biomass-fired micro-ORC system for cogeneration applications. Renewable Energy. 2020;161:1226-43.
184. Pimm AJ, Cockerill TT, Gale WF. Reducing industrial hydrogen demand through preheating with very high temperature heat pumps. Applied Energy. 2023;347:121464.
185. Yang X, Yang W, Dong S, Tan H. Flame stability analysis of premixed hydrogen/air mixtures in a swirl micro-combustor. Energy. 2020;209:118495.
186. Luo M, Zhang J, Zhang C, Chin CS, Ran H, Fan M, et al. Cold start investigation of fuel cell vehicles with coolant preheating strategy. Applied Thermal Engineering. 2022;201:117816.
187. Uzun A, Bokor B, Eryener D. PEM fuel cell performance with solar air preheating. international journal of hydrogen energy. 2020;45(60):34654-65.
188. Erdemir D, Dincer I. A perspective on the use of ammonia as a clean fuel: Challenges and solutions. International Journal of Energy Research. 2021;45(4).
189. Meng T, Cui D, Shi Y, Ji Y, Cheng M, Tu B, et al. Performance evaluation of high-efficiency SOFC-PEMFC hybrid system fueled by liquid ammonia. International Journal of Hydrogen Energy. 2023;48(79):30887-98.
190. Chen Y, Zhang B, Su Y, Sui C, Zhang J. Effect and mechanism of combustion enhancement and emission reduction for non-premixed pure ammonia combustion based on fuel preheating. Fuel. 2022;308:122017.
191. Nie Z, Huang Y, Lu Z, Tian G, Liu X. Energy efficiency analysis of ammonia-fueled power systems for vehicles considering residual heat recovery. Energy. 2024;312:133338.
192. Winter C-J. Energy efficiency, no: It's exergy efficiency! International journal of hydrogen energy. 2007;32(17):4109-11.
193. Alimoradi A. Study of thermal effectiveness and its relation with NTU in shell and helically coiled tube heat exchangers. Case Studies in Thermal Engineering. 2017;9:100-7.
194. Shahrul I, Mahbubul I, Saidur R, Khaleduzzaman S, Sabri M, Rahman M. Effectiveness study of a shell and tube heat exchanger operated with nanofluids at different mass flow rates. Numerical Heat Transfer, Part A: Applications. 2014;65(7):699-713.

195. Désenfant M, Priel M. Road map for measurement uncertainty evaluation. Measurement. 2006;39(9):841-8.
196. Désenfant M, Priel M. Reference and additional methods for measurement uncertainty evaluation. Measurement. 2017;95:339-44.
197. Brueckner S, Miró L, Cabeza LF, Pehnt M, Laevemann E. Methods to estimate the industrial waste heat potential of regions–A categorization and literature review. Renewable and Sustainable Energy Reviews. 2014;38:164-71.
198. Luberti M, Gowans R, Finn P, Santori G. An estimate of the ultralow waste heat available in the European Union. Energy. 2022;238:121967.
199. Györke G, Groniewsky A, Imre AR. A simple method of finding new dry and isentropic working fluids for organic rankine cycle. Energies. 2019;12(3):480.
200. Tian Z, Zeng W, Gu B, Zhang Y, Yuan X. Energy, exergy, and economic (3E) analysis of an organic Rankine cycle using zeotropic mixtures based on marine engine waste heat and LNG cold energy. Energy Conversion and Management. 2021;228:113657.
201. Shao Y, Soh K, Wan Y, Huang Z, Islam M, Chua K. Multi-objective optimization of a cryogenic cold energy recovery system for LNG regasification. Energy Conversion and Management. 2021;244:114524.
202. Cao S, Miao Z, Xu J. The effect of liquid charge ratio on organic Rankine cycle operation. Applied Thermal Engineering. 2019;162:114227.
203. Hwang Y, Ferreira C, Piao C. Guideline for life cycle climate performance. International Institute of Refrigeration, Paris. 2015.
204. Oyekale J, Emagbetere E. A review of conventional and exergetic life cycle assessments of organic Rankine cycle plants exploiting various low-temperature energy resources. Heliyon. 2022.